Universidade Vigo

Departamento de Ingeniería de los

Recursos Naturales y Medio Ambiente

TESIS DOCTORAL

STUDY OF THE MECHANICAL BEHAVIOR OF INTACT AND JOINTED ROCKS IN LABORATORY WITH PARTICULAR EMPHASIS ON DILATANCY

Complete stress (MPa) – strain (0.1%) curve for fresh, (1+2) jointed and (2+3) jointed specimens (σ_3 = 10 MPa)

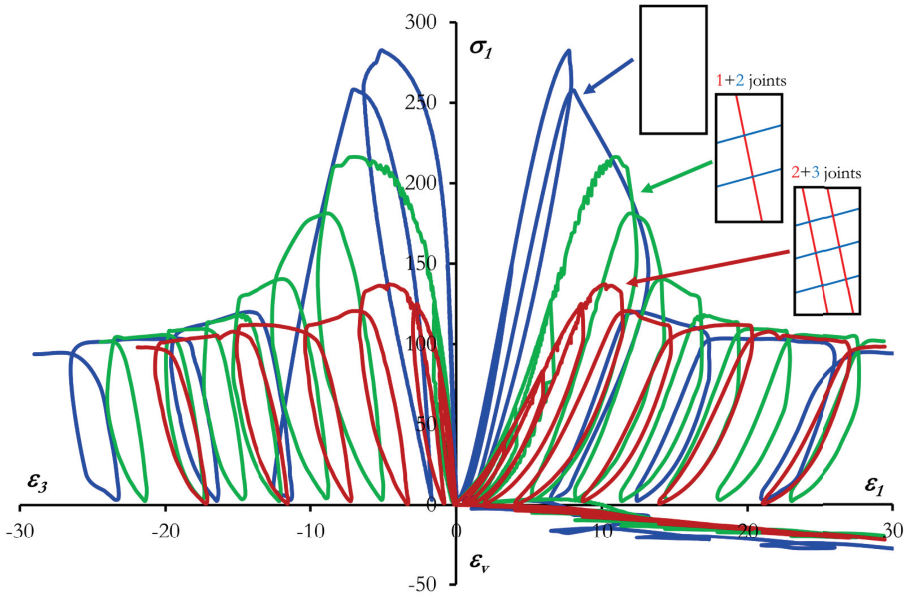

Autor:

Javier Arzúa Touriño

Director:

Leandro R. Alejano Monge

UNIVERSIDADE DE VIGO

Departamento de Ingeniería de los Recursos Naturales y Medio Ambiente

TESIS DOCTORAL

STUDY OF THE MECHANICAL BEHAVIOR OF INTACT AND JOINTED ROCKS IN LABORATORY WITH PARTICULAR EMPHASIS ON DILATANCY

Autor:

Javier Arzúa Touriño

Director:

Leandro R. Alejano Monge

UniversidadeVigo

Autorización defensa tesis de doctorado

Vigo, a 24 de Septiembre de 2015

El director D. Leandro Rafael Alejano Monge de la tesis de doctorado elaborada por D. Javier Arzúa Touriño y con título "Study of the mechanical behavior of intact and jointed rocks in laboratory with particular emphasis on dilatancy".

En cumplimiento de la normativa vigente en la Universidad de Vigo, autoriza al autor para que proceda a su presentación y defensa pública para optar al grado de Doctor por la Universidad de Vigo con Mención Internacional.

Dr. D. Leandro Rafael Alejano Monge

E.T.S. Enxeñaría de Minas
VIGO

Dedicatoria

Para Mamá, Papá, Pili y, desde hace muy poquito, para Alejandro.

Acknowledgements:

The research presented in this thesis has been made possible due to funding from my thesis supervisor, Dr. Leandro Alejano, two professors of the Department of Natural Resources and Environmental Engineering of the University of Vigo, Dr. Teresa Rivas and Dr. Javier Taboada and lately to a doctoral grant provided by the University of Vigo. I would also like to thank the Department of Natural Resources and Environmental Engineering of the University of Vigo for helping me throughout both my undergraduate and graduate education.

There are several people within the Mining Group and the University of Vigo community without whom this work would not be possible: People from the labs —too many to mention you all, but you are on my heart— thank you for creating a very nice environment to work and being always there to lend a helping hand, it helped me to not become insane, and sorry for bothering you with my noisy press; Professors, thank you for helping me with my different and weird questions; Mayka, thank you for being there, without you, the Mining Engineering School of the University of Vigo would not work.

Dr. Gabriel Walton is an outstanding person that came to Vigo for a month aiming to perform some strength tests for finishing his Ph. D., I was amazed by the amount of specimens that he brought along and his ability to catch the working of the press (finally you understood the usefulness of the manual valve). His questions and feedback helped me a lot to improve my understanding of dilation, thank you.

Dr. Carlos Carranza-Torres supported me for a three months research stay at the University of Minnesota, Duluth Campus, during 2012 winter. Apart from the scientific interest of the stay and the (amazing) amount of knowledge that Carlos could explain to me, that was probably one of the history's coldest and snowy winters in Duluth. That weather hugely allowed me —I almost could not get out of Carlos' house— to write and compose the most part of the thesis.

Without question, Dr. Leandro Alejano has surpassed my expectations of what a supervisor could be. Leandro has been a true mentor to me (not only in the geomechanics field) and has provided me with countless opportunities to learn, that otherwise would not have been available. Despite his full agenda, he always answered my questions, corrected my mistakes and focused my work. I cannot adequately express how deeply indebted I am to you.

Finally, I want to thank my parents Domingo and Elena for continuing to be my biggest supporters, and Pili for being the most important person in my world, a caring and loving partner, and for giving me my greatest achievement, Alejandro.

Abstract

Post-failure behavior of rocks and rock masses has not been widely studied in rock engineering, partly by the inherent difficulties in obtaining reliable results and partly because the engineering objective usually is avoiding failure. Nevertheless, there are some applications that require to know the parameters governing this behavior.

Following Farmer (1983) indications, the press of the *John P. Harrison Rock Mechanics' Laboratory* of the *University of Vigo* was modified in order to not only controlling axial force, but also the confining stress and to measure the volumetric strain of the specimen during triaxial tests.

Using this fully servo-controlled press, eight different rocks were tested under unconfined and confined conditions (a total of more than 200 strength tests) reaching, when possible, the residual strength. Furthermore, the tests were performed with unloading-reloading cycles in order to control the softening phase and to obtain the irrecoverable strain locus, which allows to distinguish the elastic and plastic components of the axial and volumetric strains of the specimen.

With the data obtained from the tests and using the formulation proposed by Vermeer & De Borst (1984), the evolution of the dilation angle during the tests was captured. The dilation angle is the most suitable parameter to model the dilatant behavior of a material and one of the required parameters in order to simulate the post-failure behavior of rocks and rock masses. The obtained dilation angles were fitted to the current variable dilation angle models (Alejano & Alonso, 2005; Zhao & Cai, 2010a) revealing the models' strengths and weaknesses and confirming this parameter dependencies (plasticity and confining stress).

Later, and accounting for the fact that the dilation angle also presents scale —and/or structure— dependence (Alejano & Alonso, 2005), the scale problem was addressed in a novel way: artificially jointed specimens (22 specimens) of one of the previously studied rocks were created and tested: the specimens had two joint sets (a sub-horizontal set with two discontinuities and a sub-vertical set with one discontinuity each specimen). The results of the tests are quite relevant and show very marked trends —with respect to the intact specimens—, peak strength, Young's modulus, drop modulus and peak dilation angle diminishes. Meanwhile, Poisson's ratio and residual strength do not show any relevant change.

Aimed to confirm the observed trends, a new set of jointed specimens were made and tested (20 specimens). These specimens had the same joint sets, but they were more densely fractured (three sub-horizontal discontinuities and two sub-vertical discontinuities each specimen). The results of the tests confirmed the previously observed trends. The dilation angle results of these tests, in addition, were fitted to a novel variable dilation angle model (Walton & Diederichs, 2015a).

In order to characterize post-failure behavior of rocks and rock masses, it is also required (in addition to the dilation angle) a model that links the plastic strains with the stresses after peak (an evolving failure criterion between peak and residual strength). Following an empirical approach, a mathematical equation was fitted to pairs of points of stress and plastic axial strain obtained for each test before, during and after the softening phase. Combining this stress-softening model with the variable dilation angle model, allowed to simulate the dilatant softening behavior of the tested rocks.

Finally and aimed to illustrate the differences of considering or not considering variable dilatancy when modelling rock masses, a numerical model of a deep tunnel was created and run using different post-failure behaviors, noting the differences between the models.

KEYWORDS: Rock mechanics, strength testing, geo-mechanical characterization, structure-scale, post-failure, dilation.

Resumen

El comportamiento post-rotura de rocas y macizos rocosos no ha sido muy estudiado en el campo de la ingeniería de rocas, en parte por la dificultad para obtener resultados fiables y en parte porque el trabajo del ingeniero suele ser prevenir la rotura. Sin embargo, para ciertas aplicaciones, es necesario obtener, o al menos estimar de la mejor manera posible, los parámetros que gobiernan este comportamiento.

Siguiendo las indicaciones de Farmer (1983), se modificó la prensa existente en el *Laboratorio de Mecánica de Rocas John P. Harrison* de la Universidad de Vigo, de forma que se pudiera no sólo controlar la carga axial, sino también la presión de confinamiento en los ensayos triaxiales y medir a la vez la deformación volumétrica de la probeta durante el ensayo.

Se realizaron ensayos con esta prensa completamente servo-controlada usando ocho rocas diferentes (más de 200 ensayos de compresión en total) de forma que se alcanzara el estado residual siempre que fuera posible. Además se realizaron los ensayos con ciclos de descarga y recarga, de forma que se controlara la transición desde la resistencia de pico hasta la resistencia residual y también se pudiera obtener el denominado lugar geométrico de las deformaciones irreversibles, que permite la diferenciación de las componentes elásticas y plásticas de las deformaciones axial y volumétrica de la probeta.

Con los datos de tensión y deformación de los ensayos y aplicando la formulación propuesta por Vermeer y De Borst (1984), se obtuvo la evolución del ángulo de dilatancia durante los ensayos. El ángulo de dilatancia es el parámetro más adecuado para modelizar el comportamiento dilatante de la roca y uno de los parámetros necesarios para simular el comportamiento post-rotura. El ángulo de dilatancia así obtenido para todos los ensayos se ajustó a los modelos de dilatancia variable existentes (Alejano y Alonso, 2005; Zhao y Cai, 2010a), descubriendo las debilidades y fortalezas de cada modelo y confirmando las dependencias de este parámetro (nivel de plastificación y presión de confinamiento).

En una etapa posterior y sabiendo que el ángulo de dilatancia también depende de la escala —y/o de la estructura— (Alejano y Alonso, 2005), se abordó el problema de la escala de una forma novedosa: se crearon probetas (22 probetas) de una de las rocas estudiadas previamente, atravesadas por dos familias de discontinuidades (una familia sub-horizontal, con dos discontinuidades y una familia sub-vertical con una discontinuidad). Estas probetas diaclasadas se ensayaron siguiendo la metodología anterior y se obtuvieron resultados muy relevantes que muestran tendencias marcadas —respecto a las probetas intactas— de disminución de la resistencia de pico, del módulo de Young, del módulo de descarga y del ángulo de dilatancia de pico, mientras que el coeficiente de Poisson y la resistencia residual no parecen verse afectados significativamente.

Con el objetivo de confirmar las tendencias observadas en las probetas diaclasadas, se crearon probetas con las mismas familias de discontinuidades pero con mayor densidad de fracturación (tres discontinuidades en la familia sub-horizontal y dos discontinuidades en la familia sub-vertical). Estas probetas (20 probetas más) se ensayaron siguiendo la misma metodología y se confirmaron los resultados obtenidos en la etapa anterior. Para estas probetas, además se ajustó un modelo de dilatancia variable recientemente propuesto (Walton y Diederichs, 2015a).

Para caracterizar el comportamiento post-rotura de las rocas es necesario, además de un parámetro que modele el comportamiento dilatante del material (el ángulo de dilatancia), otro modelo que ligue las deformaciones con la resistencia en esta etapa, es decir, un criterio de rotura evolutivo desde la resistencia de pico hasta la residual. Siguiendo un enfoque empírico, se ajustó una ecuación matemática a pares de puntos de tensión y deformación plástica obtenidos para cada ensayo antes, durante y después de la fase de reblandecimiento. La combinación de este modelo de la evolución de la relación entre tensión y deformación plástica con el modelo de dilatancia variable, permitió simular el comportamiento dilatante con reblandecimiento de las rocas intactas estudiadas.

Finalmente, para ilustrar las diferencias entre considerar o no una dilatancia variable, se creó un modelo numérico de un túnel profundo y se ejecutó con diferentes comportamientos post-rotura, observando las diferencias entre ellos.

PALABRAS CLAVE: Mecánica de rocas, ensayos de resistencia, caracterización geomecánica, escala-estructura, post-rotura, dilatancia.

Extended abstract

Excavation in rock masses has developed during last years a boom, primarily due to improved technology, excavation equipment and treatment processes. Examples of major projects are found in Galicia with the works of the AVE (Spanish high speed trains), which are burrowing our mountains with tunnels to deal with our whimsical terrain; in the Swiss Alps with the construction of the Gotthard Base Tunnel; large underground mines as some large projects in South America or open pit mines such as Bingham Canyon in the United States. Also urban use of underground space is being promoted; this promotion mainly begins in the coldest countries (Northern Europe) where the existing rock beneath cities presents good quality, or in countries with limited surface space (Japan). It is also necessary to use underground space when discussing physics laboratories such as CERN, a particle accelerator in Switzerland, or the U.S. Fermilab.

In addition to the excavation of the rock mass, sometimes it is only necessary to fracture the rock mass to obtain an improvement of the properties needed for a purpose, for instance, in the case of oil and gas, to cause fracturing of the rock to enhance the conductive capacity of the rock mass is a common practice, and thus obtain a higher output in less time; or, in the case of caving mining methods, it is required that the rock flows into the draw point, so it is necessary for the rock mass being sufficiently fractured.

One may realize that the best way to excavate or to fracture the rock mass is to best know its behavior under the conditions —particularly the stress state— in which the rock mass will be. This task is easy to say, but it is difficult to perform due primarily, but not only, to the natural heterogeneity of the rock mass. It should be noted here that a rock mass is a three-dimensional set or net of rock blocks crossed by geological discontinuities of different origin, so the rock mass behavior depends not only on the constituting rock, but also on the discontinuities that intersect it. Both constituents also not always behave in the same way, as there will be areas of rock that have suffered certain phenomena (weathering, metamorphism, diagenesis, failures...) that may have modified their properties locally and do not have affected nearby areas.

Since the early rock mechanics developments in the 60's – 70's of the last century, much effort has been expended to studying and modelling the elastic or prior-to-failure behavior of rock masses and, thus, there are models that reasonably represent the actual pre-failure behavior of rock masses. However, the post-failure behavior has been much less studied, due to the inherent difficulties of such study and because the primary objective of an engineer is typically to avoid failure. However, as it has already been discussed in previous paragraphs, the fracturing of the rock mass is a requirement for some applications in the mining industry, and even knowing how the rock mass in the plastic state ("broken") will behave is a key design factor in the prediction of the correct installation moment (distance to the face) for the support in a tunnel. This knowledge of post-failure rock mass behavior can also be a key when analyzing broken pillars in underground mines and proposing corrective measures.

To fully characterize a rock mass (regardless of whether their behavior is elastic-brittle, strain-softening or elastic-perfectly-plastic) one must know the elastic parameters (Young's modulus and Poisson's ratio), the peak failure criterion (typically Hoek-Brown or Mohr-Coulomb), the residual failure criterion (which has the same form as the peak failure criterion but different parameters), the evolving failure criterion from peak to residual state, the post-failure parameters linking the relationship between stress and strain and the post-failure relationship between strains. A correct characterization of post-fracture behavior can be achieved if one knows, for instance, (a) the dilation angle and the drop modulus (the slope of the axial stress-axial strain curve during softening) or (b) the dilation angle and the plastic parameter values for which dilatancy and evolving failure criterion are achieved.

This dissertation aims to improve our understanding of post-failure behavior of rock masses. Since the in situ deformability tests of rock masses are often unaffordable for various reasons (the scale of the needed equipment; the difficulty in isolating the factors that influence the outcome; or the high cost, just to mention a few), it is necessary to resort to laboratory testing, where one can more easily control the variables that come into play. Yet there are inherent difficulties in the

study of post-failure behavior of rocks that need to be addressed when proposing an experimental program:

A sufficiently large number of samples are needed to obtain a reliable result. The process of obtaining and preparing the specimens is long and must be done accurately to meet current regulations (UNE in Spain, derived from the methods suggested by the ISRM, 2007).

The press should be stiffer than the tested rock in order to be able to control and to record the transition from peak to residual strength. In the opposite case (the tested rock is stiffer than the press) the specimen will abruptly or explosively fail, making it impossible to collect reliable data on the post-failure phase.

After this required stiffness, appropriate servo-control for regulating the force exerted by the press on the specimen during the test is needed, just to, again, have control over the softening process between peak and residual strength.

The sensors used to measure the strains during the test should be accurate enough for the necessary appreciation (between thousandths and tenths of a millimeter) and a sufficiently broad range of measure to capture the deformations in the residual state. The latter precludes the use of strain gauges due to their limited range of measurement, as well as other problems associated with their use, such as the inability to capture localized strain (shear bands).

Since strain gauges cannot be used, it becomes impossible to measure the radial strain of the specimen in triaxial tests without a specifically adapted Hoek’s cell, because no measuring devices may be coupled within a standard triaxial cell. So it becomes necessary to measure the amount of fluid that must be entered or removed from the triaxial cell to maintain the confining pressure during such tests. This amount of displaced fluid can be related to the volumetric strain of the specimen and thus, using both the volumetric and the axial deformation, one can obtain the radial strain. Therefore, it is also necessary to have control over the confining pressure and to be able to measure the amount of fluid displaced, so one needs a new servo-control for this aspect.

The further processing of the data collected during the tests requires the identification of the elastic (or reversible) and plastic (or irreversible) components of the strains. While this distinction between elastic and plastic deformation is theoretically simplistic, as it does not consider inelastic phenomena (neither elastic nor plastic in the yield sense), or the defects (micro-cracks, pores...) initial closure —that gives the initial concave shape to the axial stress-axial strain curve—, it is valid for the level of detail in which the research of post failure behavior of rocks and rock masses is. The approach used in this Ph.D. thesis is sufficient, since it is assumed that the plastic strain does not begin until it reaches the stress level called *Crack Damage*.

To make this distinction between elastic and plastic strains is advisable to perform unloading-reloading cycles during the tests, especially in the softening and residual phases. These cycles allow to obtain the locus known as irrecoverable strain locus, thanks to which one can get one of the most relevant parameters of the post-failure behavior of a rock or a rock mass, the dilation angle, ψ. These cycles will also help to control and record the transition from peak to residual strength.

Still speaking of data processing, note that it is not an easy task and it is also difficult to automate because of the natural variability of the tests results. This process involves not-so-logical decisions that a computer is not always able to consider, so that each of the tests must be analyzed carefully. Moreover, the automation of the process may present some associated loss of control and monitoring of the data that can lead to errors difficult to detect.

All these reasons make the process of obtaining real data from post-failure behavior long and costly, if one also adds the already commented thought that the engineer must avoid failure, it is not difficult to understand the lack of data related to post-failure behavior of rocks and rock masses. However, over the years, as the underground excavations have grown in size and numerical simulations are becoming increasingly important, easily available and realistic, it has been shown that it is necessary to know the post-failure behavior of rocks and rock masses in order to understand the mechanisms that take place, and achieve the objective of the simulation in rock mechanics, which is simply to represent as closely as possible the actual behavior of a rock mass under certain conditions.

In order to deepen on our knowledge of the post-failure behavior of rocks, this Ph.D. thesis initially proposed an experimental programme aimed at obtaining dilation angle in rocks from laboratory tests (Chapters 3 and 4). More than 200 unconfined and confined strength tests were performed on specimens from eight different rocks. These tests included the previously mentioned unloading-reloading cycles in order to be able to identify the plastic strains that are necessary to calculate the dilation angle.

Complete stress-strain curves of each of these tests were obtained. The most relevant parameters needed to fully characterize the behavior of the rock were also computed for each test: Young's modulus and Poisson's ratio, peak and residual strength (the latter only when possible, it is known that the residual strength of an unconfined strength tests is usually null), drop modulus (also when it was possible) and the evolution of the dilation angle with increasing strain.

From these individual data, the evolution of the parameters with confining pressure was studied, showing the already known relationships, namely, with increasing pressure confinement, the Young's modulus, the peak strength and the residual strength increase, while Poisson's ratio does not seem to be affected and the drop modulus is reduced (the rock becomes more ductile).

Besides, the most used failure criteria in rock mechanics (Hoek-Brown and Mohr-Coulomb) were fitted to strength results, obtaining very good fits in both cases. Note that using the generalized Hoek-Brown criterion (Hoek et al., 2002) to fit the results of residual strength significantly improved the fit.

Finally in this part, after obtaining the evolution of the dilation angle with the strain for each test, all the data obtained for this parameter were pooled, thus revealing dependencies as targeted by Alejano & Alonso (2005), namely, the dilation angle decreases with increasing confining pressure and decreases with increasing plastic strain.

The obtained dilation angle was fitted to the existing models of evolution of this parameter. The first one (Alejano & Alonso, 2005), although very easy to implement, was not able to recover the peak dilation angle observed in the tests, though it reasonably captured the evolution of the dilation angle with the plastic strain. The second model (Zhao & Cai, 2010a) fitted the data fairly well and the behavior of the dilation angle was precisely captured. However, this model involves many difficulties due to the nine parameters with difficult physical correlation that are necessary to obtain, so its application to everyday engineer work is questionable.

Alejano & Alonso (2005) also noted that the dilation angle should also depend on the scale. The problem of scale in rock mechanics, although known, is not fully solved and this is due, again, to the natural variability of the material with which it works and to the fact that increasing the scale, the number of existing imperfections (pores, inhomogeneities, micro-cracks ...) in the sample also increases. This dissertation has attempted to address the problem of scale (chapters 5 and 6) creating two series of rock specimens crossed by two artificial joint sets (the first series of specimens had two sub-horizontal and one sub-vertical joint, and the second series had three sub-horizontal and two sub-vertical joints). Cutting and preparing these specimens was not simple: some previous tests were needed before reaching a methodology to obtain and test jointed specimens with a reasonably degree of quality.

22 and 20 of these "small-scale rock masses" were got from one of the previously studied rocks and triaxial compression strength tests were performed. It should be noted that due to the characteristics of the specimens, it was neither possible to perform unconfined compression strength nor indirect tensile (Brazilian) tests. And although these specimens could reach some strength in these conditions, these values would be very small compared to the triaxial strength values obtained, so they could reasonably be assumed zero.

The same procedures as in the previous chapters were followed for the most relevant parameters. The results obtained were compared again with the confining pressure, revealing the same dependencies explained before. But results were also compared with those of the intact specimens previously obtained, revealing very interesting trends.

The Young's modulus of the jointed specimens is significantly reduced compared to the intact specimens, which is logical if one takes into account the lower stiffness of the discontinuities relative to the rock matrix. In addition, it is the expected/observed behavior when the stiffness of the rock is compared to that of the rock mass. It was also revealed that the Young's modulus grows with confining pressure, but it does not do it linearly as hitherto believed, but rather it is a logarithmic relationship: there is a strong increase of Young's modulus for small initial increments of confining stress and then, for successive increments of confining stresses, the growth slows down.

Poisson's ratio hardly changed its value (0.16 in intact specimens to 0.16 and 0.19 in jointed specimens) so it seems reasonable to think that the general approach —in which, for good quality rock masses, one can consider the same Poisson's ratio as for the rock— is reasonably realistic.

The peak strength of the jointed specimens is smaller than that of the intact specimens, but it should be noted that the difference between these two values decreases with increasing confining pressure.

The residual strength is the same in both types of samples (considering the level of variability that occurs in rock mechanics). Not only this fact is important, but also the stress-strain curves of the jointed samples tend to mimic the behavior of intact specimens at some level of strain after the peak, both reaching the residual state approximately in the same values of strain. An explanation of this fact in terms of energy could be very interesting: it is possible that the energy used in cutting the joints of the specimens is equal to the energy difference between the two curves.

The drop modulus again showed its dependence on confining pressure and turned out to be lower in jointed specimens than in intact specimens, the same explanation that for the case of Young's modulus could be valid here.

Finally, in this part of the study, the dilation angle values were fitted to the mobilized dilation angle model by Zhao & Cai (2010a) and the last series of jointed specimens to the new proposed dilatancy model by Walton & Diederichs (2015a) and compared to the model previously obtained for intact specimens. This parameter showed its dependence on degree of fracturing (or scale) resulting in smaller dilation angles for the jointed specimens than for the intact ones at small confining pressures, but with the gap between both specimens gradually falling and reaching the same dilation angles obtained with intact specimens for confining pressures from 6 MPa onwards. Note that where the dilatant behavior of rock masses may have significance for the engineering works is on the free sides of an excavation —i.e. where the confining stresses are small— so that this discovery in the dilation angle difference between intact and jointed specimens at small confining pressures has a relevant impact on rock engineering.

Although the dilation angle is an important parameter in the post-failure behavior of rocks and rock masses, itself alone is not able to define this behavior, so hereafter (chapter 7) a model able to represent the strain-softening behavior is proposed. For this purpose —from the stress-strain curves of the first tests carried out on the three granitic rocks— the relations between the stresses and the plastic strains before, during and after the softening phase (transition from peak to residual strength) were obtained. Subsequently an empirical approach was applied and a mathematical equation was fitted to the pairs of points obtained (stress and plastic strain). Combining this model of evolution of the relationship between stresses and plastic strains with the mobilized dilation angle model previously fitted, allowed the author to simulate the dilatant softening behavior of the studied rocks. While there are still differences between the model and actual behavior, the obtained approach is much better than existing models.

Finally (chapter 8), to illustrate the differences between considering or not a variable dilatancy, a numerical model of a deep tunnel was created and different situations were compared by considering three rock mass qualities (three different post-failure behavior) with both a constant and a variable dilation angle approaches. The results show that for average rock masses (those presenting strain-softening behavior) the consideration of a variable dilation angle increases calculated strains on the face and walls of the tunnel, while it does not seem to affect the extent of the yielded zone.

Resumen extendido

La excavación en macizos rocosos ha venido desarrollando en lo últimos años un auge debido principalmente al desarrollo económico de los países emergentes, a la mejora en las tecnologías y el equipamiento de excavación y a los procesos de tratamiento. Ejemplos de grandes proyectos los encontramos en Galicia con las obras del AVE (Alta Velocidad Española), que están horadando nuestras montañas con túneles para hacer frente a nuestra caprichosa orografía; en los Alpes Suizos con la construcción del túnel base de San Gotardo; grandes minas subterráneas como algunos grandes proyectos en Sudamérica o en superficie como la de Bingham Canyon en Estados Unidos. Además se está impulsando un uso urbano de los espacios subterráneos, este impulso parte principalmente de los países más fríos (Norte de Europa) donde la roca existente bajo las ciudades es de buena calidad o de los países con poco espacio disponible en superficie como Japón. También es necesario recurrir al espacio subterráneo cuando se habla de laboratorios de física, como los aceleradores de partículas del CERN en Suiza o el del Fermilab en EEUU.

Además de la excavación propiamente dicha del macizo rocoso, a veces sólo es necesario fracturar el macizo rocoso para obtener una mejora de las propiedades necesarias para un fin, por ejemplo, en el caso de la industria del petróleo y el gas, es común provocar la fracturación de la roca para mejorar la capacidad conductiva del macizo rocoso y obtener así una mayor producción en menor tiempo; o, en el caso de los métodos mineros por hundimiento, se hace necesario que la roca fluya hacia los coladeros, por lo que es necesario que el macizo rocoso esté suficientemente fracturado.

La mejor forma de conseguir esa excavación o fracturación del macizo rocoso es conociendo lo mejor posible su comportamiento bajo las condiciones —particularmente las condiciones tensionales— en las que se va a encontrar. Esta tarea, fácil de teorizar, es complicada de llevar a cabo en la práctica debido principalmente, pero no sólo, a la heterogeneidad natural de los macizos rocosos. Conviene señalar aquí que un macizo rocoso es un conjunto o entramado tridimensional de bloques de roca surcado por discontinuidades geológicas de diverso origen, por lo que el comportamiento del macizo rocoso dependerá no sólo de la roca que lo forma, sino también de las discontinuidades que la cruzan. Ambos constituyentes, además, tampoco se comportarán siempre de la misma forma, pues habrá zonas de roca que hayan sufrido ciertos fenómenos (meteorización, metamorfismo, diagénesis, fallas…) que pueden haber modificado sus propiedades localmente, pero no necesariamente en zonas cercanas.

Desde los inicios del desarrollo de la mecánica de rocas en los años 60-70 del siglo pasado se ha dedicado mucho esfuerzo al estudio y modelización del comportamiento elástico o previo a la rotura y así es que existen modelos que representan de forma razonablemente aproximada el comportamiento real de los macizos rocosos. Sin embargo, el comportamiento de lo que ocurre después de la rotura ha sido mucho menos estudiado, debido a la dificultad de dicho estudio y a que el objetivo principal de un ingeniero suele ser evitar la rotura. Sin embargo ya se ha comentado en párrafos anteriores que la fracturación del macizo rocoso es un requerimiento para algunas aplicaciones de la industria minera e incluso saber cómo se comportará el macizo rocoso en estado plástico (“roto”) es un factor de diseño clave en la predicción del momento (distancia al frente) de instalación de sostenimiento en un túnel. Este conocimiento del comportamiento post-rotura del macizo rocoso también puede ser clave a la hora de analizar roturas de pilares en minas subterráneas y proponer medidas correctoras.

Para caracterizar completamente un macizo rocoso (independientemente de que su comportamiento sea elasto-frágil, elasto-plástico con reblandecimiento o elasto-plástico perfecto) uno debe conocer los parámetros elásticos (módulo de Young y coeficiente de Poisson), el criterio de rotura de pico (Hoek-Brown o Mohr-Coulomb típicamente), el criterio de rotura residual (que tendrá la misma forma que el criterio de rotura de pico pero diferentes parámetros), el criterio de rotura evolutivo desde el de pico hasta el residual, los parámetros que ligan la relación entre tensión y deformación en post-rotura y la relación entre las deformaciones también en post-rotura. Se puede conseguir una caracterización correcta del comportamiento post-rotura si se conoce, por ejemplo, (a) el ángulo de dilatancia y el módulo de descarga (la pendiente de la fase de reblandecimiento en la curva tensión axial-deformación axial) o (b) el ángulo de dilatancia y los valores del parámetro plástico considerado (que es una forma de medir la deformación plástica alcanzada) para los que se ha obtenido el ángulo de dilatancia y el criterio de rotura evolutivo.

Este trabajo de tesis intenta mejorar nuestro conocimiento del comportamiento post-rotura de los macizos rocosos. Dado que los ensayos tenso-deformacionales *in situ* de macizos rocosos suelen ser inabordables por varios motivos (la escala del equipamiento necesario; la dificultad en aislar los factores que influyen al resultado; o el elevado coste por citar algunos de ellos), es necesario recurrir al ensayo en laboratorio, donde se pueden controlar más fácilmente las variables que entran en juego. Aun así existen dificultades inherentes al estudio del comportamiento post-rotura de las rocas que es necesario afrontar a la hora de proponer un programa experimental:

Son necesarias un número suficientemente grande de probetas para obtener un resultado representativo y fiable. El proceso de obtención y preparación de estas probetas es largo y debe ser realizado con precisión para cumplir la normativa vigente (UNE en España, derivada de los métodos sugeridos por la ISRM, 2007).

La prensa debe tener mayor rigidez que la roca ensayada, para poder controlar y registrar el proceso de transición desde la resistencia de pico a la residual, en el caso contrario (que la roca ensayada sea más rígida que la prensa) la probeta romperá de forma brusca o explosiva, imposibilitando la toma de datos fiable en la fase post-rotura.

Tras este requerimiento de rigidez, es necesario un buen servo-control que permita regular la fuerza ejercida por la prensa sobre la probeta durante el ensayo, precisamente para, de nuevo, tener control sobre el proceso de reblandecimiento entre la resistencia de pico y residual.

Los sensores utilizados para medir las deformaciones durante el ensayo deben ser suficientemente precisos para la apreciación necesaria (entre milésimas y décimas de milímetro) y con un rango de medida suficientemente amplio para poder capturar las deformaciones en el estado residual. Este último aspecto descarta el uso de galgas extensiométricas por su limitado rango de medida, además de otros problemas asociados a su uso, como la imposibilidad de capturar deformaciones localizadas (como las bandas de cizalladura o *shear bands* en inglés).

Al no poder usar las galgas extensiométricas resulta imposible medir la deformación radial en los ensayos triaxiales sin una celda de Hoek especialmente adaptada, pues no se pueden acoplar dispositivos de medida dentro de la celda triaxial. Así que se vuelve necesario medir la cantidad de fluido que es necesario introducir o retirar de la celda triaxial para mantener la presión de confinamiento durante este tipo de ensayos. Esta cantidad de fluido desplazado se puede relacionar con la deformación volumétrica de la probeta y así, con esta última y la deformación axial, se puede obtener la deformación radial. Por tanto, es necesario también tener control sobre la presión de confinamiento y que sea además capaz de medir la cantidad de fluido desplazado, por lo que hay que introducir un nuevo servo-control para este aspecto al equipamiento.

El posterior tratamiento de los datos obtenidos durante el ensayo requiere la separación de las componentes elástica (o reversible) y plástica (o irreversible) de las deformaciones. Si bien esta diferenciación entre deformación elástica y plástica es simplista, pues no tiene en cuenta fenómenos inelásticos (no elásticos, pero tampoco plásticos en el sentido geomecánico de la palabra) como el cierre de defectos (microfisuras, poros…) inicial —que le da esa forma cóncava inicial a la curva tensión axial-deformación axial—, es válida para el nivel de detalle en el que se encuentra la investigación del comportamiento post-rotura de rocas y macizos rocosos y para la aproximación que se da en esta tesis, donde se asume que la deformación plástica no comienza hasta alcanzar el nivel de tensión denominado *Crack Damage* o nivel de resistencia a largo plazo.

Para realizar esta diferenciación entre deformaciones elásticas y plásticas es recomendable realizar ciclos de descarga-recarga durante el ensayo, sobre todo en la fase de reblandecimiento y residual, pues permitirán obtener el conocido como lugar geométrico de las deformaciones irreversibles, gracias al cual se puede obtener uno de los parámetros más importantes del comportamiento post-rotura de una roca o macizo rocoso, el ángulo de dilatancia, ψ. En la fase de reblandecimiento estos ciclos, además, ayudarán a controlar y registrar el proceso de transición desde la resistencia de pico a la residual.

Siguiendo con el tratamiento de datos, cabe señalar que tampoco es una tarea fácil y, además, difícil de automatizar, pues la variabilidad natural de los resultados de los ensayos hace necesario tomar decisiones no tan lógicas que un ordenador no siempre es capaz de considerar, por lo que cada uno de los ensayos debe ser analizado por separado. Por otra parte la automatización del proceso puede llevar asociada cierta pérdida de control y seguimiento de los datos que puede conducir a errores difícilmente detectables.

Todas estas razones hacen que el proceso de obtención de datos reales de comportamiento post-rotura sea largo y costoso, si además se añade el ya comentado pensamiento de que el ingeniero debe evitar la rotura, no es difícil entender la falta de resultados relativos al comportamiento post-rotura de rocas y macizos rocosos. Sin embargo con el paso de los años y a medida que las excavaciones subterráneas han crecido en tamaño y las simulaciones numéricas adquieren cada vez mayor importancia, se ha puesto de manifiesto que es de rigor conocer ese comportamiento post-rotura para comprender los mecanismos que tienen lugar y alcanzar el objetivo de la simulación en mecánica de rocas, que no es otro que representar lo más fielmente posible el comportamiento real de un macizo rocoso bajo ciertas condiciones.

Para obtener ese comportamiento post-rotura, en este trabajo de tesis se ha propuesto inicialmente un programa experimental enfocado a la obtención del ángulo de dilatancia en rocas a partir de ensayos de laboratorio (capítulos 3 y 4), para ello se han realizado más de 200 ensayos de compresión simple y triaxial sobre probetas de ocho rocas diferentes, estos ensayos incluyeron los ya comentados ciclos de descarga y recarga para poder identificar las deformaciones plásticas que son necesarias para el cálculo del ángulo de dilatancia.

Se obtuvieron las curvas completas tensión-deformación de cada uno de estos ensayos y se computó, también para cada ensayo, los parámetros relevantes para la caracterización completa del comportamiento de la roca. Se obtuvieron así, para cada uno de los ensayos: el módulo de Young y el coeficiente de Poisson, la resistencia de pico y residual (esta última sólo cuando fue posible, es conocido que la resistencia residual de un ensayo a compresión simple suele ser nula), el módulo de descarga (también cuando fue posible) y la evolución del ángulo de dilatancia a medida que aumenta la deformación.

A partir de estos datos individuales se estudió la evolución de los parámetros con la presión de confinamiento, demostrando las ya conocidas relaciones que presentan, a saber, al aumentar la presión de confinamiento, el módulo de Young, la resistencia de pico y la resistencia residual aumentan, mientras que el coeficiente de Poisson no parece verse afectado significativamente y el módulo de descarga se reduce (la roca se vuelve más dúctil).

Además se ajustaron los criterios de rotura más usados en mecánica de rocas (Hoek-Brown y Mohr-Coulomb) a los resultados de resistencia, obteniendo buenos ajustes en ambos casos. Cabe señalar que la aplicación del criterio de rotura de Hoek-Brown generalizado (Hoek et al. 2002) a los resultados de resistencia residual mejoró significativamente el ajuste en este caso.

Finalmente en esta parte, tras la obtención de la evolución del ángulo de dilatancia con la deformación para cada ensayo, se pusieron todos los datos obtenidos para este parámetro en común, revelando así las dependencias que presenta y que fueron apuntadas por Alejano & Alonso (2005), a saber, el ángulo de dilatancia disminuye al aumentar la presión de confinamiento y decrece a medida que aumenta la deformación.

Se intentaron ajustar los datos de ángulo de dilatancia obtenidos a los modelos existentes de evolución de este parámetro. El primero de ellos (Alejano & Alonso, 2005) basado en resultados derivados de rocas sedimentarias, aunque muy sencillo de aplicar, no fue capaz de recuperar el ángulo de dilatancia de pico observado en los ensayos, pero sí capturó de forma razonable la evolución del ángulo de dilatancia con la deformación. El segundo de los modelos (Zhao & Cai, 2010a) ajustado a los datos, sí representó bastante bien el comportamiento del ángulo de dilatancia observado en los ensayos, sin embargo este modelo implica muchas dificultades por los nueve parámetros de difícil correlación física que es necesario obtener, por lo que su aplicación al trabajo diario del ingeniero puede ser difícil.

Alejano & Alonso (2005) además apuntaron que el ángulo de dilatancia debe depender también de la escala. El problema de la escala en mecánica de rocas, aunque conocido, no está totalmente resuelto y esto es debido, nuevamente, a la variabilidad natural del material con el que se trabaja y al hecho de que al aumentar la escala, se aumenta también el número de imperfecciones (poros, heterogeneidades, microfisuras…) que existen en la roca. En esta tesis se ha intentado abordar el problema de la escala (capítulos 5 y 6) creando probetas de roca surcadas por dos familias de discontinuidades artificiales (un conjunto de probetas con dos juntas sub-horizontales y otra sub-vertical y otro conjunto de probetas con tres juntas sub-horizontales y dos sub-verticales). El corte y la preparación de estas probetas no han sido sencillos, se han tenido que realizar algunas pruebas antes de alcanzar una metodología que permitiera obtener y ensayar dichas probetas con un grado de calidad razonable.

Se obtuvieron 22 y 20 de estos “macizos rocosos a pequeña escala” respectivamente, usando una de las rocas previamente estudiadas y se realizaron ensayos triaxiales de compresión. Hay que señalar que, debido a las características de las probetas, no fue posible realizar ensayos de compresión simple ni de tracción (brasileños) y aunque estas probetas pudieran alcanzar algo de resistencia a compresión simple o a tracción, estos valores serían muy pequeños comparados con los valores de resistencia obtenidos, por lo que razonablemente se podrían suponer nulos.

Se siguieron los mismos procedimientos que en los capítulos anteriores para obtener los parámetros más relevantes a partir de los ensayos de resistencia triaxial y se volvieron a comparar los resultados no sólo frente a la presión de confinamiento, que reveló las mismas dependencias antes apuntadas, sino también a los ensayos previamente realizados sobre probetas intactas, obteniendo interesantes descubrimientos.

El módulo de Young de las probetas diaclasadas disminuye significativamente respecto de las probetas intactas, lo cual es lógico si se tiene en cuenta la menor rigidez de las discontinuidades respecto de la matriz rocosa. Además es el mismo comportamiento esperado cuando se compara la rigidez de la roca frente a la del macizo rocoso. También se reveló que el módulo de Young crece con la presión de confinamiento, pero no lo hace de forma lineal, como se había propuesto hasta ahora, si no que es más bien una relación logarítmica: hay un fuerte incremento del módulo de Young para pequeños incrementos iniciales de presión de confinamiento y luego, para sucesivos incrementos de presión de confinamiento, el crecimiento se ralentiza.

Es interesante señalar que el coeficiente de Poisson apenas varía su valor (de 0.16 en las probetas intactas a 0.16 y 0.19 respectivamente en las probetas diaclasadas) por lo que parece razonable pensar que es cierta la aproximación general en la que, para macizos rocosos de buena calidad, se puede considerar un coeficiente de Poisson similar al de la roca sana.

La resistencia de pico es menor en las probetas diaclasadas que en las intactas, pero hay que señalar que la diferencia entre estos dos valores disminuye a medida que aumenta la presión de confinamiento.

La resistencia residual es la misma en ambos tipos de probetas (considerando el nivel de variabilidad que se presenta en mecánica de rocas). No sólo este hecho es importante, sino que además las curvas tensión-deformación de las probetas diaclasadas replican el comportamiento de las probetas intactas, llegando a superponerse para cierto nivel de deformación después de la rotura, alcanzando el estado residual aproximadamente para los mismos valores de deformación en ambos casos. Una explicación de este aspecto en términos energéticos podría resultar muy interesante, es posible que la energía empleada en el corte de las discontinuidades sea igual a la diferencia de energía tenso-deformacional derivada de las curvas recuperadas para los distintos tipos de probetas.

El módulo de descarga mostró otra vez su dependencia con la presión de confinamiento y resultó ser más bajo que en las probetas intactas, la misma explicación que para el caso del módulo de Young podría ser válida aquí.

Finalmente en esta parte del estudio, el ángulo de dilatancia se ajustó al modelo de dilatancia variable de Zhao & Cai (2010a) y, para el último conjunto de probetas diaclasadas, también se ajustó al recientemente propuesto modelo de dilatancia de Walton & Diederichs (2015a) y se comparó con el modelo anteriormente obtenido para las probetas intactas. Este parámetro demostró su dependencia con el grado de fracturación (o la escala) resultando más pequeño en las probetas diaclasadas para pequeñas presiones de confinamiento, pero reduciéndose la diferencia gradualmente y llegando a obtenerse los mismos ángulos de dilatancia para presiones de confinamiento a partir de 6 MPa. Hay que señalar que donde puede tener relevancia este comportamiento expansivo de las rocas desde un enfoque ingenieril es en las caras libres de las excavaciones subterráneas, es decir, donde las presiones de confinamiento son pequeñas, por lo que esta observación empírica en la diferencia del ángulo de dilatancia entre probetas intactas y diaclasadas para pequeñas presiones de confinamiento puede ser relevante en la ingeniería práctica.

Aunque el ángulo de dilatancia es un parámetro importante en el comportamiento post-rotura de rocas y macizos rocosos, por sí solo no es capaz de definir dicho comportamiento. Por ello, a continuación (capítulo 7), se propuso un modelo que representara el comportamiento elasto-plástico con reblandecimiento. Para ello se obtuvieron, a partir de las curvas tensión-deformación de los primeros ensayos realizados sobre tres rocas graníticas, las relaciones entre las tensiones y las deformaciones plásticas antes, durante y después de la fase de reblandecimiento (transición desde la resistencia de pico a la residual). Posteriormente se aplicó un enfoque empírico y se ajustó una ecuación matemática a dichos pares de puntos. La combinación de este modelo de evolución de la relación entre tensión y deformación plástica con el modelo de dilatancia variable anteriormente obtenido, permitió simular el comportamiento dilatante con reblandecimiento de las rocas estudiadas. Si bien todavía existen diferencias entre el modelo y el comportamiento real, la aproximación obtenida es mucho mejor que los modelos existentes actualmente.

Finalmente (capítulo 8), para ilustrar las diferencias entre considerar o no una dilatancia variable, se creó un modelo numérico de un túnel profundo y se compararon diferentes situaciones al considerar tres calidades de macizos rocosos (tres diferentes comportamientos post-rotura) y un ángulo de dilatancia constante y variable. Los resultados demuestran que para macizos rocosos de calidad geotécnica media (los que presentan un comportamiento elasto-plástico con reblandecimiento) la consideración de un ángulo de dilatancia variable aumenta los desplazamientos observados en el frente y las paredes del túnel, si bien no parece afectar significativamente a la extensión de la zona plastificada.

Index

Autorización defensa tesis de doctorado v
Dedicatoria vii
Acknowledgements: ix
Abstract xi
KEYWORDS: xi
Resumen xiii
PALABRAS CLAVE: xiv
Extended abstract xv
Resumen extendido xix
Index xxv
List of Figures xxix
List of Tables: xxxv
1. Introduction 1
1.1. Preliminary comments 1
1.2. Objective 2
1.3. Justification 3
1.4. Contents of this dissertation 5
2. State of the art: rock and rock mass behavior 7
2.1. Introduction 7
2.2. Rock mass characterization 7
2.2.1. Failure criteria 8
2.2.2. Rock mass deformability 11
2.2.3. Post-failure behavior of rocks 13
2.2.4. Post-failure behavior of rock masses 19
3. Dilation in granite during servo-controlled strength tests 31
3.1. Introduction 31
3.2. Testing equipment 32
3.3. Tested rocks 34
3.4. Testing 35
3.4.1. Non-destructive tests 35
3.4.2. Destructive tests 35
3.5. Interpretation of results 41
3.5.1. Classic parameters 41
3.5.2. Dilatancy 45
3.6. Conclusions of this chapter 52
4. Dilation in other rocks based on lab strength tests 53
4.1. Introduction 53
4.2. Rocks investigated 53
4.2.1. Indiana limestone 53
4.2.2. Carrara marble 54
4.2.3. Toral de Los Vados limestone 55

4.2.4. Touro amphibolite 55
4.2.5. Noia orthogneiss 55
4.3. Methods 55
4.3.1. Test setup 55
4.3.2. Data analysis 56
4.4. Interpretation of results 58
4.4.1. Strength 60
4.4.1. Deformability 62
4.4.2. Dilatancy 64
4.5. Conclusions of this chapter 66
5. Strength and dilation of jointed granite specimens in servo-controlled triaxial tests .. 67
5.1. Introduction 67
5.2. Test setup 68
5.2.1. Testing equipment 68
5.2.2. Rock testing 68
5.2.3. Jointed specimen preparation 68
5.3. Testing 70
5.3.1. Intact test cores 72
5.3.2. Jointed test cores 72
5.4. Results interpretation 73
5.4.1. Classic parameters 74
5.4.2. Dilatancy 80
5.5. Conclusions of this chapter 85
6. Stress-strain behavior of granite specimens as a function of their structure 87
6.1. Introduction 87
6.2. Test setup 88
6.3. Testing 90
6.4. Interpretation of results 96
6.4.1. Elastic parameters 96
6.4.1. Peak strength parameters 99
6.4.2. Residual strength parameters 104
6.4.3. Drop modulus 106
6.4.4. Dilation angle 107
6.4.5. A brief comment about the irrecoverable strain locus 113
6.5. Discussion 114
6.6. Conclusions of this chapter 116
7. Strain-softening characterization of granitic rocks and numerical simulation of servo-controlled strength tests 117
7.1. Introduction 117
7.2. Methodology 119
7.2.1. Correlation between strength and plastic strain 119
7.2.2. Correlation between dilatancy and plastic strain 122
7.3. Model results 123

7.4. Numerical approach 125
 7.4.1. Implementation of behavioral model 125
 7.4.2. FLAC models 125
 7.4.3. FLAC results 127
7.5. Conclusions of this chapter 128
8. Impact of post-failure rock mass behavior on excavation response 129
8.1. Introduction 129
8.2. Laboratory characterization 131
 8.2.1. Interpretation of tests: elastic and strength parameters 133
 8.2.2. Interpretation of tests: post-failure parameters 135
8.3. Rock mass characterization and models 137
 8.3.1. Rock mass characterization techniques 137
 8.3.2. Model basics 139
 8.3.3. Rock masses parameters 140
 8.3.4. Numerical models 141
8.4. Numerical results 142
8.5. Conclusions of this chapter 146
9. Conclusions 147
10. Future research lines 149
Publications totally or partially derived from this Ph.D. thesis: 151
 Conference papers: 151
 Scientific journal papers: 151
References 153
Appendices 161
 Appendix A. Complete development of the strains relationship 163
 Appendix B. Tables of tests results 165
 Appendix C. Examples of FLAC models. 175

List of Figures

Fig. 2.1. Straight line corresponding to Mohr-Coulomb failure criterion (eq. (2.1)) and relationship between principal and shear stresses. 8

Fig. 2.2. Extrapolation of the Mohr-Coulomb failure criterion to the region of negative confinements. 9

Fig. 2.3. The four possible post-failure behavior of rocks. 14

Fig. 2.4. Results of the classic strength tests performed by Von Kármán (1911) on Carrara marble. 15

Fig. 2.5. Results of the tests performed by Hadizadeh & Rutter (1983) on quartzite. 15

Fig. 2.6. Idealized axial stress-axial strain graph of a rock that behaves in a strain-softening manner, where the three deformational phases are also indicated. 16

Fig. 2.7. Evolution from peak to residual friction angle and cohesion. a) Descending both parameters, b) following CWFS approach. 17

Fig. 2.8. a) Axial stress versus volumetric strain, and b) axial stress versus axial strain and volumetric strain versus axial strain in a triaxial compression strength test on granite. 18

Fig. 2.9. Press stiffness importance in capturing post-failure behavior of rocks (after Ramírez-Oyanguren & Alejano, 2008). 19

Fig. 2.10. Examples of anastomosed structures at different scales, from millimeters to thousands of kilometers (Archambault et al., 1993). 20

Fig. 2.11 Scale and normal stress influence on post-failure behavior of rocks and rock masses (Rodríguez-Dono & Alejano, 2012; after Archambault et al., 1993). 21

Fig. 2.12. Idealized post-failure rock mass behavior as depending on GSI. 22

Fig. 2.13. Stress-strain relationships for a compression strength test on a strain-softening coal sample with four unloading-reloading cycles, three of them in the post-failure zone. The bottom graph shows the irrecoverable strain locus or the curve that relates the plastic components of the volumetric and axial strain as well as the formulation on which it is based (Alejano & Alonso, 2005; after Medhurst, 1996). 24

Fig. 2.14. Actual stress-strain relationships for a compression strength test on a strain-softening coal sample and ideal stress-strain relationships as proposed by Alejano & Alonso (2005) dilatancy model. From top to bottom: axial stress vs. axial strain; plastic and total volumetric strain vs. total axial strain; and dilatancy angle as function of the plastic axial strain (After Alejano & Alonso, 2005). 25

Fig. 2.15. Dilation angle behavior of the seven rocks studied by Zhao & Cai (2010a) as function of the plastic shear strain for a confining pressure of 1 MPa, and range of values for the nine coefficients grouped by grain size. 27

Fig. 2.16. Differences between the dilatancy models by Alejano & Alonso (2005) and those by Zhao & Cai (2010a) and Walton & Diederichs (2015a) regarding the starting point for counting the plastic parameter. 29

Fig. 3.1. Evolution of a servo-controlled test based on a given strain function. Major principal stress in the ordinate axis and axial strain in the abscissa axis. 33

Fig. 3.2. Petrographic study of rock samples showing pictures of hand samples and thin-section photographs in white and polarized light for the three granites studied. 34

Fig. 3.3. Stress-strain graph for confined compression test on granitic rock samples. In the upper left graph it is shown how to obtain the values for peak and residual strength (σ_1^{peak} and σ_1^{res}), apparent elastic Young's modulus (E), apparent Poisson's ratio (ν) and drop modulus (M). 40

Fig. 3.4. Complete stress–strain curves for Amarelo País granite for confined strength tests at different confining pressures. The most relevant tendency is for peak strength and residual strength to increase, apparent Young's modulus to slightly increase and radial and volumetric strain to decrease as confining pressure grows. 40

Fig. 3.5. Peak and residual strength test results and fitted to Hoek-Brown and Mohr-Coulomb failure criteria. 41

Fig. 3.6. Apparent elastic Young's modulus versus confining pressure for the three rocks studied. 43

Fig. 3.7. Apparent Poisson's ratio versus confining pressure for the three rocks studied...... 43

Fig. 3.8. Drop modulus versus confining pressure for the three rocks studied. 44

Fig. 3.9. Shear banding in the three types of granitic rocks. 44

Fig. 3.10. Orientation of shear bands versus confining pressure. 45

Fig. 3.11. Complete stress-strain curve obtained in a triaxial test. 45

Fig. 3.12. Graphic estimate of axial and volumetric plastic strains. 47

Fig. 3.13. Dilation angle vs. plastic shear strain for various confining levels and laboratory results and fits for each granite type.. 49

Fig. 3.14. Variations in fitting parameters (a, b and c) at different confining stresses (abscissa axis) and the best fit for each granite type... 51

Fig. 3.15. Variations in the mobilized dilation angle for the three granites studied and for other rock types at a confining stress of 1 MPa (from Zhao & Cai, 2010a): 1. Quartzite (coarse-grained hard rock); 2. Strong sandstone (medium-grained hard rock); 3. Silty sandstone (medium-grained hard rock); 4. Mudstone (fine-grained soft rock); 5. Seaterth (fine-grained soft rock); 6. Weak sandstone (fine- to medium-grained soft rock); 7. Coal (fine- to medium-grained soft rock). ... 51

Fig. 4.1. Grain structures of Indiana limestone, Carrara marble and Toral de Los Vados limestone. Thin plate section with crossed nicols (upper) and with visible light (lower) of the Touro amphibolite and Noia orthogneiss. Remark the foliation in the amphibolite (amphibole colored crystals) and the gneiss (black biotite). 54

Fig. 4.2. Example of data used to select the crack damage stress (CD) for each test specimen; axial stress versus axial strain (top), smoothed point to point tangent modulus (middle) and volumetric strain versus axial strain (bottom) plots are shown. 57

Fig. 4.3. Typical failure mechanisms in Indiana limestone, Carrara marble, Touro amphibolite, Toral de Los Vados limestone and Noia gneiss. The inset figure (bottom middle, courtesy of Gabriel Walton) shows grain scale conjugate shearing occurring in the Carrara marble. The confining stresses that the samples were tested at are shown at the top or the bottom of each picture.. 58

Fig. 4.4. Examples of the stress-strain response of the five studied rocks during a triaxial tests with a confining pressure of 6 MPa. A comparative (bottom right) between axial stress – axial strain curves of the five rocks is also showed, cycles have been removed from the curves in this graph in order to clarify the comparison, observe the similarity in Young's moduli of the Carrara marble (grey), Toral de Los Vados limestone (yellow) and Noia gneiss (light blue). 59

Fig. 4.5. Average drop modulus values for Indiana limestone and Carrara marble............... 60

Fig. 4.6. Strength data and least-squares Mohr-Coulomb (M-C) and Hoek-Brown (H-B) fits for Carrara marble, Indiana limestone, Toral de Los Vados limestone, Touro amphibolite and Noia gneiss. In the lower right graph, Hoek-Brown failure criterion fits for all the rocks are shown together... 61

Fig. 4.7. Variation in Young's Modulus as a function of confinement, with a linear model shown for the Indiana limestone and Carrara marble (both on top); and a logarithmic model shown for the Toral de Los Vados limestone, Touro amphibolite and Noia gneiss. 63

Fig. 4.8. Variations in the mobilized dilation angle for the five rocks studied (named 11, 12, 13, 14 and 15) and for other rocks types at a confining pressure of 1 MPa (after Arzúa & Alejano, 2013, with data from Zhao & Cai, 2010a). 65

Fig. 5.1. a) Cubic Blanco Mera granite sample with a 30-cm edge, prepared for cutting to obtain the sub-vertical joint set. b) Reassembled cut rock ready to extract cores with a sub-vertical joint. c) Cores with a sub-vertical joint. d) Re-joined core prepared for cutting to obtain the sub-horizontal joint set and the final specimen length. e) and f) The cutting process for sub-horizontal joints and specimen ends. g) An artificially jointed specimen. h) Final preparation of the plastic-wrapped jointed specimens. 69

Fig. 5.2. Problem encountered if the sub-vertical joint set is cut after, rather than before, obtaining the core. 70

Fig. 5.3. Stress-strain graph for confined (σ_3 = 4 MPa) compression test on a Blanco Mera granite jointed test core. Shown also is how to obtain the values for peak and residual strength, σ_1^{peak} and σ_1^{res}; apparent elastic Young's modulus, E; apparent Poisson's ratio, ν; and the drop modulus, M. 70

Fig. 5.4. Test specimens after compression testing. a) Sketch of the jointed core pieces. b) Shearing through pieces #3 and #4 and evidence of the rock flour that usually appears in sub-horizontal joints. c) Test core inside a sheath, showing the shear bands despite low confining pressures. d) After sheath removal, pieces bounded by the sub-horizontal joints (#3 and #4) crushed in multiple pieces, with the other pieces (#1, #2, #5 and #6) almost intact or showing signs of failure through shear bands. e) Shear band crossing pieces #4 and #6. 71

Fig. 5.5. Comparison of complete stress-strain curves between intact and jointed cores for different confining pressures. a) σ_3 = 2 MPa, b) σ_3 = 4 MPa, c) σ_3 = 6 MPa, d) σ_3 = 10 MPa, e) σ_3 = 12MPa. 74

Fig. 5.6. Peak and residual strength test results and fits to Hoek-Brown (H-B) and Mohr-Coulomb (M-C) failure criteria for jointed and intact cores. 75

Fig. 5.7. Comparison between residual strengths fits. 75

Fig. 5.8. Evolution of the GSI-equivalent value with confining pressure. 77

Fig. 5.9. Residual strength test results and H-B and M-C failure criterion fits for jointed cores. It can be seen that the M-C fit was better than the H-B fit due to the linearity of the test results. 78

Fig. 5.10. Apparent elastic Young's modulus versus confining pressure. 78

Fig. 5.11. Apparent Poisson's ratio versus confining pressure. 79

Fig. 5.12. Drop modulus versus confining pressure for the intact and jointed cores. 80

Fig. 5.13. Dilation angle versus plastic shear strain for various confining levels. Laboratory results and fits for each confining level for jointed cores. 82

Fig. 5.14. Variations as follows: a) the fit for parameter a in accordance with Equations (5.6); and b) peak dilation angle for different confining pressures for jointed and intact cores. Note the strong relationship between this parameter a and peak dilation angle (almost equal). 83

Fig. 5.15. Dilation angle versus plastic shear strain fits for various confining levels, with laboratory results for both jointed and intact cores. 84

Fig. 6.1. Concepts of scale and structure in rock masses. a) rock mass sample representative of rock mass behavior at the scale of the engineering work, as for Hoek & Brown (1980b); b & c: double and quadruple diameter homothetic transformation of circle a; d & e: rock mass samples of the same size than circle a but with the original structures corresponding to a, b and c respectively. 88

Fig. 6.2. a) (1+2) (one sub-vertical, two sub-horizontal) jointed specimen, as studied in Chapter 5. b) (2+3) (two sub-vertical, three sub-horizontal) jointed specimen, this study. c) and d) sketches of the different relative orientations of the sub-vertical and sub-horizontal joints of the (2+3) jointed specimen, explained in the text. 89

Fig. 6.3. Complete stress-strain curve result of a confined (σ_3 = 4 MPa) compressive strength test with unloading-reloading cycles and the indication of where the relevant parameters are obtained. 90

Fig. 6.4. Picture of the 2+3 jointed specimen JBM11 a) before, and b) and c) after testing; b) inside the sleeve; c) once the pieces of broken rock have been removed from the sleeve. Original and broken pieces have been lettered and the observed macroscopic failure trace surface has been marked in red. 91

Fig. 6.5. Example of complete stress-strain curves with unloading-reloading cycles of three of these specimens representative of each type (fresh –B13TRX – blue; (1+2) joints - BMD18 – red; and (2+3) joints – JBM11 - green) confined to 10 MPa. In the lower right graph together with actual volumetric-axial strain response, the irrecoverable strain locus is delineated in dotted lines. 92

Fig. 6.6. Example of axial stress-axial strain curves with unloading-reloading cycles of triaxial tests in intact rock submitted to confinement stresses of 2, 4, 6, 10 and 12 MPa and averaged general trends representative of tests in intact rock. 93

Fig. 6.7. Example of axial stress-axial strain curves with unloading-reloading cycles of triaxial tests in (1+2) artificially jointed rock specimens submitted to confinement stresses of 2, 4, 6, 10 and 12 MPa and averaged general trends representative of tests in (1+2) artificially jointed rock. 94

Fig. 6.8. Example of axial stress-axial strain curves with unloading-reloading cycles of triaxial tests in (2+3) artificially jointed rock specimens submitted to confinement stresses of 2, 4, 6, 10 and 12 MPa and averaged general trends representative of tests in (2+3) artificially jointed rock. 95

Fig. 6.9. Graphical representation of the apparent a) tangent (or average) and b) secant elastic Young's moduli. 97

Fig. 6.10. Graphical representation of Poisson's ratios vs. confining pressure. 98

Fig. 6.11. Peak strength of the 2+3 jointed specimens depending on the relative orientation of the joints. 99

Fig. 6.12. Representation of maximum shear strength line (blue) in p-q axes, Mohr-Coulomb line (red) in τ-σ_n axes and their correlation. 100

Fig. 6.13. Peak strength tests results and Mohr-Coulomb failure criterion fit for intact, (1+2) and (2+3) jointed specimens in terms of a) p-q line and b) results in σ_1-σ_3 axes. 100

Fig. 6.14. Peak strength tests results and Hoek-Brown failure criterion fit for intact, (1+2) and (2+3) jointed specimens in terms of a) $(\sigma_1-\sigma_3)^2$ - σ_3 axes and b) results in σ_1-σ_3 axes. 102

Fig. 6.15. Residual strength tests results and Mohr-Coulomb failure criterion fit for intact, (1+2) and (2+3) jointed specimens and all tests together in terms of a) p-q line and b) results in σ_1-σ_3 axes. 104

Fig. 6.16. a) Residual strength tests results and generalized Hoek-Brown failure criterion fit for intact, (1+2) and (2+3) jointed specimens. b) Residual strength GSI equivalent results for intact, (1+2) and (2+3) jointed specimens, suggesting a more relevant confinement effect in jointed samples. 106

Fig. 6.17. Estimated drop modulus indicator results, ω, for the case of jointed samples b) ω values for (2+3) artificially jointed samples with normal pattern (Fig. 6.2.c) and representation of eq. 8 for the case of GSI 40. 107

Fig. 6.18. Variations in fitting parameters (a, b and c) at different confining pressures and the best fit for each type of specimen. The parameters b and c of the jointed specimens (1+2 and 2+3) are the same than those of the intact specimens. 108

Fig. 6.19. Zhao & Cai (2010a) dilatancy model fits for different confining pressures and for the three types of specimens (intact, (1+2) joints and (2+3) joints). Please note the different vertical scale. 109

Fig. 6.20. Variation of the parameter γ' of the Walton & Diederichs (2015a) dilation model with confining pressure for the three types of specimens tested. 111

Fig. 6.21. Walton & Diederichs (2015a) dilatancy model fits for different confining pressures and for the three types of specimens (intact, (1+2) joints and (2+3) joints). Please note the different vertical scale. 112

Fig. 6.22. Volumetric strain vs. axial strain response of three characteristic samples as in Fig. 6.5, where also the irrecoverable strain locus is delineated in dotted lines. Observe that moving the irrecoverable strain loci of fissured samples downwards and rightwards, these irrecoverable strain loci tend to superpose over the locus corresponding to intact rock sample. 113

Fig. 6.23. An approach to estimate rock mass parameters based on tested jointed samples representative of rock mass structure and comparison with the traditional approach based on GSI. 114

Fig. 6.24. Deduced behavior of intact and increasingly fissured rock samples in parallel with decreasing quality rock masses in terms of a) axial stress-axial strain, b) strength, c) volumetric strain response and d) elastic moduli. 115

Fig. 7.1. Theoretical (simple strain-softening) and actual stress-strain response of a rock sample submitted to a triaxial test in the laboratory. 117

Fig. 7.2. Tested samples in the lab. 118

Fig. 7.3. Complete stress-strain curve from a triaxial test. 118

Fig. 7.4. Estimate of relevant σ_1-γ^p points from stress-strain complete curves as explained in the text. 119

Fig. 7.5. Representation of σ_1-γ^p points for triaxial tests with $\sigma_3 = 4$ MPa for Amarelo País granite. 120

Fig. 7.6. Fitted curves relating σ_1 and γ^p for different confining stresses together with points derived from tests on Amarelo País granite samples. 121

Fig. 7.7. Fitted curves relating σ_1 and γ^p for different confining stresses together with points derived from tests on Blanco Mera granite samples. 121

Fig. 7.8. Fitted curves relating σ_1 and γ^p for different confining stresses together with points derived from tests on Vilachán granite samples. 121

Fig. 7.9. Model and actual complete stress-strain curves of tests for samples of the three studied granites (Amarelo País, Blanco Mera and Vilachán), submitted to a confinement stress of 6 MPa. 124

Fig. 7.10. Boundary conditions and example of two grids used to numerically model the triaxial tests. 126

Fig. 7.11. Complete stress-strain curve (σ_1 - ε_1, σ_1 - ε_3 and ε_v - ε_1) for two triaxial tests (2 and 6 MPa) in Amarelo País granite. Actual tests and FLAC results with mesh size 15 x 60 corresponding to such confining pressures. 127

Fig. 7.12. Complete stress-strain curve (σ_1 - ε_1, σ_1 - ε_3 and ε_v - ε_1) for a triaxial test (6 MPa) in Amarelo Pais granite. Actual test and FLAC results with meshes 10x40, 20x80 and 40 x160. 127

Fig. 8.1. Schematic behavior of rock masses according to rock mass quality, as suggested by Hoek & Brown (1997). 129

Fig. 8.2. Confined compressive test of a rock sample with unloading-reloading cycles and comparison to rock mass behavior, as explained in the text. 131

Fig. 8.3. Typical stress-strain graph for a) unconfined compression test on granite rock sample. It is shown how to obtain the values of peak and residual strength, apparent elastic Young's modulus, apparent Poisson's ratio and drop modulus b) confined triaxial tests for different values of confinement. 132

Fig. 8.4. Peak and residual strength test results and M-C and H-B failure criteria fit for the tested granite. 134

Fig. 8.5. Graphic estimate of axial and volumetric plastic strains. 136

Fig. 8.6. Dilation angle vs. plastic shear strain for various confinement levels. Lab results and fits.. 136

Fig. 8.7. Stress-strain relationships for a modelled SS rock mass to estimate the value of γ^{p*}. 138

Fig. 8.8. FLAC mesh used to perform the tunnel simulations to investigate face behavior. 140

Fig. 8.9. Stress-strain behavior response of a strain-softening and mobilized dilation angle model material, as that representing a rock mass. 141

Fig. 8.10. Dilation angle model for the granitic rock mass (GSI = 50) obtained based on lab data and following the approach suggested by Zhao & Cai (2010b). 141

Fig. 8.11. Dilation angle distribution around tunnels. The dark sections indicate the plastic zones and the values attained by the dilation angle. The illustrated values of R_{pl}, R_{pl}^{f}, u_r and u_f are shown in Table 8.5 for all the models performed... 143

Fig. 8.12. Displacement distributions around the tunnel face for different behaviors of the average quality rock mass. 145

Fig. A.1. Unconfined test diagram, idealized deformational behavior and notation used. .. 163

Fig. A.2. Comparison between approximate and true formulations for deformation model. 164

List of Tables:

Table 2.1. Guide for the estimation of the disturbance factor D (Hoek et al. 2002). 12

Table 3.1. Quantitative modal analysis of the studied rocks derived from petrography analysis of thin sections. 35

Table 3.2. Summarized results of density, tilt and Brazilian tests for the three granitic rocks studied (mean results, and standard deviation between brackets). 36

Table 3.3. Results of testing on Amarelo País granite samples. 37

Table 3.4. Results of testing on Blanco Mera granite samples. 38

Table 3.5 Results of testing on Vilachán granite samples.. 39

Table 3.6. Geomechanical results for Amarelo País (m subscript refers to average values). 41

Table 3.7. Geomechanical results for Blanco Mera (m subscript refers to average values). . 42

Table 3.8. Geomechanical results for Vilachán (m subscript refers to average values). 42

Table 3.9. Fit coefficients for dilation angle-plastic parameter curves for the three granitic rocks studied.. 50

Table 3.10. Plastic shear strain parameters and confining pressure dependent dilation angle model as proposed by Zhao & Cai (2010a), for the three studied granitic rocks (this study) and two other rocks (Zhao & Cai, 2010a).. 50

Table 4.1: Number of tests performed on each rock and at each confining pressures. 56

Table 4.2. Strength fit data. 62

Table 4.3. Poisson’s ratio information. 62

Table 4.4. Young’s Modulus model information. 64

Table 4.5. Mobilized dilation angle fit parameters for the rocks tested. 64

Table 4.6. Parameters defining full mobilized dilation angle model. 65

Table 5.1. Results of testing on intact cores. 72

Table 5.2. Results of testing on jointed cores. 73

Table 5.3. Basic geomechanical results for intact cores of Blanco Mera granite. 76

Table 5.4. Basic geomechanical results for jointed cores of Blanco Mera granite. 76

Table 5.5. Plastic shear-strain parameters and confining-pressure-dependent dilation angle model as proposed by Zhao & Cai (2010a) for both jointed and intact test cores. 82

Table 6.1. Tangent and secant elastic moduli for unconfined and various confinement levels as derived from fittings to test data. 98

Table 6.2. Mohr-Coulomb peak failure criterion parameters derived from two fit approaches. 101

Table 6.3. Hoek-Brown failure criterion parameters derived from various fit approaches for peak strength. 103

Table 6.4. Hoek-Brown failure criterion GSI and parameters derived from fitting the strength results obtained in jointed samples reduced to a 70 %. 103

Table 6.5. Mohr-Coulomb residual failure criterion parameters derived from two fit approaches. 105

Table 6.6. Hoek-Brown failure residual criterion parameters derived from fit approaches of GSI and D. 105

Table 6.7. Coefficients of the plastic shear strain and confining pressure dependent dilation angle model as proposed by Zhao & Cai (2010a) for the three types of specimens tested. 109

Table 6.8. Parameters of the dilation angle model proposed by Walton & Diederichs (2015a) for the three types of Blanco Mera granite specimens tested. 111

Table 7.1. Fit of parameters a, b, c and d dependent on σ_3 for the three different tested granites. 120

Table 7.2. Parameters of the plastic shear strain and confining stress dependent dilation angle model as proposed by Zhao & Cai (2010a) for the three studied granitic rocks. 122

Table 7.3. Values of friction and cohesion for different values of the plastic parameters (first γ^{p}, and then, e^{ps}, obtained from γ^{p}, and dilatancy) for the case of Vilachán granite with a confining stress of 6 MPa (similar tables are obtained for different confinements and for the different granites). 126

Table 8.1. Results of compressive tests on granite. 133

Table 8.2. Basic geomechanic results of Amarelo País granite. 134

Table 8.3. Parameters of the plastic shear strain and confining stress dependent dilation angle model for the studied granite (this study) and two other rocks (Zhao & Cai, 2010a). 137

Table 8.4. Relevant parameters of the modelled rock masses. 140

Table 8.5. Results of the extent of the plastic zone and displacement observed in tunnel models, as obtained with FLAC, except those obtained with RocSupport. 144

Table B.1. Summary of results of elastic, strength and post-failure parameters obtained for each tested specimen of the Amarelo País granite. 165

Table B.2. Summary of results of elastic, strength and post-failure parameters obtained for each tested specimen of the Vilachán granite. 166

Table B.3. Summary of results of elastic, strength and post-failure parameters obtained for each tested specimen of the Carrara marble. 167

Table B.4. Summary of results of elastic, strength and post-failure parameters obtained for each tested specimen of the Indiana limestone. 168

Table B.5. Summary of results of elastic, strength and post-failure parameters obtained for each tested specimen of the Toral de los Vados limestone. 169

Table B.6. Summary of results of elastic, strength and post-failure parameters obtained for each tested specimen of the Noia gneiss. Observe that this rock should be classified as Class II (Hudson et al., 1972) due to its brittleness (results of drop modulus > 0, marked in bold in the table). 170

Table B.7. Summary of results of elastic, strength and post-failure parameters obtained for each tested specimen of the Touro amphibolite. 171

Table B.8. Summary of results of elastic, strength and post-failure parameters obtained for each tested specimen of the Blanco Mera granite. 172

1. Introduction

1.1. Preliminary comments

Growth of any society is directly related to the consumption of raw materials and to better infrastructure development. This statement, though not new or unknown, has become clear in recent years with the development of countries like China or India, which, without being the highest real economic growth (Positions #16 and #13 respectively in the world rank, both have 7.4% of the Gross Domestic Product (GDP) growth in the period 2010-2014 compared to, for instance, Ethiopia —#3—, with 9.9% of GDP growth in the same period or the United States —#108— with 2.4% of GDP growth, or Spain —#137— with 1.4% of GDP growth —Source: World Bank Group, 2015), given the huge population they have, represented an impact on the world economy, becoming major importers of raw materials. This increase in imports by China and India, has encouraged exploration and exploitation of new mineral deposits and the reopening of old workings due to the increased price of the aforementioned raw materials.

Exploration and exploitation of coltan (columbite, niobium ore; and tantalite, tantalum ore) and the minerals known as rare earth materials are being driven because of their worldwide strategic value since they are crucial in technological development. China appears here as a major producer and exporter, although the United States is trying to encourage exploration of these minerals in order to reduce dependence on the Chinese market of these minerals (USGS, 2013). Also the high prices reached by gold and copper have promoted development of new mines as well as reopening of closed old mines.

Important infrastructure works are being undertaken around the world: our hackneyed AVE (acronym of *Alta Velocidad Española*, Spanish High Speed in English) is burrowing Galicia with railway tunnels in order to address our pretty fanciful orography; major construction works being carried out in some Arab countries (e.g. Dubai in the United Arab Emirates); the huge reclaimed island to build Kansai International Airport in Osaka Bay in Japan; the Panama Canal expansion; or the Gotthard base tunnel under the Alps in Switzerland are examples, among many others, of major infrastructure works completed or under construction in the last years.

So, despite the global crisis in which we find ourselves, there are numerous mining operations or infrastructure works in which the rock masses are excavated for the benefit of society. Due to this increased number of excavation works and the increasing scale of the operations, we should also increase our knowledge of the rock masses to prevent accidents during the stages of construction, operation and abandonment, not only because accidents can cost lives, which should always be our top priority, but because it also leads to progress stops (with the consequent delay in the execution and financial costs to the company) or can cause severe environmental damage.

Some of the accidents with more media coverage include breaking of the tailings dam of the Aznalcóllar mine near Doñana National Park in 1998; the collapse of the San Jose mine in Chile in 2010, where 33 miners were trapped for 70 days some 700 meters deep until they could be rescued; or the northeast slope slippage of Bingham Canyon copper mine in Utah, USA, in April of 2013.

To avoid these accidents it is necessary, as already mentioned, to get the most possible knowledge of the materials one is working with, which are, for purposes of this thesis, the rock masses. A rock mass is a set of elements of intact rock blocks crossed by geological discontinuities of various kinds, so that the behavior of the rock mass does not only depends on intact rock's behavior, but also on the discontinuities' behavior, as well as other characteristics like, for instance, in situ stress level.

Thus, the behavior of a rock mass is complex and also difficult to estimate because it has a marked control by scale, that is, it cannot be extrapolated directly to the observed behavior at the laboratory scale of the work, so a standard application of the scientific method is not valid for this field of engineering, in which the heuristic, the case studies and numerical models are necessary investigative techniques. Keeping in mind that the amount of information available for carrying out a project that includes excavation in a rock mass is often scarce and although it increases as the work is done, even when it ends there is no assurance that one gets to know each and every one of the details that control the behavior of the rock mass.

However, for design and analysis of excavations in rock masses it is necessary to know their deformation and strength features. As a first approach, when information is scarce on the rock mass, empirical methods are currently used (Bieniawski, 1976, 1989, Barton et al., 1974; Barton & Grimstad, 1994) which are classic tools used in rock engineering, but often underestimate these parameters, returning, generally, conservative designs.

When the information about the rock mass is deeper, these geotechnical classifications are used to estimate the elastic parameters and peak failure criterion of rock masses (Hoek & Brown, 1980a, 1997; Hoek et al., 2002). This approach has been and still is widely applied in a number of projects. However, it is noteworthy that the application of this method was limited to rock mass behavior only up to the stress corresponding to the peak strength.

However, for certain tasks, such as application of the Convergence-Confinement method to the design of tunnels, or to deal with a yielded pillar into an underground mine, or in caving mining methods, it is necessary to know the rock mass behavior beyond the peak stress level.

The background for studying the post-failure behavior of rock masses is the post-failure behavior of rock samples at laboratory. There is a notable lack of compression strength test data, where tests have passed the peak strength and have continued to reach the residual strength. Only a few authors (Crouch, 1970; Farmer, 1983; Hassani et al., 1984; Medhurst, 1996) have published results of laboratory tests on rock specimens performing the tests beyond failure and up to a large enough strain level.

Although some authors have begun to study post-failure behavior of rocks and rock masses (Hoek & Brown, 1997; Crowder & Bawden, 2004, Carranza-Torres et al., 2002, Cai et al, 2004, 2007; Alejano & Alonso, 2005; Alonso et al., 2008; Alejano et al., 2009a, Alejano et al., 2009b; Zhao & Cai, 2010a, 2010b; Zhao et al., 2010; Walton & Diederichs, 2012, 2015a,2015b; Walton et al., 2015) there still are many aspects of interest to study. Precisely the lack of empirical data, has made that it is still necessary to identify application ranges in which they operate properly, and the advantages and problems they may have in terms of their applications.

1.2. Objective

This dissertation project aims to increase knowledge about post-failure behavior of rocks and rock masses, by performing both uniaxial and triaxial compression tests using the fully servo-controlled press that exists in the *John P. Harrison Rock Mechanics' Laboratory* of the Mining Engineering School of the University of Vigo, reaching, whenever possible, a strength level corresponding to the residual state and performing strain measurements —axial and radial in the case of uniaxial testing, meanwhile axial and volumetric in the case of the triaxial tests— during the course of the tests. These tests will be performed with several unloading-reloading cycles, with the intention of being able to identify the elastic and plastic components of strains.

A complete geomechanical characterization will be performed on the tested rock samples with the aim that the results obtained in this dissertation serve to make comparisons and identify the main features that make a rock behaves in one way or another.

Furthermore, a novel series of tests will be conducted in which two joint sets will be created in each specimen, thus, turning the specimens into a sample rock mass at laboratory scale. While this aspect still requires much more research, it stands to reason that it opens a door to understanding the scale and structure effects and the behavior of the rock mass compared to that of intact rock.

The results from this research could serve to:

- Improve knowledge of post-failure behavior of rocks at laboratory scale, aspect that several of the aforementioned authors have labelled as scarce.
- Delve into the already known but complex and therefore not entirely solved problem of scale in rock masses.

- Improve design techniques, stability estimation and underground excavation control and therefore safety in the implementation and use of tunnels, underground urban spaces or mining.
- Check the validity and range of application of the models of post-failure behavior recently proposed that, given the lack of information, are still in their early stages of development.

The author would like to state here that the main original objective of the present study was being able to carry out laboratory complete stress-strain tests in rock able to provide empirical results, in order to check the validity of proposed dilatancy models (as shown in chapters 3 and 4). This main aim has been largely fulfilled and, in addition, a number of experimental works and numerical simulations have also been carried out to continue on researching the post-failure behavior of rocks and rock masses.

1.3. Justification

As discussed in the previous section, the first approach for the design of underground excavations is based on classic geomechanical classifications (Bieniawski, 1976, Barton et al., 1974). Next step involves analyzing the stress level in the excavation once the stresses are redistributed in the surrounding rock mass. At this point, it is necessary to know the strength characteristics of the material forming the rock mass —i.e. the intact rock and the discontinuities— because if the modified in situ stresses are below the strength of the material, problems of failure through existing discontinuities should be analyzed by means of classic techniques (Hoek & Brown, 1980b) or by modelling software as Unwedge (Rocscience, 2013). If the modified in situ stresses reach values close to or greater than the strength of the rock mass, stress-strain analyses of the rock mass are needed to appreciate stability and propose support and reinforcement when necessary.

No doubt that the excavation of an underground work modifies in situ stresses in the vicinity of the excavation. Stresses supported by excavated rock, once removed, must be supported by the surrounding rock that has not been excavated. Assuming that the failure is not structurally controlled, if the surrounding rock can withstand that excess stress without reaching the failure criterion, the excavation will be self-supporting and additional support will not be strictly necessary. However, it is known that the rock masses tend to lose bearing capacity over time, this fact can lead to failure if no support is installed. This behavior will result in the release of rock blocks through pre-existing discontinuities. To long term prevent of such rock falls is desirable the installation of support, which will convert this discontinuous behavior (failure through discontinuities) in a more continuous behavior and generally in the inelastic or plastic range (stress relief in the form of irreversible rock material strain).

Design of an excavation requires, therefore, to know the mechanical behavior of the rock mass, which is defined by its elastic behavior, its failure criterion and its post-failure behavior. The first two aspects have been investigated from the early developments of rock mechanics, so they can be assumed to be reasonably well known, whereas post-failure behavior has been less studied and there are still gaps in the knowledge of the parameters governing that behavior.

Since rock mechanics is a relatively young discipline, it is hardly surprising that little attention has been paid to post-failure behavior of rock and rock masses —since engineering objective usually is to prevent failure—. During last 20 years some authors have begun working to try to understand how rock masses behave after they reach the peak failure criterion.

Hoek & Brown (1997), based in their experience in the engineering and numerical analysis of a variety of real cases, proposed three basic types of post-failure behavior for rock masses: an elastic-brittle behavior for good quality rock masses (Geological Strength Index, GSI > 75); an elastic-perfectly plastic behavior for poor quality rock masses (GSI < 25) and strain-softening behavior for average quality rock masses (25 < GSI < 75).

Archambault et al. (1993) also demonstrated qualitatively that the post-failure behavior must also necessarily depend on the confining stress to which the material is subjected.

It is therefore necessary to establish behavior frameworks and to obtain parameters that allow us to better understand and put numbers to this post-failure behavior. Among these parameters one can cite: dilatancy (for the three types of behavior); residual failure criterion (for elastic-brittle and strain-softening) and evolutionary failure criterion regarding softening parameter (for strain-softening). And it must be remembered that these parameters may be dependent on state variables, as the confining stress or the plasticity level.

The residual failure criterion can be obtained as recommended by Cai et al. (2004, 2007) who introduce the concept of GSI for the rock mass residual state (GSI_r). In these publications, the authors also propose an extended GSI classification system, which includes two simplified parameters for classification, the volume of the block and the joints condition factor. These two parameters are essentially descriptive and can be reasonably estimated, which would allow to get the value of this extended GSI.

Evolutionary failure criterion is only necessary in the case of a material showing strain-softening behavior, which is characterized by a gradual transition from the peak failure criterion to the residual failure criterion and this gradual transition is governed by a plastic or softening parameter, η. This evolutionary failure criterion therefore depends not only on the stress tensor, but also on that softening parameter (Rodríguez-Dono & Alejano, 2012).

The first approaches that were taken into account for the dilatancy considered two options: first, consider the dilatancy angle, ψ (which is the appropriate parameter to evaluate the dilatant behavior of a material) always equal to the friction angle, ϕ, which was termed as associated flow rule; and second, consider that the dilatancy angle was constant and, in general, equal to zero.

Vermeer & De Borst (1984) have noted that an associated flow rule does not necessarily represent post-failure behavior of rocks. Moreover, Detournay (1986) warned that the use of a constant dilatancy might lead to calculation errors and proposed a plastic strain dependent formulation. This dependence on plastic strain is observable as well as it is the dependence on the confining stress (Detournay 1986; Archambault et al, 1993; Farmer, 1983; Medhurst & Brown, 1998; Yuan & Harrison, 2004). Moreover, the dependence on the scale of the dilation has not been investigated, although it is a widely accepted topic when discussing discontinuities' dilatancy.

Despite these considerations, aiming to provide guidelines to apply in daily engineering design and based on their extensive practical engineering experience, Hoek & Brown (1997) recommended the use of values of the dilatancy angle, ψ, dependent on the quality of the rock mass and related to the friction angle, ϕ: considering $\psi = \phi / 4$ for good quality rock masses and $\psi = 0$ for poor quality rock masses.

Alejano & Alonso (2005) proposed a dilatancy model computable in two parts that included the dependence on confining pressure, on plastic strain and, indirectly, on scale. The first part of the model is concerned with obtaining the peak dilatancy angle and the second part simulates the decay as plastic strain progresses. It should be noted that this model considered certain simplifications, although it was very attractive to simulate dilatancy due to its simplicity (only one parameter dependent). In attempting to apply this model to the rocks studied in this research work, some discrepancies in the peak dilatancy angle between the results and those predicted by the model arose, however the evolution of this parameter with the plastic strain seemed to catch the actual behavior of rock. It should be noted that the model was obtained from tests performed by other authors (Medhurst, 1996; Farmer, 1983) in sedimentary rocks, while igneous and metamorphic rocks are the main focus of this work, this reason could lie behind the observed differences in the peak dilation angle.

Zhao & Cai (2010a) proposed a dilation model by fitting a curve to the results of testing a number of rocks ranging from soft to hard rock and including different types of rocks (igneous, metamorphic and sedimentary ones). This model included the dependence on confining stress and plastic strain, also capturing well the results obtained in our tests. However it is necessary to obtain nine parameters with little or no physical significance and the solution is also not unambiguous (various sets of parameters can provide equally accurate results).

Walton & Diederichs (2015a) have recently proposed a new dilation model that requires between four and seven parameters —depending on the available data— to completely characterize the dilatational behavior of rocks, being the main focus brittle rocks. It is mathematically based in a piecewise function that separates pre-mobilization of dilatancy, mobilization of peak dilatancy and post-mobilization of dilatancy. This division not only allows to consider each part separately, but it also allows a more detailed study of the influence of each parameter on the model and correlations with other geomechanical parameters.

It is reasonable to think that in coming years, models that simulate the dilatant behavior of rocks will be proposed, which do not make so many assumptions like Alejano & Alonso (2005) model and are not as complicated as that of Zhao & Cai (2010a). They should be ultimately based on laboratory studies (such as those presented here), numerical models and observations and measurements of the practical behavior of rock masses at large scale in the field. It is my expectation that the information gathered in this Ph.D. thesis can be of help for carrying out these tasks.

1.4. Contents of this dissertation

This Ph.D. thesis is structured in ten chapters, four of them corresponding to published papers: two of these were published in the International Journal of Rock Mechanics and Mining Sciences, and the other two correspond to oral presentations in rock mechanics symposiums (ARMA 2012 and Eurock2013). The first two chapters include the objectives, justification and an introduction to rock and rock mass behavior. The next four chapters (3, 4, 5 and 6) present the experimental work of this thesis developed along the last four years. This experimental part is the core of the doctoral work where more than 400 tests, some of them quite unconventional (such as those obtaining complete stress-strain curves with unloading-reloading cycles performed with artificially jointed specimens), have been performed starting from recovering the samples and preparing the specimens. The following chapters (7 and 8) show further developments seeking to extend the laboratory information recovered to numerical models in order to gather information on the implementation of dilation models in numerical codes and to explore the extrapolation of data to the rock mass scale and its impact on excavation behavior, being this line (numerical code simulation) the next natural step in the research. Chapter 9 outlines the general conclusions, based on the partial concluding remarks presented in every chapter. Finally, the last chapter suggest future research lines. In the following paragraphs, these chapters are briefly described.

The first and current chapter is a general overview of the post-failure behavior of rocks and rock masses and an introduction to the present dissertation.

The second chapter encompasses a literature review of rock mass behavior, particularly focusing the post-failure or post-peak part, which is the more complex and less researched one, as well as the main focus of the research project in which this dissertation is included.

The third chapter has already been published as a paper in the *International Journal of Rock Mechanics and Mining Sciences* (Arzúa & Alejano, 2013). This chapter explains the first successful attempt in recovering dilatant behavior of rocks starting from laboratory tests. Three granitic rocks were fully characterized. The most relevant pre- and post-failure parameters were obtained and fitted to the existing models. More than 200 tests were performed using, when available, rock mechanics standards (ISRM, 2007), 90 of them being unconfined and confined strength cycled tests.

The fourth chapter is the continuation of the laboratory testing, expanding the obtained results to a wider range of rock types including sedimentary and metamorphic rocks. The results of these chapters are a collaboration with Dr. Gabriel Walton and M.Sc. Ignacio Pérez-Rey and have also been published elsewhere (Walton et al., 2015; Pérez-Rey et al., 2014). In this chapter, five different rocks (two different limestones, a marble, an amphibolite and an orthogneiss) were tested in order to fully characterize them. The same procedures that in the previous chapter were used. More than 110 unconfined and confined strength cycled tests were performed. The different behaviors of the different rocks were captured and the most relevant pre- and post-failure parameters were obtained and fitted to existing models.

The fifth chapter has been published in the *International Journal of Rock Mechanics and Mining Sciences* (Arzúa et al., 2014). In this chapter, confined strength cycled tests were performed in 28 intact rock specimens and 22 artificially jointed rock specimens of one of the previously studied granites. These jointed specimens were intended to simulate a small scale rock mass. Comparison of intact specimen results with jointed ones revealed some key questions regarding post-failure scale problems. These questions were answered and explained in the text. This type of testing opens interesting opportunities to study the role of structure and scale in rock mass deformability, strength and post-failure behavior.

In the sixth chapter the author deepened a bit more in the small scale rock mass introduced in the previous chapter. We created the same jointed specimens but with more joints, aimed to confirm the previously observed trends. These last two chapters would probably be the most relevant contribution of this thesis to rock engineering knowledge. A comprehensive publication is being prepared reflecting the main findings of the results in the context of the information presented in previous chapters.

The seventh chapter is based on a paper presented in the *Eurock2013 Symposium* (Arzúa et al., 2013) where the author tried to find a model that characterizes post-failure behavior of the granitic rocks studied in the third chapter (strain-softening behavior). To achieve this model an empirical approach was used, fitting a mathematical equation to the actual axial stress-plastic strain relationship from the previously performed tests. It has to be noted that the comparison between this newly performed model and the actual tests unveils some differences due to the initial assumptions and inaccuracies associated to geometric and numerical simplifications needed to carry out tests. Nevertheless, the implemented model is a better approach than currently available strain-softening models.

Eighth chapter covers the results presented in a paper presented in the *ARMA2012 Symposium* (Alejano et al., 2012b). The chapter highlights the difference between considering or not considering a variable dilation angle in the excavation of a tunnel. Numerical models were performed on both different post-failure behavior and different quality rock masses in order to determine the amount of deformation in the walls and face of the tunnel and the extent of the plastic zone around the excavation for the different models considered.

Ninth chapter highlights the most relevant conclusions achieved in the course of the present dissertation.

Tenth chapter presents some possible future research lines that arose all along the process of study and research that ultimately crystallized in the present document.

2. State of the art: rock and rock mass behavior

2.1. Introduction

Rocks are naturally occurring solid aggregates formed by one or various minerals, and they appear in the Earth's crust forming rock masses, which are portions of rocks crossed by discontinuities of different geological origin (faults, joints, folds…) in such a way that a rock mass can be defined as a three-dimensional puzzle of rock blocks and discontinuities (Alonso, 2001).

It becomes evident, therefore, that the rock mass behavior will be controlled by the constitutive rock, as well as by discontinuities' distribution behavior. In this apparently simple and logical idea, lies the difficulty on studying rock mass behavior, which is very influenced by its scale, since the number of discontinuities considered when studying a rock mass grows as rock mass size grows (Hoek & Brown, 1997).

The same occurs when considering intact rock specimens for laboratory testing. It is well known that rock is a heterogeneous material composed of different mineral grains and presenting defects like pores, micro-fractures or weakness planes, so, under the same logic than for rock masses, the number of imperfections inside the rock specimen will grow as the rock sample increases in size.

Despite this problem —known as scale effect— is not completely solved, there are widely accepted approaches that work reasonably well while the elastic —i.e. before peak strength— and strength behaviors of the rock mass are considered. The same cannot be stated when studying post-peak behavior of rock masses. There are some gaps still unsolved that do not allow engineers to fully characterize the rock mass behavior.

Although mechanical features of rocks and discontinuities are reasonably known from the point of view of their application to engineering problems, henceforth it is not yet possible to perform a full characterization of the complex network of rocks and discontinuities that form a rock mass. Therefore, the knowledge of its actual behavior is limited, mainly due to its inherent complexity, its heterogeneity and the difficulties associated to its observation, among other issues.

The main aim of this chapter is presenting the parameters associated to a proper characterization of rock masses to fully characterize their behavior. This includes estimates of elastic parameters, definition and parameters of the most used failure criteria and possible approaches to characterize post-failure behavior, with particular emphasis on dilation. Comments on relevant and still open issues of this approach will be highlighted.

A similar and older version of this chapter dealing with rock mass behavior, but with a more mathematically rigorous background can be consulted in Alonso (2001).

2.2. Rock mass characterization

In order to build an engineering underground work in a rock mass it is necessary to know its features, structure and attributes to ensure the feasibility of the construction from a technical or engineering point of view or, in case that construction is not initially viable, to propose the suitable actions to carry out the construction in a safe and economical way.

Nevertheless, it has to be pointed out that a geotechnical study has limitations regarding the fact of being working with a natural and heterogeneous material, so it is not possible to know a priori each of the geological, structural and geomechanical details of a site.

Therefore, the objective of a geotechnical study should be limited to quantify and know the construction relevant characteristics, including stratigraphy, structure, lithology, contacts, morphology, groundwater table and thickness and characteristics of the altered part of the rock. The effects of variability of parameters and lack of geotechnical knowledge on rock mass response is probably one of the key issues in rock engineering design. As the construction moves forward, more information of the actual features will be available, which can be used to confirm or fine-tune the initial design.

The fundamental parameters of the rock (strength, deformability, density…) as well as those of the discontinuities (number of joint sets, mean spacing and length, main geotechnical features…) shall be known. It is also necessary to measure or estimate the in situ stress and consider the effects of other neighboring constructions.

In the following, the characterization of failure criteria, elastic parameters and post-failure behavior of rock masses are briefly revisited.

2.2.1. Failure criteria

A failure criterion is a set of equations that predicts the stress states at which a material will fail. In the context of this dissertation, the material will be a rock or a rock mass. Two failure criteria are typically used in rock engineering: Mohr-Coulomb and Hoek-Brown, which are briefly reviewed in the following sections.

2.2.1.1. Mohr- Coulomb failure criterion

The Mohr-Coulomb failure criterion is the simplest and still most widely used failure criterion (Jaeger et al., 2007). This criterion postulates that the shear strength of rocks has two components: cohesion and friction. Coulomb (1773) assumed that failure in a rock takes place along a plane making an angle β, to the horizontal, due to the shear stress, τ, acting along that plane. Motion is assumed to be resisted by a frictional-type force whose magnitude equals the normal stress, σ_n, acting along this plane, multiplied by some constant factor, $\mu=\tan\phi$, being μ the coefficient of internal friction and ϕ the internal friction angle of the material. Furthermore, motion along the initially intact failure plane is also assumed to be resisted by an internal cohesive force of the material, c. Such a force reflects the fact that, in the absence of a normal stress, a finite shear stress, S_0, is still needed in order to initiate failure. This can be expressed as:

$$\tau = c + \sigma_n \cdot \tan\phi \tag{2.1}$$

Equation (2.1) defines a straight line on the (σ_n, τ) plane (Fig. 2.1) indicating the stress states at which the failure will occur.

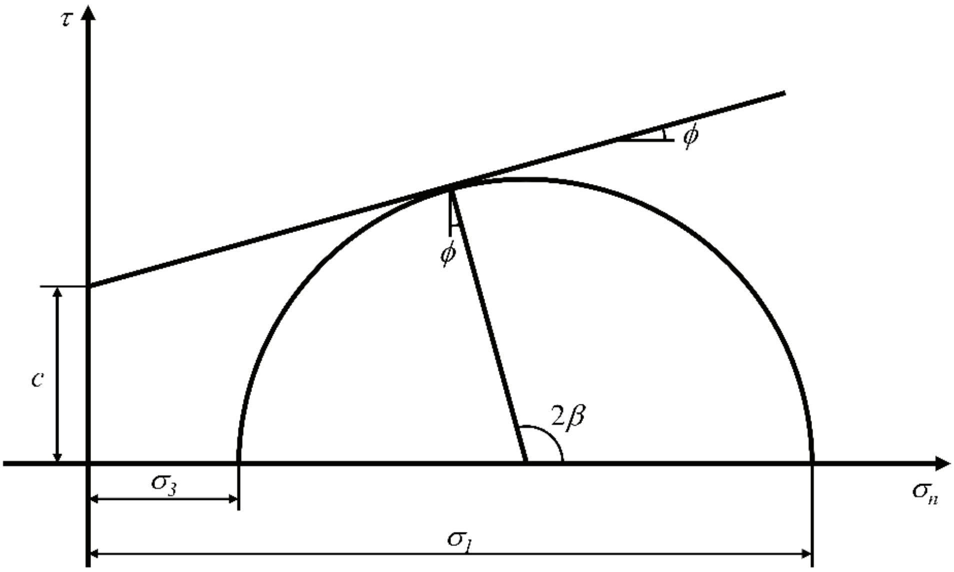

Fig. 2.1. Straight line corresponding to Mohr-Coulomb failure criterion (eq. (2.1)) and relationship between principal and shear stresses.

Normal and shear stresses of the failure plane can be related to the principal stresses using Fig. 2.1:

$$\begin{aligned}\sigma_n &= \frac{1}{2}(\sigma_1+\sigma_3)+\frac{1}{2}(\sigma_1-\sigma_3)\cdot\cos 2\beta \\ \tau &= \frac{1}{2}(\sigma_1-\sigma_3)\cdot\sin 2\beta\end{aligned} \tag{2.2}$$

Thus, the Mohr-Coulomb failure criterion can also be written as a function of major, σ_1, and minor, σ_3, principal stresses:

$$\sigma_1 = 2c\frac{\cos\phi}{1-\sin\phi}+\sigma_3\frac{1+\sin\phi}{1-\sin\phi} \tag{2.3}$$

Being the first term of the equation (2.3), $\left(2c\frac{\cos\phi}{1-\sin\phi}\right)$, the uniaxial compressive strength, and the slope of the line, $\left(\mathrm{K}_\phi=\frac{1+\sin\phi}{1-\sin\phi}\right)$, the coefficient of active earth pressure.

This failure criterion is valid for both peak and residual strength, but due to its linearity, it is not able to correctly predict the tensile strength of the rock. This failure criterion predicts ratios of unconfined compressive strength to unconfined tensile strength between 1 and 5.83 (Jaeger et al., 2007), while experimental values of this ratio tend to be on the order of ten or so.

Henceforth, Mohr-Coulomb failure criterion is not applicable to failure planes on which the normal stress is tensile. The standard practice for determining the failure stress states for negative normal stresses implies to interrupt the straight line of the criterion when tensile strength determined from laboratory tests (T_0) is reached (Fig. 2.2).

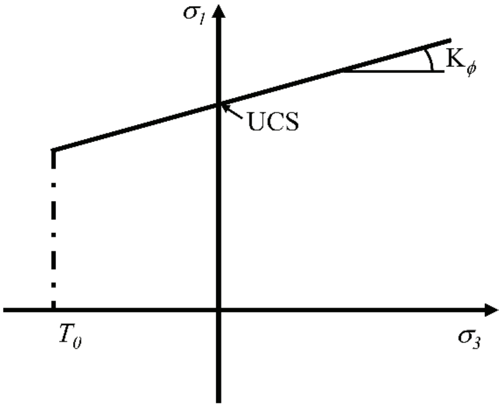

Fig. 2.2. Extrapolation of the Mohr-Coulomb failure criterion to the region of negative confinements.

The linearity of the criterion also implies that the compressive strength will increase linearly with the confining stress, but experiments typically show that σ_1 increases at a less-than-linear rate with σ_3. In order to correct these deficiencies, Mohr (1900) suggested that Coulomb's equation could be replaced by a more general, possibly nonlinear, relation.

2.2.1.2. Hoek-Brown failure criterion

Hoek-Brown failure criterion (Hoek & Brown, 1980a) is the most widely accepted and used one when studying rock masses behavior. It was initially proposed aimed to help in the design of underground excavations in competent rock masses. This failure criterion has suffered a number of modifications over the years in order to make it applicable for a greater number of rock engineering situations. The original failure criterion expression in terms of principal stresses is showed in equation (2.4).

$$\sigma_1 = \sigma_3 + \sqrt{m \cdot \sigma_3 \cdot \sigma_c + s \cdot \sigma_c^2} \tag{2.4}$$

where m, s and σ_c (the uniaxial compressive strength) are constants of the intact rock. If the rock is an intact rock, $s = 1$ by definition, which allows to obtain m and σ_c from uniaxial and triaxial strength tests. If these strength tests cannot be performed, there are tables on the available bibliography based on a number of performed tests (Hoek, 1983; Doruk, 1991; Hoek et al., 1992) which can provide rough values of these parameters. Hoek (1983) performed a brief analysis of the characteristics and limitations of this failure criterion version.

The main advantage of this failure criterion expressed by equation (2.4) against Mohr-Coulomb criterion is its non-linearity.

Hoek & Brown (1980a, 1988) add the relationship between m, s and a modified version of the Rock Mass Rating (RMR, Bieniawski, 1976) and distinguish between disturbed and intact or undisturbed rock masses.

For the disturbed rock masses:

$$m_b = m_i \cdot e^{\left(\frac{\mathrm{RMR}-100}{14}\right)} \tag{2.5}$$

$$s = e^{\left(\frac{\mathrm{RMR}-100}{6}\right)} \tag{2.6}$$

And for the undisturbed rock masses:

$$m_b = m_i \cdot e^{\left(\frac{\mathrm{RMR}-100}{28}\right)} \tag{2.7}$$

$$s = e^{\left(\frac{\mathrm{RMR}-100}{9}\right)} \tag{2.8}$$

where m_b and m_i are the constants for the broken and intact rock respectively.

This addition allowed to extend the failure criterion from rocks ($s = 1$) to rock masses ($s < 1$).

In 1992, Hoek et al. modified the criterion to take into consideration the fact that very jointed rock masses have no tensile strength, which led to get next equation:

$$\sigma_1 = \sigma_3 + \sigma_c \cdot \left(\frac{m_b \cdot \sigma_3}{\sigma_c} + s \right)^a \tag{2.9}$$

where m_b, s and a are constants of the rock mass depending on the structure and joints conditions.

Hoek (1994) and Hoek et al. (1995) introduce the generalized Hoek-Brown failure criterion aimed to deal with very poor quality rock masses. In this version of the failure criterion, the authors use the Geological Strength Index (GSI) to replace the RMR, in order to overcome the shortcomings of the RMR in such rock masses. The GSI classification is a simplified version of the RMR where neither the occurrence of water nor the role of joint orientation are taken into account. This approach is founded on the fact that numerical or analytical approaches can manage these issues without resorting to empirical methods. The authors also dismiss the concept of disturbed and undisturbed rock masses arguing that the disturbance is generally generated by engineering activities and it can be evaluated by means of decreasing GSI value.

In this version of the criterion (Hoek, 1994; Hoek et al., 1995) equation (2.9) is used, but the authors differentiate between very poor quality rock masses (GSI < 25) and the rest (GSI > 25).

For very poor rock masses, GSI < 25:

$$s = 0 \tag{2.10}$$

$$a = 0.65 - \frac{\mathrm{GSI}}{200} \tag{2.11}$$

For the rest of the rock masses, GSI > 25:

$$m_b = m_i \cdot e^{\left(\frac{\mathrm{GSI}-100}{28}\right)} \tag{2.12}$$

$$s = e^{\left(\frac{\mathrm{GSI}-100}{9}\right)} \tag{2.13}$$

$$a = 0.5 \tag{2.14}$$

One should take into account that the generalized Hoek-Brown criterion for rock masses with GSI > 25 is the same as the original one, only changing RMR by GSI.

Later, and since this criterion was being used (because of the lack of alternatives) in rock masses where the criterion was not applicable, Hoek et al. (2002) modified the failure criterion again to take into consideration the disturbance of the rock mass due to blasting and stress relief. The basic equation of the criterion is, again, equation (2.9), but *s* and *a* parameters are modified and a new factor, *D*, is added to consider that disturbance:

$$m_b = m_i \cdot e^{\left(\frac{\mathrm{GSI}-100}{28-14D}\right)} \tag{2.15}$$

$$s = e^{\left(\frac{\mathrm{GSI}-100}{9-3D}\right)} \tag{2.16}$$

$$a = \frac{1}{2} + \frac{1}{6} \cdot \left(e^{\frac{-\mathrm{GSI}}{15}} - e^{\frac{-20}{3}} \right) \tag{2.17}$$

D ranges from 0 (undisturbed rock masses) to 1 (very disturbed rock masses). This parameter has a great effect on rock mass strength and can be estimated using Table 2.1 (Hoek et al., 2002) which was proposed based on the expertise on tunnel and slope design of many authors. It has to be taken into consideration that the parameter *D* depends on many other factors and it may be impossible to quantify in a precise way them all, so the results are estimates and each case has to be particularly studied.

Hoek-Brown failure criterion in its last version (Hoek et al., 2002) can be used in intact rock specimens as well as in poor to good quality rock masses, but it does not adequately represent the behavior of very good rock masses, where spalling associated to brittle failure is meant to take place.

2.2.2. Rock mass deformability

In order to simulate rock mass behavior before the failure criterion is attained, it is certainly needed to know deformability parameters, which indicate how the rock mass will deform under load conditions. There are two parameters to estimate pre-failure deformability of an isotropic rock mass:

- Elastic modulus, also called Young's modulus, of the rock mass: E_m
- Poisson ratio of the rock mass: ν_m

If the rock mass is transversely isotropic, both parameters should be estimated for each of the principal directions and it should be added the parameter called shear modulus, *G*.

Nevertheless, it is very difficult to obtain an actual value of the Young's modulus of the rock mass from in situ or laboratory tests because this parameter mainly depends on the structure of the rock mass rather than on the rock itself, especially when a very good quality rock mass is considered. That is why empirical formulae have been developed that relate Young's modulus to the geotechnical quality of the rock mass. Among them the most used ones are those by Bieniawski (1976) and Serafim & Pereira (1983), whose expressions are, respectively:

$$E_m(\mathrm{GPa}) = \left(2 \cdot \mathrm{RMR}\right) - 100 \tag{2.18}$$

$$E_m\left(\mathrm{GPa}\right)=10^{\frac{\mathrm{RMR}-10}{40}} \tag{2.19}$$

Bieniawski's equation (eq. 2.18) is valid for rock masses with a RMR value between 60 and 100, whereas the second equation (eq. 2.19), which is based in a good number of in situ tests performed in dam sites in Portugal, presents a slightly larger range of applicability, being valid for rock masses with a RMR value between 40 and 100.

Table 2.1. Guide for the estimation of the disturbance factor D (Hoek et al. 2002).

Appearance of rock mass	Description of rock mass	Suggested value of *D*
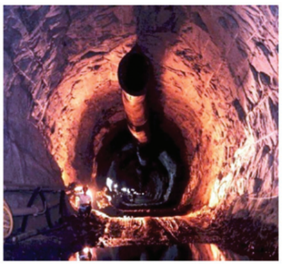	Excellent quality controlled blasting or excavation by Tunnel Boring Machine results in minimal disturbance to the confined rock mass surrounding a tunnel.	$D = 0$
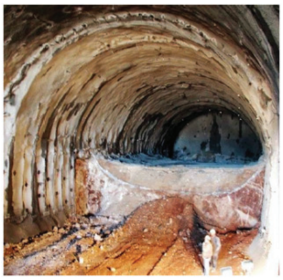	Mechanical or hand excavation in poor quality rock masses (no blasting) results in minimal disturbance to the surrounding rock mass. Where squeezing problems result in significant floor heave, disturbance can be severe unless a temporary invert, as shown in the photograph, is placed.	$D = 0$ $D = 0.5$ No invert
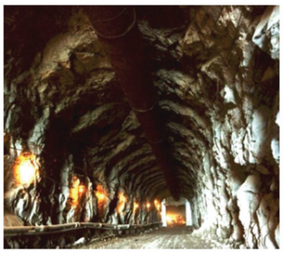	Very poor quality blasting in a hard rock tunnel results in severe local damage, extending 2 or 3 m in the surrounding rock mass.	$D = 0.8$
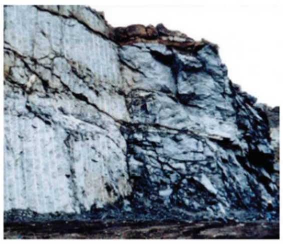	Small scale blasting in civil engineering slopes results in modest rock mass damage, particularly if controlled blasting is used as shown on the left hand side of the photograph. However, stress relief results in some disturbance.	$D = 0.7$ Good blasting $D = 1.0$ Poor blasting
	Very large open pit mine slopes suffer significant disturbance due to heavy production blasting and also due to stress relief from overburden removal. In some softer rocks, excavation can be carried out by ripping and dozing and the degree of damage to the slope is less.	D = 1.0 Production blasting D = 0.7 Mechanical excavation

Hoek & Brown (1988) recommend to use Serafim & Pereira (1983) equation (2.19) when handling their failure criterion. Later, the same authors (Hoek & Brown, 1997) modified this equation to consider rock masses whose forming rocks have a uniaxial compressive strength below 100 MPa, and also including the GSI instead of the RMR:

$$E_m\left(\mathrm{GPa}\right)=\sqrt{\frac{\sigma_{ci}}{100}}\cdot 10^{\frac{\mathrm{GSI}-10}{40}} \tag{2.20}$$

In the last version of their failure criterion (Hoek et al., 2002) they included the disturbance factor on the equation:

$$E_m\left(\mathrm{GPa}\right)=\left(1-\frac{D}{2}\right)\sqrt{\frac{\sigma_{ci}}{100}}\cdot 10^{\frac{\mathrm{GSI}-10}{40}} \tag{2.21}$$

More recently, Hoek & Diederichs (2006), based on a thorough analysis of a number of geotechnical studies —many of them performed with deformation measurements by means of plate-jacking tests or flat-jacks tests— proposed a new expression —which the authors call Simplified Hoek and Diederichs equation— where the Young's modulus of the intact rock is not considered:

$$E_m\left(\mathrm{GPa}\right)=100\cdot\left(\frac{1-\frac{D}{2}}{1+e^{\frac{75+25\cdot D-\mathrm{GSI}}{11}}}\right) \tag{2.22}$$

If the available information is larger and the elastic modulus of the intact rock is available, the same authors in the same paper (Hoek & Diederichs, 2006) propose another equation in which the Young's modulus of the intact rock is included:

$$E_{rm}\ (\mathrm{MPa})=E_i\left(0.02+\frac{1-D/2}{1+e^{\left(\frac{60+15D-GSI}{11}\right)}}\right) \tag{2.23}$$

There are also other equations based on the Q index of Barton (Barton et al., 1974), as well as other equations specifically applicable to stratified and relatively low strength rock masses (Ramamurthy, 1986) where the rock mass elastic modulus is related to the elastic modulus of the intact rock (E_R) and the RMR.

Regarding Poisson's ratio of the rock mass, it has to be noted that its estimation usually does not get much attention because its influence on rock mass response is usually quite small, as it is its natural range of variation (0.15 – 0.45). Its value for a rock mass can be estimated using the tables presented by Hoek & Brown (1988) and for good quality rock masses it is accepted to be the same of the intact rock as obtained from laboratory tests.

2.2.3. Post-failure behavior of rocks

Brittle solid materials, like glass, fail after reaching their elastic limit and are unable to support any load after failure. In contrast, many rocks (and concrete) show a residual strength after reaching certain level of plastic (irreversible) strain. There are four types of post-failure behavior (Fig. 2.3), depending on how this residual strength is reached:

a) Upper left graph of Fig. 2.3 represents the Strain-Hardening (SH) behavior, characterized by increasing its strength after reaching the elastic limit, but it only occurs for the case of rocks when there is a great confining pressure, far away from the engineering construction orders of magnitude for rocks, but not for clays or evaporitic rocks.

b) Upper right graph of Fig. 2.3 represents the Elastic-Perfectly-Plastic (EPP) behavior, where the material is able to support its ultimate strength after reaching it and for large levels of plastic strain.

c) Lower left graph of Fig. 2.3 represents the Elastic-Brittle (EB) behavior, characterized by a sudden drop in strength from its ultimate strength to the residual strength, this sudden transition shows no plastic strain and, after the residual strength is reached, the rock material begins to deform plastically.

d) Lower right graph of Fig. 2.3 represents the Strain-Softening (SS) behavior, where there is a progressive drop in strength from peak to residual accompanied by plastic strains.

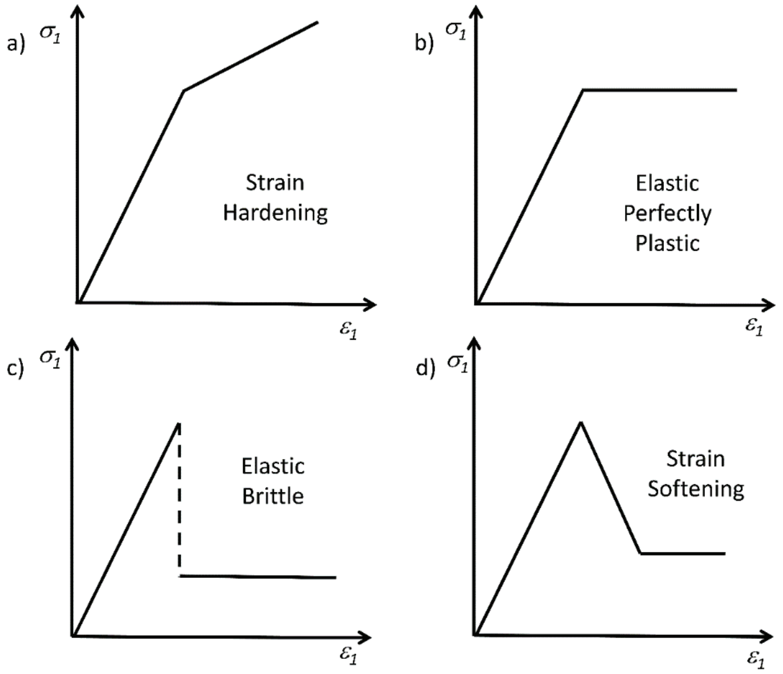

Fig. 2.3. The four possible post-failure behavior of rocks.

As commented above, rock mass behavior is influenced by its forming rock and discontinuities' behavior, so it is reasonable to believe that scarcely jointed rock mass behavior should be similar to the observed intact rock behavior. Hoek & Brown (1997) reached this same conclusion based in their own experience in diverse rock mass modelling, as they indicated that a good quality rock mass (GSI > 75) will present an elastic-brittle behavior, whereas a poor quality rock mass (GSI < 25) will present an elastic-perfectly-plastic behavior. A mean quality rock mass (25 > GSI > 75) will behave in a strain-softening manner.

It also has to be pointed out that elastic-perfectly-plastic behavior and elastic-brittle behavior are the limiting cases of a strain-softening behavior, i.e. elastic-brittle behavior will occur if the transition from peak to residual is sudden and elastic-perfectly-plastic behavior will occur if there is no transition. So considering strain-softening behavior is a comprehensive approach able to accommodate most commonly observed rock mass behavior.

Post-failure behavior of a rock depends, in addition, on the confining stress, as evidenced by the classic tests performed by Von Kármán (1911) on Carrara marble (Fig. 2.4). In this figure it can be observed an elastic-brittle or strain-softening behavior prior reaching 50 MPa of confining stress, while for a confining stress of 110 MPa the rock behaves almost in an elastic-perfectly-plastic manner because it can reach strains of almost 5% without evident lose in strength. For larger confinements, 360 MPa (conditions to be encountered around 15 km deep in the Earth's crust), strain-hardening behavior appears.

This phenomenon was also observed by Hadizadeh & Rutter (1983) (Fig. 2.5).These authors tested a quartzite for different confining pressures and graphed the results of the deviatoric stress (σ_1 - σ_3) versus the axial strain (ε_1). These graphs also show that the peak strength grows as confining pressure grows, meanwhile the post-failure slope of the curve becomes less steep.

Brittleness of a rock is defined by the slope of the axial stress-axial strain curve once peak strength has been achieved, i.e. following nomenclature on Fig. 2.6:

$$\frac{\sigma_1^M - \sigma_1^R}{\varepsilon_1^R - \varepsilon_1^M} \tag{2.24}$$

where σ refers to strength, ε refers to strain, M superscript refers to peak, R superscript refers to residual and subscript 1 refers to the major principal direction.

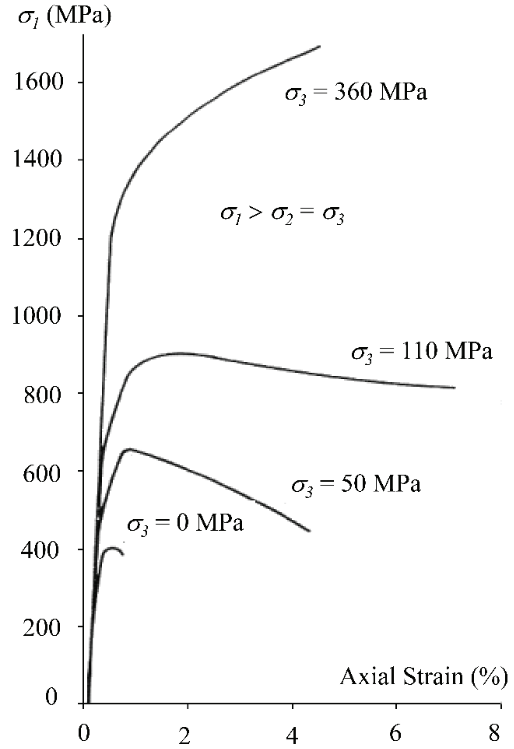

Fig. 2.4. Results of the classic strength tests performed by Von Kármán (1911) on Carrara marble.

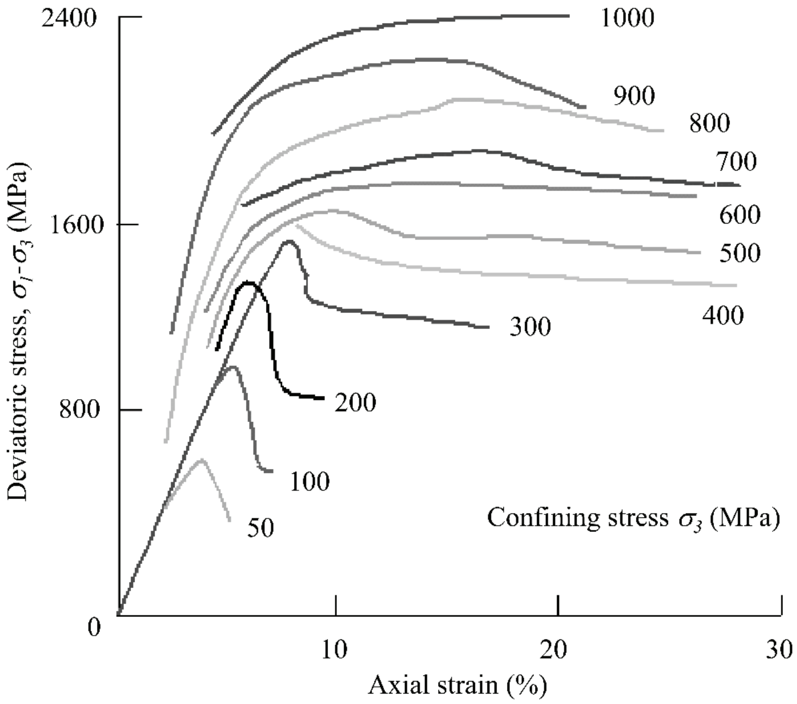

Fig. 2.5. Results of the tests performed by Hadizadeh & Rutter (1983) on quartzite.

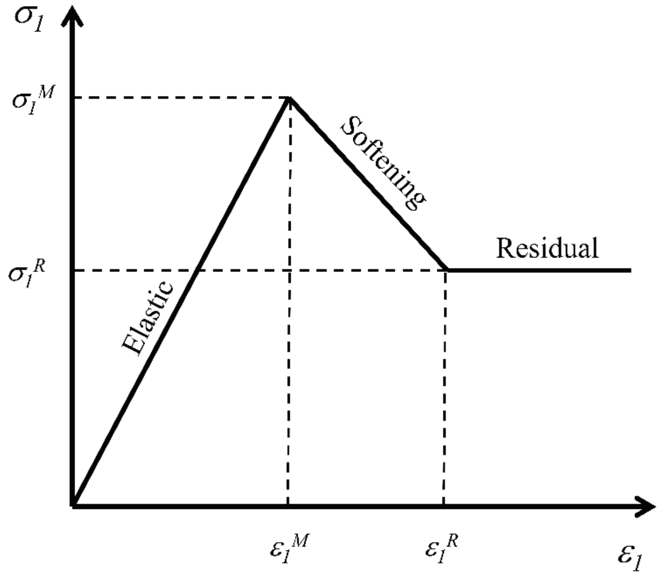

Fig. 2.6. Idealized axial stress-axial strain graph of a rock that behaves in a strain-softening manner, where the three deformational phases are also indicated.

Fig. 2.6 shows in an idealized way the three deformational phases that exhibits this kind of material: an almost elastic zone between the beginning of the test and the peak strength; a softening zone between peak and residual strengths; and the residual phase. These three phases can be expressed in terms of the failure criterion as follows:

$$F(\sigma_1,\sigma_3,0)=0 \tag{2.25}$$

representing the failure criterion of the intact rock,

$$F(\sigma_1,\sigma_3,\eta)=0, \text{ with } 0<\eta<\eta^* \tag{2.26}$$

representing the evolving failure criterion during softening and

$$F(\sigma_1,\sigma_3,\eta)=0, \text{ with } \eta\geq\eta^* \tag{2.27}$$

representing the residual failure criterion corresponding to a perfect plasticity state.

where η, known as softening parameter, controls the transitional failure criterion between peak and residual failure criteria. This parameter will be, generally, dependent on the plastic strains.

Elastic state exists while this softening parameter is null (eq. 2.24), softening state occurs when the softening parameter is not null but it does not reach a specific value η^*, known as critical softening parameter (eq. 2.25) and the residual state appears when the softening parameter surpass this critical value (eq. 2.26).

Softening portion slope (Fig. 2.6) is known as softening or drop modulus. If the rock material behaves in an elastic-brittle manner, this drop modulus tends to infinity, whereas if the behavior is elastic-perfectly-plastic, this modulus becomes null.

Therefore, in order to correctly describe post-failure behavior of a rock, it will be necessary to know:

a) Peak and residual failure criteria and, if there is a transition (i.e. strain-softening behavior), evolving failure criterion between peak and residual strengths. Residual failure criterion allows to estimate the strength of the broken material, consequently it will present the same equation that peak failure criterion (Hoek-Brown, Mohr-Coulomb…) but different parameters.

b) Relationship between stresses and strains as the strength decreases from peak to residual state. This relationship can be defined by the softening modulus and the critical softening parameter (η^*) or by a specifically designed function. It has to be noted that this stresses-strains relationship is hard to know because it depends on the confining pressure.

c) A flow rule that drives how the strains develop (mainly the principal plastic strains) once peak strength failure criterion has been achieved and defines them once the residual state has been reached. It is typically assumed to have the same shape as a failure criterion (Hoek-Brown, Mohr-Coulomb…) with strains substituting the stresses.

When the flow rule is equal to the failure criterion in each moment, it is known as associated flow rule, if Mohr-Coulomb failure criterion is used, associated flow rule means that the dilation angle, ψ, equals friction angle, ϕ, at each moment. If flow rule is different from the failure criterion, one will speak of non-associated flow rule.

One of the classic ways to implement the softening model using Mohr-Coulomb failure criterion consists in utilizing a function of the principal stresses, σ_1 and σ_3, and of the softening parameter, η (Carranza-Torres, 1998; Itasca, 2011):

$$F\left(\sigma_1,\sigma_3,\eta\right)=\sigma_1-\mathrm{K}_p\left(\eta\right)\cdot\sigma_3-q_u\left(\eta\right)=0 \tag{2.28}$$

The functions $\mathrm{K}_p(\eta)$ and $q_u(\eta)$ represent the evolution of the material cohesion and friction values as depending on the softening parameter:

$$\mathrm{K}_p\left(\eta\right)=\frac{1+\sin\phi\left(\eta\right)}{1-\sin\phi\left(\eta\right)} \tag{2.29}$$

$$q_u\left(\eta\right)=2\cdot c\left(\eta\right)\cdot\sqrt{\mathrm{K}_p\left(\eta\right)} \tag{2.30}$$

The variation of the friction angle, ϕ, and the cohesion, c, as depending on the softening parameter can be considered linear by parts, as they appear on a general form in Fig. 2.7. It has to be pointed out that the classical way to implement this behavior is considering a descending trend of both parameters (Fig. 2.7.a, top). But a relatively new approach considers that the failure will occur first losing the cohesion and then, mobilizing the friction angle (Fig. 2.7.b, bottom), it is the approach known as Cohesion-Weakening-Friction-Strengthening (CWFS). This latter approach was developed to fit observations of hard rocks behavior at depth, where brittle phenomena such as spalling are typically observed.

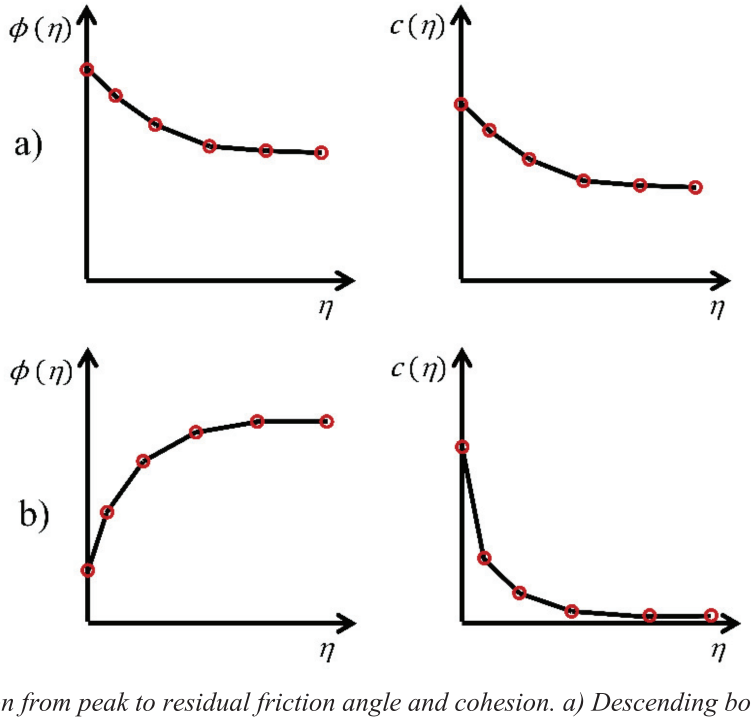

Fig. 2.7. Evolution from peak to residual friction angle and cohesion. a) Descending both parameters, b) following CWFS approach.

When a strength test (uniaxial or triaxial) is performed on a rock specimen, the rock behaves modifying its volume, and this change in volume becomes more evident once its peak strength is overpassed —i.e. in the post failure state. If this volume change is measured with the appropriate equipment, one can relate this volumetric strain to the axial stress (Fig. 2.8.a) or to the axial strain (Fig. 2.8.b).

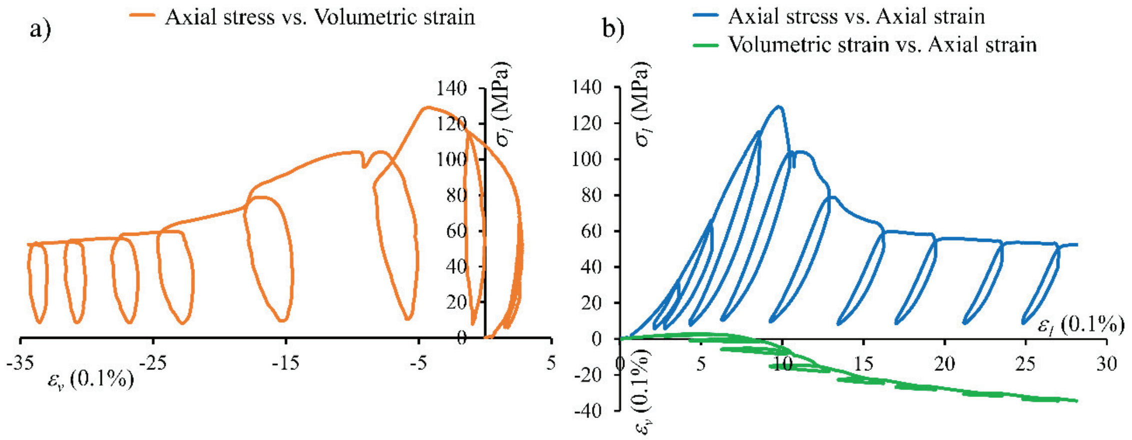

Fig. 2.8. a) Axial stress versus volumetric strain, and b) axial stress versus axial strain and volumetric strain versus axial strain in a triaxial compression strength test on granite.

It becomes evident from Fig. 2.8 that the volumetric behavior of the specimen during the test is not easy to reproduce, let us remember the sign convention: positive means contraction and negative means expansion. During the initial phase of the test, the specimen reduces its volume due to the closure of existing micro-cracks and pores; before reaching peak strength, the specimen begins to rise its volume due to the formation of new micro-cracks; just moments before failure the specimen gets an actual increase in volume; and, from here onwards, the specimen continues rising its volume, but it does not rise always at the same rate as well as it cannot do it indefinitely (Alejano & Alonso, 2005; Zhao & Cai, 2010a).

That is to say rocks present a complex dilatant behavior. Dilatancy can be defined as a change in volume as results of the shear distortion of an element into a material. A suitable parameter to measure this dilatant behavior is the dilatancy angle, ψ, which relates the incremental plastic strains (Alejano & Alonso, 2005). This issue will be analyzed in more detail later on.

However, it should be noted that this kind of tests where the residual state is reached, can only be performed in press machines stiffer than the specimens tested. This is another reason that could explain why there are not more tests which correctly capture post-failure behavior and reach a sufficiently large strain level to ensure the attainment of residual state. This high stiff presses are expensive and difficult to handle, so they are not common in standard rock mechanics laboratories. To understand the importance of the stiffness of the machine in the results of the tests an energy balance approach is convenient (Fig. 2.9).

This Fig. 2.9 shows what happens with a) a less and b) a more stiff press than the tested specimen. Let us consider the peak strength (A), if the specimen deforms a small amount $\Delta\varepsilon_1$, reaching G, the load should be reduced from σ_A to σ_G. The energy needed to reach that strain is the area ACDG below the stress-strain curve.

In the case of a stiffer rock specimen, for the same amount of strain ($\Delta\varepsilon_1$) the press can only reduce its stress to F and the freed energy by the press is the area ACDF, larger than the energy needed to deform the test specimen, i.e. there is an excess of energy ($+\Delta E$) which gives rise to the explosive failure of the rock specimen just after reaching its peak strength.

In the case of a stiffer press, the stored energy in the machine is fewer ($-\Delta E$) than the needed to continue the deformation process of the rock specimen, so it is necessary to provide external energy to continue the test. This necessity for additional energy allows, aided by a servo-control system, to control the test once peak strength is overcome, obtaining in such a way a reliable record of the post-failure behavior of the tested specimen. There are some very brittle rocks that require really high stiff machines and with a very good servo-control in order to correctly study their post-failure behavior.

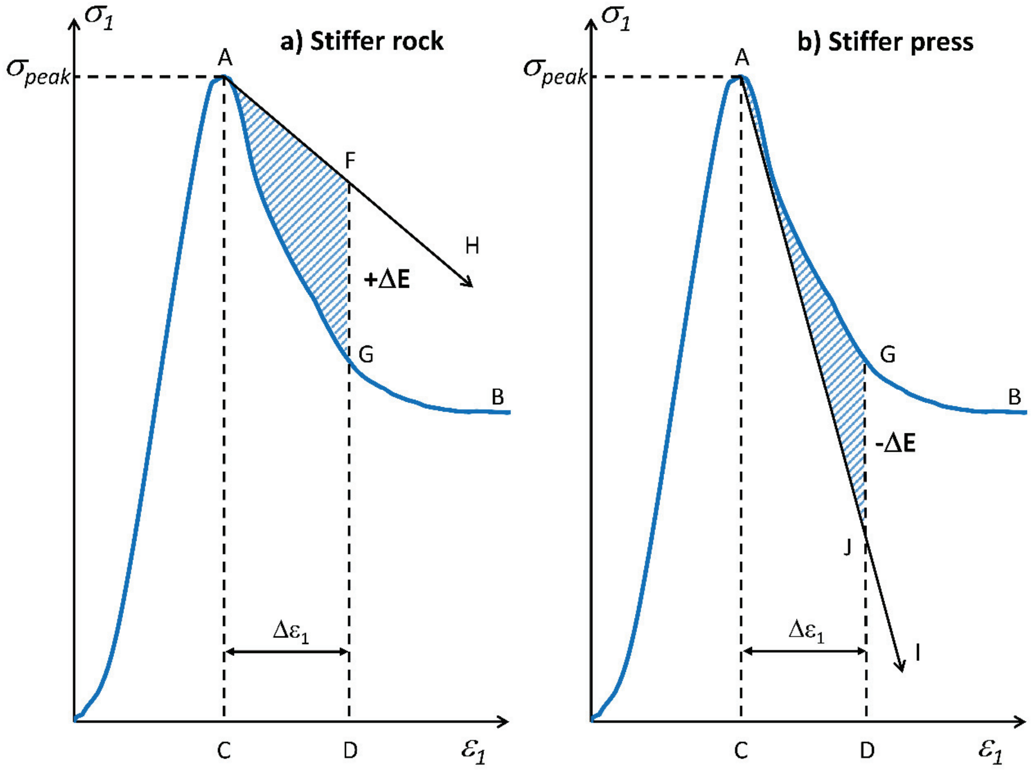

Fig. 2.9. Press stiffness importance in capturing post-failure behavior of rocks (after Ramírez-Oyanguren & Alejano, 2008).

2.2.4. Post-failure behavior of rock masses

Pre-failure behavior of rock masses has been largely studied and it can be reasonably well estimated, which is hardly surprising since, usually, engineers try to avoid failure, as Panet (1995) commented in an analysis of underground excavations. Nonetheless, post-failure behavior has not been studied in such a detail, first due to the point of view of Panet and second, due to the complexity of its study, which needs both understanding the occurring phenomena and trying to set parameters in order to characterize that behavior.

2.2.4.1. General frame of rock masses' post-failure behavior

Generic post-failure behavior of rocks can be, generally, extrapolated to rock masses. As commented previously in section 2.2.3, the general approach for post-failure of rock masses is that proposed by Hoek & Brown (1997), funded in the vast experience of these authors in the analysis of a great variety of actual case studies. As said before, there are three types (actually four, but strain-hardening behavior does not usually appear at the stress levels found in rock engineering works) of post-failure behavior depending on the geotechnical quality of the rock mass.

These authors propose an elastic-brittle behavior for the rock masses exhibiting a GSI more than or equal to 75, because they have observed in situ sudden drops in strength. For rock masses with a GSI lower than 25 they propose an elastic-perfectly-plastic behavior because when analyzing tunnel failures in this kind of rock masses, they observed great levels of strain without apparent loss in strength meanwhile there was not a significant change in volume related to this failure. Finally, for mean quality rock masses (GSI between 25 and 75), the authors propose that residual failure criterion could be estimated progressively reducing the GSI, consequently this criterion would not be equal to that of the rock mass when failing (perfect plasticity) nor null (elastic-brittleness), so it would be between them, i.e. strain-softening.

Diederichs & Martin (2010) specified even more precisely the range of application of these behavior models adding the relationship between uniaxial compressive strength of the intact rock (UCS_i) and tensile strength (T). When this relationship (UCS_i/T) is lower than 15, which approximately corresponds to soft rocks, strain-softening behavior model could be extended up to a GSI equal to 80. On the other hand, if the relationship is larger than 15, which roughly corresponds to hard rocks, strain-softening behavior should only be applied up to a GSI 65.

Archambault et al. (1993) reviewed the different aspects that contribute to shear failure in rocks and rock masses, showing that the anastomosed jointed structures (Fig. 2.10) created by shear or tensile stress and the scale effects in shear strength of rocks and rock masses are the final result of a progressive softening mechanism of the rock mass.

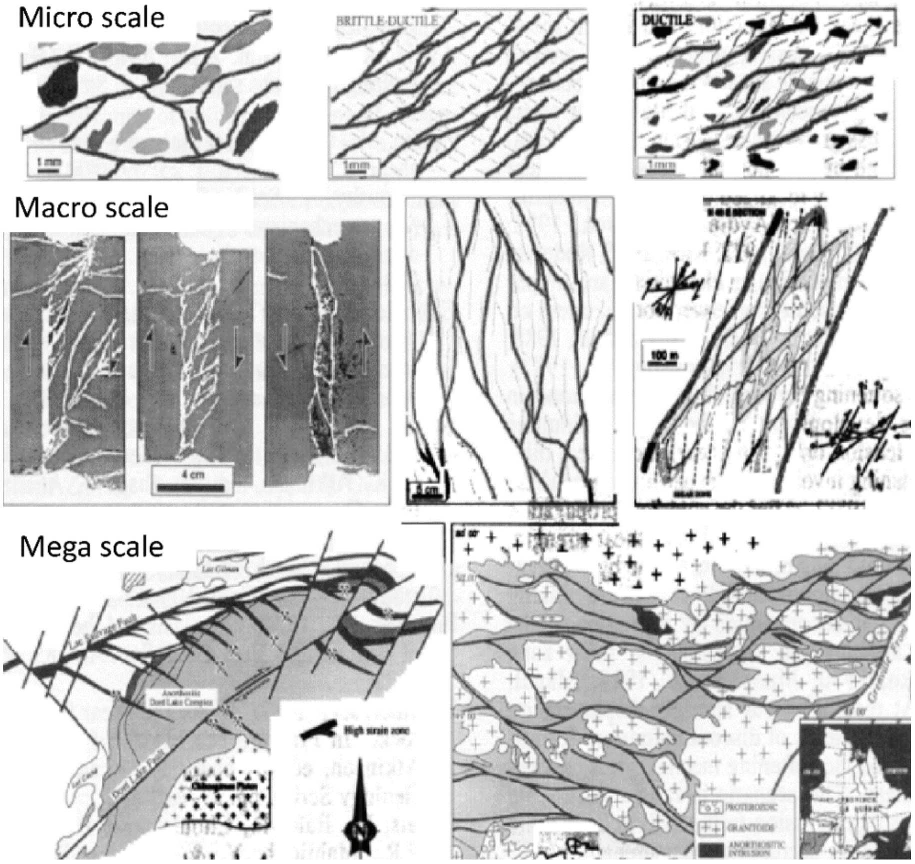

Fig. 2.10. Examples of anastomosed structures at different scales, from millimeters to thousands of kilometers (Archambault et al., 1993).

According to these authors, when applying shear stresses to rocks and rock masses, simple heterogeneous shear strains are generated and high values of shear or tensile stresses are concentrated (high gradients) in narrow bands where the strain is localized or where the tensile cracks are propagated. These discontinuity zones (due to shear or tensile stress) develop during a hardening phase which is characterized by an increase in the dilatancy, driving to an expansion in the shear zone. When the maximum level of shear stress is reached and the discontinuities are completely propagated, a new phase of unstable softening begins, giving rise to new discontinuities. When the residual strength is finally reached, anastomosed discontinuities structures will have formed where the softening mechanism concentrates, moreover, this phenomenon occurs at any scale (Fig. 2.10) according to the authors.

Fig. 2.11 shows the interdependence between the acting variables in this phenomenon (shear stress, τ; shear displacement, δ_h; normal stress, σ_n; normal displacement, δ_n) and the scale dependence (Rodríguez-Dono & Alejano, 2012; after Archambault et al. 1993).

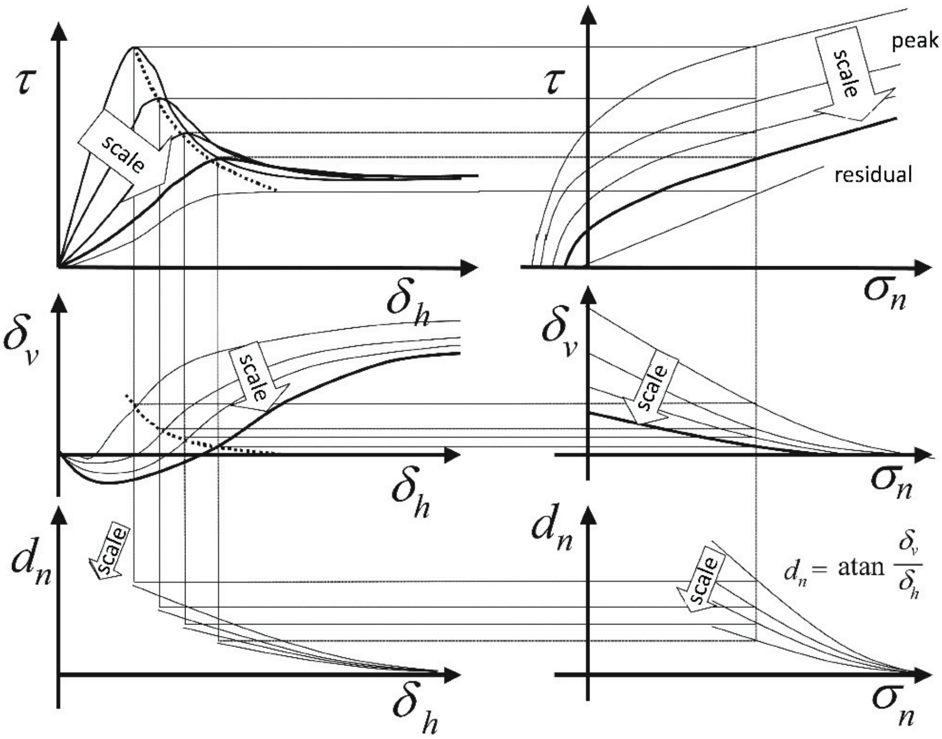

Fig. 2.11 Scale and normal stress influence on post-failure behavior of rocks and rock masses (Rodríguez-Dono & Alejano, 2012; after Archambault et al., 1993).

Aimed to find a physical meaning of the dilatancy in soils, concrete and rocks, Vermeer & De Borst (1984) considered a shear strength test on a soil. The material in the interface between the two halves of the shear zone forms a thin failure zone. If one consider δ_v as the normal or vertical displacement and δ_h as the shear or horizontal displacement, dilation angle of the shear band can be estimated according to:

$$\tan\psi = \frac{\delta_v}{\delta_h} \tag{2.31}$$

Considering this definition, the graph showed by Archambault et al. (1993) (Fig. 2.11) can be reinterpreted:

- When increasing analysis scale one can observe: (i) peak strength decreases, (ii) residual strength remains the same, (iii) peak dilatancy decreases, (iv) strains increase and (v) the material begins dilating for a bigger plastic strain level.
- When increasing normal stress (σ_n) for a specific scale: (i) peak and residual strengths increase, (ii) peak dilatancy decreases and (iii) dilatancy angle becomes null for a lower plasticity level.

From these observations one can extend the rock masses natural trend for withstanding softening processes that, in any case, are difficult to generically translate into a model, because it is not an easy task to get the representative values of all the relevant parameters in order to correctly simulate that strain-softening behavior (Alejano et al., 2012a).

Having in mind that the introduction of a geotechnical quality index (RMR, GSI, Q…) is only a way to consider the scale effect, one can observe that this reasoned approach by Archambault et al. (1993) matches the Hoek & Brown (1988) proposal, because all in all, they point that the drop of strength between peak and residual failure criteria will be larger at lower scale, i.e. at better geotechnical quality.

2.2.4.2. Transitional and residual failure criteria

Residual failure criterion for rock masses can be, if not calculated, at least estimated from the appointments by Hoek & Brown (1997). This failure criterion would be well below the peak failure criterion of good quality rock masses (GSI > 75) and would tend to be similar to peak failure criterion of poor quality rock masses (GSI < 25). Following this trend it is reasonable to believe that average quality rock masses will maintain the form of the failure criterion from that of the very good quality rock masses to that of the poor quality rock masses (Fig. 2.12).

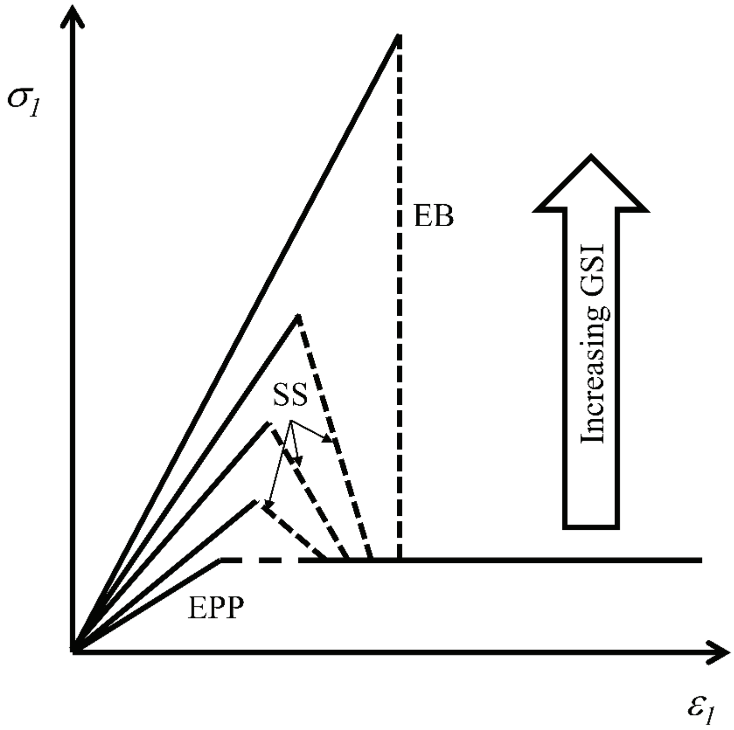

Fig. 2.12. Idealized post-failure rock mass behavior as depending on GSI.

One of the classical ways to implement this strain-softening behavior model was previously presented when commenting post-failure behavior of rocks (Eqs. 2.27, 2.28 and 2.29 and Fig. 2.7) and it could be extrapolated to the case of rock masses.

Another way to estimate residual failure criterion of coal rock masses was proposed by Duncan-Fama et al. (1995) using a strain-softening behavior model. The authors used the Hoek-Brown failure criterion for both peak and residual values. Obtained results seem to adapt quite well to the classic empirical formulae of coal pillar strength as well to certain in situ observations.

2.2.4.3. Plastic parameter

The parameter known as plastic parameter is an indicator of the plastic damage suffered by a rock. It is null all along the elastic phase and it starts to grow as soon as plastic strain appears, growing as far as plastic deformation unfolds.

The most traditional way to define a plastic parameter is based on the plastic shear strain:

$$\gamma^p = \varepsilon_1^p - \varepsilon_3^p \tag{2.32}$$

Or an incremental parameter like that used by FLAC code (Itasca, 2011):

$$\Delta e^{ps} = \left\{ \frac{1}{2}\left(\Delta\varepsilon_1^{ps} - \Delta\varepsilon_m^{ps}\right)^2 + \frac{1}{2}\left(\Delta\varepsilon_m^{ps}\right)^2 + \frac{1}{2}\left(\Delta\varepsilon_3^{ps} - \Delta\varepsilon_m^{ps}\right)^2 \right\}^{1/2} \tag{2.33}$$

where:

$$\Delta\varepsilon_m^{ps} = \frac{1}{3}\left(\Delta\varepsilon_1^{ps} + \Delta\varepsilon_3^{ps}\right)$$

$\Delta\varepsilon_j^{ps}$ with $j = 1, 2, 3$ are the increments of the shear strain in the principal directions.

This formulation of the incremental plastic parameter can be related to one dependent on the internal variables using:

$$e^{ps} = \frac{\sqrt{3}}{3}\sqrt{1 + \mathrm{K}_{\psi} + \mathrm{K}_{\psi}^{2}}\,\frac{\gamma^{p}}{1 + \mathrm{K}_{\psi}} \qquad (2.34)$$

where $\mathrm{K}_{\psi} = \dfrac{1 + \sin\psi}{1 - \sin\psi}$

If null dilatancy is considered, this relationship simplifies to:

$$e^{ps} = \frac{\gamma^{p}}{2} \qquad (2.35)$$

Although, like Alejano & Alonso (2005) commented, no significant error is incurred if this relation (eq. 2.34) is considered with variable dilatancy, so the authors recommend to use this much easier approach.

2.2.4.4. Critical softening parameter

Critical softening parameter, η^*, indicates the level of plastic deformation when the residual state is reached, i.e. when the residual state of the rock mass begins. To know which value this parameter should have, it would be necessary to get at least one actual stress-strain curve of the rock mass, which is a very difficult task, if not impossible.

From the appointments regarding generic rock mass behavior stated by Hoek & Brown (1997), from the in situ observations and numerical simulations of coal pillars by Duncan-Fama et al. (1995), and from the laboratory observations of different sized coal specimens by Medhurst & Brown (1998), it can be proposed that the critical softening parameter can vary between 0.01 and 0.001 strains, i.e. between 1 and 0.1 % of the axial strain.

2.2.4.5. Flow rule

It was already commented in section 2.2.3 that a flow rule is the law governing the way strains evolve once peak failure criterion is reached. It was also commented that an associated flow rule takes place when the flow rule is equal to the failure criterion at every moment and non-associated in any other case.

Therefore, it is necessary to know if the flow rule is associated or non-associated and, in the latter case, it is also necessary to know the shape and parameters of this flow rule —which in its simple form can be related to a Mohr-Coulomb equivalent— characterized by the parameter denoted as dilation angle and explained in the following section. It has to be pointed out that there is controversy over this subject. Some prestigious authors (Hoek, Fairhurst) indicate that the efforts should be put in non-associated flow rules and, particularly for soft rock masses, a null or almost null dilatancy should be considered; while other authors specialized in localization (Vardoulakis & Sulem, 1995) are able to show that a frictional material with a non-associated flow rule cannot be numerically stable, so they propose associated flow rules (Carranza-Torres, 2000).

Regarding dilation angle, ψ, as a first approach and since there was an evident lack of data, Hoek & Brown (1997), propose values dependent on the friction angle, ϕ, and the quality of the rock mass, $\psi = \phi / 4$ in the case of competent rock masses, $\psi = \phi / 8$ in the case of average quality rock masses and, $\psi = 0$ in the case of soft rock masses, the latter corresponds to the case of constant volume deformation.

In order to analyze the general behavior of a rock mass, one should suppose that the rock mass will show a strain-softening behavior, so in addition to the peak failure criterion, one should add a residual failure criterion, a transition relationship and a flow rule.

2.2.4.6. Alejano & Alonso dilatancy model (2005)

Alejano & Alonso (2005) presented a review of a number of performed studies and a fit for a number of already performed laboratory tests in order to propose a reasonable estimation model regarding the dilation angle, aimed to its implementation in numerical methods. The proposed dilation angle estimation model, showed dependencies both on confining stress and on plastic shear strain and, indirectly, scale dependency was also included through the friction angle, obtained from the Hoek-Brown failure criterion.

This model was founded on the reinterpretation of triaxial strength test results using a servo-controlled press performing unloading-reloading cycles and direct measure of the volumetric strain (by means of displaced oil) on rock specimens of different sizes (Medhurst, 1996) that allow to get test results as those showed in next figure (Fig. 2.13).

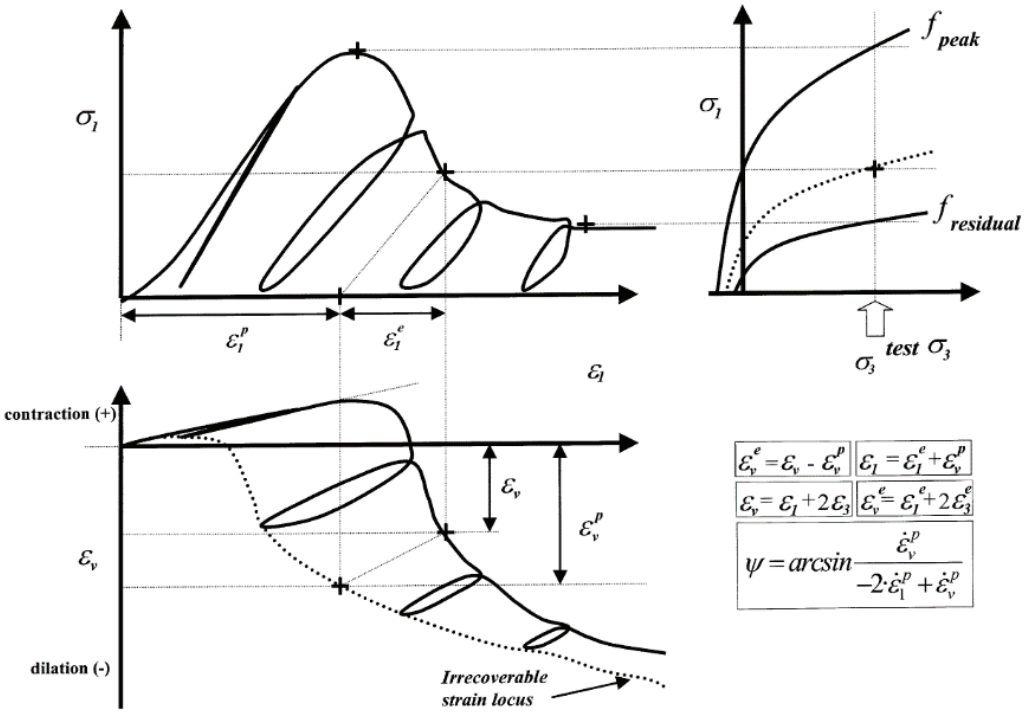

Fig. 2.13. Stress-strain relationships for a compression strength test on a strain-softening coal sample with four unloading-reloading cycles, three of them in the post-failure zone. The bottom graph shows the irrecoverable strain locus or the curve that relates the plastic components of the volumetric and axial strain as well as the formulation on which it is based (Alejano & Alonso, 2005; after Medhurst, 1996).

Irrecoverable strain locus (ε_v^p - ε_1^p curve) can be obtained for each test, and from that curve, dilatancy angle can be calculated using the equation proposed by Vermeer & De Borst (1984):

$$\psi = \arcsin \frac{\dot{\varepsilon}_v^p}{-2\cdot\dot{\varepsilon}_1^p + \dot{\varepsilon}_v^p} \tag{2.36}$$

It has to be noted that the Alejano & Alonso (2005) proposed model discards various inelastic (but not plastic) phenomena that occur during strength tests before peak strength is reached, i.e. in the elastic zone:

i. Initial perpendicular to the major principal stress micro-cracks closure, which give that initial concave shape to the axial stress-axial strain curve.

ii. The phase between stable propagation of cracks (onset of dilatancy or Crack Initiation, CI) and unstable propagation of cracks (or Crack Damage, CD), where the axial strain is elastic, but radial strain is not, which would give rise to, due to the equation used, dilation angles tending to minus infinity.

iii. Final phase before failure occurs, between long term strength (or CD) and the instantaneous or ultimate strength, also called maximum or peak strength, where a hardening behavior appears and the micro-cracks coalesce, giving rise to the macro-cracks that produce the failure.

Discarding these phenomena allows the interpretation of test results although some inaccuracies arise that avert the model from the actual behavior, but it does not make an important difference if working with secant elastic modulus instead of tangent one. This difference between the model and the reality can be observed in Fig. 2.14.

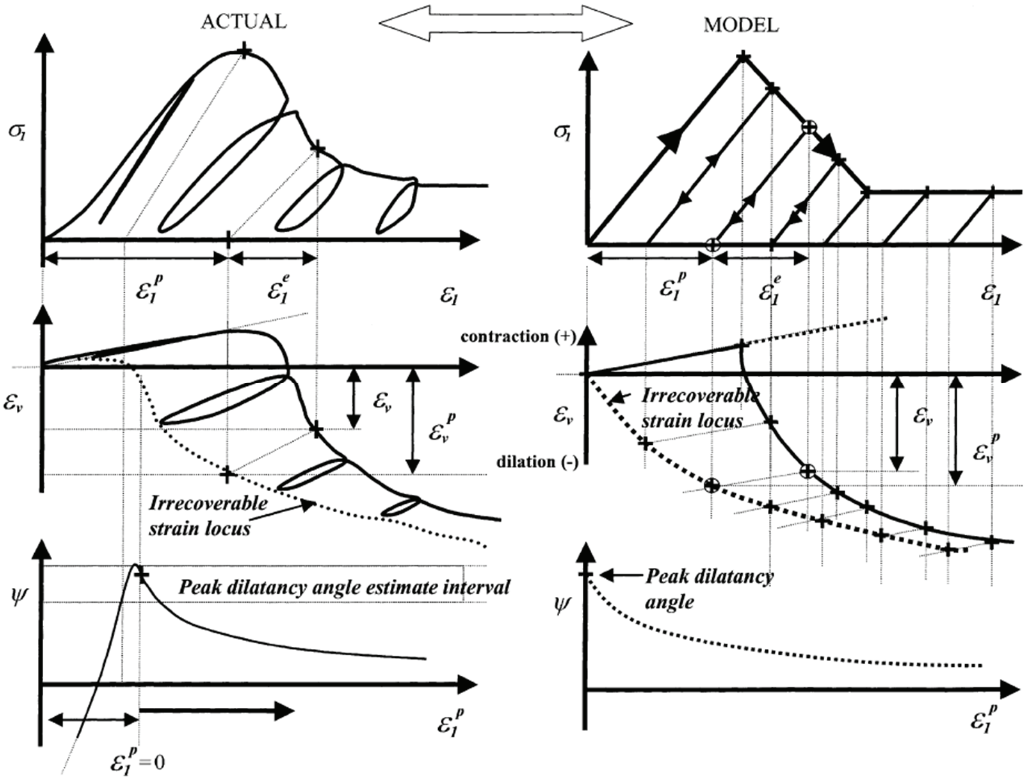

Fig. 2.14. Actual stress-strain relationships for a compression strength test on a strain-softening coal sample and ideal stress-strain relationships as proposed by Alejano & Alonso (2005) dilatancy model. From top to bottom: axial stress vs. axial strain; plastic and total volumetric strain vs. total axial strain; and dilatancy angle as function of the plastic axial strain (After Alejano & Alonso, 2005).

Alejano & Alonso (2005) proposed a dilatancy angle model divided in two parts, first it is calculated the peak dilatancy angle:

$$\psi_{peak} = \frac{\phi}{1+\log\sigma_{ci}} \cdot \log\left(\frac{\sigma_{ci}}{\sigma_3+0.1}\right) \tag{2.37}$$

And then, the dilatancy angle decay is calculated as the plasticity grows:

$$\mathrm{K}_{\psi} = 1 + \left(\mathrm{K}_{\psi_{peak}} - 1\right) \cdot e^{\frac{-\gamma^p}{\gamma^{p*}}} \tag{2.38}$$

where:

$$\mathrm{K}_{\psi} = \frac{1+\sin\psi\left(\sigma_3, \gamma^p\right)}{1-\sin\psi\left(\sigma_3, \gamma^p\right)} \tag{2.39}$$

Dilation angle can be obtained for each stress-strain situation depending on the confining stress, σ_3 (MPa), and the plastic shear strain, γ^p (mstr.), from an initial value of peak friction angle corresponding to that stress and to the specimen scale, ϕ (°), the uniaxial compressive strength of the intact rock, σ_{ci} (MPa), and a parameter that governs the decrease of the dilatancy with the plasticity level, called $\gamma^{p}*$ (mstr.).

Alejano & Alonso (2005) compare their model results to the obtained results from Medhurst (1996) tests getting a reasonably good fit of the dilatancy behavior on coal specimens and other sedimentary rocks (Farmer, 1983) regarding both, peak dilatancy angle and its decay as the plasticity moves forward.

It has to be pointed out that the model requires the parameter γ^{p*}, which depends on the rock type, but the authors give estimated values of this parameter for the studied rocks.

The main advantages of this model are that it does not increase the number of needed parameters in order to simulate a rock mass (only a parameter, γ^{p*}, is needed, instead of a constant dilation angle) and, despite its simplicity, it allows to get more realistic values of dilatancy as depending on confining stress, plasticity level and for different scales, so it can be implemented into commonly used numerical codes.

The results obtained during the compression strength tests performed for the present dissertation have been fitted to this model and, although the model is capable to capture the correct dilation angle decay with plasticity, it is not able to accurately compute peak dilation angle, systematically underestimating this value for the tested rocks.

2.2.4.7. Zhao & Cai dilatancy model (2010a)

Zhao & Cai (2010a) introduced a dilatancy angle model much more complex than that of Alejano & Alonso (2005), using an empirical approach, they found a mathematical function depending on the plastic shear strain that fits very well the test results:

$$\psi = \frac{a \cdot b \cdot \left(e^{-b \cdot \gamma^p} - e^{-c \cdot \gamma^p} \right)}{c - b} \tag{2.40}$$

where a, b and c are fitting coefficients and γ^p is the plastic shear strain obtained from the internal variables (eq. 2.27) in %.

Coefficients a, b and c control the shape of the curve and, although this control is not absolutely independent, each coefficient mainly affects one aspect of the curve, i.e. a coefficient mainly controls peak dilation angle value, b coefficient mainly controls the position of the peak dilation angle and c coefficient mainly controls the evolution of the dilation angle.

The model also considers the confining stress dependence by means of another three equations that modify the values of the coefficients a, b and c. These equations have been obtained, again, using an empirical approach:

$$a = a_1 + a_2 \cdot e^{\frac{-\sigma_3}{a_3}} \tag{2.41}$$

$$b = b_1 + b_2 \cdot e^{\frac{-\sigma_3}{b_3}} \tag{2.42}$$

$$c = c_1 + c_2 \cdot \sigma_3^{c_3} \tag{2.43}$$

where a_i, b_i and c_i with $i = 1, 2, 3$ are, again, fitting coefficients and σ_3 is the confining stress.

Using this approach, the authors were able to characterize the dilatancy angle behavior of seven different rocks and they also grouped the nine needed coefficients as a function of the grain size of the rock (Fig. 2.15).

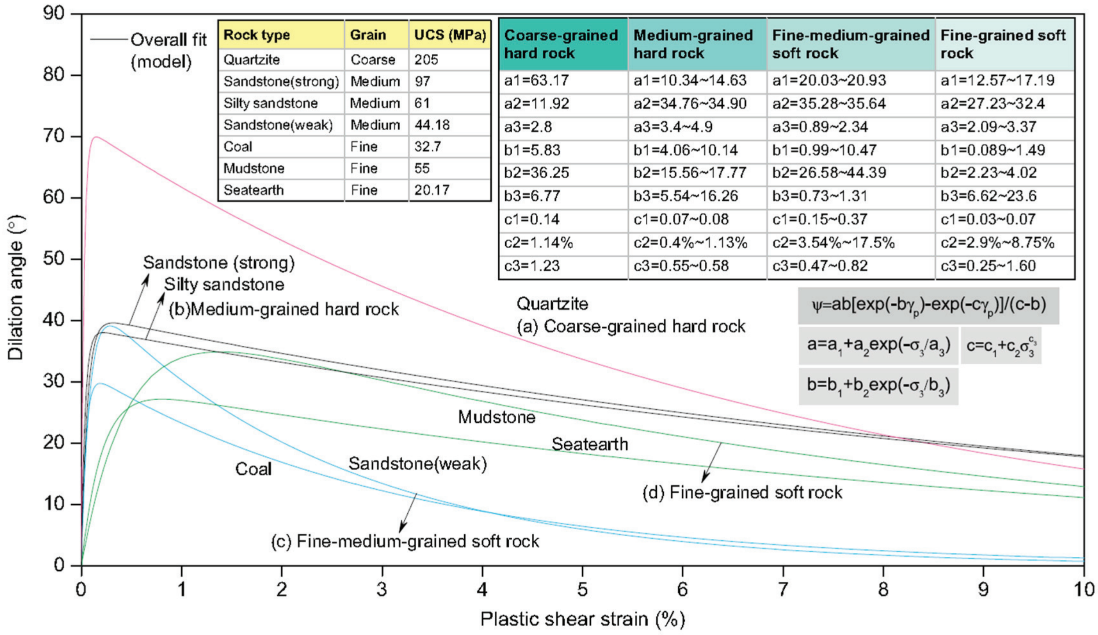

Rock type	Grain	UCS (MPa)
Quartzite	Coarse	205
Sandstone(strong)	Medium	97
Silty sandstone	Medium	61
Sandstone(weak)	Medium	44.18
Coal	Fine	32.7
Mudstone	Fine	55
Seatearth	Fine	20.17

Coarse-grained hard rock	Medium-grained hard rock	Fine-medium-grained soft rock	Fine-grained soft rock
a1=63.17	a1=10.34~14.63	a1=20.03~20.93	a1=12.57~17.19
a2=11.92	a2=34.76~34.90	a2=35.28~35.64	a2=27.23~32.4
a3=2.8	a3=3.4~4.9	a3=0.89~2.34	a3=2.09~3.37
b1=5.83	b1=4.06~10.14	b1=0.99~10.47	b1=0.089~1.49
b2=36.25	b2=15.56~17.77	b2=26.58~44.39	b2=2.23~4.02
b3=6.77	b3=5.54~16.26	b3=0.73~1.31	b3=6.62~23.6
c1=0.14	c1=0.07~0.08	c1=0.15~0.37	c1=0.03~0.07
c2=1.14%	c2=0.4%~1.13%	c2=3.54%~17.5%	c2=2.9%~8.75%
c3=1.23	c3=0.55~0.58	c3=0.47~0.82	c3=0.25~1.60

$\psi = ab[\exp(-b\gamma_p) - \exp(-c\gamma_p)]/(c-b)$

$a = a_1 + a_2\exp(-\sigma_3/a_3)$ $c = c_1 + c_2\sigma_3^{c_3}$

$b = b_1 + b_2\exp(-\sigma_3/b_3)$

Fig. 2.15. Dilation angle behavior of the seven rocks studied by Zhao & Cai (2010a) as function of the plastic shear strain for a confining pressure of 1 MPa, and range of values for the nine coefficients grouped by grain size.

Finally, the authors implemented their model into FLAC (Itasca, 2011) getting a reasonably good representation of the actual test results.

The authors (Zhao & Cai, 2010b) have also applied this mobilized dilation angle model for predicting the failure shape of a tunnel and the rock mass displacement distributions showing that their simulations are in good agreement with the field measurement results.

It has to be pointed out that even though the model is capable to well capture the dilation angle behavior, the inherent complexity in adjusting the nine needed coefficients which do not have a physical meaning and also considering that the solution is not univocal from a practical point of view —different sets of coefficients can result in almost the same fit— make the model unpractical for a number of rock engineering purposes.

2.2.4.8. Walton & Diederichs dilatancy model (2015a)

Walton & Diederichs (2015a) have recently proposed a new dilation model (more complex than that of Alejano & Alonso (2005), but less complex than that of Zhao & Cai (2010a)) that requires between four and seven parameters (α_0, α', γ_m, β_0, β', γ_0 and γ') —depending on the available data and rock idiosyncrasy— to completely characterize the dilatational behavior. It is mathematically based in a piecewise function that separates pre-mobilization of dilatancy, mobilization of peak dilatancy and post-mobilization of dilatancy. This division allows to consider each part separately, to perform a detailed study of the influence of each parameter on the model and to study correlations with other geomechanical parameters.

The model is defined by the following piecewise function:

$$\psi\left(\sigma_3,\gamma^p\right)=\begin{cases}\dfrac{\alpha\cdot\gamma^p\cdot\psi_{peak}}{e^{\left(\frac{\alpha-1}{\alpha}\right)}\gamma_m} \text{ when } \gamma^p<\gamma_m\cdot e^{\left(\frac{\alpha-1}{\alpha}\right)} \\ \psi_{peak}\cdot\left(\alpha\cdot\ln\left(\dfrac{\gamma^p}{\gamma_m}\right)+1\right) \text{ when } \gamma_m\cdot e^{\left(\frac{\alpha-1}{\alpha}\right)}\le\gamma^p<\gamma_m \\ \psi_{peak}\cdot e^{\left(\frac{-\left(\gamma^p-\gamma_m\right)}{\gamma^*}\right)} \text{ when } \gamma^p\ge\gamma_m\end{cases} \tag{2.44}$$

where:

$$\alpha=\alpha_o+\alpha'\cdot\sigma_3 \tag{2.45}$$

$$\gamma^*=\begin{cases}\gamma_0 \text{ when } \sigma_3=0 \\ \gamma' \text{ when } \sigma_3\ne 0\end{cases} \tag{2.46}$$

and:

$$\psi_{peak}\left(\sigma_3\right)=\begin{cases}\text{For sedimentary rocks:} \\ \dfrac{\phi_{peak}}{1+\log_{10}\left(\text{UCS}\right)}\cdot\log_{10}\left(\dfrac{\text{UCS}}{\sigma_3+0.1}\right) \\ \text{For crystalline rocks:} \\ \begin{cases}\phi_{peak}\cdot\left(1-\dfrac{\beta'}{e^{-\left(\frac{1-\beta_0-\beta'}{\beta'}\right)}}\cdot\sigma_3\right) \text{ when } \sigma_3<e^{-\left(\frac{1-\beta_0-\beta'}{\beta'}\right)} \\ \phi_{peak}\cdot\left(\beta_0-\beta'\cdot\ln\left(\sigma_3\right)\right) \text{ when } \sigma_3>e^{-\left(\frac{1-\beta_0-\beta'}{\beta'}\right)}\end{cases}\end{cases} \tag{2.47}$$

being:

ψ the dilation angle.

σ_3 the confining stress.

γ^p the plastic shear strain.

ψ_{peak} the peak dilation angle.

γ_m a parameter that defines the plastic shear strain at which peak dilation is achieved.

α_0 and α' are parameters that determine the curvature of the pre-mobilization portion of the model for unconfined and confined conditions respectively.

γ_0 and γ' are parameters that define the decay rate of the dilation angle for unconfined and confined conditions respectively.

ϕ_{peak} the peak friction angle.

UCS the uniaxial compressive strength of intact rock as obtained from the laboratory.

β_0 and β' are parameters that define the dependence of the peak dilation angle with σ_3 for low and high confining stresses respectively. The authors (Walton & Diederichs, 2015a) define what are low and high confining stresses comparing the confinement with an exponential function depending on β_0 and β'.

The authors give some indications on the range of variability of each of the parameters depending on the rock type. It has to be noted that due to the novelty of the model, the parameters still have to be checked and its application range has to be determined.

As part of his Ph.D. thesis Gabriel Walton (2014, 2015b) applied this new dilation model to the prediction of the yield and displacements of a pillar in a deep underground mine. The use of this variable dilation model was able to correlate well with the measurements performed into a very deep room and pillar mine in Canada, where yield of the pillars took place for a significant time, with evolving stress conditions (increase of mining in the surroundings of the monitored pillar) and in other excavations where extensometric data were available (Walton et al. 2015b).

It is relevant to remark that whereas the Alejano & Alonso (2005) dilatancy model starts to count plasticity (γ^p) from peak strength, both the models by Zhao & Cai (2010a) and Walton & Diederichs (2015a) start counting γ^p from the called Crack Damage point (CD) or point of unstable propagation of cracking. Therefore, both these approaches set $\gamma^p = 0$ after the stress level corresponding to CD, whereas Alejano & Alonso (2005) approach considers peak stress as the starting point of plastic strains (Fig. 2.16).

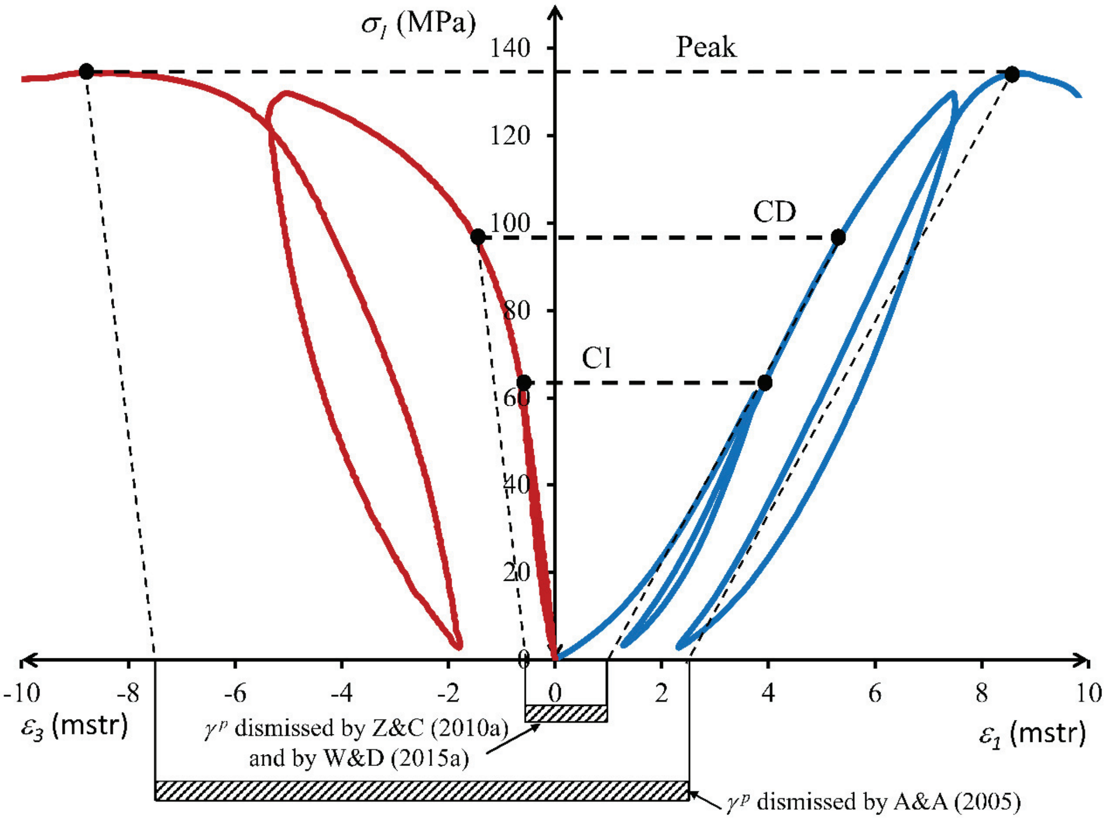

Fig. 2.16. Differences between the dilatancy models by Alejano & Alonso (2005) and those by Zhao & Cai (2010a) and Walton & Diederichs (2015a) regarding the starting point for counting the plastic parameter.

Walton & Diederichs' (2015a) approach was partially derived from the results presented in the core of this dissertation (Chapter 3). It reflects some of the observations associated to granite testing, showing that peak dilatancy values were well below peak friction angle estimates as suggested by Alejano & Alonso (2005).

3. Dilation in granite during servo-controlled strength tests

3.1. Introduction

Granites, very common in Galicia (NW of Spain) as in many other parts of the globe, are typically used as slabs and plaques in construction and civil engineering works and also as aggregate. Underground excavations in granite rock masses for civil engineering and mining applications are also very common, so a better understanding of granite behavior should contribute to improving design capabilities, construction techniques and safety in the execution of excavations in this type of rock mass.

In the late 1960s and early 1970s, a number of authors (Hudson et al., 1971a; Rummel & Fairhurst, 1970; Wawersik & Brace, 1971; Wawersik & Fairhurst, 1970) were able to study the behavior of rock failure beyond the peak of the stress-strain curve using a closed loop servo-controlled test machine. In this period also, Crouch (1970) improved existing testing capabilities in experimentally determining volumetric strain in the post-failure range of compressive tests. Since then, many other authors (e.g., Medhurst in his doctoral thesis, 1996; Elliot & Brown, 1985; Cipullo et al., 1985) have performed tests in both soft and hard rocks (including coal, limestone, marble, sandstone, quartzite and granite) aimed at obtaining complete stress-strain curves. Although a good knowledge of this curve is of paramount relevance to rock mechanics (Wawersik, 1975; Singh, 1997), it is no easy task to estimate it at the scale of the rock mass.

Since avoiding rock mass failure is usually a major rock mechanics goal, knowledge of what happens after failure could seem to be of little or no interest. However, a number of authors (Medhurst & Brown, 1998; Hudson et al., 1971b) have indicated that knowing the post-failure plastic parameters for rock masses is necessary to achieve modelling objectives, understand certain rock behavior mechanisms and estimate the extent of plastic zones around excavations.

Moreover, the use of numerical modelling has increased substantially in recent years and not only relies on reliable input parameters but also opens up possibilities for more complex and realistic models. Accordingly, now more than ever, it is important to be able to provide realistic representations of the complete stress-strain curve and to correctly characterize rock behavior in numerical models.

A reasonable parameter for evaluating plastic behavior is the dilation angle, ψ. However, due to inherent difficulties in obtaining it, dilatancy has seldom been taken into consideration in initial numerical models; and when it was considered, the approach, typically poorly developed and simplistic, generally consisted of an associated flow rule (friction angle made equal to the dilation angle, $\phi = \psi$) or a non-associated flow rule (usually considering $\psi = 0$). Neither approach is realistic enough (Jaeger et al., 2007; Price & Farmer, 1979) and so could result in possible calculation errors.

In an attempt to provide a more correct approach to dilatancy, a number of authors (Kudoh et al., 1999; Vermeer & de Borst, 1984; Detournay, 1986; Yuan & Harrison, 2004; Alejano & Alonso, 2005; Zhao & Cai, 2010a; Cook, 1970; Holcomb, 1978) have proposed parameters or models that fit the dilatant behavior of rocks. The need for real data to compare with modelling results is a common issue in all of these studies and serves as the starting point for this study. In other words, for samples of three granitic rocks, actual confined and unconfined stress test data for a press with fully servo-controlled loading are provided.

In recent years, a number of authors have argued that some rocks and rock masses behave in a strain-softening manner (Hoek & Brown, 1997), which means that, after achieving maximum stress, they can still withstand some load. Strain-softening is founded in the incremental theory of plasticity and has been developed to model plastic deformation processes. One of the main features of strain-softening is that the failure criterion and the plastic potential do not only depend

A version of this chapter has been published with the following citation: Arzúa, J., & Alejano, L. R. 2013. *Dilation in granite according to servo-controlled strength tests*. International Journal of Rock Mechanics and Mining Sciences, 61, 43-56.

on the stress tensor, σ_{ij}, but also on a plastic parameter —generically denoted as η or γ^p— which takes account for the processes and mode of strength transition, in such a way that this plastic parameter is null in the elastic region, and if $\eta > 0$, the strain softening appears until the residual strength is reached. Thus, the behavior model is plastic-strain-dependent.

In order to characterize a strain-softening rock or rock mass, the following basic information is needed: (a) Elastic parameters; (b) Peak, evolving and residual failure criteria; and (c) Post-failure deformability parameters.

To completely characterize post-failure behavior, one needs to know not only the evolving and residual failure criteria, but also the parameters that link the post-failure stress-strain relationship and the relationship between strains. A correct description could be achieved, for instance, if one knows either (a) the dilation angle and the drop modulus (computed as the mean negative slope of the curve $\sigma_1 - \varepsilon_1$ after peak strength and in the first 50% of softening) or (b) the dilatancy and the plastic parameter values for which dilatancy and evolving failure criterion are achieved.

Due to the complex nature of this kind of behavior, standard presses cannot properly compute rock sample strain once peak strength is surpassed. Therefore, a press with servo-controlled loading capable of controlling post-failure processes is necessary to study this second part of stress-strain curves.

3.2. Testing equipment

For previous studies the *John P. Harrison Rock Mechanics' Laboratory* had set up a servo-control system in a standard 200-tonne press, in such a way that the servo could control the loading rate in terms of stress or strain and perform different types of tests as required, for instance, tests with a number of unloading-reloading cycles (Fig. 3.1). Quite reproducible post-failure results were obtained for unconfined compressive tests in moderately weathered granite (Alejano et al., 2009a).

Developed to classify the shape of the complete stress-strain curve for a particular rock according to its strain monotonicity was the concept of classes, with Class I indicating monotonicity and Class II indicating non-monotonicity. Various authors (Hudson et al., 1972) showed that this may depend on the stress-path and the particular strain being controlled. In reference to this dissertation, the tested granites were shown to be Class II under uniaxial compression; however, under confined conditions they could be considered as Class I rocks so their post-failure behavior could be readily analyzed. Due to the strain velocity capacity of the press, the initial stress drop of post-failure behavior of uniaxial tests could not be considered reliable in terms of stress control; however the relationship between strains (axial and radial) represented actual volumetric relationships. The reliability of the post-failure part of the tests was analyzed by performing unloading-reloading cycles to analyze whether the stress path represented actual rock behavior or merely reflected press stiffness.

Axial strain was measured by means of linear variable differential transformers (LVDTs) attached to the lower press platen using industrial magnets. For unconfined tests, radial strain was also measured by an apparatus fixed to the rock sample in such a way that two measurements of the variation in diameter were obtained. Although it is also possible to measure radial strain with a chain, which provides homogeneous results, it was difficult to adapt it to our system and so such a chain was not used. The use of strain gauges was also ruled out due to the limited range in measuring strain —too large in the post-failure stage— and due to the occurrence of localized failure phenomena, as also pointed out by other authors (Zhao & Cai, 2010a).

A next step in improving the laboratory equipment was to install a servo-control for confining stress in triaxial tests to ensure not only confining stress control and modification during testing but also to measure the volume of hydraulic fluid shifted into or out of Hoek's triaxial cell during triaxial testing —as proposed by Crouch (1970) and later modified and applied by Cipullo et al. (1985), Wawersik (1975), Singh (1997), Medhurst & Brown (1998) and others. Using water as a hydraulic fluid and under the reasonably realistic assumption of incompressibility, it is possible to relate the displaced volume of hydraulic fluid to the volumetric strain of the rock sample.

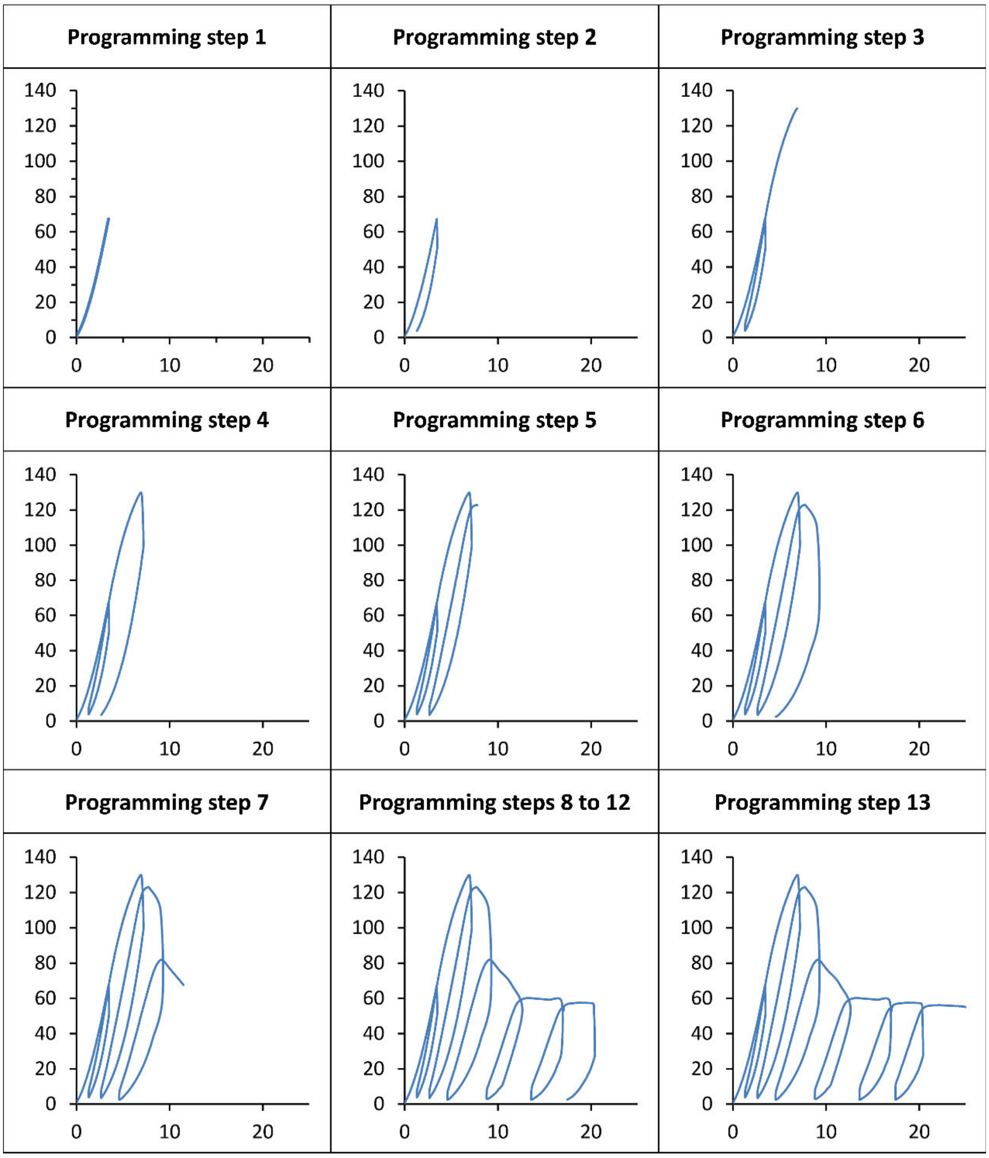

Fig. 3.1. Evolution of a servo-controlled test based on a given strain function. Major principal stress in the ordinate axis and axial strain in the abscissa axis.

The new equipment consisted of a computer-controlled servo, which, like a syringe, pumps a small-diameter plunger inside a tube and so controls water pressure; and since the tube is connected to the Hoek's cell, confining stress during the triaxial tests is also controlled. Confining stress was measured by a simple pressure sensor at the end of the tube.

As for measuring the volume of water entering or leaving the Hoek's cell, it is known how much the plunger is going forwards or backwards inside the tube because the servo turn is controlled so as to modify pressure when necessary. Since both inner diameter and plunger displacement are known, it is possible to calculate the volume of displaced water.

It is important to note that the equipment measures the amount of hydraulic fluid displaced into or out of the Hoek's cell; it, thus, does not measure volumetric strain itself but its lateral component. This lateral component of volumetric strain can be related to volumetric strain as follows (Farmer, 1983):

$$\varepsilon_v = \frac{\Delta V}{V}(\%) = \frac{100}{V}\left[fV_0 - \left(\pi r^2 - \frac{F}{E} \right) l \right] \qquad (3.1)$$

where V_0 is the volume of water displaced; V is the original rock sample volume; f is the compressibility factor for the hydraulic fluid, in our case, reasonably assumed to be equal to one since water was used as the hydraulic fluid; r is the radius of the Hoek's cell; F is the axial force acting on the ram; *E* is the elasticity modulus of the ram's steel; and *l* is the measured axial displacement.

We can only measure the addition of axial displacements of the ram and of the rock specimen together. However, it was possible to calculate the axial strain, and subsequently the axial displacement, of the ram since both the elasticity modulus of the steel and force at every moment of the tests were known. In this way the axial strain of the rock specimen can be computed.

The confining equipment allowed for a modest theoretical confining pressure of up to 20 MPa, which, if this limit was reached, locked the system. The latter turned out to be an issue since, when failure occurred, a shock wave was generated that raised pressure rapidly. This increase in pressure could lock the system if more than 14 MPa were programmed as confining stress for the test. For this reason, triaxial tests for up to 12 MPa were performed, although some rock samples tested 'out-of-range' at 15 MPa and 14 MPa yielded some valuable data.

To minimize errors arising from inaccurate sample shapes (a slight lack of parallelism between faces or a slight lack of perpendicularity between the axis and faces), the laboratory press had a spherical seat in the upper platen but not in the lower platen. To avoid inaccuracies derived from sample shape, a set of steel ball-and-socket joints was added below the core sample.

Since LVDTs were used between the press platens and the strain of steel is significant compared to that of rock, steel strain had to be subtracted from the measured strains. This important aspect also had to be considered in triaxial tests.

Drilling equipment and circular diamond saws were used to carve the rock specimens, all in accordance with rock mechanics standards (ISRM, 2007).

3.3. Tested rocks

An experimental programme was planned to study three granitic rocks locally known as Amarelo País, Blanco Mera and Vilachán, all hard rocks extensively used as building and ornamental materials.

Amarelo País, classified as slightly weathered granite, has a tan color and is a coarse-grained hard rock (1–3 mm). Blanco Mera is a bright white-colored granite, also a coarse-grained hard rock (1–6 mm). Vilachán, classified as a micaceous granite, is a pale-colored, medium-grained hard rock (0.5–1 mm).

To evaluate the geological and chemical nature of the rocks, samples were characterized using an optical microscope. Thin sections of rock (Fig. 3.2) were cut and prepared for study, then exposed to white and polarized light under a petrographic optical microscope in order to analyze the samples and perform a modal analysis. These thin sections could be described quantitatively by point counting and qualitatively in terms of dominant minerals. The modal analysis of the transparent dominant minerals in the three rocks is presented in Table 3.1.

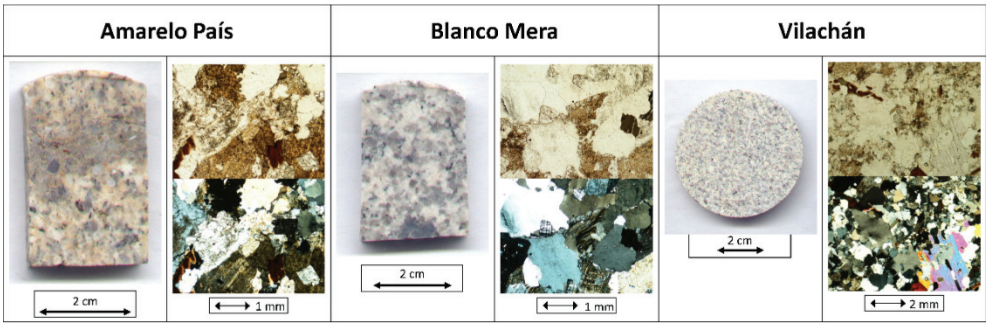

Fig. 3.2. Petrographic study of rock samples showing pictures of hand samples and thin-section photographs in white and polarized light for the three granites studied.

Table 3.1. Quantitative modal analysis of the studied rocks derived from petrography analysis of thin sections.

Mineral phases	Modal analysis (%)		
	Amarelo País	Blanco Mera	Vilachán
Quartz	26	20	41
Alkaline feldspar	25	27	15
Plagioclase	22	35	12
Biotite	6	5	4
Muscovite	18	7	16
Sericite	1	1	-
Chlorite	-	4	3
Opaques	1	-	-
Accessories	< 1	< 1	9

3.4. Testing

Samples were cut from 40 cm cubes taken from the sawing facilities of a rock supplier. Some 30 specimens measuring 54 mm in diameter (NX size) were cut for each rock type in order to have a reliable number of samples to test.

Unconfined and confined (0–15 MPa) compression strength tests were performed on around 30 samples representing each rock type. Other tests, namely, density, tilt and Brazilian tests, aimed at characterizing the rocks were also performed, always applying the best rock mechanics standards (ISRM, 2007). Some 200 non-destructive and destructive tests were performed in total.

3.4.1. Non-destructive tests

3.4.1.1. Density tests

In order to determine density, twelve tests were performed on Amarelo País, fourteen tests on Blanco Mera, and nineteen tests on Vilachán. The values of the means and standard deviations for the tests for each rock are presented in Table 3.2.

3.4.1.2. Tilt tests

The recommended method for characterizing the basic friction angle of a smooth joint in rock mechanics standards (ISRM, 2007) is based on shear strength tests. However, applying the definition for this parameter, as proposed by Barton (1976), it is possible to obtain the friction angle as the inclination of a sawed rock slab placed over another slab of the same rock at the point when the upper slab starts to slide along the lower slab. Using this method, eighteen tests were performed on Amarelo País, twelve tests on Blanco Mera, and six tests on Vilachán (Table 3.2).

The *John P. Harrison Rock Mechanics' Laboratory* has an automated tilt table developed by the author, his supervisor and other laboratory mates that served to perform the tests.

3.4.2. Destructive tests

3.4.2.1. Brazilian tests

Standard Brazilian tests were performed in order to obtain the tensile strength of the three rocks studied. Since this kind of test is easy and rapid, a large number of tests were performed on each rock: 26 on Amarelo País, 20 on Blanco Mera, and 19 on Vilachán (Table 3.2).

Table 3.2. Summarized results of density, tilt and Brazilian tests for the three granitic rocks studied (mean results, and standard deviation between brackets).

Rock	Density (g/cm^3)	ϕ_b (°)	T (MPa)
Amarelo País	2.61 (0.01)	29 (2)	6.65 (1.05)
Blanco Mera	2.60 (0.01)	33 (3)	6.12 (0.99)
Vilachán	2.59 (0.01)	28 (2)	6.93 (0.72)

3.4.2.2. Uniaxial compressive tests

A total of thirty-six uniaxial compressive tests were performed. Pictures of all samples were taken before and after testing and, if a shear band occurred, its orientation was measured.

As explained above, in these tests the granites were characterized as having Class II behavior. Hence, after failure, the stress-strain relations obtained were not significant, due to the extremely brittle nature of the rock samples in the press: usually the rock crushed in an explosive manner, splitting the sample into fragments. Whenever possible, however, the parameters were estimated. Results for the unconfined strength tests are presented in Table 3.3 to Table 3.5, together with confined strength test results.

3.4.2.1. Triaxial tests

A total of fifty-four triaxial compressive tests were performed. Like in the case of uniaxial tests, pictures of all specimens were taken before and after testing and, if a shear band occurred, its orientation was measured. Typical results for confined strength tests are shown in Fig. 3.3. The first graph shows how to obtain the main geotechnical parameters: peak strength, σ_1^{peak}; residual strength, σ_1^{res}; apparent elastic Young's modulus, E; apparent Poisson's ratio, ν; and drop modulus, M.

First to be observed from Fig. 3.3 is the high degree of radial deformation occurring for the peak strength level in the three granitic rocks. For some granites (for instance, Lac du Bonnet as described in Martin & Read, 1996), the radial strain at peak corresponds to roughly half the axial strain; for the rocks studied here, the peak radial and axial strain are roughly equal.

It was previously commented that it is not possible in triaxial tests to directly measure radial deformation, as the use of strain gauges has to be ruled out. It is possible, however, to measure volumetric strain and, based on this value, to estimate the radial deformation using the following formula (Vermeer & de Borst, 1984):

$$\varepsilon_v = \varepsilon_1 + 2\varepsilon_3 \Rightarrow \varepsilon_3 = \frac{\varepsilon_v - \varepsilon_1}{2} \tag{3.2}$$

We found that a more accurate calculation is provided as follows:

$$\varepsilon_3 = 1 - \sqrt{\frac{1-\varepsilon_v}{1-\varepsilon_1}} \tag{3.3}$$

The derivation of the estimate and the accuracy of the approach used for Eq. (3.3) are presented in Appendix A. For the analyzed tests the difference between the two formulations is not relevant.

It was now possible to obtain the complete stress-strain curves for each performed test (as shown in Fig. 3.3). It was also possible to compare the curves for each rock in such a way as to view the main deformational behavior tendencies according to increasing confining pressure, as shown in Fig. 3.4. Table 3.3 to Table 3.5 summarize the results obtained for the uniaxial and triaxial compression tests on granitic samples. These results are also shown in Appendix B.

Table 3.3. Results of testing on Amarelo País granite samples.

Sample	σ_3	σ_1^{peak}	σ_1^{res}	E	ν	M
	MPa	MPa	MPa	GPa	-	GPa
A1 RCS	0	77.50	--	21.67	0.13	--
A2 RCS	0	84.64	--	22.36	0.19	--
A3 RCS	0	76.66	2	17.63	0.20	--
A4 RCS	0	75.60	5	22.92	0.18	--
A5 RCS	0	80.34	2	20.27	0.15	--
A6 RCS	0	76.91	2	18.59	0.18	--
A7 RCS	0	68.47	--	17.60	0.21	--
A8 RCS	0	77.19	2	19.30	0.17	--
A9 RCS	0	74.85	2	18.97	0.17	--
A10 RCS	0	76.17	--	16.35	0.19	--
A11 RCS	0	80.08	--	15.95	0.16	--
A12 RCS	0	74.74	1	16.00	0.15	-19.11
A1 TRX	2	130.42	32	30.54	0.19	-17.39
A2 TRX	2	117.33	30	23.40	0.19	-16.00
A3 TRX	2	112.29	27	22.32	0.22	-16.67
A4 TRX	2	110.31	31	23.95	0.20	-17.65
A5 TRX	4	134.20	44	25.06	0.19	-21.06
A6 TRX	4	130.02	43	24.36	0.22	-17.39
A7 TRX	4	129.89	54	25.25	0.20	-17.15
A8 TRX	4	129.50	46	23.84	0.22	-22.10
A9 TRX	6	153.90	51	27.48	0.21	-21.05
A10 TRX	6	170.72	45	30.02	0.21	-19.55
A11 TRX	6	175.43	48	30.01	0.20	-19.05
A12 TRX	6	169.00	51	30.40	0.18	-17.57
A13 TRX	10	192.75	80	28.06	0.22	-19.03
A14 TRX	10	213.99	75	35.49	0.19	-21.69
A15 TRX	10	200.71	87	33.69	0.15	-21.74
A16 TRX	10	193.09	68	29.45	0.21	-20.18
A17 TRX	12	214.99	81	31.20	0.20	-18.52
A18 TRX	12	230.14	80	36.08	0.20	-20.00

Table 3.4. Results of testing on Blanco Mera granite samples.

Sample	σ_3	σ_1^{peak}	σ_1^{res}	E	ν	M
	MPa	MPa	MPa	GPa	-	GPa
B1 RCS	0	125.77	--	33.11	0.15	--
B2 RCS	0	116.50	--	33.83	0.18	--
B3 RCS	0	110.18	--	29.48	0.15	--
B4 RCS	0	100,48	--	27.63	0.10	--
B5 RCS	0	121,32	--	34.14	0.17	--
B6 RCS	0	79.26	--	29.44	--	--
B7 RCS	0	84.57	2	25.40	0.16	--
B8 RCS	0	110.77	--	33.66	0.14	--
B9 RCS	0	106.66	--	25.17	0.08	--
B10 RCS	0	118.26	--	33.26	0.13	--
B11 RCS	0	111.43	--	31.64	0.16	--
B12 RCS	0	125.34	--	30.88	0.10	--
B1 TRX	2	187.03	30	42.86	0.16	-25.00
B2 TRX	2	183.41	42	44.19	0.17	-21.05
B3 TRX	2	172.44	40	42.18	0.16	-23.52
B4 TRX	2	177.82	34	43.07	0.18	-18.47
B5 TRX	4	216.71	38	45.86	0.15	-18.38
B6 TRX	4	212.58	50	42.82	0.16	-17.24
B7 TRX	4	196.84	52	42.65	0.18	-21.52
B8 TRX	4	214.13	54	45.55	0.17	-22.72
B9 TRX	6	235.39	65	42.86	0.18	-24.46
B10 TRX	6	228.20	51	43.41	0.18	-20.83
B11 TRX	6	218.35	70	44.10	0.17	-17.24
B12 TRX	6	240.16	74	45.17	0.20	-18.97
B13 TRX	10	282.30	93	47.28	0.15	-22.05
B14 TRX	10	252.18	74	41.49	0.21	-22.56
B15 TRX	10	259.22	115	46.17	0.16	-21.74
B16 TRX	10	269.80	85	47.12	0.17	-22.25
B17 TRX	14	311.62	180	46.96	0.18	-21.82
B18 TRX	12	307.62	112	48.26	0.15	-19.76
B19 TRX	12	291.80	82	44.66	0.17	-24.88

Table 3.5 Results of testing on Vilachán granite samples.

Sample	σ_3	σ_1^{peak}	σ_1^{res}	E	ν	M
	MPa	MPa	MPa	GPa	-	GPa
C1 RCS	0	127.45	--	27.27	0.11	--
C2 RCS	0	116.92	--	25.84	0.17	--
C3 RCS	0	114.17	--	22.92	--	--
C4 RCS	0	121.22	--	23.09	0.19	--
C5 RCS	0	119.09	--	25.53	0.15	--
C6 RCS	0	104.30	--	21.13	0.17	--
C7 RCS	0	129.18	--	23.51	0.12	--
C8 RCS	0	117.96	--	23.07	0.28	--
C9 RCS	0	113.53	--	21.88	0.19	--
C10 RCS	0	106.61	--	21.03	0.14	--
C11 RCS	0	113.60	--	24.09	0.20	--
C12 RCS	0	108.77	--	22.39	0.11	--
C1 TRX	2	146.25	--	24.00	0.11	-13.37
C2 TRX	2	141.99	40	23.16	0.17	-15.32
C3 TRX	2	140.91	34	24.45	0.20	-17.97
C4 TRX	2	146.13	36	24.14	0.22	-18.18
C5 TRX	4	169.53	52	29.41	0.17	-15.68
C6 TRX	4	160.13	53	27.82	0.18	-19.05
C7 TRX	6	185.76	50	29.27	--	-15.29
C8 TRX	4	161.01	43	27.21	0.22	-15.49
C9 TRX	4	160.88	35	27.04	0.20	-20.07
C11 TRX	6	187.84	49	27.79	0.19	-19.17
C12 TRX	6	195.46	47	31.70	0.18	-19.05
C13 TRX	10	239.61	71	33.10	0.20	-22.03
C14 TRX	10	241.22	70	34.85	0.18	-21.51
C15 TRX	10	209.77	64	27.82	0.21	-22.72
C16 TRX	10	231.61	63	30.23	0.17	-19.84
C17 TRX	15	266.22	--	32.12	0.14	-21.74
C18 TRX	15	259.45	--	31.29	0.19	-21.13

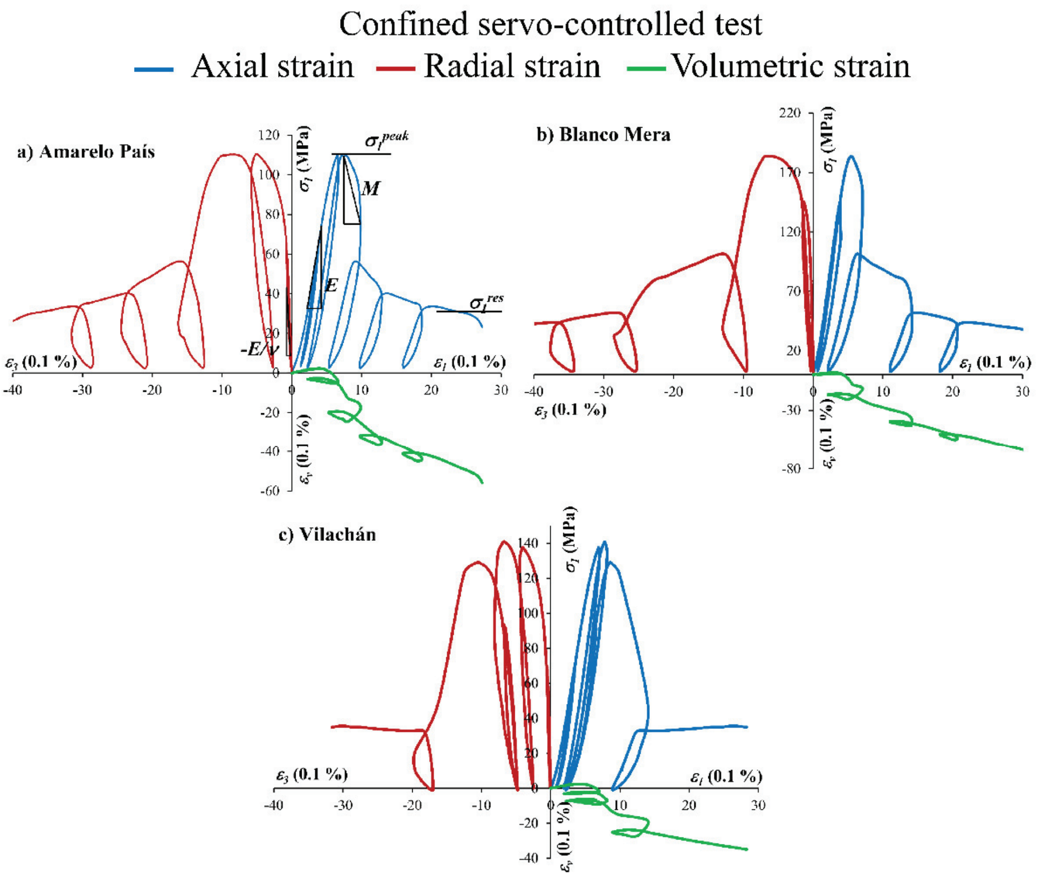

Fig. 3.3. Stress-strain graph for confined compression test on granitic rock samples. In the upper left graph it is shown how to obtain the values for peak and residual strength (σ_I^{peak} and σ_I^{res}), apparent elastic Young's modulus (E), apparent Poisson's ratio (ν) and drop modulus (M).

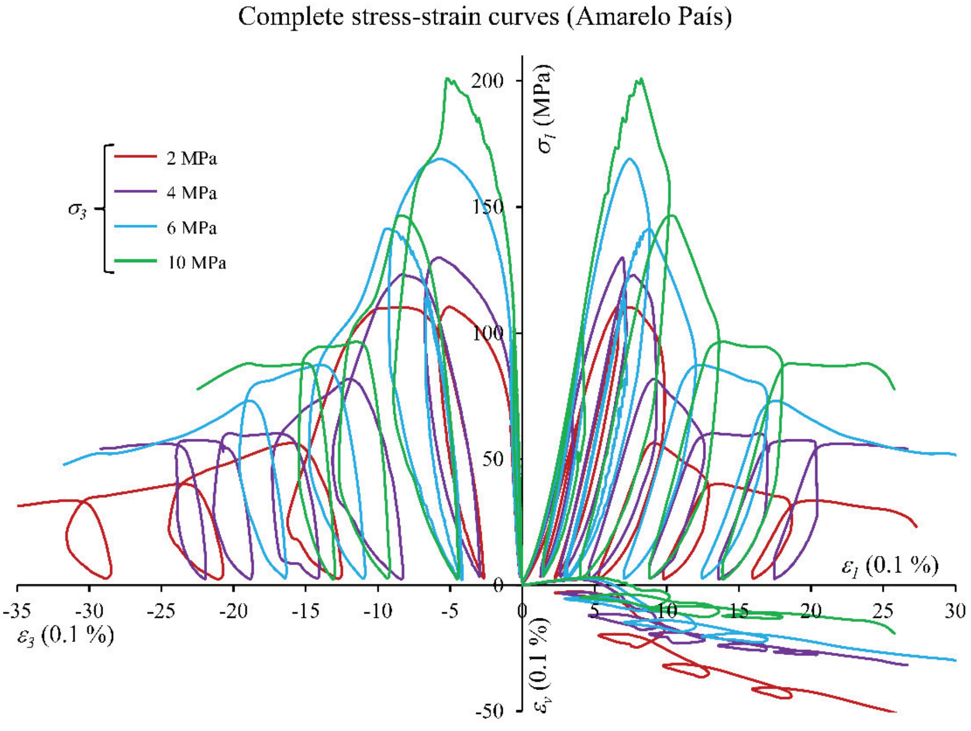

Fig. 3.4. Complete stress–strain curves for Amarelo País granite for confined strength tests at different confining pressures. The most relevant tendency is for peak strength and residual strength to increase, apparent Young's modulus to slightly increase and radial and volumetric strain to decrease as confining pressure grows.

3.5. Interpretation of results

3.5.1. Classic parameters

The results obtained in Table 3.3 to Table 3.5 were analyzed in order to deduce the main geomechanical features of the rocks. First, peak and residual Mohr-Coulomb (M-C) and Hoek-Brown (H-B) failure criteria were fitted to the peak and residual strength values obtained as a result of testing. These fits, together with the original test data, are presented in Fig. 3.5 and the main results are shown in Table 3.6 to Table 3.8. Residual strength has been generally estimated as the lowest principal strength value observed in each test. In tests where final stress and strain values were associated with an unloading cycle, the residual strength value was approximated.

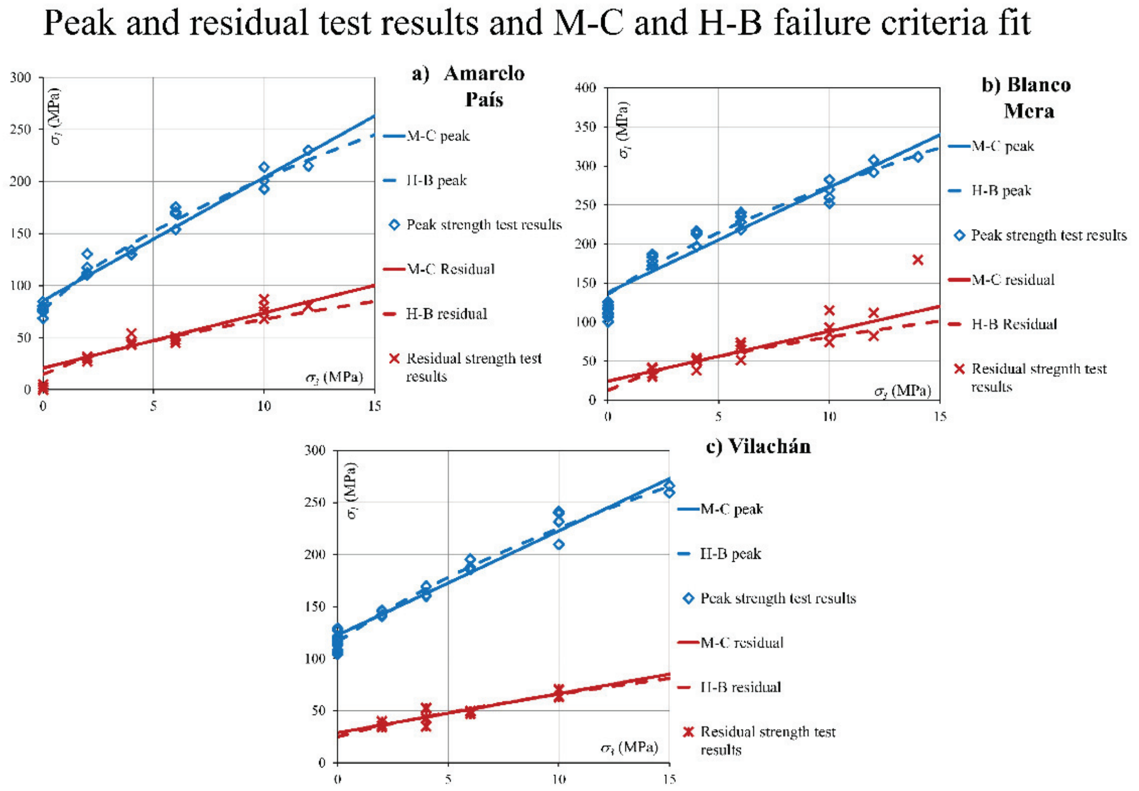

Fig. 3.5. Peak and residual strength test results and fitted to Hoek-Brown and Mohr-Coulomb failure criteria.

Table 3.6. Geomechanical results for Amarelo País (m subscript refers to average values).

	Hoek-Brown	Mohr-Coulomb
Peak Strength	$\sigma_c^{peak} = 76.59$ MPa $m = 40.96$ $R^2 = 0.990$	$\sigma_c^{peak} = 85.45$ MPa $\phi_{peak} = 57.59^{o}$ $c_{peak} = 12.42$ MPa $R^2 = 0.999$
Residual strength	$\sigma_c^{res} = 14.68$ MPa $m = 21.14$ $R^2 = 0.979$	$\sigma_c^{res} = 20.71$ MPa $\phi_{res} = 43.04^{o}$ $c_{res} = 4.50$ MPa $R^2 = 0.994$
σ_t	$\sigma_{t,m} = 6.65$ MPa	
E	$E = 1.26\cdot\sigma_3 + 19.92$ GPa	$E_{m,\sigma 3=0} = 18.97$ GPa
ν	$\nu_m = 0.19$	
M	$M_{m,\sigma 3\neq 0} = -19.73$ GPa	

Table 3.7. Geomechanical results for Blanco Mera (m subscript refers to average values).

	Hoek-Brown	Mohr-Coulomb
Peak Strength	$\sigma_c^{peak} = 135.52$ MPa $m = 37.82$ $R^2 = 0.982$	$\sigma_c^{peak} = 137.96$ MPa $\phi_{peak} = 59.52^{\circ}$ $c_{peak} = 18.79$ MPa $R^2 = 0.998$
Residual strength	$\sigma_c^{res} = 12.51$ MPa $m = 38.89$ $R^2 = 0.988$	$\sigma_c^{res} = 24.27$ MPa $\phi_{res} = 46.84^{\circ}$ $c_{res} = 4.80$ MPa $R^2 = 0.998$
σ_t	$\sigma_{t,m} = 6.12$ MPa	
E	$E = 1.28 \cdot \sigma_3 + 33.97$ GPa	$E_{m,\sigma 3=0} = 30.64$ GPa
ν	$\nu_m = 0.16$	
M	$M_{m,\sigma 3\neq 0} = -21.30$ GPa	

Table 3.8. Geomechanical results for Vilachán (m subscript refers to average values).

	Hoek-Brown	Mohr-Coulomb
Peak Strength	$\sigma_c^{peak} = 116.29$ MPa $m = 28.23$ $R^2 = 0.994$	$\sigma_c^{peak} = 122.65$ MPa $\phi_{peak} = 54.91^{\circ}$ $c_{peak} = 19.39$ MPa $R^2 = 0.999$
Residual strength	$\sigma_c^{res} = 25.20$ MPa $m = 9.88$ $R^2 = 0.944$	$\sigma_c^{res} = 28.90$ MPa $\phi_{res} = 35.38^{\circ}$ $c_{res} = 7.46$ MPa $R^2 = 0.992$
σ_t	$\sigma_{t,m} = 6.93$ MPa	
E	$E = 0.69 \cdot \sigma_3 + 23.78$ GPa	$E_{m,\sigma 3=0} = 23.48$ GPa
ν	$\nu_m = 0.18$	
M	$M_{m,\sigma 3\neq 0} = -19.08$ GPa	

Since triaxial tests were only performed for up to 12 MPa of confinement, the curvature of the enveloping failure was not very marked. Consequently, both studied failure criteria fitted well with the results.

Note the very good regression analysis obtained at peak for the M-C failure criterion (Table 3.6 to Table 3.8) and also the good fit for the H-B criterion. As for residual data, M-C criterion seems to fit results slightly better than H-B criterion. When trying to fit H-B criterion to residual data some problems arose ($\sigma_{ci}^2 < 0$), so some tests were excluded from the analysis to obtain reasonable data. In the final output, the very high values of the H-B parameter, *m,* and the friction angle, ϕ, can be observed and, in addition, the fact that these friction angles moderately diminish from peak to residual, especially for the Amarelo País and Blanco Mera granites. Accordingly, it is to be noted how the strength drop occurs mainly in the cohesive component.

The apparent elastic Young's modulus for the different samples was obtained as the slope of the $\sigma_1 - \varepsilon_1$ curve between 30% and 60% of peak strength. Contradicting some authors (Bukowska, 2005) but in line with other approaches (Brown et al., 1987), a tendency for E to grow as σ_3 increases was observed for these low confinement values. This is illustrated in Fig. 3.6 in the line fitted to the three rocks; note also that regression coefficients are not very high (R^2 around 0.7). These trends, together with average values for unconfined tests ($E_{m,\sigma 3=0}$), are numerically presented in Table 3.6 to Table 3.8 for the tested granites.

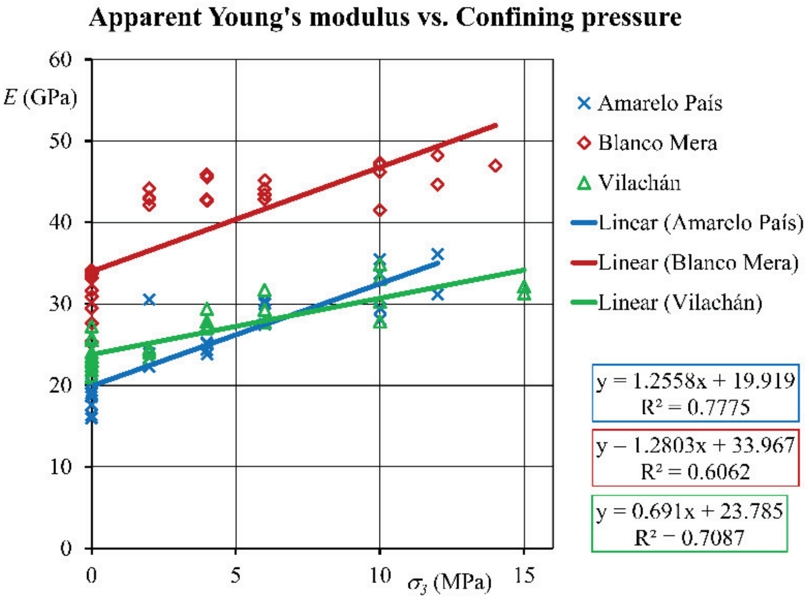

Fig. 3.6. Apparent elastic Young's modulus versus confining pressure for the three rocks studied.

Unconfined strength tests for Blanco Mera granite seems to result in lower values for Young's modulus than anticipated and also compared with those obtained for the other two granites. The fact that Blanco Mera seems stiffer than the two other granites may be attributed to its lower mica content.

Apparent Poisson's ratios were calculated as the relationship between the slopes for the radial and axial strains between 20% and 40% of peak strength. The values obtained (Table 3.6 to Table 3.8) are in line with those reported in the literature for granites (Gercek, 2007), and they also remain constant within the natural variability of these parameters, as can be observed in Fig. 3.7. It is important to select an adequate range of stresses to estimate this parameter, since, if selected over the 'onset-of-dilatancy' point, abnormally high values may be obtained.

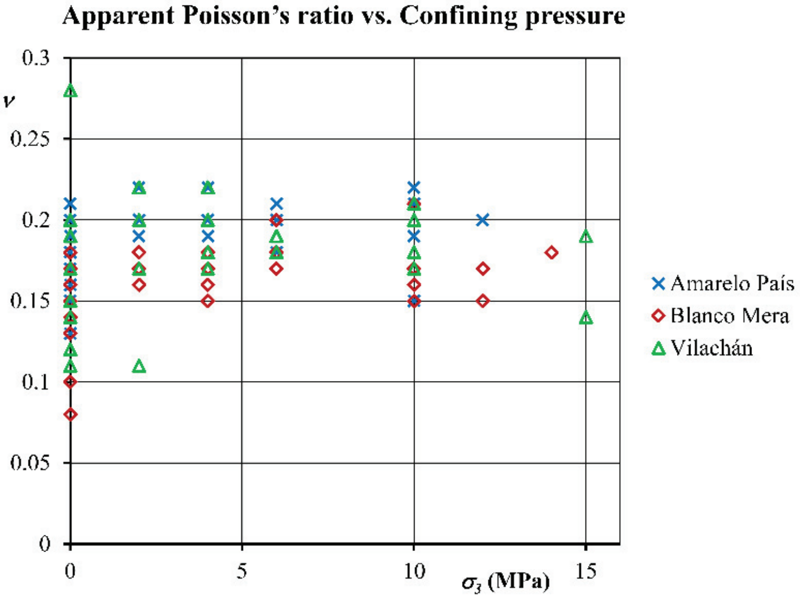

Fig. 3.7. Apparent Poisson's ratio versus confining pressure for the three rocks studied.

The drop modulus *M* was computed as the mean negative slope of the curve $\sigma_1 - \varepsilon_1$ after peak strength and in the first 50% of softening. A general perspective on the results of our tests indicates that this modulus tends not to remain constant all along the softening process. Therefore, the estimates of *M* in the different triaxial tests are indicative, average values for this parameter

($M_{m,\sigma3\neq0}$) are shown in Table 3.6 to Table 3.8. Future studies will focus on a detailed analysis of the softening process and correlation of the stress drop with a softening or plastic parameter.

Fig. 3.8 shows estimated values for the drop modulus graphed against the confinement. At such low confining stress values and for such brittle materials, a slightly decreasing trend can be observed as confining pressure grows, as reported in classic studies by Von Kármán (1911). The drop modulus results for the unconfined strength tests are excluded for mean estimates due to the brittleness of the materials used, commented above; even if calculated rigorously, these results would have to be used with care.

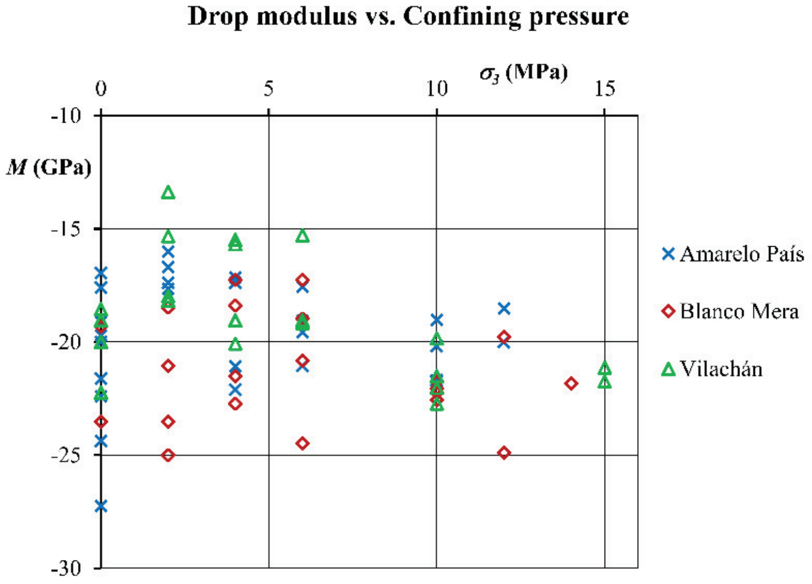

Fig. 3.8. Drop modulus versus confining pressure for the three rocks studied.

Note that peak and residual strength criteria, elastic parameters and drop modulus, together with the dilation angle values presented in next section provide a complete set of parameters to simulate the (strain-softening and variable dilatancy) mechanical behavior of the tested rock specimens. This model is much more realistic than those traditionally used in rock engineering applications (elastic-perfectly-plastic); however, further studies are needed to propose models better able to represent rock behavior, particularly for large strain situations.

Finally, the orientation of shear bands (Fig. 3.9) was tracked, measuring the angle known as β as the slope of the shear band with a horizontal line, whenever possible and compared with confining pressure. Results similar to those reported by other authors (Besuèlles et al., 2000) were obtained, with shear band inclinations becoming less sharp with confinement. This trend is graphed in Fig. 3.10. Future research will focus on providing further insights on this issue (Vardoulakis & Sulem, 1993).

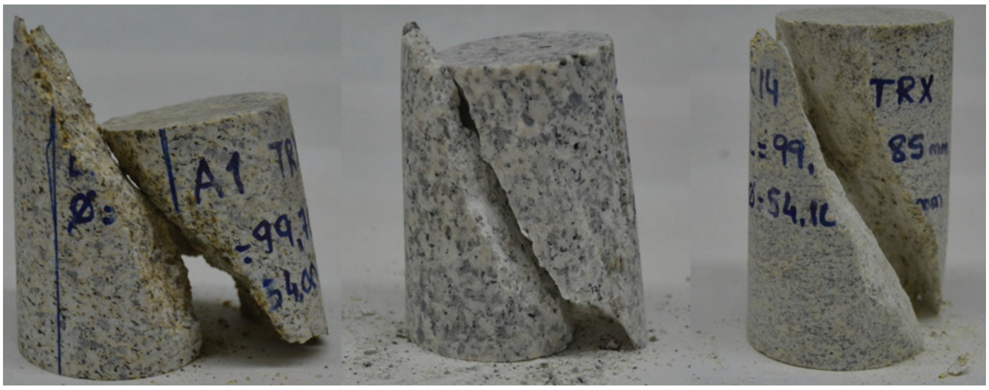

Fig. 3.9. Shear banding in the three types of granitic rocks.

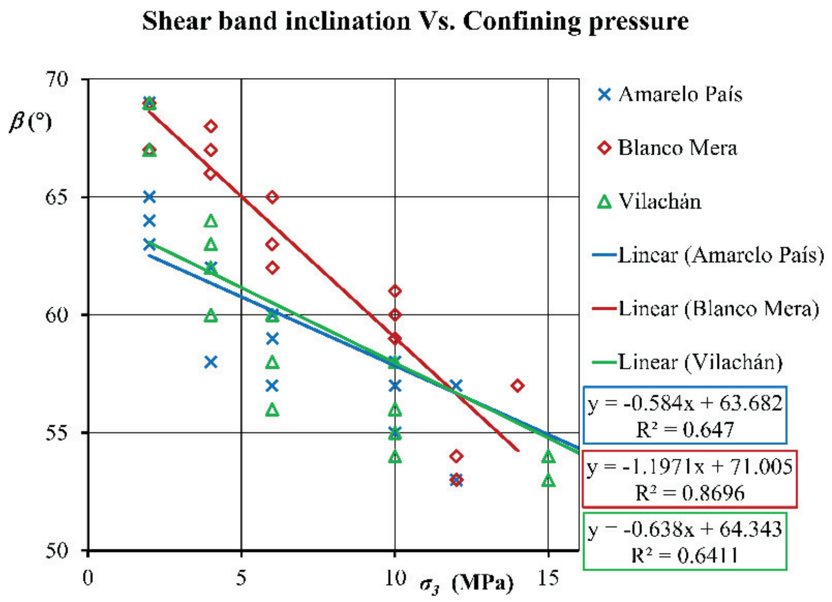

Fig. 3.10. Orientation of shear bands versus confining pressure.

3.5.2. Dilatancy

Due to the confining pressure equipment incorporated in the servo-controlled press, the complete stress-strain curve in triaxial tests could be now obtained, as depicted in Fig. 3.11. These curves are still relevant in rock mechanics and, in the last thirty years, although significant success has been achieved in terms of methodologies for estimating reasonably good elastic parameters and failure criteria in rocks, joints and rock masses, this has not been the case for post-failure behavior, mainly due to the difficulties associated with defining a model that adequately reflects observed complete stress-strain curves. In routine engineering applications, therefore, dilatancy seems to receive relatively little attention; this is hardly surprising since, apart from the inherent difficulties in estimating dilatancy, many problems in rock mechanics are solved by simply avoiding failure.

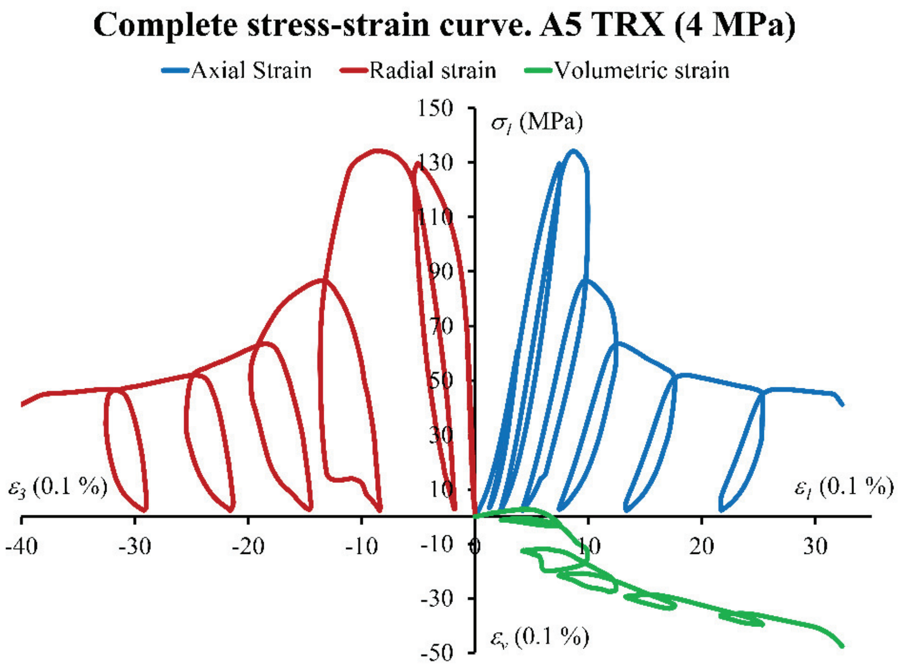

Fig. 3.11. Complete stress-strain curve obtained in a triaxial test.

Dilatancy can be defined as a change in volume resulting from the shear distortion of an element in a material. The dilation angle, ψ, is a suitable parameter for describing the behavior of a dilatant material, since —as will be shown below— it represents the ratio of plastic volume change to plastic shear strain.

With the increasingly successful use of numerical models in rock engineering in recent decades, excavation design has often come to rely greatly on numerical studies. Due to the difficulties in estimating dilatancy, in order to create a complete stress-strain curve model and extrapolate data to rock masses, excavation designs tend to use simple behavior models, such as elastic-perfectly-plastic models. More complex behavior models, like strain-softening models, are seldom used and the role of dilatancy is often simply ignored.

In an attempt to fill this gap and explore the topic in more depth, some authors have proposed models to fit existing data to deformational behavior. Alejano & Alonso (2005), in a study based on results for tests on sedimentary rocks, described a novel model for estimating the dilation angle in rocks and rock masses that showed dependencies on confining stress, on the plasticity suffered by the material and, indirectly, on the scale. Zhao & Cai (2010a) proposed an evolved mobilized dilation angle model; based on the response combined with grain size description and uniaxial compressive strength for rocks, the approach was generalized for different rock types, including hard ones, and later extended to rock masses (Zhao & Cai, 2010b).

One of the main aims of this doctoral work was to study dilatancy and to contribute to the post-failure database, given that information on granitic rocks is lacking (Zhao & Cai, 2010a).

3.5.2.1. Computing the dilation angle

For granular soils, rocks and concrete, Vermeer & De Borst (1984) pointed to a dilation angle that is significantly smaller than the friction angle and proposed the following equation for assessing the dilation angle in its more general form:

$$\psi = \arcsin \frac{\dot{\varepsilon}_v^p}{-2\dot{\varepsilon}_1^p + \dot{\varepsilon}_v^p} \tag{3.4}$$

The advantage of this formulation is that not only does it commence with the plastic volumetric strain rate, and is also valid for the interpretation of triaxial tests, but it can also be applied to the analysis of plane strain conditions and even in true triaxial situations. It should be pointed out that the fraction denominator represents, in absolute terms, the plastic parameter defined from internal variables in plane strain conditions as follows:

$$\gamma^p = \varepsilon_1^p - \varepsilon_3^p \tag{3.5}$$

For a standard triaxial test in which confining stress is applied peripherally to a sample, it is clear that, under homogeneous deformation conditions, $\varepsilon_2 = \varepsilon_3$; therefore, as commented previously $\varepsilon_v = \varepsilon_1 + 2\varepsilon_3$. Thus, the dilation angle in standard triaxial tests can also be computed from:

$$\sin\psi = \frac{\dot{\varepsilon}_1^p + 2\dot{\varepsilon}_3^p}{-\dot{\varepsilon}_1^p + 2\dot{\varepsilon}_3^p} \tag{3.6}$$

In the present study, the Vermeer & De Borst (1984) equation (Eq. (3.4)) was used, since the values for the axial and volumetric strains were related directly to the measures performed during the triaxial tests.

Consequently, to calculate the dilation angle it was necessary to obtain the incremental plastic strains. This was achieved selecting some arbitrary segments in a complete stress–strain curve in order to decompose the total strains into their elastic and plastic parts:

$$\varepsilon_i = \varepsilon_i^e + \varepsilon_i^p \tag{3.7}$$

This decomposition can be depicted graphically. In the case of axial strain it was only necessary to plot straight lines —with slope equal to the apparent Young's modulus— from arbitrary normal stress-axial strain curve values and then to read the plastic axial strain in the abscissa axis, as shown in Fig. 3.12.

To obtain a reasonably accurate value for volumetric strain, it was necessary to implement some unloading–reloading cycles in order to obtain the irrecoverable volumetric strain locus by linking the points of minimum strain in each cycle, as shown in Fig. 3.12 (Crouch, 1970). Once the irrecoverable strain locus is obtained, the procedure is the same as for axial strain: a straight line is plotted, parallel to the previously explained cycles (from the same arbitrary strain values used for axial strain), from the strain volumetric strain curve up to the irrecoverable volumetric strain locus; the volumetric plastic strain is that value in the ordinates axis, as shown in Fig. 3.12.

Repeating this process several times for a number of arbitrary strain values and for each compression test (both confined and unconfined whenever possible), a point cloud was obtained for the dilation angle as a function of the plastic parameter and confining pressure. Nevertheless, analysis of dilation angles from a standard triaxial compression test is difficult due to the inelastic behavior of the stress-strain curve, variability in the elastic parameters and the occurrence of non-homogeneous deformation modes (bifurcation and subsequent axial splitting and shear banding).

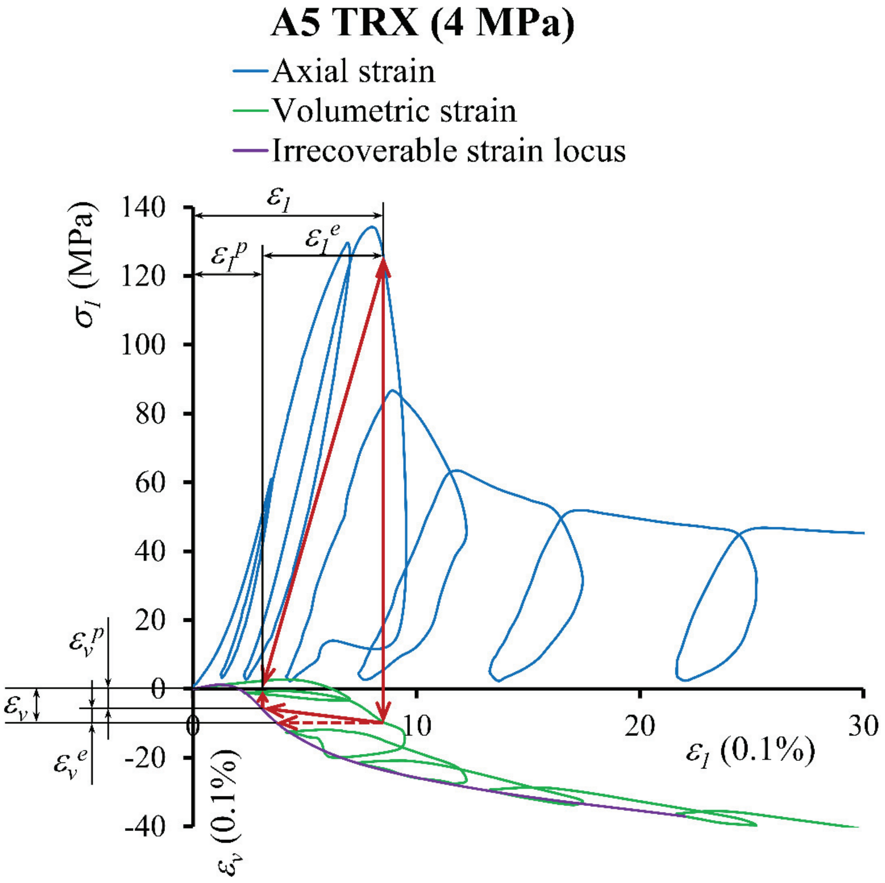

Fig. 3.12. Graphic estimate of axial and volumetric plastic strains.

It is also important to be aware of some of the issues raised in investigating complete stress-strain curves in rock masses (Hudson et al., 1971b; Jaeger et al., 2007; Price & Farmer, 1979). Between the onset of stable fracture propagation and unstable fracture propagation, ε_3^p is a negative value whereas ε_1^p is null, in other words, there is no inelastic axial strain for initial small values of the plastic parameters. This means that the dilation angle tends to minus infinity in this stage. Other inelastic and non-strictly plastic effects (such as crack closure in the early stages of stress application —resulting in the initial concave form of the stress-strain curve— and rock damage over long-term peak stress) add to the difficulty in obtaining more or less accurate dilation angle values (Alejano & Alonso, 2005).

The concept of dilatancy as defined above only makes sense in the post-failure zone, even if, at the peak strength point, the plastic parameter is in the order of some milistrains and inelastic volumetric strain attains values in the range 0.04% to over 0.1% (Scholz, 1968).

3.5.2.2. Dilatancy results

Using the above mentioned approach to estimation, point clouds —for the dilatancy value against the plastic parameter γ^p— were produced for each type of granite at different confinement levels, plotted as shown in Fig. 3.13. The figure reveals dilation angle dependencies as pointed out by Alejano & Alonso (2005), that is, the dilation angle depends, first, on confining pressure (i.e., as confining pressure grows, the dilation angle diminishes) and, second, on plastic shear strain (i.e., as plastic shear strain develops, the dilation angle decays). Note the wide dispersion of the unconfined test results, reflecting the type of measurement of volumetric strain (derived from radial strain in one diameter). Since around twelve unconfined tests were performed for each granite rock, even if there is wide dispersion, the average values can be considered to be reasonably representative of actual behavior.

The laboratory results were compared with the models proposed by Alejano & Alonso (2005) and by Zhao & Cai (2010a). The Alejano & Alonso (2005) model is divided into two parts, one referring to the peak dilation angle and the second part related to dilation angle decay with plasticity. This model did not fit the laboratory data in terms of peak friction angle, since the peak dilatancy values recovered were well below the expected ones. However, the process of dilation decay was reasonably well represented. The differences may well be due to the different nature of the rocks analyzed here (plutonic rocks) and those used for the Alejano & Alonso (2005) model (sedimentary rocks).

The model proposed by Zhao & Cai (2010a) required laboratory data to be fitted to the equation below relating dilation angle with plastic shear strain (γ^p, expressed in percentage of deformation):

$$\psi = \frac{ab\left(e^{-b\gamma^p} - e^{-c\gamma^p}\right)}{c-b} \tag{3.8}$$

As indicated in Zhao & Cai (2010a), parameters *a*, *b* and *c* control the shape of the curve. Although each affects the entire curve, they mainly control just one aspect of shape. Thus, *a* mainly controls the peak dilation angle, *b* mainly controls peak dilation angle location and *c* mainly controls rate of decay.

Table 3.9 presents the best fit parameters for dilation angle-plastic parameter curves for the three granitic rocks studied. Fig. 3.13 shows the fitted points cloud for each rock and each confining pressure.

The parameters *a*, *b* and *c* also show confining pressure dependency, as depicted in Fig. 3.14. As confining pressure increases, *a* and *b* decrease whereas *c* increases. These behaviors were evaluated against the expressions below proposed by Zhao & Cai (2010a), resulting in a very good fit to results for the previously obtained coefficients.

$$\begin{gathered} a = a_1 + a_2 \cdot \mathrm{e}^{\frac{-\sigma_3}{a_3}} \\ b = b_1 + b_2 \cdot e^{\frac{-\sigma_3}{b_3}} \\ c = c_1 + c_2 \cdot \sigma_3^{c_3} \end{gathered} \tag{3.9}$$

Using Eq. (3.9), three coefficients are necessary to fit each of the confining dependent parameters in Eq. (3.8). These coefficients are presented in Table 3.10, together with coefficients as obtained by Zhao & Cai (2010a) for a quartzite and a strong sandstone for comparison purposes, indicating values to be within a reasonable range. Using these coefficients it is possible to compare variations in fitted parameters at different confining stresses and their best fits.

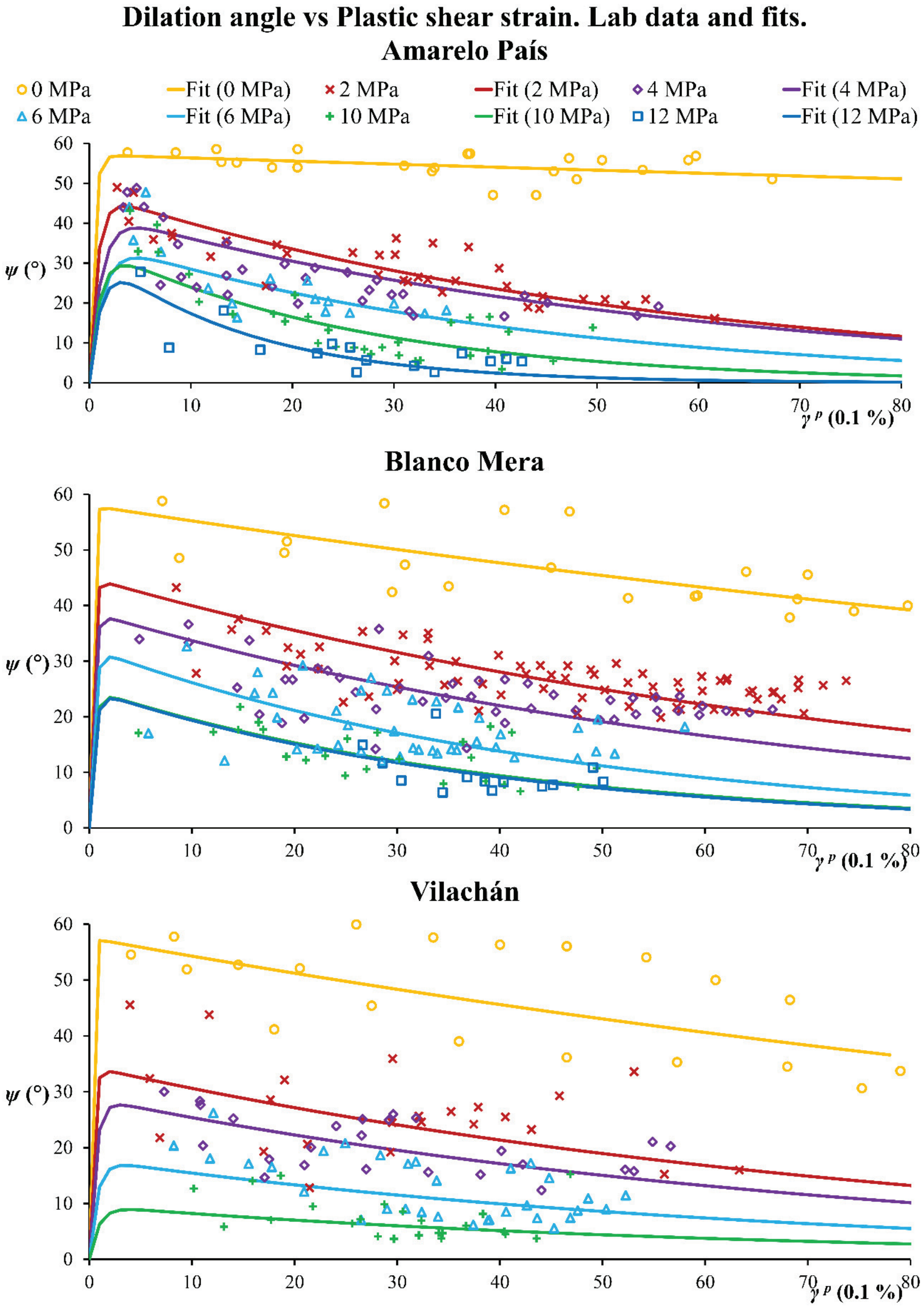

Fig. 3.13. Dilation angle vs. plastic shear strain for various confining levels and laboratory results and fits for each granite type.

Table 3.9. Fit coefficients for dilation angle-plastic parameter curves for the three granitic rocks studied.

Rock	σ_3 (MPa)	*a*	*b*	*c*	R^2
Amarelo País	0	57.15	25.00	0.014	0.999
	2	47.03	12.94	0.176	0.983
	4	42.00	8.67	0.170	0.987
	6	34.90	7.72	0.233	0.994
	10	33.51	9.75	0.375	0.971
	12	30.95	8.97	0.654	0.898
Blanco Mera	0	57.95	50.00	0.049	0.997
	2	44.83	35.97	0.118	0.990
	4	38.64	28.85	0.142	0.987
	6	32.06	24.22	0.213	0.974
	10	24.66	22.46	0.244	0.978
	12	24.54	20.99	0.250	0.992
Vilachán	0	57.48	60.01	0.058	0.996
	2	34.39	30.68	0.120	0.988
	4	28.72	16.82	0.131	0.991
	6	17.70	13.43	0.147	0.992
	10	9.47	11.15	0.156	0.994

Table 3.10. Plastic shear strain parameters and confining pressure dependent dilation angle model as proposed by Zhao & Cai (2010a), for the three studied granitic rocks (this study) and two other rocks (Zhao & Cai, 2010a).

*	a_1	a_2	a_3	b_1	b_2	b_3	c_1	c_2	c_3
1	63.17	11.92	2.80	5.83	36.25	6.77	0.14	1.14	1.23
2	29.01	28.05	4.76	8.26	17.49	1.5	0.014	0.0749	0.711
3	21.13	36.71	4.92	20.63	29.44	2.97	0.047	0.049	0.589
4	3.79	53.65	4.46	10.38	49.69	2.19	0.058	0.050	0.295
5	14.63	34.90	3.40	4.06	15.56	5.54	0.08	0.40	0.58

* 1. Quartzite (Zhao & Cai, 2010a), 2. Amarelo país, 3. Blanco Mera, 4. Vilachán, and 5. Strong sandstone (Zhao & Cai, 2010a)

At this point it is possible to show (Fig. 3.15) the models obtained for the three granitic rocks studied here and the rocks studied by Zhao & Cai (2010a) for the case of 1 MPa confinement. The graph shows how the granites are located between a harder and stiffer rock (quartzite, labelled 1) and a softer rock (sandstone, labelled 2) as was anticipated.

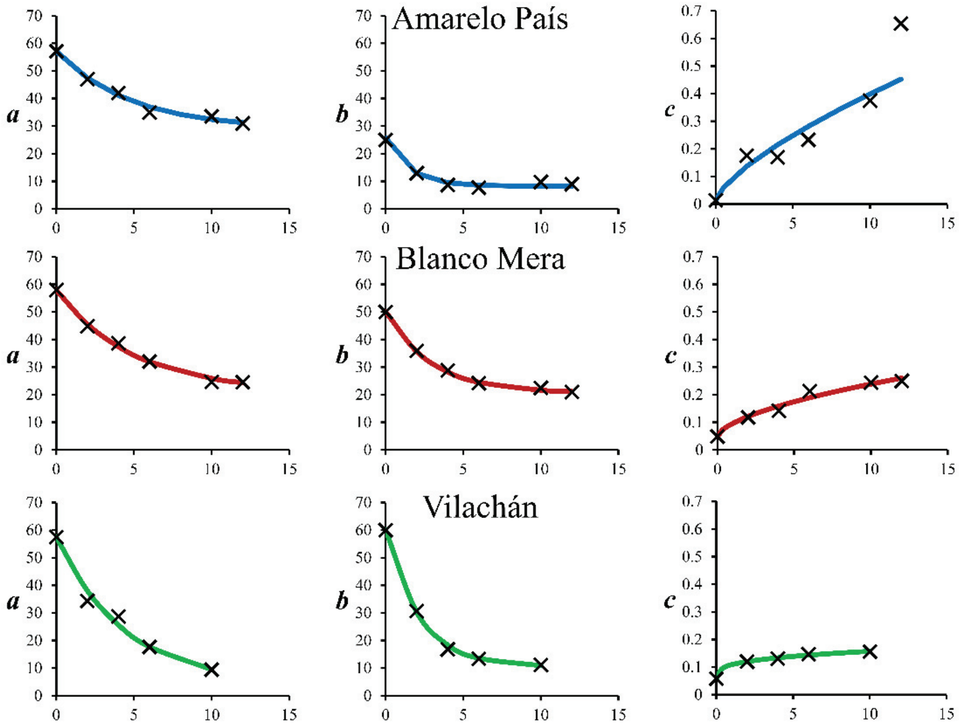

Fig. 3.14. Variations in fitting parameters (a, b and c) at different confining stresses (abscissa axis) and the best fit for each granite type.

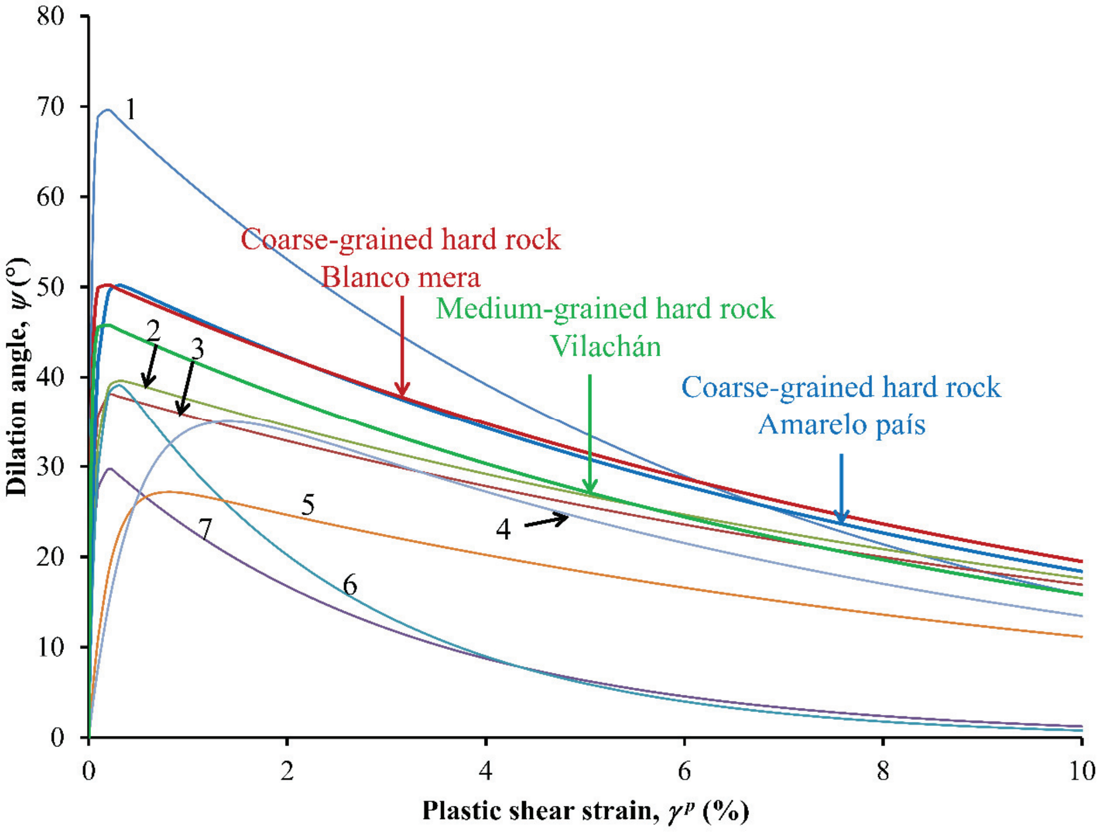

Fig. 3.15. Variations in the mobilized dilation angle for the three granites studied and for other rock types at a confining stress of 1 MPa (from Zhao & Cai, 2010a): 1. Quartzite (coarse-grained hard rock); 2. Strong sandstone (medium-grained hard rock); 3. Silty sandstone (medium-grained hard rock); 4. Mudstone (fine-grained soft rock); 5. Seaterth (fine-grained soft rock); 6. Weak sandstone (fine- to medium-grained soft rock); 7. Coal (fine- to medium-grained soft rock).

3.6. Conclusions of this chapter

Within the framework of a study of the post-failure behavior of rocks and rock masses, an experimental programme based on a press with fully servo-controlled loading was set up in order to test and study post-failure stress-strain behavior in granite samples. A total of around 90 unconfined and confined compression strength tests with unloading-reloading cycles and computation of volumetric strain in confined tests were performed. This ensured for every cycle that the strength attained represents the point of an evolving strength criterion; it also allowed to locate what is known as the irrecoverable strain locus, which would enable to obtain reliable values for the dilation angle.

Peak and residual strength, apparent Young's modulus, apparent Poisson's ratio, estimated drop modulus and shear band inclination were estimated for each test and dilation angle behavior was computed all throughout the deformation process.

The dilation angle was computed from data in each of the compression tests when this was possible. As previously observed, this angle was shown to be dependent on both confining stress and plastic shear strain. Test results were compared with previously proposed models and the obtained data fitted reasonably well with those of the Zhao & Cai (2010a) model. Accordingly, best fit parameters for the data were calculated, obtaining adjustment curves very similar to those reported by Zhao & Cai (2010a) for analogous rocks, since the tested granite dilation angle results were located between those for a harder rock (quartzite) and a softer rock (strong sandstone). In conclusion, this study has shown that even if dilation in hard igneous rock (such as granite) follows similar confining stress and plastic strain dependent dilation trends as observed so far on studies in sedimentary and metamorphic rocks, previous approaches (Alejano & Alonso, 2005) are not accurate enough to properly model observed behavior. Therefore, this study contributes to the experimental rock mechanics database in terms of completing it with information on the relationships between dilation angle model parameters and different rock types —in this case granites—, to date unreported in the literature.

A nine-parameter complex dilation model as presented in the literature (Zhao & Cai, 2010a) has been demonstrated to be a good approach for the presented data. A one-parameter dilation model (Alejano & Alonso, 2005) did not fit well with the obtained results. Looking to the future, it could be interesting to investigate new dilation models that are neither as complex as Zhao & Cai's nor as inaccurate as the former approach —reasonably accurate for sedimentary rock but not for igneous materials.

Some drawbacks of the testing set-up became apparent that need to be overcome in the future so as to continue improving its testing capacity. Improvements will include the option for performing unconfined tests with specimens inside a Hoek's cell to obtain more homogeneous volumetric strain results and controlling press stiffness to better reflect post-failure behavior trends in very low confinement tests.

Future work will include a more detailed study of the post-failure part of the curve, in order to assess the evolution of the principal stresses in relation to a suitable plastic parameter, and implementation of the resulting approach in numerical models. It is also planned to extend the observations to rock mass behavior, following the lines previously developed by the author's research group (Alejano & Alonso, 2005; Alejano et al., 2009b; Alejano et al., 2010; Alejano et al., 2012a), and also to larger parts of the Earth's crust.

4. Dilation in other rocks based on lab strength tests

4.1. Introduction

In the field of geomechanics, developing an improved understanding of the behavior of rocks like those studied in this chapter (three carbonate rocks: two limestones and a marble; an amphibolite; and a gneiss) is of interest for a number of reasons, e.g. carbonate rocks form economic petroleum reservoirs in many parts of the world; all of them are used extensively as ornamental and aggregate building materials; and they also are of interest for infrastructure projects. Some examples of projects involving excavation in these kind of rocks include the Lotschberg and Gotthard base tunnels in Europe and the deep geological repository (DGR) for nuclear waste currently going through the licensing process in Canada (Loew et al., 2000; NWMO, 2015).

By understanding the reaction of different rock types to changes in their stress states, it is possible to predict and even control the behavior of rocks for engineering projects (i.e. through hydraulic fracturing in the petroleum industry or through the use of support in excavations). A classic approach to study rock behavior is to investigate the stress-strain relations of a cylindrical sample tested under compressive conditions. Based largely on these types of tests, many authors have contributed significantly to a general understanding of the strength and elastic deformability of many different rock types (Wawersik & Fairhurst, 1970; Crouch, 1970; Price & Farmer, 1979). Following the attainment of peak strength, however, most tests do not continue to significantly larger strains. Because of the relative scarcity of data in the post-peak region as well as the increased behavior complexities and system dependencies at large strains, our understanding of this component of rock behavior remains relatively poor (Diederichs, 1999).

Advances in testing techniques, starting in the 1960s and 1970s have allowed a significant increase in the general capabilities of the rock mechanics community to perform post-peak compression tests (Rummel & Fairhurst, 1970; Wawersik & Brace, 1971; Hudson et al, 1971a). Since this time, several authors have published work focused specifically on post-peak testing results (Elliot & Brown, 1985; Cipullo et al, 1985; Medhurst, 1996; Arzúa & Alejano, 2013).

The goal of this study is to investigate the differences in the elastic, strength, and post-peak properties between the tested rocks. It is the hope of the author that continuing to improve the existing database of post-peak tests will encourage the development of increasingly accurate and manageable models for complex rock behavior.

4.2. Rocks investigated

The carbonate rocks selected for this study (the two limestones and the marble) were selected both because of their relative uniformity, and because of the differences in their petrologic properties. The other two rocks (the amphibolite and the gneiss, metamorphic rocks like the marble) were precisely selected because of their inhomogeneity. Close-up photos of the carbonates rocks showing the differences in their grain structures and thin plates sections pictures of the other two rocks can be seen in Fig. 4.1.

4.2.1. Indiana limestone

Indiana limestone is a Mississippian aged carbonate rock, and can be classified as a grainstone, based on Dunham's classification (Hill, 2013; Dunham, 1962). Because of its extremely uniform

This chapter contains some of the results published in the following citations:

Pérez-Rey, I., Arzúa, J., Barbiero, J., Alejano, L.R. & Walton G. *A lab-testing based geomechanical characterization of metamorphic rocks focusing on post-failure behavior*. EUROCK2014 - Rock Engineering and Rock Mechanics: Structures in and on Rock Masses – Alejano, Perucho, Olalla & Jiménez (Eds). 27-29, May. Vigo, Spain. CRC Press, Taylor and Francis Group, London.

Walton, G., Arzúa, J., Alejano, L.R., Diederichs, M.S. 2015. *A Laboratory testing-based study on the strength, deformability and dilatancy of carbonate rocks at low confinement*. Rock Mechanics and Rock Engineering. 48:941-958.

grain size and structure, it has been widely used as a building stone starting in 1827. Indiana limestone is quite pure, consisting of at least 97% $CaCO_3$ with small amounts (1.2%) of $MgCO_3$ (Hill, 2013). Grain sizes range from approximately 0.3 mm to 0.5 mm. Indiana limestone is by far the most porous of the rocks studied in this work, with porosities generally in the range from 12% to 20% (Vajdova et al, 2004). The samples tested were determined to have a mean density of 2.31 g/cm^3 with a standard deviation of 0.01 g/cm^3.

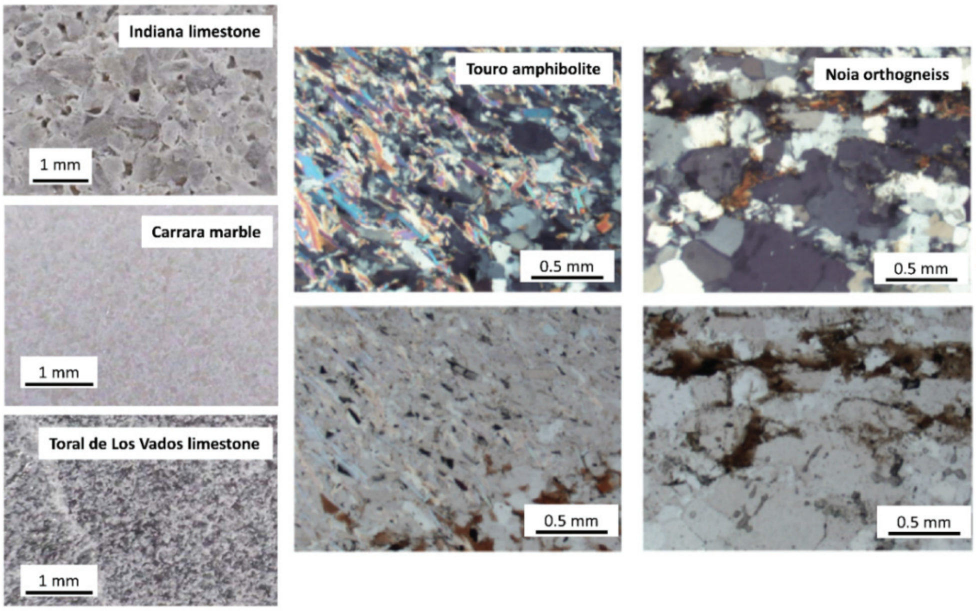

Fig. 4.1. Grain structures of Indiana limestone, Carrara marble and Toral de Los Vados limestone. Thin plate section with crossed nicols (upper) and with visible light (lower) of the Touro amphibolite and Noia orthogneiss. Remark the foliation in the amphibolite (amphibole colored crystals) and the gneiss (black biotite).

Because of its wide usage and its uniform and repeatable behavior, Indiana limestone has been widely studied in the literature. Some previous studies have focused on brittle failure mechanisms in Indiana limestone (Robinson, 1959; Wawersik & Fairhurst, 1970; Zheng et al, 1989), tensile fracturing (Hoagland et al, 1973; Peck et al, 1985), poroelastic properties (Hart & Wang, 1995), fracture toughness (Schmidt & Huddle, 1977), and compaction (Vajdova et al, 2004; Ji et al, 2012).

4.2.2. Carrara marble

Carrara marble is a metamorphic rock of Triassic age formed from the metamorphism of an ancient carbonate shelf. There are several varieties of Carrara marble depending on the purity of the marble and the prevalence of microstructures in the rock. The white Carrara marble used in this study is 100% calcite (Howarth & Rowlands, 1987). Grain sizes of Carrara marble of 0.1 mm (Edmond & Paterson, 1972), 0.23 mm (Fredrich et al, 1990), and 0.3 mm (Howarth & Rowlands, 1987) have been reported in the literature. Most grains in the samples studied are closest to approximately 0.1 mm in size. The porosity of Carrara marble is very low, in the range of 0.7% (Fredrich et al, 1990) to 1.1% (Edmond & Paterson, 1972). The samples tested were determined to have a mean density of 2.70 g/cm^3 with a standard deviation of 0.01 g/cm^3.

Previous studies on the Carrara marble have focused on the brittle-ductile transition of sedimentary and/or carbonate rocks at moderate to high confining pressures and/or temperatures (Turner et al, 1954; Griggs et al, 1960; Mogi, 1966; Edmond & Paterson, 1972; Fredrich et al, 1989; Ord, 1991). Other studies have used Carrara marble to study the influence of grain size on rock yield (Olsson, 1974; Howarth & Rowlands, 1987; Fredrich et al, 1990).

4.2.3. Toral de Los Vados limestone

The Toral de Los Vados limestone corresponds to Cambrian strata found in the western area of the province of León (NW of Spain). It is found in a sedimentary series of mid-Cambrian age that has locally suffered low degree metamorphism, so some of the original mudstones and limestones have become slates and marbles. In situ, this limestone presents tabular bedding, also showing fine laminations and local dolomitic levels. Various high stress periods over the geological history of the area have fissured the rock. During the alpine orogeny some re-crystallization has occurred, which is apparent in the form of re-crystallized calcite veins. This re-crystallization has overprinted most primary sedimentary structures that existed within the rock.

As a consequence of this process, the rock does not present significant porosity. Observed grain sizes range from non-visible to 0.1 mm. The texture is granoblastic to aphanitic. A granoblastic texture describes equigranular crystals which adopt a polygonal morphology, often seen in the products of thermal metamorphism. The term aphanitic describes fine-grained rocks in which all crystals, other than phenocrysts, cannot be seen with the naked eye. The rock is quite heterogeneous showing locally rusty patterns. Chemical analysis showed not only calcite (principal mineral), but also moderate levels of dolomite (15-25 %) and also small quantities of quartz and silicates (5-10 %).

4.2.4. Touro amphibolite

The garnet amphibolite tested is a compact brownish to greenish grey, somewhat banded, medium size grained (0.1 to 0.2 mm). It is a metamorphic rock formed through recrystallization under conditions of high viscosity and directed pressure. It is composed mainly of amphibole minerals (actinolite) and plagioclase feldspar, it also contains relevant quantities of quartz, garnets and pyroxenes.

The metamorphism has somewhat flattened and elongated the mineral grains to produce a banded texture (in between schistose and coarse grained, see Fig. 4.1). The samples were recovered in an old copper mine in Touro, a little town located some kilometers west of Santiago de Compostela in NW of Spain.

4.2.5. Noia orthogneiss

This rock is a very compact high grade regional metamorphic rock derived from granite and composed by quartz, feldspar (alkaline and plagioclase), mica (mainly biotite) and small quantities of hornblende. It is a medium to coarse foliated rock, characterized by discontinuous alternating light and dark layers, the former usually having a coarsely granular texture (0.3 to 0.5 mm) while the latter may be more foliated (see Fig. 4.1). The material was recovered in an aggregate quarry two kilometers south of Noia in La Coruña province, in NW of Spain.

4.3. Methods

4.3.1. Test setup

For each rock type, compression tests were carried out under uniaxial and triaxial conditions with confining pressures of 1 MPa, 2 MPa, 4 MPa, 6 MPa, 8 MPa, 10 MPa, and 12 MPa when possible. At this point, it has to be noted that the testing in gneiss was limited to a maximum confining pressure of 6 MPa due to its high compressive strength (UCS > 250 MPa) and in order to avoid further problems with the testing equipment. These confining pressures were selected based on their relevance for near excavation conditions, and also because of the upper limit pressure of 20 MPa of the hydraulic system. The numbers of samples tested at each confining pressure are shown in Table 4.1. The results of all the tests are shown in Appendix B

Table 4.1: Number of tests performed on each rock and at each confining pressures.

Confining pressure (MPa)	0	1	2	4	6	8	10	12
Indiana limestone	10	3	3	3	3	3	3	3
Carrara marble	6	3	3	3	3	2	2	2
Toral de Los Vados limestone	5	0	3	3	3	2	2	2
Touro amphibolite	5	0	3	3	3	0	3	3
Noia gneiss	1	0	4	5	4	1*	1*	1*

* Triaxial testing at these confining pressures overpassed the limiting confinement of 20 MPa after failure, so post-failure data was not used.

Axial loading was applied using a standard press setup. To obtain reliable post-peak results, unloading-reloading cycles were again performed for each test after the attainment of peak strength as required. These cycles helped avoid sudden strength loss, which can lead to unreliable (underestimated) weakening rates based on the stiffness contrast between the press and the sample and the strain velocity of the press and also allowed to identify recoverable (or elastic) and irrecoverable components of the strains.

Axial and radial strain in unconfined tests and axial and volumetric strains in triaxial tests were measured as indicated in the previous chapter.

4.3.2. Data analysis

As explained earlier. In the case of the unconfined tests, the calculation of volumetric strains was performed according to the relation:

$$\varepsilon_v = \varepsilon_1 + 2 \cdot \varepsilon_3 \tag{4.1}$$

And in the case of the triaxial tests, the total volumetric strain was calculated according the following equation (after Farmer, 1983):

$$\varepsilon_v = \frac{1}{V}\left(f \Delta V_f - l \pi r^2\right) \tag{4.2}$$

With all of the relevant stresses and strains available, apparent Young's modulus values were calculated as the slope of the linear segment of the axial stress-axial strain curve for each test, roughly between 30% and 60% of the peak strength. Poisson's ratio values were calculated over the portion of the axial stress-radial strain which is linear, between approximately 20% and 40% of the peak strength.

For each unloading-reloading cycle performed on a given test, multiple pieces of information were recorded. Of particular interest were the irrecoverable axial and volumetric strains in the unloaded state; if such strains are considered to be purely plastic in nature, then the differences in strains between consecutive unloading states can be used to calculate the instantaneous dilation angle, ψ (Vermeer & De Borst, 1984):

$$\sin\psi = \frac{\Delta\varepsilon_v}{-\Delta\varepsilon_v + 2\Delta\varepsilon_1} \tag{4.3}$$

When using a plasticity model to describe rock, it is important that an appropriate definition of yield is adopted to properly constrain the onset of plastic behavior. For this study, the crack damage stress (CD) has been adopted as the yield point, as per the definition of Diederichs & Martin (2010). This yield point corresponding to the onset of unstable cracking in a test specimen is defined as the start of non-linearity in the axial stress-axial strain curve (Diederichs, 2003), which coincides with the volumetric strain reversal point under unconfined conditions (Martin, 1997). For each sample, CD was manually picked based on the axial stress-axial strain curve, a smoothed point to point tangent modulus plot, and the volumetric strain-axial strain curve (see Fig. 4.2).

Another consideration when working with plasticity models for rock is the appropriate quantification of accumulated damage following yield. This is typically achieved by using a measure of plastic strain. One common approach is to select the plastic parameter to be function of internal variables, in particular the plastic shear strain:

$$\eta = \gamma^p = \varepsilon_1^p - \varepsilon_3^p \tag{4.4}$$

As an alternative to this approach, an incremental plastic parameter can be used which is based on plastic strain increments. One definition for such a parameter is:

$$\dot{\eta} = \sqrt{\frac{2}{3}\left(\dot{\varepsilon}_1^p \dot{\varepsilon}_1^p + \dot{\varepsilon}_2^p \dot{\varepsilon}_2^p + \dot{\varepsilon}_3^p \dot{\varepsilon}_3^p\right)} \tag{4.5}$$

(Vermeer & de Borst, 1984).

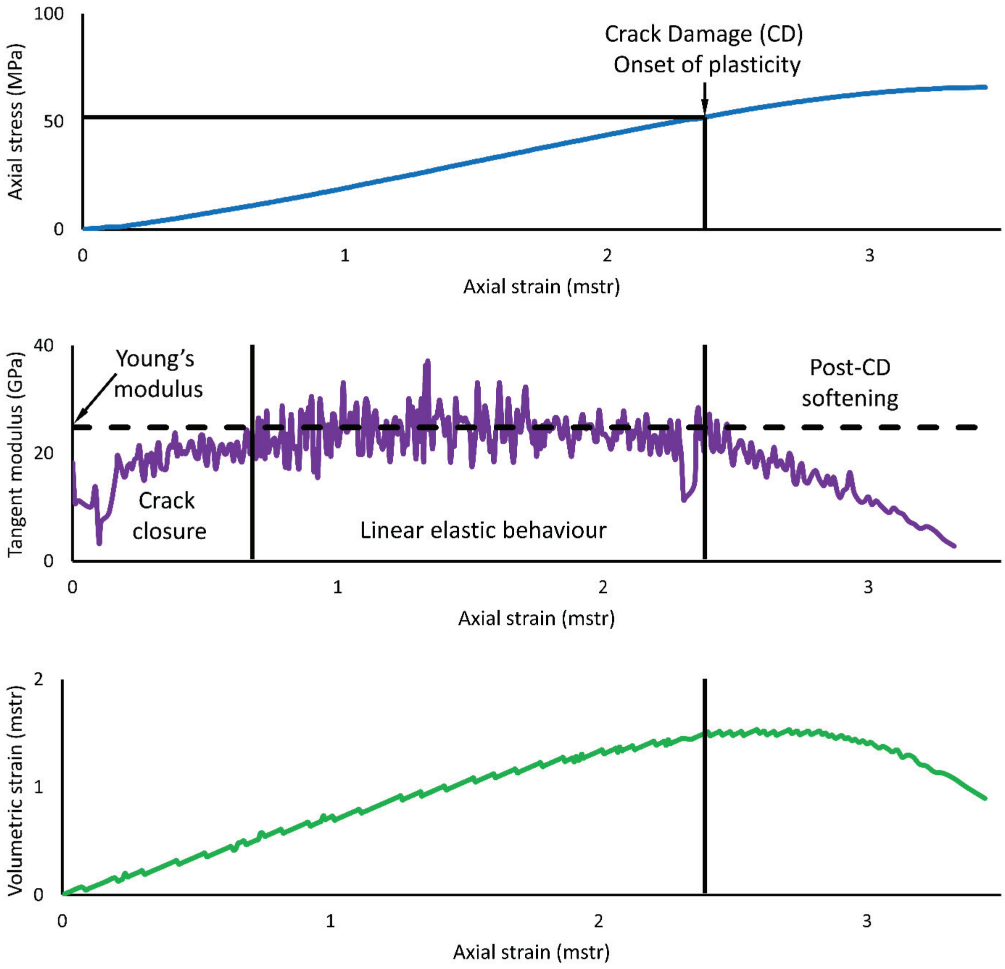

Fig. 4.2. Example of data used to select the crack damage stress (CD) for each test specimen; axial stress versus axial strain (top), smoothed point to point tangent modulus (middle) and volumetric strain versus axial strain (bottom) plots are shown.

In the commonly used finite-difference codes FLAC and FLAC3D, the incremental plastic parameter is defined as:

$$\Delta e^{ps} = \left\{ \frac{1}{2}\left(\Delta\varepsilon_1^{ps} - \Delta\varepsilon_m^{ps}\right)^2 + \frac{1}{2}\left(\Delta\varepsilon_m^{ps}\right)^2 + \frac{1}{2}\left(\Delta\varepsilon_3^{ps} - \Delta\varepsilon_m^{ps}\right)^2 \right\}^{1/2} \tag{4.6}$$

where:

$$\Delta\varepsilon_m^{ps} = \frac{1}{3}\left(\Delta\varepsilon_1^{ps} + \Delta\varepsilon_3^{ps}\right) \tag{4.7}$$

(Itasca, 2011).

When the dilation angle is a constant, it can be shown that the cumulative plastic parameter, e^{ps}, is directly proportional to the plastic shear strain, γ^p. The constant of proportionality varies between 1/2 and $1/\sqrt{3}$, depending on whether the dilation angle is closer to 0° or 90°, respectively (after Alonso et al, 2003). In practice, when using numerical models with a non-constant (mobilized) dilation angle model, Alejano & Alonso (2005) have found that dividing γ^p by 2 to obtain e^{ps} introduces minimal errors into the plastic strain calculations. In this study, γ^p is used as the plastic parameter representing accumulated damage and strain.

4.4. Interpretation of results

An interesting range of behaviors can be observed in the five rock types studied. Examples of the stress-strain curves can be seen in Fig. 4.4, where the results from triaxial tests at 6 MPa of confining stress are showed for the five rocks studied. In this figure also a graph (bottom right) showing the axial stress-axial strain curve without the unloading-reloading cycles for the five studied rocks is showed for comparative purposes. One must take into account that while vertical axes have different scales, the horizontal axis is maintained the same in all the graphs in order to compare the different deformability behavior of the different rocks.

It is relevant to remark that because of the brittleness of the Noia gneiss, and also the Touro amphibolite and the Toral de Los Vados limestone up to certain extent, it was difficult to control the failure of the samples and achieve a stability transition from peak to residual strength, this suggests that the rate of strength loss observed could be a function of the press strain velocity and not of the rock itself. So even if the strength data in this portion of the tests cannot be considered reliable, the axial strain-radial strain relationships should still be representative. Typical failure mechanisms of each rock type at low and high confinements are illustrated in Fig. 4.3.

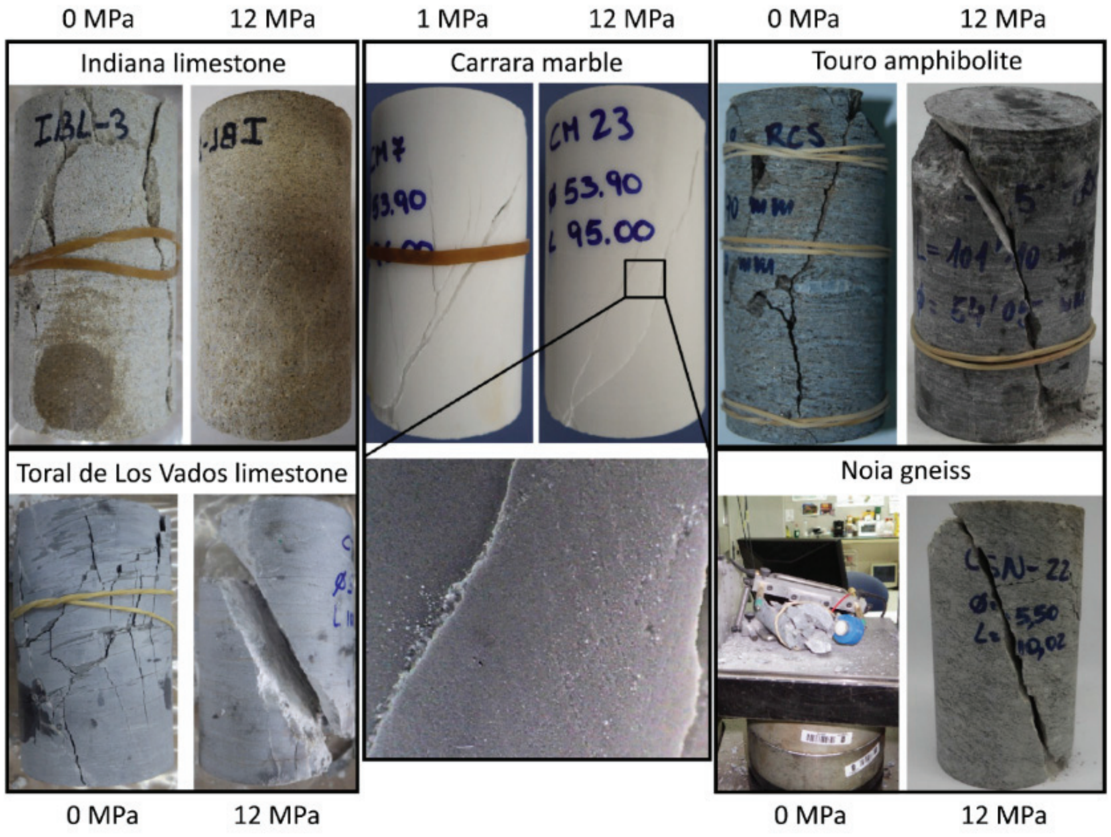

Fig. 4.3. Typical failure mechanisms in Indiana limestone, Carrara marble, Touro amphibolite, Toral de Los Vados limestone and Noia gneiss. The inset figure (bottom middle, courtesy of Gabriel Walton) shows grain scale conjugate shearing occurring in the Carrara marble. The confining stresses that the samples were tested at are shown at the top or the bottom of each picture.

The Indiana limestone was observed to display brittle behavior at low confinements, but transitioned to relatively ductile behavior over a small range of confining pressures. This is likely associated with the relatively high porosity and low strength of the limestone. The brittle-ductile transition typically occurs at lower confining stresses for rocks which display lower strengths, and the critical confining stress is typically lower for carbonate rocks than for other rock types, particularly those with a higher porosity (Mogi, 1966). At low confinements, the limestone failed through axial cracking, or in shear, with the shear fracture appearing to have formed through the coalescence of small, axially oriented cracks. At higher confinements, the failure occurs over a wider shear zone.

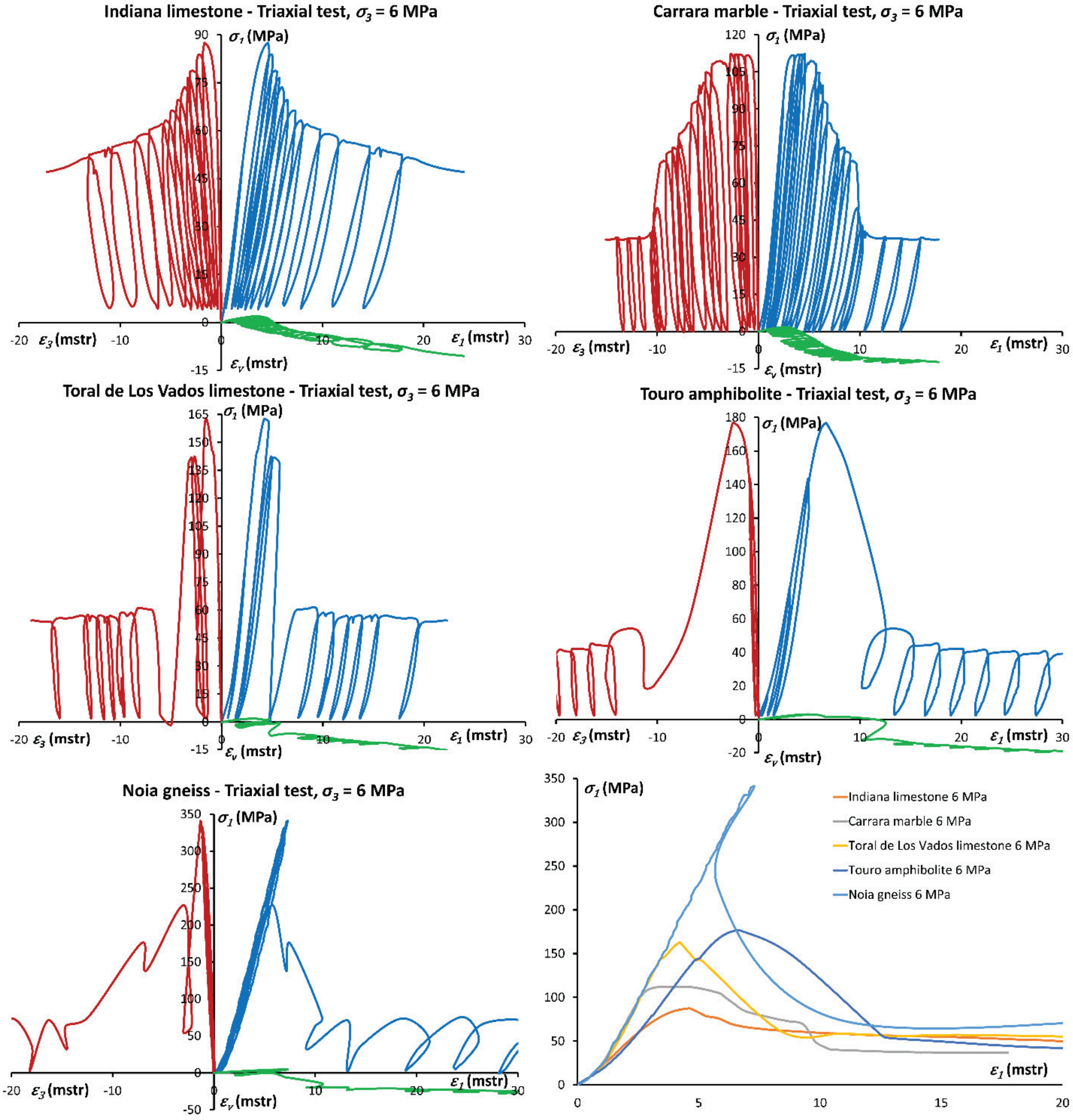

Fig. 4.4. Examples of the stress-strain response of the five studied rocks during a triaxial tests with a confining pressure of 6 MPa. A comparative (bottom right) between axial stress – axial strain curves of the five rocks is also showed, cycles have been removed from the curves in this graph in order to clarify the comparison, observe the similarity in Young's moduli of the Carrara marble (grey), Toral de Los Vados limestone (yellow) and Noia gneiss (light blue).

The Carrara marble, in contrast, is relatively ductile, even at unconfined conditions. In many cases, the marble would display elastic-perfectly-plastic behavior for small intervals of strain before experiencing a sudden, but relatively small drop in strength. The kind of behavior can be observed in Fig. 4.4. This observation is consistent with other studies in the literature, which note that Carrara Marble deforms in a stable, ductile manner (Fredrich et al, 1990) and that crystalline calcite can initiate ductile deformation mechanisms at relatively low temperatures and pressures (Turner et al, 1954; Griggs et al, 1960). At low confinements, the marble failed in shear, sometimes with axial cracks being present as well. At higher confinements, the deformation occurred through localized grain-scale shearing in a wide shear band.

The Toral de Los Vados limestone presents a brittle failure at low confining stresses, showing axial cracking with the cracks connected laterally by fractures along sub-horizontal planes of weakness. At higher confinements (4 to 6 MPa) this rock showed a more ductile behavior, presenting shear failure across structures.

The Touro amphibolite shows a similar behavior to that of Toral de Los Vados limestone, presenting axial cracking at low confinement and a more ductile failure with shear planes for medium to high confining pressures (6 to 8 MPa). It has to be noted that axial failure was also connected by fractures along planes of weakness, as it occurred in the Toral de Los Vados limestone.

The Noia gneiss is the strongest and most brittle of the five rocks studied. This rock maintained its brittle behavior until the highest confining pressures allowed by our system were reached (10 to 12 MPa). The failure in these conditions led to an even higher confining pressure that locked the system. It was not possible to collect post-failure data of this rock for confining pressures higher than 6 MPa.

The relative ductility of the Carrara marble when compared to as the Indiana limestone can be seen by plotting the drop modulus (calculated based on data in Fig. 4.4 as the slope of the curve from peak to residual strength) versus confining pressure (see Fig. 4.5). Both curves display a roughly logarithmic trend, with the Carrara marble samples having drop moduli significantly lower in magnitude than the Indiana limestone samples. The drop moduli corresponding to Touro amphibolite, Noia gneiss and Toral de Los Vados limestone curves are in the range of -35 GPa to -45 GPa; although these numbers may not be representative of the rock, they can be thought of as an upper bound on the drop modulus.

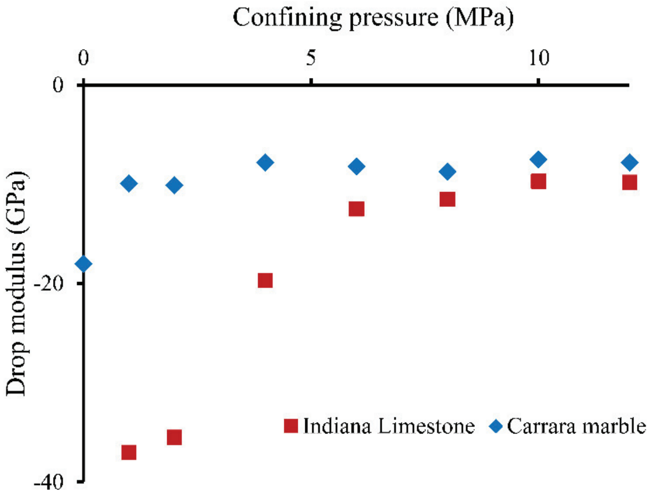

Fig. 4.5. Average drop modulus values for Indiana limestone and Carrara marble.

4.4.1. Strength

For each sample, ultimate strength and residual strength were recorded. Two strength models were fit to each of these strength envelopes using least squares regression. The linear Mohr-Coulomb criterion and the curved generalized Hoek-Brown criterion (Hoek et al, 2002):

$$\sigma_1 = \frac{2c}{\cos\phi} + \frac{1+\sin\phi}{1-\sin\phi}\cdot\sigma_3 \tag{4.8}$$

$$\sigma_1 = \sigma_3 + \sigma_{ci}\left(m\frac{\sigma_3}{\sigma_{ci}} + s\right)^a \tag{4.9}$$

where c is the cohesion, ϕ is the friction angle, σ_{ci} is the uniaxial compressive strength of the intact rock, and m, s and a are material constants. The raw data and the resulting fits are plotted in Fig. 4.6, and the material constants obtained from the strength fits can be seen in Table 4.2. In general, the strength results are consistent with those in the literature when available (Carrara marble peak UCS = 94.3 MPa, Howarth & Rowlands, 1987; Indiana limestone peak UCS = 62.6 MPa, Cargill & Shakoor, 1990; Indiana limestone peak m = 7.1, Ramamurthy, 2001).

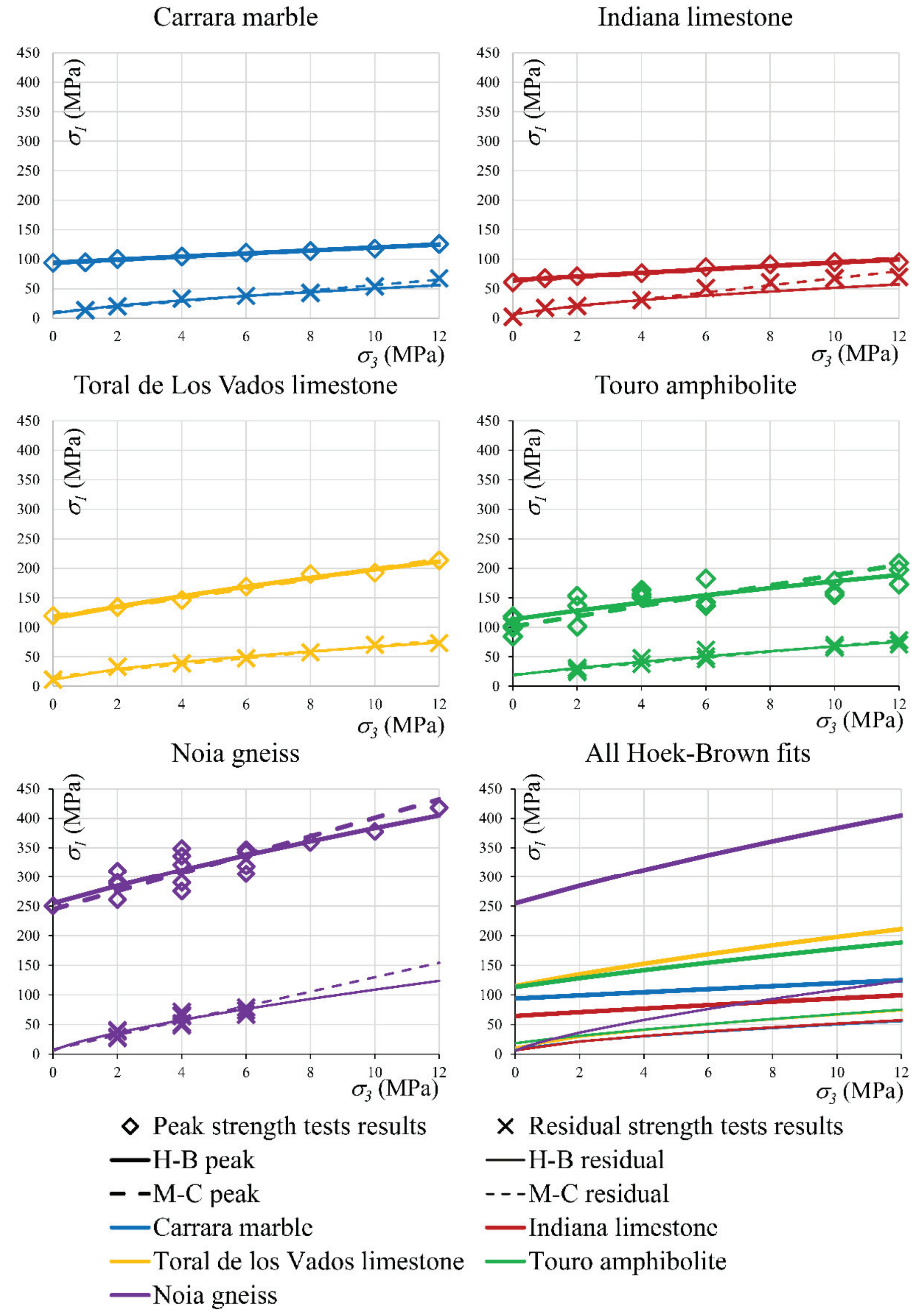

Carrara marble

Indiana limestone

Toral de Los Vados limestone

Touro amphibolite

Noia gneiss

All Hoek-Brown fits

Fig. 4.6. Strength data and least-squares Mohr-Coulomb (M-C) and Hoek-Brown (H-B) fits for Carrara marble, Indiana limestone, Toral de Los Vados limestone, Touro amphibolite and Noia gneiss. In the lower right graph, Hoek-Brown failure criterion fits for all the rocks are shown together.

In all cases, the Mohr-Coulomb criterion represents the observed strength data as well as the Hoek-Brown criterion, over the range of confining stresses tested. Observing the residual strength data (along with the corresponding fit parameters), it can be clearly seen that for these rocks, the principal drop in strength occurs in the cohesive component and in some cases like the Indiana limestone and Carrara marble, the friction angle increases. Both the decrease in cohesive component of the strength and the increase in the frictional component of the strength fit well the model known as Cohesion-Weakening-Friction-Strengthening (CWFS) but this aspect is out of the scope of the present study.

Table 4.2. Strength fit data.

		σ_{ci} (MPa)	m	s	a	ϕ (°)	c (MPa)
Indiana limestone	Peak	62.6	7.1	1	0.5	35.8	16.2
	Residual	62.6*	6.5	0.010	0.67	48.4	1.2
Carrara marble	Peak	94.3	5.5	1	0.5	33.2	25.6
	Residual	94.3*	4.4	0.004	0.66	46.2	1.3
Toral de Los Vados limestone	Peak	116.8	21.8	1	0.5	53.2	19.8
	Residual	116.8*	4.2	0.021	0.59	46.2	3.1
Touro amphibolite	Peak	113.5	13.47	1	0.5	52.6	17.7
	Residual	113.5*	3.11	0.048	0.6	41.2	4.5
Noia gneiss	Peak	255.0	29.21	1	0.5	61.6	30.9
	Residual	255.0*	6.25	0.004	0.68	58.1	1.1

* These values correspond to the fixed σ_{ci} used for the generalized Hoek-Brown criterion fit in the residual state.

4.4.1. Deformability

The Young's Modulus and Poisson's ratio values obtained from the linear portions of the axial stress-axial strain and axial stress-radial strain curves were found to show limited variability. The calculated Poisson's ratio values are shown in Table 4.3.

Table 4.3. Poisson's ratio information.

	Mean	Standard deviation
Indiana limestone	0.13	0.026
Carrara marble	0.15	0.020
Toral de Los Vados limestone	0.08	0.016
Touro amphibolite	0.14	0.038
Noia gneiss	0.09	0.022

The apparent Young's modulus values were found to vary significantly with confinement. The more homogeneous Indiana limestone and Carrara marble displayed a linear relationship, while the Toral de Los Vados limestone, Touro amphibolite and Noia gneiss showed a nearly constant Young's modulus under triaxial conditions and a distinct Young's modulus under uniaxial conditions. Although it would be reasonable to model the Young's modulus of these rocks using two distinct values, a slightly more complex model can capture not only the distinction between uniaxial and triaxial conditions, but also any further trend at higher confinements (see Fig. 4.7). Such a behavior was observed in the highly heterogeneous Blanco Mera granite (Chapter 3), and can be fitted using a logarithmic model:

$$E = \lambda \cdot \ln\left(\sigma_3\right) + E_1 \qquad (4.12)$$

where λ is a coefficient, and E_1 is the model's Young's modulus at σ_3 = 1 MPa. To address the issue of the lack of definition of the natural logarithm at σ_3 = 0 MPa, the function can simply be transitioned into a tangent linear section wherever the tangent ray of the log function intersects the known uniaxial modulus.

It is interesting to note that in both the case of this study and the granites studied in the previous chapter, the linear model for Young's Modulus values tends to apply to the slightly weaker rocks with more homogeneous grain structures, whereas the logarithmic model applies to the stronger rocks with more heterogeneous grain structures. With this in mind, in the case of the more complex logarithmic model, the rapid increase in stiffness over the first few MPa of confinement can be hypothesized by a transition from localized elastic deformation in softer parts of the sample to more homogenous deformation.

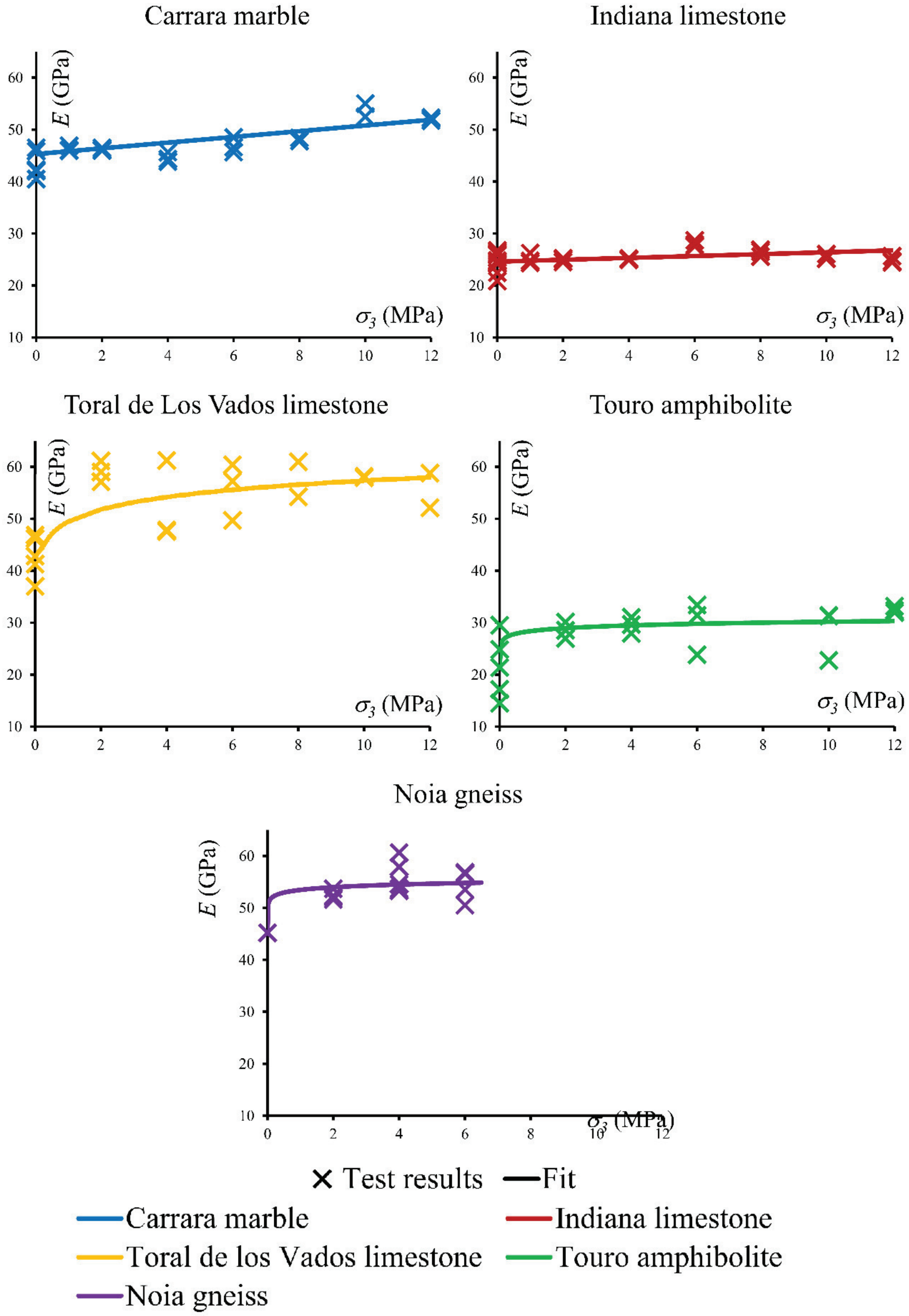

Fig. 4.7. Variation in Young's Modulus as a function of confinement, with a linear model shown for the Indiana limestone and Carrara marble (both on top); and a logarithmic model shown for the Toral de Los Vados limestone, Touro amphibolite and Noia gneiss.

The relevant model parameters for the proposed Young's modulus models can be seen in Table 4.4.

Table 4.4. Young's Modulus model information.

	Young's Modulus at $\sigma_3 = 0$ MPa (GPa)	Linear fit slope	Logarithm coefficient	Logarithm constant term (GPa)	R^2
Indiana limestone	24.6	0.18	-	-	0.38
Carrara marble	45.3	0.55	-	-	0.55
Toral de Los Vados limestone	40.6	-	3.42	49.5	0.63
Touro amphibolite	21.5	-	0.76	28.4	0.49
Noia gneiss	45.2	-	0.74	53.4	0.48

4.4.2. Dilatancy

The dilation angle data obtained based on the unloading-reloading cycles were found to show a trend similar to that of the model proposed by Zhao & Cai (2010a) for lab specimens dilatancy:

$$\psi = \frac{ab\left(e^{-b\gamma^{p}} - e^{-c\gamma^{p}}\right)}{c-b} \tag{4.13}$$

One set of parameters were fit to all data obtained at each confining stress for each rock type using least-squares regression. These parameters are shown in Table 4.5. A comparison of the dilation angle data for low confining stress between various rock types is given in Fig. 4.8.

Table 4.5. Mobilized dilation angle fit parameters for the rocks tested.

	σ_3 (MPa)	0	1	2	4	6	8	10	12
Indiana limestone	a	-	34.5	15.4	37.2	22.9	15.7	11.0	9.0
	b	-	202.12	107.63	14.12	31.48	465.42	38.83	322.30
	c	-	0.636	0.441	1.577	0.739	0.678	0.482	0.770
	R^2	-	0.70	0.17	0.88	0.50	0.42	0.23	0.27
Carrara marble	a	45.82	63.36	58.08	52.67	47.10	42.83	41.74	45.53
	b	8.42	2.44	4.33	3.48	4.28	5.71	4.25	3.68
	c	0.011	0.715	0.838	0.651	0.885	1.151	0.663	0.926
	R^2	0.155	0.851	0.862	0.883	0.811	0.936	0.923	0.912
Toral de Los Vados limestone	a	-	-	34.0	31.2	32.2	26.6	39.7	43.4
	b	-	-	100.54	101.17	101.17	101.91	100.06	97.19
	c	-	-	0.189	0.281	0.304	0.268	0.471	0.798
	R^2	-	-	0.70	0.72	0.42	0.52	0.88	0.86
Touro amphibolite	a	-	-	40.00	39.59	34.00	-	30.00	34.42
	b	-	-	0.90	0.89	0.70	-	0.62	0.49
	c	-	-	0.312	0.400	0.590	-	1.047	0.674
	R^2	-	-	0.273	0.716	0.189	-	0.453	0.351
Noia gneiss	a	-	-	35	30.19	27.64	-	-	-
	b	-	-	50.00	32.00	22.04	-	-	-
	c	-	-	0.156	0.170	0.209	-	-	-
	R^2	-	-	0.507	0.330	0.719	-	-	-

The main advantage of the Zhao & Cai (2010a) model over others is its ability to fit observed data at a wide variety of confining stresses and over a large range of strains. Unlike the Alejano & Alonso (2005) model, that of Zhao & Cai (2010a) includes the interval between CD and peak strength, where unloading data show an increase in the dilation angle from 0° to a maximum value. The main disadvantage of this model is its complexity, with 3 parameters (a, b, c) required to define the evolution of the dilation angle with respect to strain. Each of these parameters can be further decomposed to account for their variability with respect to confinement, leading to a 9 parameter model (a_1, a_2, a_3, b_1, b_2, b_3, c_1, c_2, c_3). These nine parameters that define the full dilation angle model for each rock type have been calculated according to the method of Zhao & Cai (2010a) and are presented in Table 4.6. Note that given the lack of constraints on the "lower bound" dilation angle, given by a_1, the least-squares value of this parameter was found to be zero for the two limestones.

Table 4.6. Parameters defining full mobilized dilation angle model.

	a_1	a_2	a_3	b_1	b_2	b_3	c_1	c_2	c_3
Indiana limestone	0	39.6	8.7	26.5	450.6	1.08	0.551	0.011	1.01
Carrara marble	41.9	28.9	3.4	4.4	3.9	0.06	0.008	0.504	0.29
Toral de Los Vados limestone	0	36.6	29.6	97.2	225.2	0.99	8e-4	0.181	0.24
Touro amphibolite	22.8	21.9	10.2	1e-4	1.1	15.1	1e-4	0.214	0.57
Noia gneiss	24.8	19.3	3.1	11.4	72.3	3.18	0.082	0.054	0.48

In general, the complexity of this model is problematic, since there is often not enough data in the first few milistrains of deformation to properly constrain the whole model. The number of parameters combined with the complexity of each parameter's influence on the model makes it difficult to provide any physical meaning to the individual parameters.

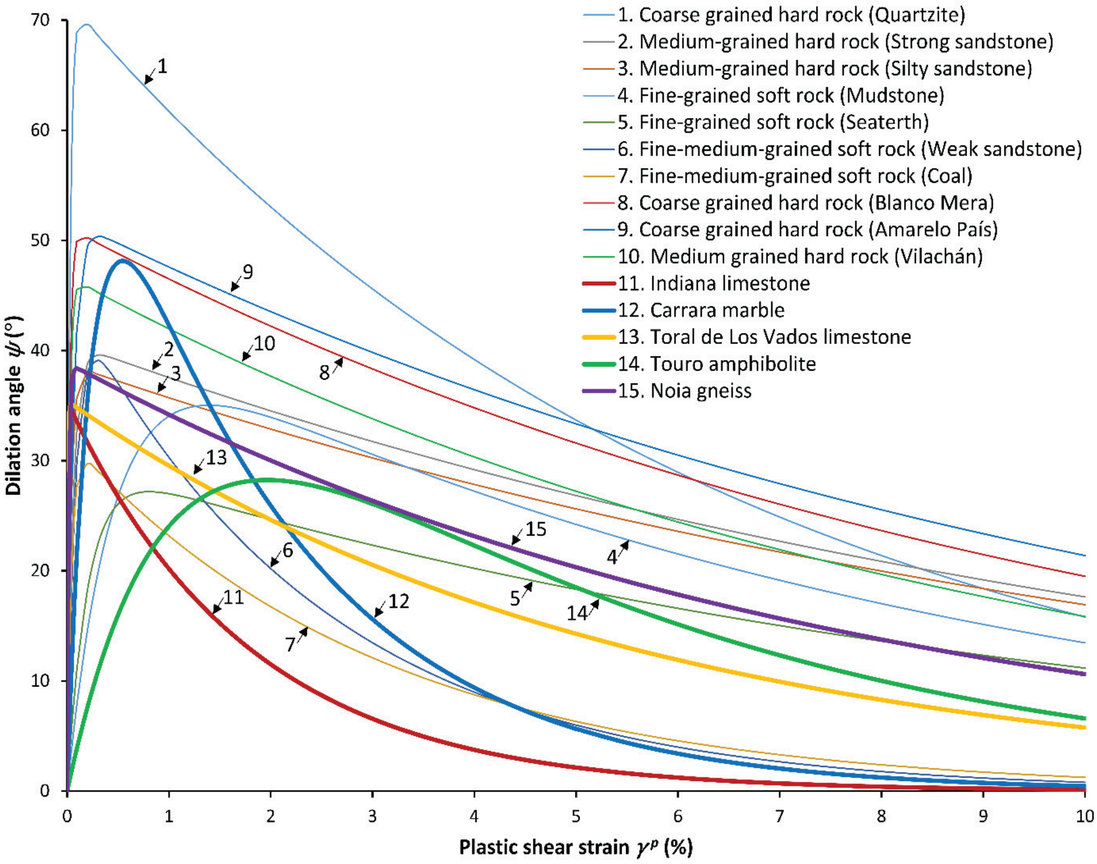

Fig. 4.8. Variations in the mobilized dilation angle for the five rocks studied (named 11, 12, 13, 14 and 15) and for other rocks types at a confining pressure of 1 MPa (after Arzúa & Alejano, 2013, with data from Zhao & Cai, 2010a).

4.5. Conclusions of this chapter

Uniaxial and triaxial compression tests were conducted with the goal of studying the constitutive behavior of five different rocks within a plasticity framework. A total of 112 unconfined and confined strength tests were conducted, with unloading-reloading cycles both used to ensure stability of the system during loading and also to help constrain the evolution of irrecoverable strains. All these tests were carried out in the *John P. Harrison Rock Mechanics' Laboratory* of the University of Vigo, but those corresponding to sedimentary rocks were performed by Gabriel Walton in association with his Ph.D. thesis.

The Carrara marble was found to be the most ductile of the five rocks tested, with shear failure modes being prominent even in uniaxial conditions. The Indiana limestone showed a brittle failure under unconfined conditions, whereas failure at even modest confinements tended to be controlled by more ductile shear. The Toral de Los Vados limestone and the Touro amphibolite showed a similar behavior, they showed a brittle failure under unconfined conditions failing by axial cracking and opening along previous weakness planes, and a more ductile failure when the confining pressure reached a medium value. Finally the Noia gneiss was found to be extremely brittle, needing a high confining pressure to begin to show some ductile failure trough shear planes.

The restrictions imposed by the equipment led to limit the confinement of the gneiss' triaxial tests. It could only be reached a confining pressure of 6 MPa because, at higher confinements, the combination of strength and brittleness of the gneiss caused a sudden increase in confining pressure after failure. This sudden increase in pressure locked the system if more than 20 MPa were reached.

Peak and residual strength envelopes were determined for each of the rocks. Finding that the residual friction angle of the Indiana limestone and the Carrara marble are higher than the friction angle at peak strength, while the Noia gneiss' friction angle only shows a slight decrease and the more foliated Touro amphibolite and the laminated Toral de Los Vados limestone present a significant reduction in the residual friction angle respect to the peak. The former rocks could fit a Cohesion-Weakening-Friction-Strengthening (CWFS) model, although this aspect is out of the scope of the present study, it could be an interesting matter for further research.

An investigation of the elastic parameters of the rocks found that all five examined types have statistically different Young's moduli under unconfined and confined conditions. The sample stiffness values were found to increase as a linear function of confinement for the homogenous Indiana limestone and Carrara marble, but the Toral de Los Vados limestone, Touro amphibolite and Noia gneiss displayed a significant (non-linear) increase in stiffness when changing from uniaxial to triaxial loading conditions.

Dilation angle values were calculated as a function of plastic strain, where sufficient post-yield data existed. These data were found to fit reasonably well with the model of Zhao & Cai (2010a) in most cases, although a lack of data constraints at small plastic strains led to not so reliable results in some cases.

These results extend the database of dilatancy on different types of rocks: coal, sandstone, siltstone as shown in Alejano & Alonso (2005); quartzite and weak and strong sandstones as recovered by Zhao & Cai (2010a); granites as presented in the previous chapter and now some carbonate and regional metamorphic rocks. This is a necessary background to further improve existing dilation models

5. Strength and dilation of jointed granite specimens in servo-controlled triaxial tests

5.1. Introduction

Hoek & Brown (1980a) stated, 35 years ago, that the strength and behavior of a rock mass were not only controlled by the intact rock itself but also by rock structure —which could be quantified starting from Bieniawski's Rock Mass Rating (RMR) (Bieniawski, 1976)— and scale. In the current experimental study, rocks that included an artificial rock structure were tested, including three joints belonging to two different sets, with results indicating an important and consistent decrease in strength. This decrease is clear experimental evidence of the role of structure in rock strength. Moreover, it opens the door for further testing to better understand the role of structure in rock mass behavior —including not only strength (typically included in most rock mechanics developments following updated techniques (Hoek & Brown, 1997; Marinos & Hoek, 2000; Hoek et al., 2002; Cai et al., 2004, 2007) but also post-failure behavior of rock masses and, particularly, post-failure volumetric behavior.

Dilation (also called dilatancy) controls the change in rock volume when this undergoes different stress states and strain levels. It has long been recognized as an important and pervasive property in rock and rock mass behavior (Hudson et al., 1971b; Jaeger et al. 2007) and this is particularly true for post-failure or post-peak behavior (Medhurst & Brown, 1998). Early researchers in rock mechanics found that this parameter was not easy to estimate, partly due to the difficulties in controlling the post-failure phase of strength tests. To properly understand how a particular rock dilates, multiple volumetric strain-controlled compression tests at varying confining stress levels are needed and these tests should preferably include a number of unloading-reloading cycles in order to identify the elastic and plastic components of the strains.

Detournay (1986) suggested that dilation largely depends on the plastic or irreversible deformation suffered by the material. Alejano & Alonso (2005) proposed a confinement stress and plasticity dependent dilatancy behavior model which fits quite well to triaxial test results on samples of sedimentary rocks. This model also has the important advantage that it depends on a single parameter and also that it can be extended to rock masses without difficulty, even if results cannot be easily compared to actual data.

However, Zhao & Cai (2010a) and Arzúa & Alejano (2013) clearly showed that this model (Alejano & Alonso, 2005) is not suitable for tests on igneous and metamorphic rocks. Zhao & Cai (2010a) fitted a model to generic dilatancy outputs which adapted to a broad database of results quite well, covering sedimentary, metamorphic and igneous rocks, but requiring nine parameters of minor physical significance. This model was used by Arzúa & Alejano (2013) to fit dilatancy results in a good number of triaxial tests on three kinds of intact granite specimens.

Understanding the applicability to rock masses of dilatancy models like that of Zhao & Cai (2010a) is a necessary next step in this field of research. Alejano & Alonso (2005) suggested that peak dilation for the unconfined case can be identified using the peak friction angle and that this also applies for rock masses. Zhao & Cai (2010b) also extended their model to rock masses based on the same assumption, presenting an application to deformation modelling that shows that their model is an improvement over conventional (constant dilatancy) approaches. Zhao et al. (2010) further applied this model to the case of typically brittle rock masses showing Cohesion-Weakening-Friction-Strengthening yield processes. Other authors have shown that relevant conclusions can be derived from non-standard dilation models used for underground excavation modelling (Alejano et al., 2012b; Walton & Diederichs, 2012).

Within this general framework, the author considered that, in order to foster research into rock mass behavior, it could be useful to perform complete stress-strain tests on rock specimens with a number of equally oriented and equally spaced artificial discontinuities (joints). The main aim of this research, therefore, was to assess the differences between the behavior of the rock mass

A version of this chapter has been published with the following citation: Arzúa, J., Alejano, L.R., Walton, G. 2014. *Strength and dilation of jointed granite specimens in servo-controlled triaxial tests*. International Journal of Rock Mechanics and Mining Sciences. 69:93-104.

analogues and the corresponding intact specimens. Previous trials to study the behavior of fissured rock specimens (Kulatilake et al., 1997, 2001) used materials built from plaster of Paris and silica sand and, moreover, only investigated unconfined behavior.

In the following sections, first, the equipment and techniques required to prepare the samples and perform the triaxial tests in such a way that the complete stress-strain curves could be obtained up to a sufficiently large level of strain are explained. Common geomechanical parameters were obtained for each test —including apparent elastic modulus and Poisson's ratio, drop modulus and peak and residual strength envelopes— and are compared to those derived from intact rock specimens. Finally, following previously explained techniques (Chapters 3 and 4), the evolution of the dilation angle was determined over the course of each test. Once it became clear that the Alejano & Alonso (2005) model did not adequately fit the results, the Zhao & Cai (2010a) dilation model was applied to obtain the corresponding dilation parameters; again, a comparison was made to the results obtained for intact specimens.

5.2. Test setup

5.2.1. Testing equipment

As described in the previous chapters and published elsewhere (Arzúa & Alejano, 2013), the *John P. Harrison Rock Mechanics' Laboratory* has a fully servo-controlled press capable of performing compression tests with unloading-reloading cycles and of measuring the amount of displaced hydraulic fluid needed to maintain confining pressure at its nominal value. For the sake of brevity and bearing in mind that the used equipment has been explained in detail in a previous chapter, the description below is greatly abridged.

Axial strain is measured by means of a pair of linear variable differential transformers attached to the lower platen of the press using industrial magnets. Volumetric strain is determined based on the volume of hydraulic fluid displaced during triaxial compression tests. Using axial and volumetric strain parameters it is possible to accurately compute radial strain. The complete stress-strain curves obtained, of paramount importance in rock mechanics (Hudson et al., 1971b), are the basis for the characterization of rock behavior.

5.2.2. Rock testing

For this study, a granitic rock locally known as Blanco Mera was tested. This rock has been characterized in terms of its geological and chemical nature using an optical microscope to study thin sections of the rock (Chapter 3). The results of tests on intact specimens of this rock, presented in Chapter 3 were added to the results obtained in newly performed tests and compared in this research to the results obtained for the jointed specimens.

5.2.3. Jointed specimen preparation

Jointed specimens were prepared in order to simulate rock mass behavior at the laboratory scale. All cores tested contained the same three joints belonging to two joint sets —one sub-vertical joint and two sub-horizontal joints. This task was not trivial and several trials had to be performed in order to obtain jointed specimens of a reasonable quality. The final procedure used is described in what follows.

To obtain the desired samples, a cubic sample of the rock with a 30-cm edge was cut (Fig. 5.1.a) in order to create the sub-vertical joint set. Then, the pieces were reassembled (Fig. 5.1.b) and the 54-mm diameter cores (NX size) were drilled. In this way a potential reduction in the core diameter was avoided (see Fig. 5.2). Once these sub-vertically jointed specimens were obtained (Fig. 5.1.c), adhesive tape was used to re-join the two pieces of the core (Fig. 5.1.d). Finally, the sub-horizontal joints (two sub-horizontal joints per specimen) and also the ends of each specimen were cut (Fig. 5.1.e and Fig. 5.1.f). The frictional behavior of the cut surfaces is discussed elsewhere (Alejano et al., 2012c). Thus, 22 artificially jointed test cores composed of six parts were obtained (Fig. 5.1.g). The cut surfaces of the jointed specimens were planar and smooth with a very slightly rough surface due to sawing.

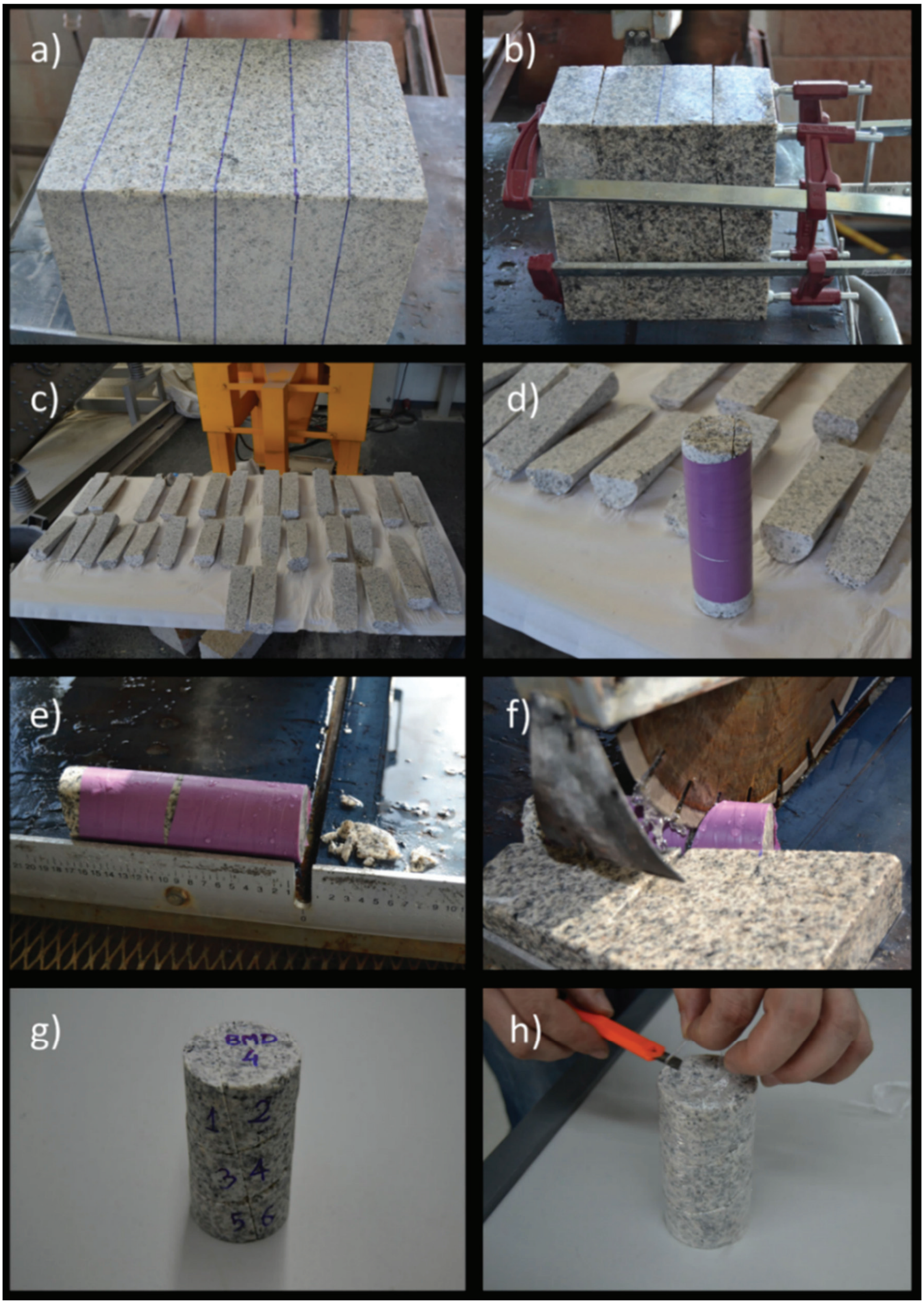

Fig. 5.1. a) Cubic Blanco Mera granite sample with a 30-cm edge, prepared for cutting to obtain the sub-vertical joint set. b) Reassembled cut rock ready to extract cores with a sub-vertical joint. c) Cores with a sub-vertical joint. d) Re-joined core prepared for cutting to obtain the sub-horizontal joint set and the final specimen length. e) and f) The cutting process for sub-horizontal joints and specimen ends. g) An artificially jointed specimen. h) Final preparation of the plastic-wrapped jointed specimens.

The mean dips of the joint sets were measured as 23.5 ± 0.8° for the sub-horizontal joints, and 85 ± 2° for the sub-vertical joints. Even though they were carefully cut, the relative orientation between both joint sets showed a slight variation, although this did not seem to affect the final results. Another slight problem noted when starting the compression tests was the fact that the jointed specimens had to be re-joined in a specific manner and kept immobile while being placed in the Hoek's cell and as the test was prepared. Transparent plastic food wrap was used, which was sufficiently strong to hold the test core pieces together without interfering significantly with the deformational behavior of the jointed specimen. Once the jointed test core was wrapped in plastic, the plastic borders were removed and the jointed specimens were ready to be tested (Fig. 5.1.h).

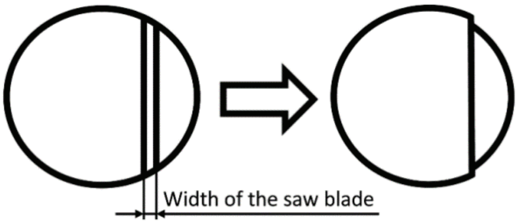

Fig. 5.2. Problem encountered if the sub-vertical joint set is cut after, rather than before, obtaining the core.

5.3. Testing

In addition to the tests performed on the intact cores (shown in Chapter 3), another 28 confined compression tests with intact cores and 22 confined compression tests with jointed cores were performed. These 50 newly performed tests had confining pressures in the range 0.2-12 MPa. It was not physically possible to carry out properly unconfined tests on the jointed specimens.

As previously mentioned, radial strain is calculated using axial and volumetric strain by means of Eq. (5.1).

$$\varepsilon_v = \varepsilon_1 + 2\cdot\varepsilon_3 \Rightarrow \varepsilon_3 = \frac{\varepsilon_v - \varepsilon_1}{2} \qquad (5.1)$$

A typical graphical result for a confined strength test is shown in Fig. 5.3, which also depicts how to obtain the most significant geotechnical parameters: peak strength, σ_1^{peak}; residual strength, σ_1^{res}; apparent elastic Young's modulus, *E*; apparent Poisson's ratio, *ν;* and drop modulus, *M*.

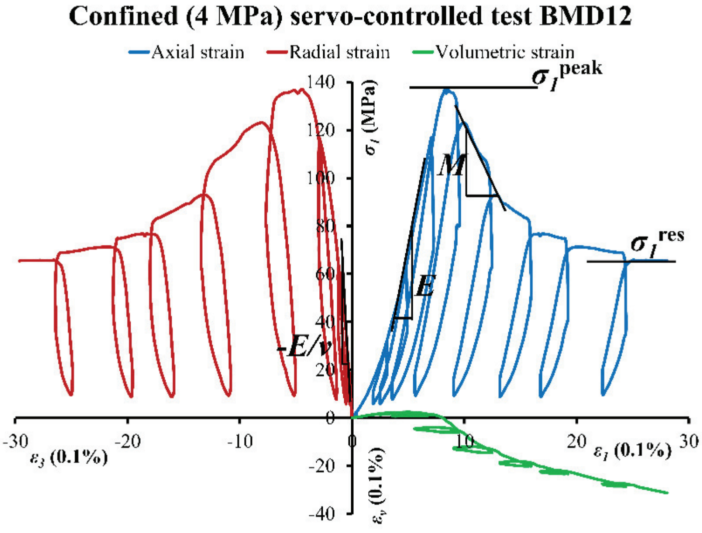

Fig. 5.3. Stress-strain graph for confined (σ_3 = 4 MPa) compression test on a Blanco Mera granite jointed test core. Shown also is how to obtain the values for peak and residual strength, σ_1^{peak} and σ_1^{res}; apparent elastic Young's modulus, E; apparent Poisson's ratio, ν; and the drop modulus, M.

Pictures of all the specimens were taken before and after testing (Fig. 5.1 and Fig. 5.4). It should be noted that failure in the jointed specimens most commonly appeared in the form of shear bands (Fig. 5.4.b, Fig. 5.4.c and Fig. 5.4.e), not always associated with the pre-existing sub-vertical joint. The fracturing and straining associated with failure tended to be concentrated in the intermediate layer of rock located between the sub-horizontal joints (Fig. 5.4.d).

The sub-horizontal joints showed evidence of frictional sliding in the form of rock flour, with the amount of rock flour increasing with confining stress. For the BMD19 jointed test specimen (σ_3 = 10 MPa), Fig. 5.4.b shows pieces #3 and #4 presenting a marked shear band and evidence of rock flour.

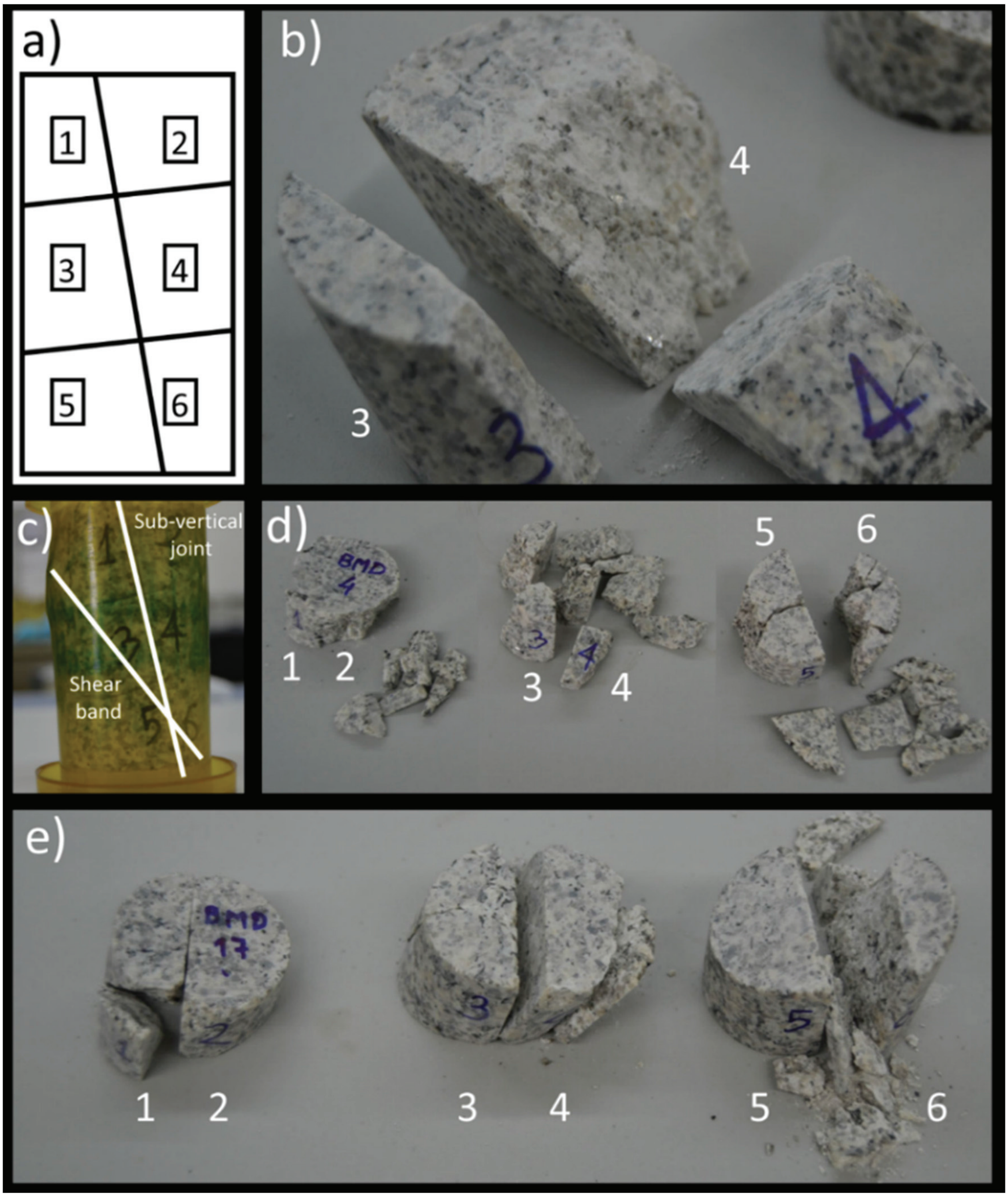

Fig. 5.4. Test specimens after compression testing. a) Sketch of the jointed core pieces. b) Shearing through pieces #3 and #4 and evidence of the rock flour that usually appears in sub-horizontal joints. c) Test core inside a sheath, showing the shear bands despite low confining pressures. d) After sheath removal, pieces bounded by the sub-horizontal joints (#3 and #4) crushed in multiple pieces, with the other pieces (#1, #2, #5 and #6) almost intact or showing signs of failure through shear bands. e) Shear band crossing pieces #4 and #6.

5.3.1. Intact test cores

A total of 28 triaxial tests with intact cores were performed applying rock mechanics suggested methods (ISRM, 2007). Results for these intact specimens are presented in Table 5.1 and in Appendix B.

5.3.2. Jointed test cores

Triaxial testing was set up for confining stresses in the range 0.5 MPa to 12 MPa. Basic geotechnical parameter results for these artificially jointed specimens are reproduced in Table 5.2 and in Appendix B. It can be observed that there was greater variability in outputs (peak and residual strength, elastic parameters and drop modulus) for jointed than for intact specimens, attributable to the presence of joints complicating the post-yield strain bifurcation process. However, typical behavior patterns, namely, increasing peak and residual strength as well as elastic moduli with confinement, can still be observed.

Table 5.1. Results of testing on intact cores.

Specimen	σ_3	σ_1^{peak}	σ_1^{res}	E	ν	M
	MPa	MPa	MPa	GPa	-	GPa
BM1	0.2	132.44	-	38.80	0.14	-9.02
BM2	0.2	107.69	-	25.88	0.29	-15.24
BM3	0.2	134.51	-	39.18	0.20	-20.18
BM4	0.2	136.37	-	38.74	0.24	-13.71
BM5	0.2	132.07	14	37.74	0.14	-21.83
BM6	0.2	137.56	-	39.55	0.16	-10.20
BM7	0.2	131.83	13	38.18	0.08	-8.36
BM8	0.2	126.45	9	33.89	0.11	-21.56
BM9	0.2	143.21	11	37.48	0.17	-
BM10	0.2	91.53	12	22.46	0.23	-14.28
BM11	4	148.20	60	25.75	0.20	-12.17
BM12	0.2	93.05	10	27.52	0.20	-17.30
BM13	2	154.62	28	37.76	0.18	-23.94
BM14	2	164.39	25	38.42	0.18	-17.93
BM15	2	152.73	-	37.96	0.20	-19.59
BM16	2	155.38	32	37.69	0.20	-31.04
BM17	4	178.45	50	42.45	0.17	-24.86
BM18	4	176.58	53	40.50	0.19	-11.39
BM19	4	185.87	45	43.24	0.21	-17.26
BM20	6	214.27	60	45.23	0.17	-31.24
BM21	6	227.03	55	44.98	0.19	-19.17
BM22	6	220.59	67	43.32	0.18	-16.92
BM23	10	254.57	80	43.95	0.14	-21.74
BM24	10	246.52	65	44.76	0.13	-22.15
BM25	12	291.85	95	46.92	0.12	-26.65
BM26	12	268.67	76	46.06	0.16	-24.67
BM27	12	292.11	120	48.84	0.16	-19.57
BM28	12	289.11	90	48.54	0.14	-

Table 5.2. Results of testing on jointed cores.

Specimen	σ_3 MPa	σ_1^{peak} MPa	σ_1^{res} MPa	E GPa	ν -	M GPa
BMD1	6	144.87	76	20.45	0.23	-19.67
BMD2	2	66.34	35	14.3	0.39	-8.64
BMD3	0.5	44.24	20	9.46	0.18	-2.13
BMD4	0.5	60.17	20	7.62	0.12	-18.27
BMD5	0.5	50.20	20	8.93	0.08	-5.92
BMD6	1	69.34	25	9.95	0.15	-
BMD7	1	62.90	20	12.25	0.27	-7.64
BMD8	1	79.94	20	14.16	0.24	-14.05
BMD9	2	94.66	33	16.03	0.14	-8.17
BMD10	2	96.09	40	14.21	0.26	-6.33
BMD11	4	108.12	60	14.23	0.13	-6.22
BMD12	4	137.08	65	22.61	0.22	-10.92
BMD13	4	129.13	33	17.85	0.11	-14.60
BMD14	6	129.63	68	17.93	0.10	-9.32
BMD15	6	156.33	73	23.45	0.09	-57.37
BMD16	10	193.13	105	27.07	0.12	-40.55
BMD17	10	165.14	120	16.49	0.11	-19.16
BMD18	10	216.38	100	27.84	0.18	-25.05
BMD19	10	177.76	80	24.01	0.11	-8.99
BMD20	12	210.30	130	24.59	0.15	-26.69
BMD21	12	175.51	110	14.84	0.13	-
BMD22	12	213.35	115	26.94	0.09	-

5.4. Results interpretation

Although the data collected during tests are significant in themselves, much can be learned from a comparison of the intact and jointed core test results, as clearly illustrated by Fig. 5.5. One interesting feature of these data is that, in all cases, the stress-strain response of the jointed cores began to approximate that for the intact cores for large strains; this was true for both the lateral and axial strain curves. It should be noted that the point at which the two curves began to match appeared to move closer to the curve peak as the confining stress increased.

Jointed cores compared to intact cores presented a smaller Young's modulus. This makes sense, given the expected lesser stiffness of the joints as compared to the intact rock matrix. It is also consistent with the general trend noted on comparing intact rock and rock mass stiffness (Hoek & Diederichs, 2006). The jointed core stiffness increased very quickly as a function of confining stress; additionally, the difference between the observed stiffness of the jointed and intact core decreased with increasing confinement. This trend is consistent with observations regarding brittle-ductile transition (Wawersik & Fairhurst, 1970; Farmer, 1983).

Peak strength reduced from the intact cores to the jointed cores, as was to be expected, and the difference became smaller as confining pressure grew. For σ_3 = 2 MPa, peak strength for the jointed cores was approximately 50% of that for the intact cores; meanwhile, for σ_3 = 12 MPa, peak strength in jointed cores increased to approximately 70% of the values for intact cores.

Residual strength was basically the same for both jointed and intact specimens and for all the tests; the differences observed in some cases were similar to those expected due to the natural heterogeneity of the rock. It appears that all these observed trends are consistent with a brittle-ductile transition at a high confinement stress level, at which the rock or rock mass would behave in an elastic-perfectly-plastic or ductile manner, although this transition would be influenced by many other factors which are beyond the scope of this study.

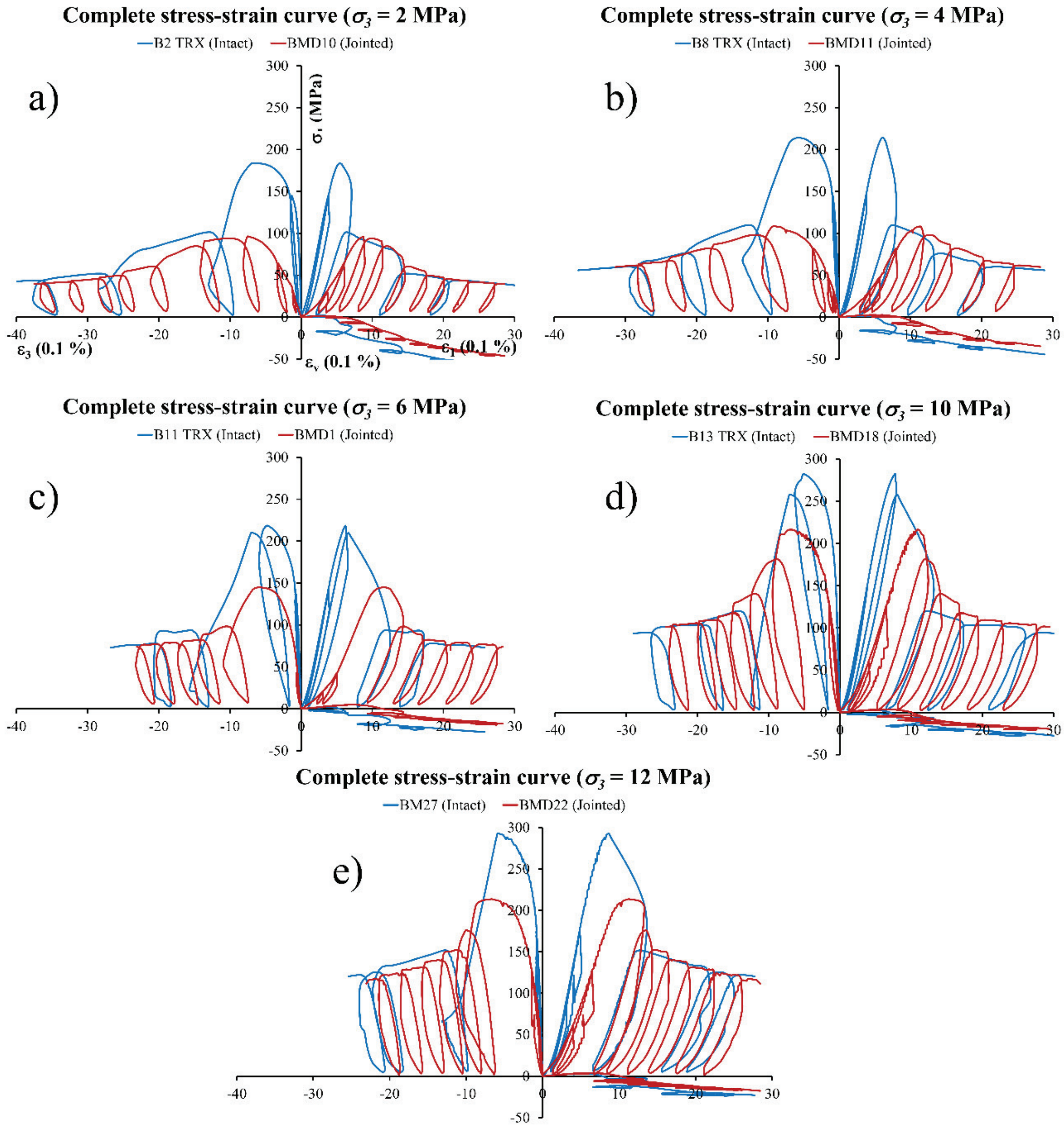

Fig. 5.5. Comparison of complete stress-strain curves between intact and jointed cores for different confining pressures. a) σ_3 = 2 MPa, b) σ_3 = 4 MPa, c) σ_3 = 6 MPa, d) σ_3 = 10 MPa, e) σ_3 = 12MPa.

Finally, it should be noted that the measured volumetric strains were smaller in jointed cores than in intact cores, which indicates a lower tendency for the jointed specimens to dilate. This can be explained by the existence of smooth (i.e. non-dilatant) fractures which may limit the need for new, dilatant extension cracks to form during the deformation process. Furthermore, volumetric strain curves for jointed cores seemed to have a similar curvature to the intact rock curves. Qualitatively, this would suggest that the dilation angle decay pattern was similar in both cases.

5.4.1. Classic parameters

The results obtained and presented in Table 5.1 and in Table 5.2 were analyzed for the main geomechanical features of the rock. Results obtained in this study with intact cores were added to the already existing data yielded by previous tests (Chapter 3). First, peak and residual Mohr-

Coulomb (M-C) and Hoek-Brown (H-B) failure criteria were fitted to the peak and residual strength values obtained as a result of testing. These fits, along with a comparison between jointed and intact cores, are shown in Fig. 5.6. Table 5.3 and Table 5.4 show the main rock geomechanical results for intact and jointed cores of Blanco Mera granite.

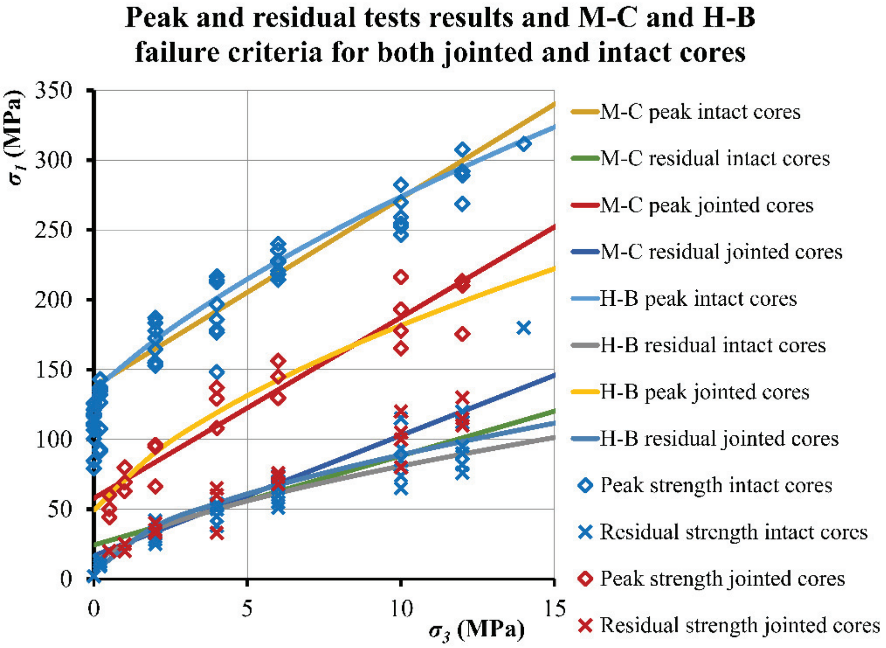

Fig. 5.6. Peak and residual strength test results and fits to Hoek-Brown (H-B) and Mohr-Coulomb (M-C) failure criteria for jointed and intact cores.

Fig. 5.7 shows the residual strength results in more detail. According to the typical levels of accuracy usually encountered in rock engineering, the residual strength can be said to be the same in the intact and jointed cores. Fig. 5.7 shows that the linear fit for all the cores has an intermediate coefficient of determination between the regular cores and the jointed cores, which indicates, statistically speaking, that all values belong to the same set.

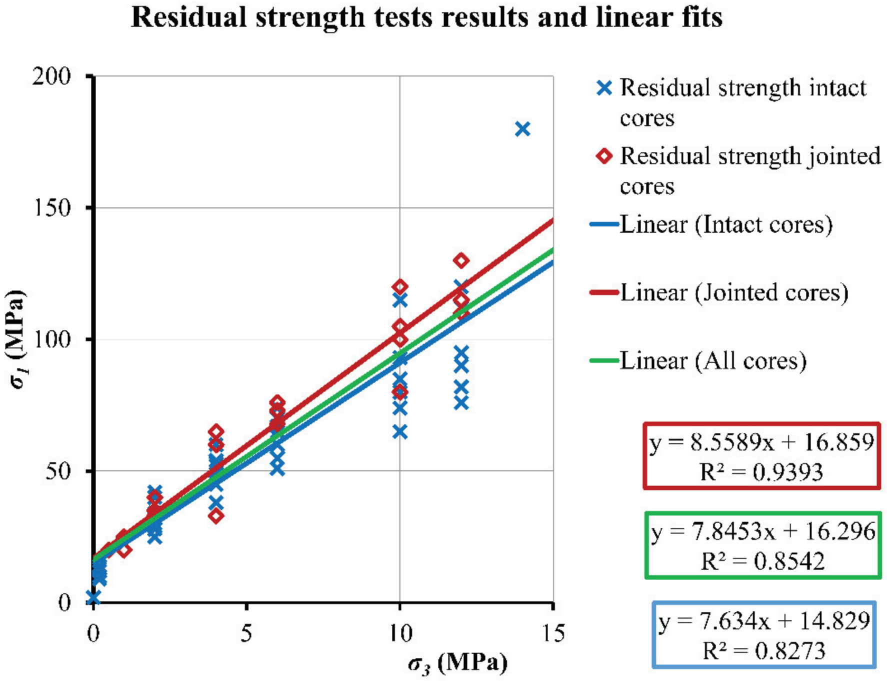

Fig. 5.7. Comparison between residual strengths fits.

With respect to peak strength, the M-C fits suggest a loss in cohesion strength from the intact to jointed cores, while the frictional component remained approximately equivalent. It should also be noted that the loss in strength from peak to residual was primarily due to a drop in the cohesive strength component.

Since the H-B failure criterion in laboratory testing is intended for intact rock, it is convenient to consider jointed test cores as small-scale rock masses. This involves finding an equivalent geological strength index (GSI) value that will estimate the generalized H-B failure criterion for the case of jointed specimens.

Table 5.3. Basic geomechanical results for intact cores of Blanco Mera granite.

	Intact core results	
	Hoek-Brown	Mohr-Coulomb
Peak strength	$\sigma_c^{peak} = 122.73$ MPa $m = 41.61$ $R^2 = 0.9914$	$\sigma_c^{peak} = 126.68$ MPa $\phi_{peak} = 60.37°$ $c_{peak} = 16.76$ MPa $R^2 = 0.9995$
Residual strength	$\sigma_c^{res} = 14.30$ MPa $m = 32.70$ $R^2 = 0.8284$	$\sigma_c^{res} = 16.74$ MPa $\phi_{res} = 48.54°$ $c_{res} = 3.17$ MPa $R^2 = 0.9979$
σ_t	$\sigma_{t,m} = 6.12$ MPa	
E	$E_{m,\sigma 3=0} = 27.95$ GPa	$E = 2.04 \cdot \ln(\sigma_3) + 38.15$
ν	$\nu = 0.17$	
M	$M_{m,\sigma 3 \neq 0} = -25.41$ GPa	

Table 5.4. Basic geomechanical results for jointed cores of Blanco Mera granite.

	Jointed core results	
	Hoek-Brown	Mohr-Coulomb
Peak strength	GSI = 81.5 $\sigma_c^{peak} = 49.37$ MPa* $m = 19.57$ $R^2 = 0.9186$	$\sigma_c^{peak} = 57.79$ MPa $\phi_{peak} = 58.95°$ $c_{peak} = 8.03$ MPa $R^2 = 0.9992$
Residual strength	GSI = 43.8 $\sigma_c^{res} = 5.38$ MPa* $m = 5.26$ $R^2 = 0.6056$	$\sigma_c^{res} = 16.65$ MPa $\phi_{res} = 52.36°$ $c_{res} = 2.84$ MPa $R^2 = 0.9997$
σ_t	$\sigma_{t,m}$ = N/A	
E	$E_{m,\sigma 3=0}$ = N/A	$E = 4.62 \cdot \ln(\sigma_3) + 11.95$
ν	$\nu = 0.16$	
M	$M_{m,\sigma 3 \neq 0} = -14.65$ GPa	

* Value of the fit for the jointed test specimens at $\sigma_3 = 0$, not the value of σ_{ci} as calculated by the generalized Hoek-Brown criterion as explained in the text.

Using the known intact properties and with a fixed disturbance factor ($D = 0$), the expected rock mass strength for many values of GSI (based on the relations defined by Hoek et al., 2002) were calculated. Comparing these expected values to the jointed core values, the GSI value that provided the best strength fit for each confining pressure was determined. For the peak-strength state, this GSI-equivalent value was found to be between 77.3 and 83.9, for a mean value of 81.5 and a standard deviation of 2.3. For the residual strength state, the GSI-equivalent value ranges between 33.5 and 52.5, for a mean value of 43.8 and a standard deviation of 6.3. Although a mean GSI-equivalent value was considered, a slight dependence on confinement can be observed, that was more significant in the residual state, as can be seen in Fig. 5.8.

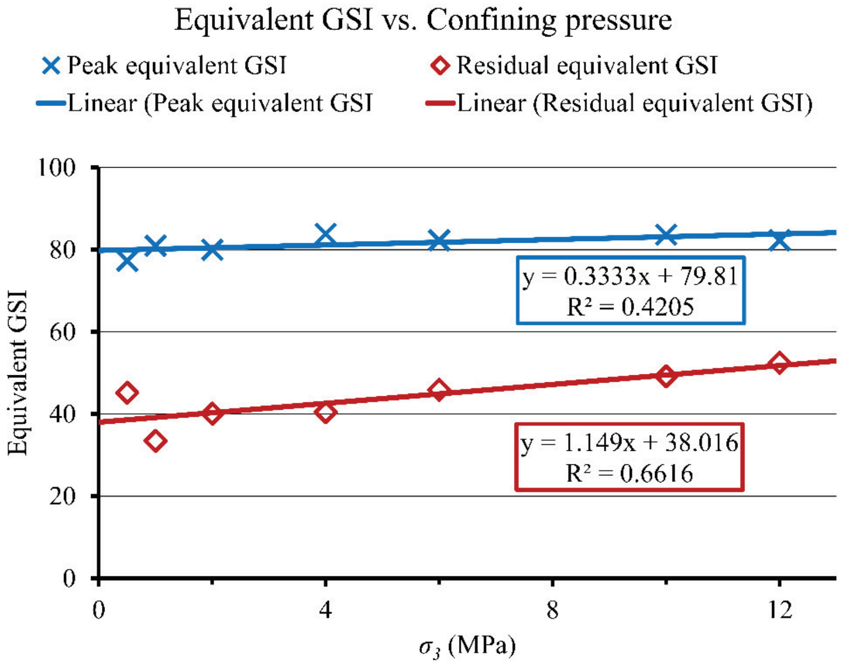

Fig. 5.8. Evolution of the GSI-equivalent value with confining pressure.

In view of the GSI classification scheme proposed by Marinos & Hoek (2000) and further developed by Cai et al. (2004), the structure of the jointed cores can be classified as "blocky" (given their scale relative to the size of the system) and that the surface condition can be considered to be fair-good (although the artificial joints did not directly match any of the descriptions given). Based on these classifications, the actual GSI value of the jointed cores should be in the 60-70 range. The fact that the actual GSI was less than the GSI required to fit the strength of the cores is consistent with practical experience which suggests that the GSI strength reduction method of Hoek et al. (2002) may underestimate rock mass strength. The increase in the calculated GSI as a function of confinement (and therefore also the difference between calculated and actual GSI values) is also consistent with ongoing work that finds that the equations of Hoek et al. (2002) become increasingly inaccurate at higher GSI values.

Knowing the appropriate GSI values, the generalized H-B failure criterion can be fit to the jointed core data. This failure criterion calculates a value for σ_{ci} which corresponds to the unconfined compressive strength of the intact rock, although, in this case, the value obtained for jointed cores ($\sigma_{ci,jointed}$ = 137.97 MPa) was slightly larger than that obtained for intact cores ($\sigma_{ci,intact}$ = 122.73 MPa). Even if $\sigma_{ci,\, jointed}$ was forced to coincide with $\sigma_{ci,\, intact}$, differences between m ($m_{peak,forced} = 22$, $m_{residual,\, forced} = 5.23$) and fits for peak and residual σ_c ($\sigma_{c,peak,\, forced}$ = 43.91 MPa, $\sigma_{c,residual,\, forced}$ = 5.41 MPa) were not significant due to the natural variability of the materials. The σ_c^{peak} and σ_c^{res} values shown in Table 5.4 correspond to those for the fits of the jointed specimens at null confining pressure.

When trying to fit the H-B criterion to the residual data, some of the fits were found to produce $\sigma_{ci}^2 < 0$. This could be fixed by excluding some tests from the analysis to obtain reasonable data. It was commented above that the residual strength was roughly the same for both the intact and jointed cores (see Fig. 5.5, Fig. 5.6 and Fig. 5.7). However, using the generalized H-B criterion to account for GSI correction, the approach produced a value of σ_c^{res} lower than expected (see Table 5.4). Moreover, the resulting coefficient of determination was quite poor (0.6056). However, the M-C criterion calculated a more reasonable value for this parameter (as it is more or less the same as for intact cores), with a very high coefficient of determination (0.9997). This can be attributed to the fact that residual strength results tend to align and therefore can be better represented by means of the M-C approach, as can be seen in Fig. 5.9.

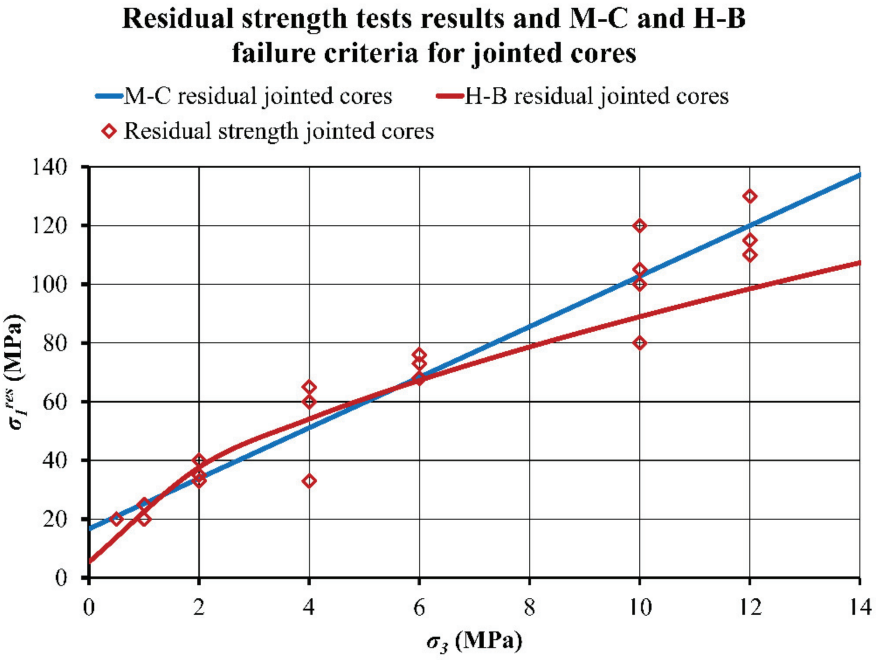

Fig. 5.9. Residual strength test results and H-B and M-C failure criterion fits for jointed cores. It can be seen that the M-C fit was better than the H-B fit due to the linearity of the test results.

In the previous study on intact cores (Chapter 3), the apparent Young's modulus, *E*, was fitted with a linear function according to confining stresses. As can be seen in Fig. 5.10, intact cores appeared to be fit well by a linear function, and the only points which deviated from this trend were those corresponding to σ_3 = 0 MPa (and now σ_3 = 0.2 MPa). After performing these tests in jointed test cores, it became evident that a better fit for Young's modulus was a logarithmic function depending on confining stress (see Fig. 5.10); these are the fits that appear in Table 5.3 and in Table 5.4.

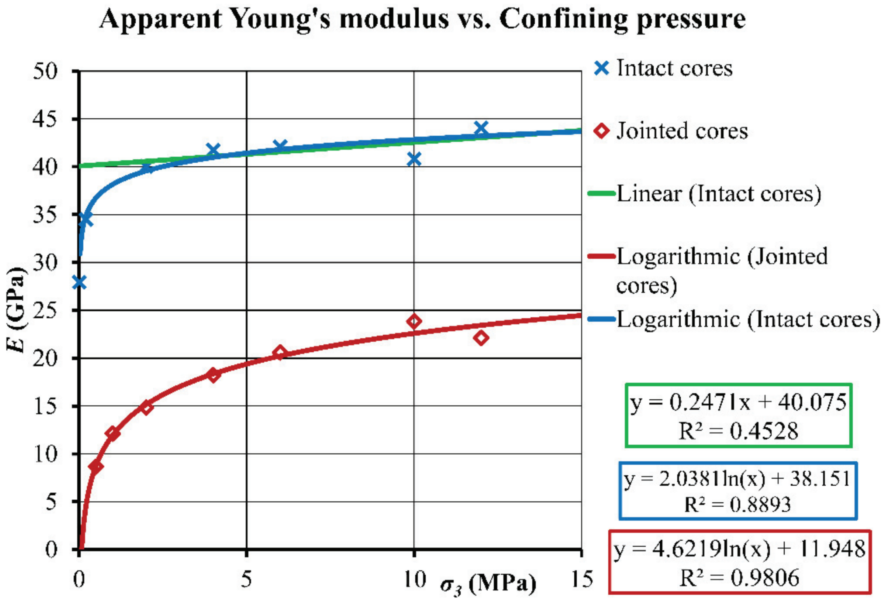

Fig. 5.10. Apparent elastic Young's modulus versus confining pressure.

It should be noted that a logarithmic function cannot be valid for unconfined conditions because as σ_3 = 0 MPa is approached, the apparent Young's modulus, *E*, would tend to minus infinity. Therefore, it is necessary to truncate it at a value near to σ_3 = 0 MPa. In the case of the intact cores and for this granitic rock, the logarithmic expression could be truncated at σ_3 = 0.1 MPa and a separate value of *E* for σ_3 = 0 MPa (i.e. the mean of the values obtained in unconfined tests, $E_{m,\sigma 3=0}$ = 27.95 GPa) could be recorded. In the case of the jointed cores, the value of E for $\sigma_3 = 0$ MPa could be considered equal to or near to zero, since the jointed specimens could not sustain much load without significant joint slip occurring. This is why no elastic modulus value is reported for unconfined conditions in Table 5.4. The same logic can be applied to account for the lack of recorded tensile strength for the jointed cores.

The apparent Poisson's ratio was also graphed versus confining pressure and compared for the intact and jointed cores. This parameter was approximately constant with respect to confining stress, although there was a fair degree of variability, particularly at lower confining stresses (Fig. 5.11).

The drop modulus, M, was computed as the mean negative slope of the axial stress-axial strain curve after peak strength and in the first 50% of softening in terms of strength difference. It should be noted that, since the softening portion of the stress-strain curve was non-linear, the drop modulus was not actually a constant, so the results should only be taken as reasonably representative estimates. Average values for this parameter are shown in Table 5.3 and in Table 5.4.

Fig. 5.12 shows estimated values for the drop modulus graphed against σ_3. At these relatively low confining pressure values and for such brittle materials, a slightly decreasing trend could be observed as confining pressure grew, as reported in classic studies by Von Kármán (1911). The drop modulus results for the unconfined strength tests are excluded due to the brittleness of the granitic rock used and the corresponding likelihood of significant system influences on the softening process. Bearing this in mind, it is still clear that the drop modulus for the jointed cores was less extreme than that for the intact cores —as would be expected, since jointed cores present less brittle behavior.

As mentioned previously, the stress-strain curves for the jointed cores approximated those of the intact cores following the attainment of some specific strain; as such, one can consider the jointed cores to be "pre-softened". In other words, it is as if the jointed cores had already undergone the deformations corresponding to the earlier, steeper part of the softening portion of the curve.

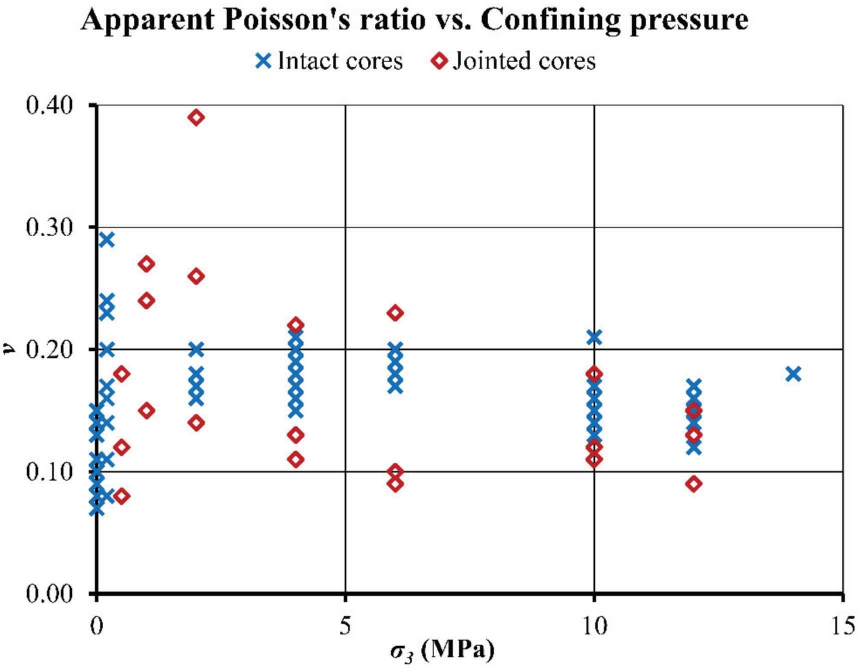

Fig. 5.11. Apparent Poisson's ratio versus confining pressure.

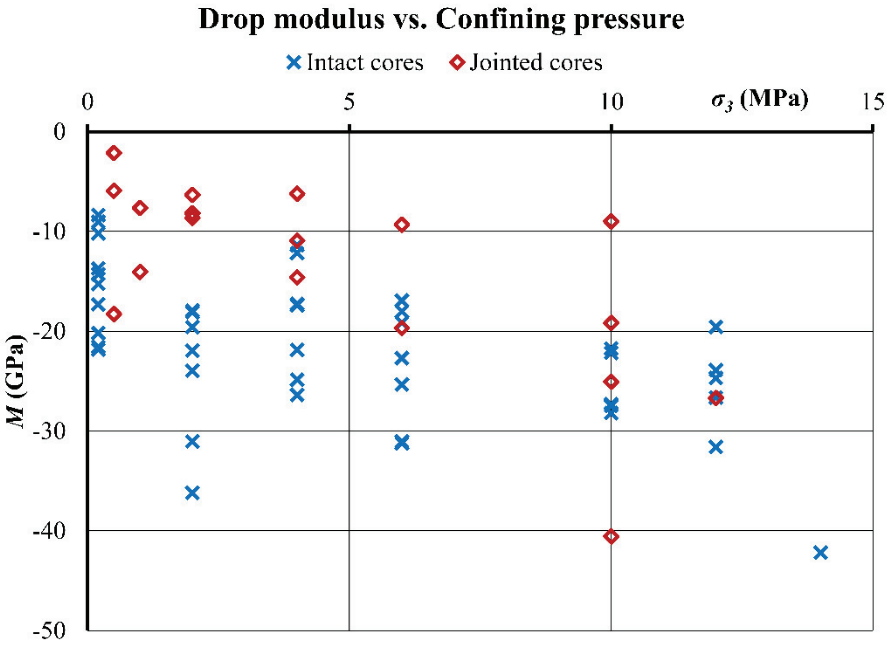

Fig. 5.12. Drop modulus versus confining pressure for the intact and jointed cores.

5.4.2. Dilatancy

The confining pressure equipment incorporated in the servo-control press available at the *John P. Harrison Rock Mechanics' Laboratory* allowed to obtain the complete stress-strain curve for standard rock specimens in triaxial tests (Chapter 3). It is useful to have these data for both intact and jointed specimens, so as to be able to compare the dilatancy of these two different laboratory-scale rock mass analogues.

Dilatancy is defined as a volume change resulting from the shear distortion of an element in a material. The dilation angle, ψ, is an appropriate parameter for describing the behavior of a dilatant material, as it represents the ratio of plastic volume change to plastic shear strain under plane-strain conditions.

Increasingly, excavation design has come to rely on numerical studies. Due to the difficulties in estimating material parameters and in properly extrapolating lab data to rock masses, designs are often based on simple behavior models, such as elastic-perfectly-plastic models. More complex behavior models, like strain-softening models, are used far less frequently and the role of dilatancy is often ignored, even if some modelers have recently invested efforts to account for dilation phenomena (Zhao et al., 2010; Alejano et al., 2012b; Walton & Diederichs, 2012; Levkovitch et al., 2010).

The main aim of this research was to extend the study of dilatancy to jointed rocks and rock masses and to further enlarge the post-failure database available in the literature, given that information on jointed rocks is lacking.

5.4.2.1. Estimating confining stress and plastic parameter dependent dilation angles

The dilation angle was computed, as shown in previous chapters, based on the equation proposed by Vermeer & De Borst (1984):

$$\psi = \arcsin \frac{\dot{\varepsilon}_v^p}{-2\dot{\varepsilon}_1^p + \dot{\varepsilon}_v^p} \tag{5.2}$$

Note that the denominator fraction represents, in absolute terms, the recommended plastic parameter (Alonso et al., 2003), defined starting from internal variables in plane-strain conditions, as follows:

$$\gamma^p = \varepsilon_1^p - \varepsilon_3^p \tag{5.3}$$

This formulation requires decomposition of the total strain into their elastic and plastic components:

$$\varepsilon_i = \varepsilon_i^e + \varepsilon_i^p \tag{5.4}$$

This can be done graphically as shown in Chapter 3 (Fig. 3.12), particularly with the help of unloading-reloading cycles, which allow differentiation between the reversible (elastic) and irreversible (plastic) components. Even so, analysis of dilation angles from a standard triaxial compression test is still difficult, due to the inelastic behavior of the stress-strain curve, variability in the elastic parameters and the occurrence of non-homogeneous deformation modes (bifurcation and subsequent axial splitting and shear banding).

It is still important to be aware of some of the issues raised in investigating complete stress-strain curves in rock masses (Hoek & Brown, 1980a; Bieniawski, 1976; Price & Farmer, 1979). Between the onset of stable fracture propagation —also named crack initiation (Diederichs, 1999; Carter et al., 2008)—, and unstable fracture propagation —also named crack damage— (Price & Farmer, 1979; Diederichs, 1999) or long-term uniaxial compressive strength— ε_3^p is a negative value whereas ε_1^p is null, so the dilation angle has limited physical meaning in this range. Adding to the difficulty in obtaining accurate dilation angle values (Alonso et al., 2003) are other inelastic and non-strictly plastic effects, such as crack closure in the initial stages of stress application (resulting in the initial concave form of the stress-strain curve) and rock damage over long-term peak stress.

Some authors have studied dilation in the pre-peak stage (Kwásniewski & Rodríguez-Oitabén, 2012), but the concept of dilatancy as defined above only makes sense in the post-failure stage, even if, at the peak strength level, the plastic parameter is in the order of some milistrains and inelastic volumetric strain attains values in the range 0.04% to over 0.1% (Scholz, 1968).

5.4.2.2. Dilatancy results

Using the approach described in Chapter 3, point clouds for the dilation angle value against the plastic parameter, γ^p, were produced for each confinement level. Jointed specimens dilation angles were plotted as shown in Fig. 5.13, revealing dilation angle dependencies like those described in Alejano & Alonso (2005): the dilation angle depends, first of all, on confining stress (i.e. as confinement grows, the dilation angle diminishes) and then on plastic shear strain (i.e. as plastic shear strain develops, the dilation angle decays).

Zhao & Cai (2010a) proposed an expression to fit laboratory data that relates dilation angle to plastic shear strain (γ^p, expressed in percentage deformation):

$$\psi = \frac{ab\left(e^{-b\gamma^p} - e^{-c\gamma^p}\right)}{c-b} \tag{5.5}$$

As previously observed (Zhao & Cai, 2010a; Arzúa & Alejano, 2013), although each parameter (*a, b* and *c*) in the Zhao & Cai (2010a) model affects the whole curve, each one mainly controls just one aspect. Thus, parameter *a* mainly controls peak dilation angle, parameter *b* mainly controls peak dilation angle location, and parameter *c* mainly controls rate of decay.

Zhao & Cai (2010a) accounted for confinement dependency by making these three parameters confining stress dependent using Eqs. (5.6), which introduce coefficients to define each parameter:

$$
\begin{aligned}
a &= a_1 + a_2 \cdot \mathrm{e}^{\frac{-\sigma_3}{a_3}} \\
b &= b_1 + b_2 \cdot e^{\frac{-\sigma_3}{b_3}} \\
c &= c_1 + c_2 \cdot \sigma_3^{c_3}
\end{aligned}
\tag{5.6}
$$

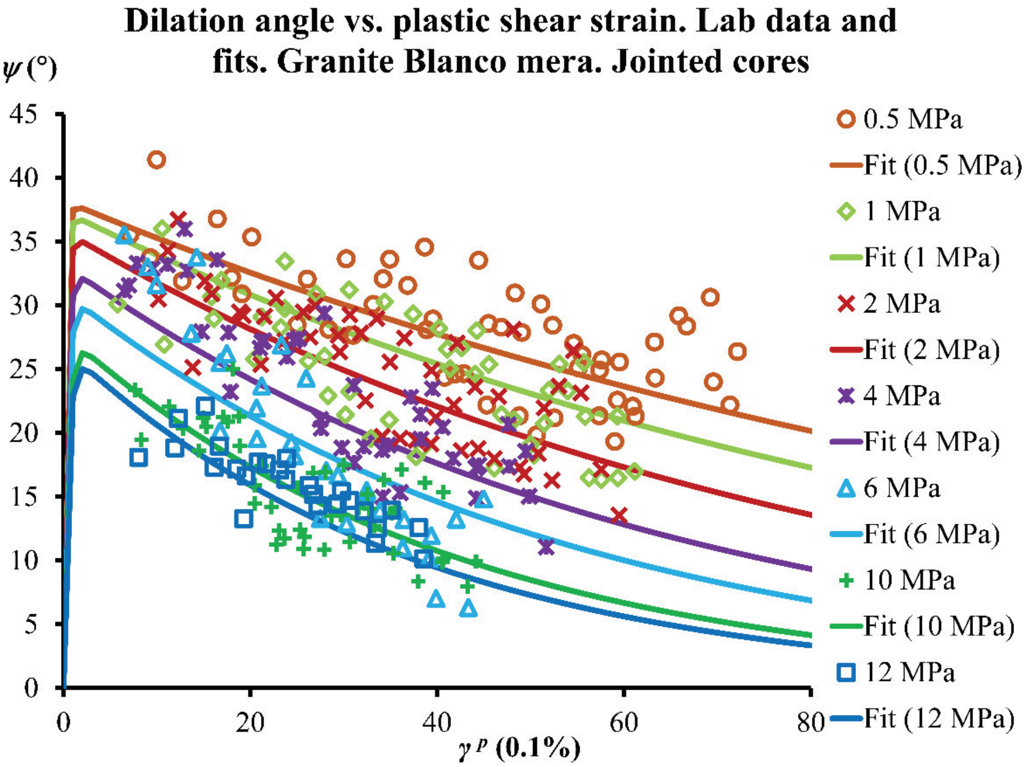

Fig. 5.13. Dilation angle versus plastic shear strain for various confining levels. Laboratory results and fits for each confining level for jointed cores.

Based on the previous comment regarding the similarity in dilation decay trends between intact and jointed cores, parameters b and c (i.e. b_1, b_2, b_3, c_1, c_2 and c_3) in the Zhao & Cai (2010a) model were set to be the same as those for the intact cores. In other words, only the component parameters for a (i.e. a_1, a_2 and a_3) were varied in an attempt to locate the best fitting model. This method of fitting to the data provided satisfactory models, as can be seen in Fig. 5.13 and in Fig. 5.15.

The individual component parameters used to define a, b and c for both jointed and intact specimens are presented in Table 5.5. It is interesting to note that, in the fit process to obtain the a parameter using Equations (5.6), a value of a_1 equal to that for the intact cores was estimated, whereas the a_2 coefficient decreased to about half and a_3 approximately doubled.

Table 5.5. Plastic shear-strain parameters and confining-pressure-dependent dilation angle model as proposed by Zhao & Cai (2010a) for both jointed and intact test cores.

*	a_1	a_2	a_3	b_1	b_2	b_3	c_1	c_2	c_3
1	21.13	17.92	9.85	20.63	29.44	2.97	0.047	0.049	0.589
2	21.13	36.71	4.92						

* 1, jointed test cores; 2, intact test cores

Fig. 5.14.a shows variations in the a parameter in line with confining pressure, the fit (Equations 5.6) obtained with the coefficients a_1, a_2 and a_3 for the jointed specimens and the previously obtained fits for the intact cores (Chapter 3). Fig. 5.14.b shows the peak dilation angle as a function of confining pressure (strongly linked with the a parameter); it also shows a slight dispersion of the *a* parameter for the jointed cores compared to the intact cores. This discrepancy may be due to the fact that *b* and *c* parameters have been fixed. With slight variations in the *c* parameter (which would not significantly affect the fit), a better fit for *a* could be obtained, but I do not believe that this improvement justifies the increased complexity that would be associated with such a decision. Similar to the dilation approach to rock masses by Zhao & Cai (2010b), re-estimating six coefficients that are basically the same as for the intact cores was avoided, even if some accuracy is lost.

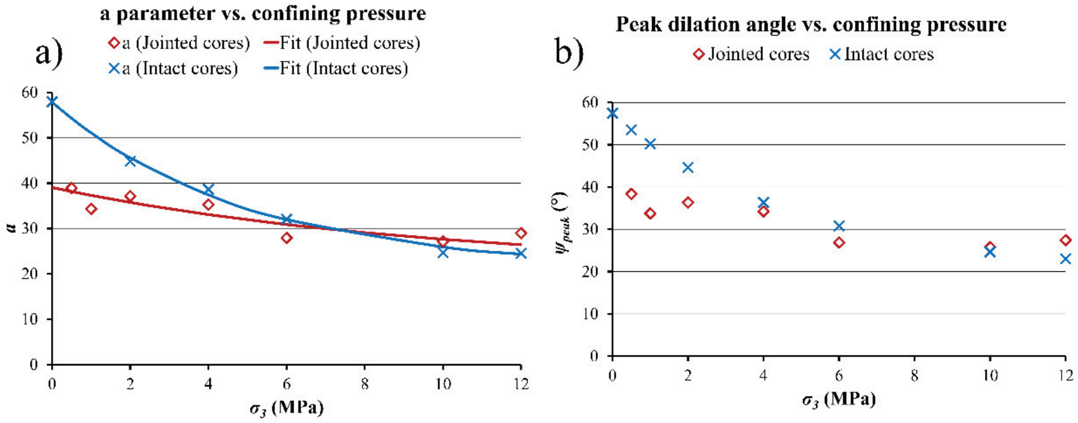

Fig. 5.14. Variations as follows: a) the fit for parameter a in accordance with Equations (5.6); and b) peak dilation angle for different confining pressures for jointed and intact cores. Note the strong relationship between this parameter a and peak dilation angle (almost equal).

Fig. 5.15 shows laboratory data and fit for each confining pressure, comparing jointed test cores with intact cores. Although there is no data for intact cores at confining pressures of 0.5 MPa and 1 MPa, the previously obtained fits (Chapter 3) were added for comparison purposes. A similar image for confining pressure of 0 MPa in jointed cores is not shown because, as previously mentioned, in the context of this testing campaign, jointed cores could not sustain any significant load in unconfined conditions. In this Fig. 5.15 it can also be clearly seen, as commented above, that with fixed values for the *b* and *c* parameters, the Zhao & Cai (2010a) model fitted all the data reasonably well.

It is also evident that the dilation angle was lower for jointed cores than for intact cores at low confining pressures (i.e. 0.5 MPa, 1 MPa, 2 MPa, and 4 MPa). For $\sigma_3 > 4$ MPa, however, the angles were almost equal. In most excavation settings, yield zones tend to occur near free faces and so have low confinement stress values, making this an important feature of the behavior to be noted.

Based on these observations it becomes apparent that as plastic shear strain grows, the dilation angle tends to be equal in jointed and intact cores, but when the difference in peak dilation angle is large (confining pressures are low), a very large amount of strain is required before the curves approach each other.

Summing up, in addition to the already known dilation angle dependencies on confining pressure and plastic shear strain, it is evident that dilatancy also depends on the level of jointing in the rock mass. In the future, this relationship could be quantified using GSI or some other joint or geotechnical quality index, but in a complex form that probably requires much more testing and further research.

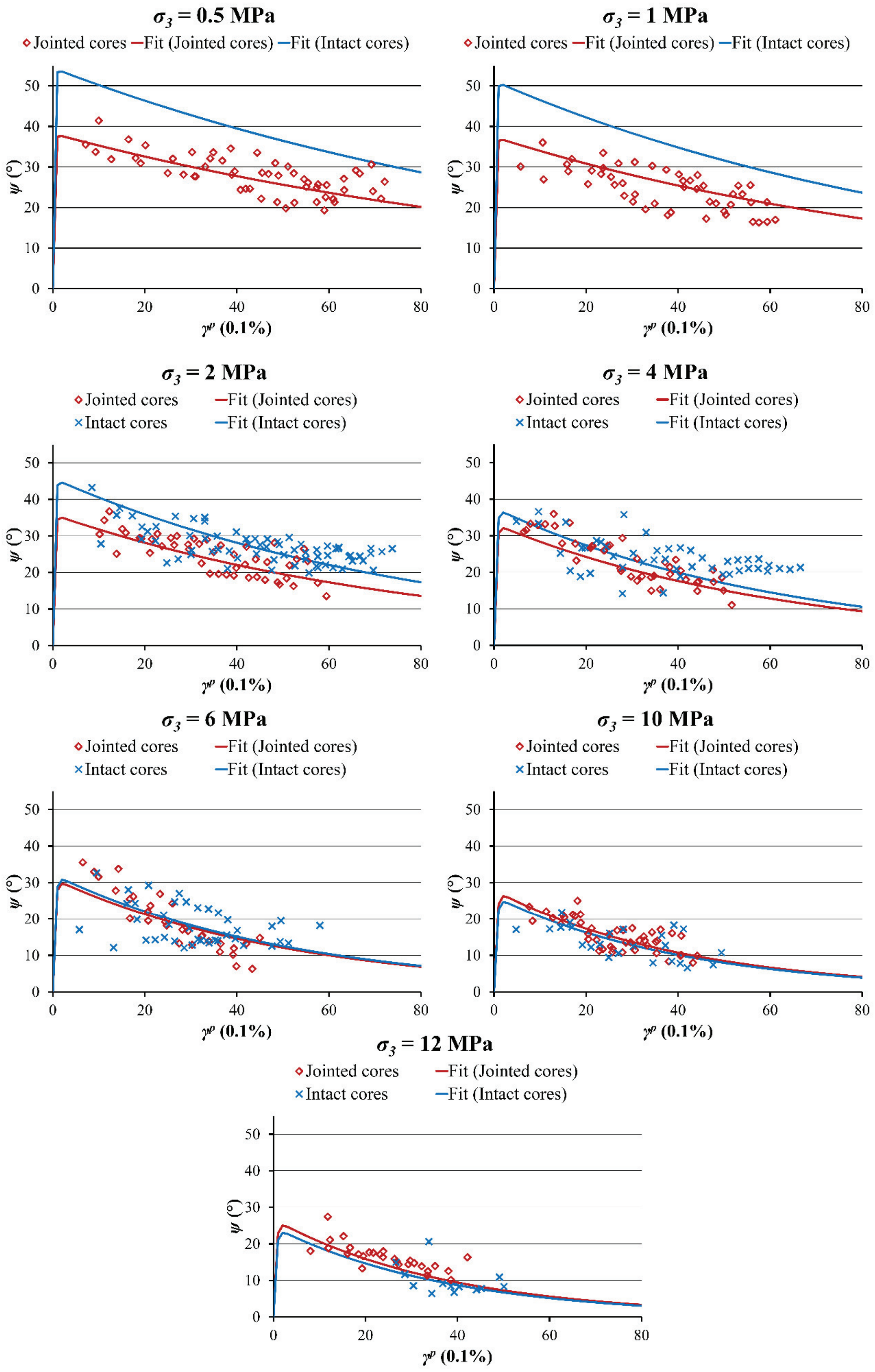

Fig. 5.15. Dilation angle versus plastic shear strain fits for various confining levels, with laboratory results for both jointed and intact cores.

5.5. Conclusions of this chapter

Within the general framework of a research project referring to the post-failure behavior of rocks and rock masses, an experimental programme was set up to first study post-failure stress-strain behavior in standard granite specimens, and to then extend the study to artificially jointed granite specimens. The triaxial strength tests were performed with unloading-reloading cycles and volumetric strain measurements. This allowed to locate the irrecoverable strain locus and to obtain reliable values for the dilation angle. In a previous study, 31 strength tests on Blanco Mera granitic rock were performed. In this study a further 28 confined strength tests on intact cores and 22 confined strength tests on artificially jointed specimens intended to simulate a small-scale rock mass were conducted. These artificially jointed specimens were obtained from the same original intact rock.

Peak and residual strength, apparent Young's modulus, apparent Poisson's ratio and approximate drop modulus were estimated for each test. Results were compared to those for the same kind of tests performed on intact rock specimens. While peak strength presented much lower values than for intact rock, residual strength envelopes for jointed and intact rock samples were more or less the same. Since jointed specimens are intended —as mentioned— to simulate a small-scale rock mass, a GSI-equivalent value was obtained to be able to fit the generalized H-B criterion to test results. This GSI-equivalent value could be used in future to check obtained results against real rock mass behavior and to analyze scale problems. Apparent elastic and drop moduli were less extreme in jointed rocks than in intact rocks.

It is also interesting to note that axial and radial strain curves (represented against stress) in jointed specimens, even if they started differently from those in standard specimens, tended to mimic these curves starting from a particular stress level in the descending branches of these curves. An interpretation of this observation in energy terms could be a topic for further research.

The evolution of the dilation angle was computed throughout the deformation process for each tested specimen. As previously observed in standard tests, this angle was shown to be dependent on both confining stress and plastic shear strain, and it appears that it is also dependent on the level of jointing in the specimen. This relationship could be related to the GSI or to some other joint or geotechnical quality index reflecting the structure of the rock. So future research will seek dilation models that have fewer parameters than the Zhao & Cai (2010a) model, while not sacrificing accuracy significantly.

At low confinement stress levels, the jointed rock specimens tended not to dilate as much as the intact rock specimens (as if volumetric strain were controlled by existing planar joints), but dilated in a similar way to intact rock specimens submitted to higher confinement stress. Although test results were fitted to the Zhao & Cai (2010a) model, obtaining very good results, further experimentation will be required in order to be able to propose a sufficiently reliable and more general rock mass dilation model. In particular, the impact of varying joint spacing, orientation and surface conditions need to be researched further. Future work will also encompass implementation of the derived approaches in numerical models.

6. Stress-strain behavior of granite specimens as a function of their structure

6.1. Introduction

The Hoek-Brown failure criterion is an empirical yield surface used to predict the failure of rocks and rock masses (Hoek & Brown, 1980a, Hoek & Brown, 1980b; Hoek et al., 2002). When applied to rock samples, its main difference with the also popular Mohr-Coulomb failure criterion is its non-linearity, which better reflects rock peak strength as derived from laboratory triaxial tests. However, the main breakthrough of the Hoek-Brown approach for the rock mechanics community was the possibility it opened to empirically estimate the failure criterion of the rock mass at the scale of the engineering project. The basic idea of the Hoek-Brown criterion was to start with the properties of the intact rock and to add factors —initially the RMR (Hoek & Brown, 1980a; Bieniawski, 1976) and then the GSI (Hoek et al., 2002; Hoek et al., 1998; Marinos & Hoek, 2000)— to reduce those properties because of the existence of joints (structure) in the rock. In parallel with this failure criterion, a number of correlations have been proposed to estimate in a more or less accurate way other relevant geomechanic parameters of the rock mass such as the elastic modulus (Hoek & Diederichs, 2006) or post-failure behavior features (Hoek & Brown, 1997).

The Hoek-Brown criterion has been extensively applied with reasonable success to a wide quantity and variety of rock engineering projects all over the world in the last decades. This seems a clear indicator that the approach is sound and/or conservative enough so as to provide appropriate designs and good explanations to the questions asked in practice. Additionally, large scaled in situ shear tests have shown a reasonable degree of agreement between observed shear strength and Hoek-Brown estimates (Cai et al, 2004).

The reduction of strength properties in line with the diminishing of the rock mass quality reflected in the Hoek-Brown approach implies strength reduction with scale and jointing undifferentiated. At small scale, samples from a few centimeters up to one meter showed a significant strength reduction for coal (Bieniawski, 1968) probably due to cleat (Medhurst & Brown, 1998), but not such a significant reduction (up to 80% of the original value) for a number of igneous rocks (Martin et al., 2014) where the Representative Elementary Volume (REV) seems to be much smaller than in coal. This value diminishes to 70% if one accounts for Hoek & Brown classic results on testing various diameter samples of different rocks (Hoek & Brown, 1980a). In this way an interesting question to be answered is whether strength and deformability reduction (and also post-failure behavior) are linked to the scale or to the structure (understood as the set of discontinuities crossing the rock sample analyzed), or to both of them, and up to what extent each.

Starting from the classic Hoek & Brown's idealized diagram showing the transition from intact to heavily jointed rock mass with increasing size (Hoek & Brown, 1980b), let's select a sufficiently large circle representing rock mass behavior for tunneling design purposes. This is called circle 'a' in red color in Fig. 6.1. If an homothetic transformation of circle 'a' is performed keeping its original joints to produce double diameter and quadruple diameter circles, circles 'b' green and 'c' blue respectively as in Fig. 6.1 will be obtained. If now circles of the same size than circle 'a' but within circles 'b' and 'c' respectively are selected, circles 'd' and 'e' respectively will be got.

If one could know the behavior of these (representative rock mass) samples to obtain conclusions; one should have clear that 1) circles 'a', 'b' and 'c' have different sizes (scale) but their structure is (homothetic) the same 2) circles 'a', 'd' and 'e' have the same size (scale) but their structures are different. So in order to study the role of the structure on the behavior of a rock mass, it is interesting to study the behavior of circles 'a', 'd' and 'e'. One cannot test circles, so, in this chapter, stress-strain results of tests on classic rock specimens with variable structure are shown. Additionally, it is relevant to recall that based on studies by different authors focusing

This chapter contains some of the results presented at the 13th ISRM Congress with the following citation: Arzúa, J., Alejano, L.R. & Pérez-Rey, I. 2015. *Effect of scale and structure on the strength and deformability of rocks.* 13th ISRM Congress 2015. International Symposium on Rock Mechanics. 10-13, May. Montreal, Canada on hard rock and compiled by Martin et al. (2014), the role of scale (alone) may not be as important as it is in coal.

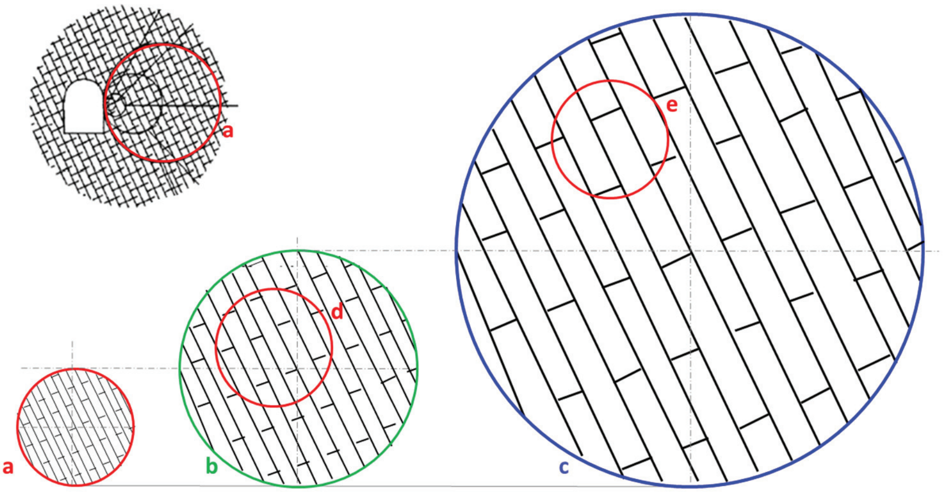

Fig. 6.1. Concepts of scale and structure in rock masses. a) rock mass sample representative of rock mass behavior at the scale of the engineering work, as for Hoek & Brown (1980b); b & c: double and quadruple diameter homothetic transformation of circle a; d & e: rock mass samples of the same size than circle a but with the original structures corresponding to a, b and c respectively.

If this is true, behavior of circles 'a', 'b' and 'c' may not be too different. If this is the case, the behavior of a standard rock specimen presenting a simple structure as those showed in this chapter could be related to that of an equivalent rock mass with a similar structure.

Though this way of thinking can be considered speculative, it is true that efforts to perform complete triaxial testing on rock samples of the same rock with different simple structures have been scarce in the past. Therefore, this chapter presents results of complete stress-strain curves on triaxial tests in granite samples including intact and two differently structured types of samples. Interpretation of results provides some insight in rock and rock mass behavior, including post-failure behavior, where less information is typically available. Previous trials to study the behavior of fissured rock specimens used materials built from plaster of Paris and silica sand and, either, only investigated unconfined behavior (Kulatilake et al., 1997; Kulatilake et al., 2001) or they focused on the role of sliding through pre-existing joints (Ramamurthy & Arora, 1994; Brown & Trollope, 1970).

6.2. Test setup

The testing equipment has been described in previous chapters and is available elsewhere (Arzúa & Alejano, 2013; Arzúa et al., 2014) so only a brief summary is presented here. The *John P. Harrison Rock Mechanics' Laboratory* of the University of Vigo has available a fully servo-controlled press that allows to perform compression triaxial tests with unloading-reloading cycles and to measure the lateral component of the volumetric strain by means of the amount of hydraulic fluid that gets in (or out) the triaxial cell in order to maintain the confining pressure. The axial strain is measured using linear variable differential transformers (LVDTs) attached to the lower platen of the press by means of industrial magnets. The radial strain can be computed based on axial and volumetric strains.

The rock tested was a granitic rock locally known as Blanco Mera, which is bright, white-colored and coarse-grained. This rock has been already characterized in terms of its geological and chemical nature (Chapter 3) and has been previously tested, both on intact (Chapters 3 and 5) and 1+2 (one sub-vertical and two sub-horizontal joints) jointed specimens (Chapter 5). All samples, including those newly tested came from the same block of this homogenous granite.

The jointed specimens preparation has also been described in Chapter 5 and it is published elsewhere (Arzúa et al., 2014) but in this case, instead of having one sub-vertical and two sub-horizontal joints (Fig. 6.2.a), the specimens have two sub-vertical and three sub-horizontal joints (i.e. 2+3) (Fig. 6.2.b). Specimen size and joint surface features are also the same as in Chapter 5, the only differences are that the mean dip of the sub-vertical joints is 77.9±1.2º, the mean dip of the sub-horizontal joints is 22.7±0.8º and the size of the pieces forming the specimen is smaller.

Remark that this low sub-horizontal angle was chosen to avoid sliding through these joints, since if it is the case, strength results will be controlled by the strength of the joints as in other studies (Kulatilake et al., 1997; Kulatilake et al., 2001; Ramamurthy & Arora, 1994; Brown & Trollope, 1970) and not by the general structure. Two different relative orientations of the joint sets (Fig. 6.2.c and d) have been studied in order to try to determine whether this feature has any influence on the results or not. The jointed specimens were re-joined enveloping them by means of food wrap and then, they were located inside the triaxial cell.

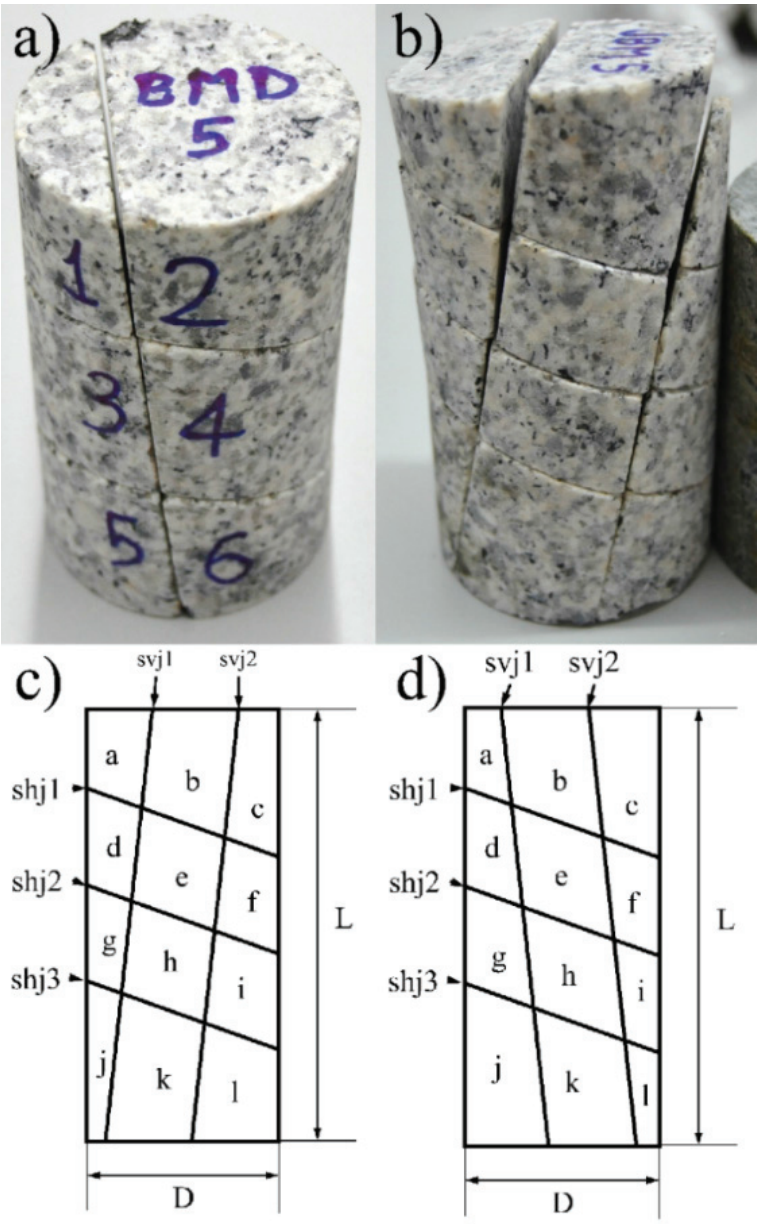

Fig. 6.2. a) (1+2) (one sub-vertical, two sub-horizontal) jointed specimen, as studied in Chapter 5. b) (2+3) (two sub-vertical, three sub-horizontal) jointed specimen, this study. c) and d) sketches of the different relative orientations of the sub-vertical and sub-horizontal joints of the (2+3) jointed specimen, explained in the text.

Dershowitz & Herda (1992) defined fracture density or intensity (P32) as the area of fractures in a volume of rock. In the tested specimens, and for quantification purposes, this fracture density is calculated in 33 m^2/m^3 for (1+2) jointed specimens and 50 m^2/m^3 for the (2+3) jointed specimens. No simple way exists to relate this fracture density in terms of RQD, GSI or any other commonly used classification system.

6.3. Testing

In addition to the tests performed in intact (Chapters 3 and 5) and (1+2) jointed cores (Chapter 5) another 20 confined compression strength tests have been performed, 12 with the relative orientation of the joints showed in Fig. 6.2.c and 8 with the relative orientation showed in Fig. 6.2.d. The confining pressure of the tests ranged from 1 to 12 MPa.

Axial strain is measured by means of two LVDTs, and volumetric strain is derived from fluid and platen displacement, so it is possible to compute the radial strain (Medhurst & Brown, 1998; Arzúa & Alejano, 2013; Farmer, 1983). In this way, it is possible to obtain the complete stress-strain curve for a single test, as depicted in Fig. 6.3. This Fig. 6.3 also illustrates how the most significant geomechanical parameters are obtained, including peak strength, σ_1^{peak}, residual strength, $\sigma_1^{\text{residual}}$, apparent tangential (or average) and secant elastic Young's moduli, E_t and E_s, and apparent Poisson's ratio, ν. Additionally Fig. 6.3 shows the variable nature of the known as drop modulus, M, and how it is possible to delineate the locus known as irrecoverable strain locus, which can be used to investigate post-failure behavior.

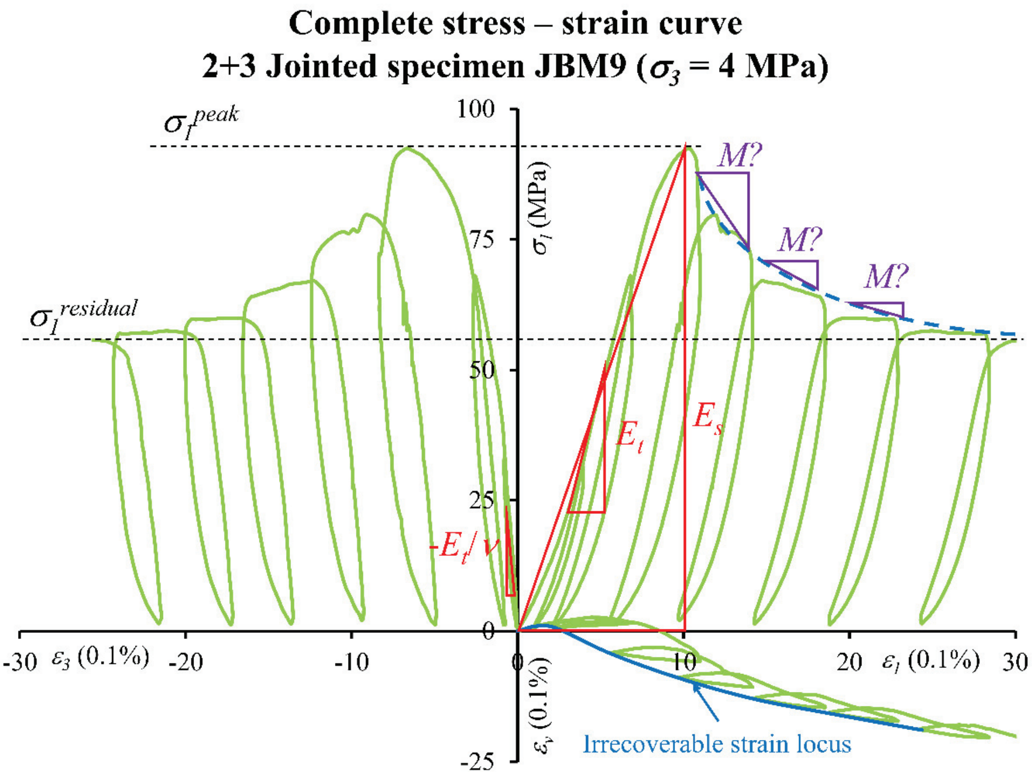

Fig. 6.3. Complete stress-strain curve result of a confined (σ_3 = 4 MPa) compressive strength test with unloading-reloading cycles and the indication of where the relevant parameters are obtained.

The tests were performed with unloading-reloading cycles. This is done to check that failure criteria are evolving, that is, once attained peak strength, in every forward reloading cycle, the peak axial stress attained marks the strength of the already yielded rock characterized by a particular damage level or plastic parameter. Unloading-reloading cycles can be also used to obtain the irrecoverable volumetric strain locus, which links the lowest volumetric strain value of each cycle (Fig. 6.3) and allows estimating the dilation angle as proposed by Medhurst & Brown (1998) and used by others (Alejano & Alonso, 2005; Walton et al., 2015a).

Pictures of the specimens were taken before (Fig. 6.4.a) and after (Fig. 6.4.b and c) each test was performed. Whereas failure in sound samples is typically due to newly formed shear bands or axial splitting cracks, in these jointed samples failure occurs due to irregular cracking following partially newly formed shear bands and partially pre-existing joints. Sometimes shear bands cross pre-existing joints, whilst other times these joints arrest the growing of these shear bands. These phenomena are illustrated in Fig. 6.4.b, where a shear band crosses piece ‘e’ of the sample and then piece ‘h’ but it is arrested in the joint between this piece and pieces ‘k’ and ‘l’.

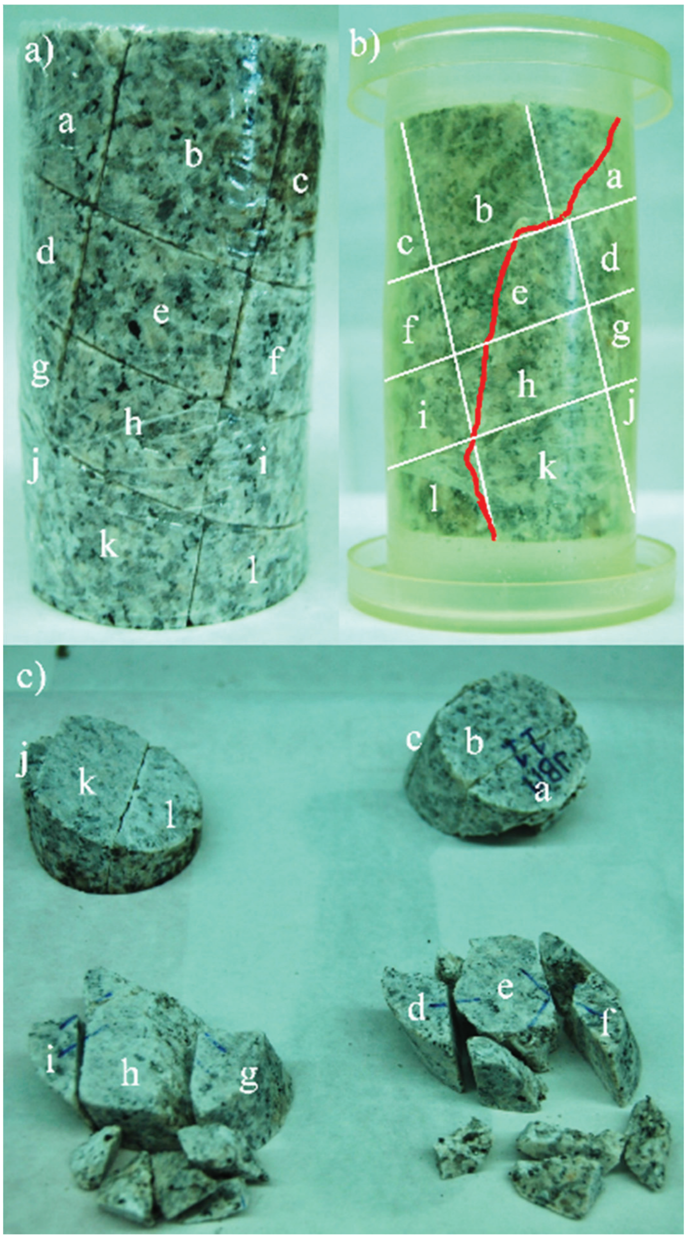

Fig. 6.4. Picture of the 2+3 jointed specimen JBM11 a) before, and b) and c) after testing; b) inside the sleeve; c) once the pieces of broken rock have been removed from the sleeve. Original and broken pieces have been lettered and the observed macroscopic failure trace surface has been marked in red.

A relevant and consistent (reasonably constant) decrease in strength is observed from sound samples to (1+2) jointed and even more (2+3) jointed samples (Fig. 6.5). This decrease is attributable to the fact that observed failure surface partially follows pre-existing joints as well as newly formed shear bands and/or axial splitting cracks. A painstaking observation of broken samples showed that, in most cases central pieces (i.e. pieces d, e, f, g, h and i as identified in Fig. 6.2.c and d and in Fig. 6.4) are very damaged, while top and bottom pieces usually look pretty sound or at least not so damaged (Fig. 6.4.c).

Fig. 6.5 shows complete stress-strain curves for the three types of samples in the case of tests confined at 10 MPa. Clear trends can be observed in this graph, which are quite representative of general results obtained. This figure illustrates a clear strength and stiffness decrease when analyzing sound, jointed and even more jointed samples. Additionally, the stress drop after peak tends to be milder for more jointed samples, but the residual strength shows to be sensibly equal in all cases. On the other hand, volumetric strain is not as large in the jointed specimens as it is in sound samples, which clearly indicates an expected decrease in dilation associated to the possibility of finding failure paths partially following pre-existing planar joints. A more detailed interpretation of these results based on actual numeric data is presented in the next section.

Since a number of researchers are in the process of investigating rock mass behavior by means of advanced numerical techniques (Martin et al., 2014; Mas Ivars et al., 2011; Zhou et al., 2014), the main parameters derived from our results are presented in Table B.8 in Appendix B. This can be used as a database to further study the behavior of these small-scale rock mass analogues.

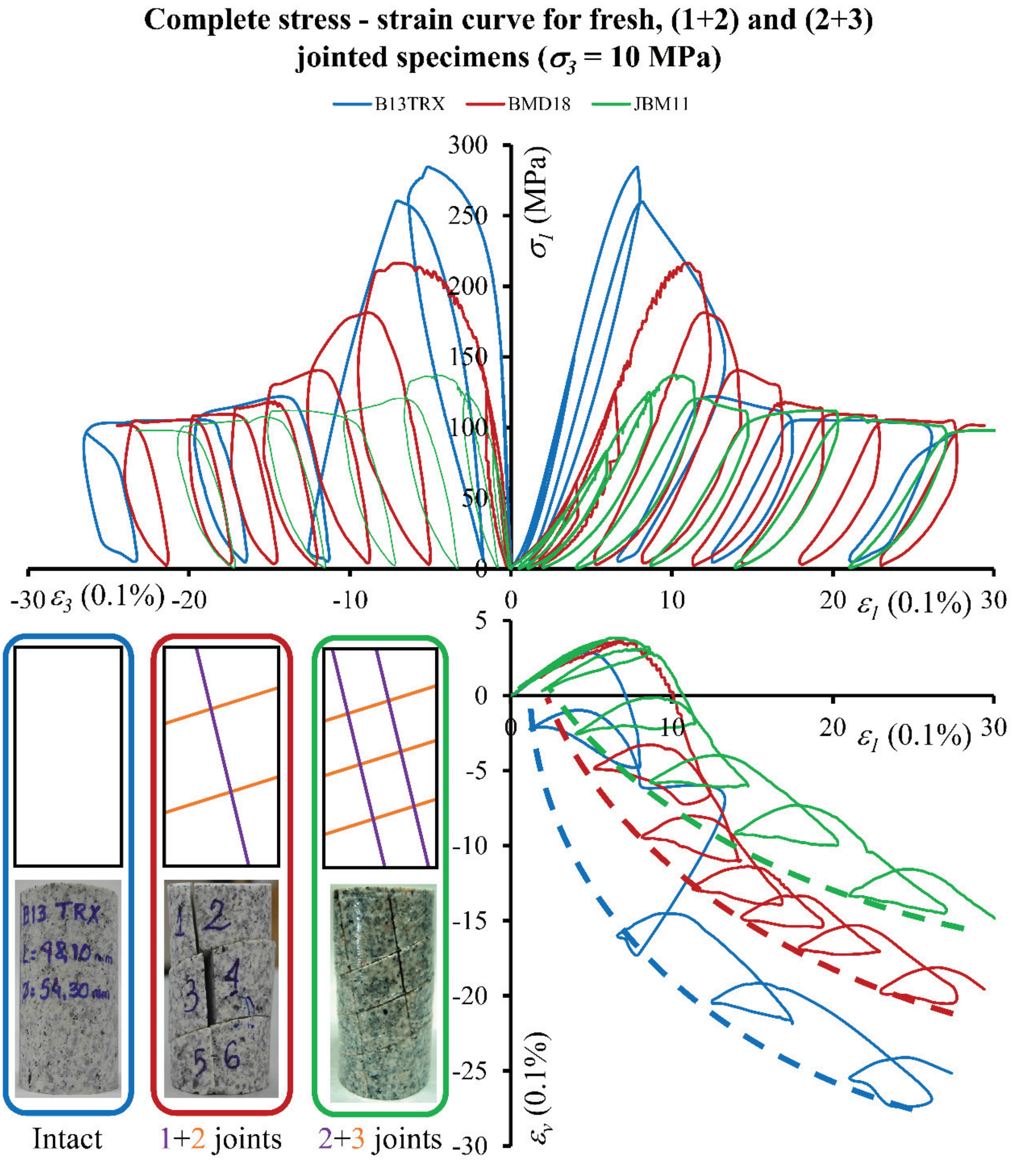

Fig. 6.5. Example of complete stress-strain curves with unloading-reloading cycles of three of these specimens representative of each type (fresh –B13TRX – blue; (1+2) joints - BMD18 – red; and (2+3) joints – JBM11 - green) confined to 10 MPa. In the lower right graph together with actual volumetric-axial strain response, the irrecoverable strain locus is delineated in dotted lines.

Fig. 6.6, Fig. 6.7 and Fig. 6.8 show the axial stress-axial strain curves for groups of tests corresponding to the intact, (1+2) jointed and even more (2+3) jointed cases respectively, for typically relevant confinement values of 2, 4, 6 10 and 12 MPa. A rough hand draw (averaged from various tests for each confinement) is shown in the last graph of every figure for comparative purposes.

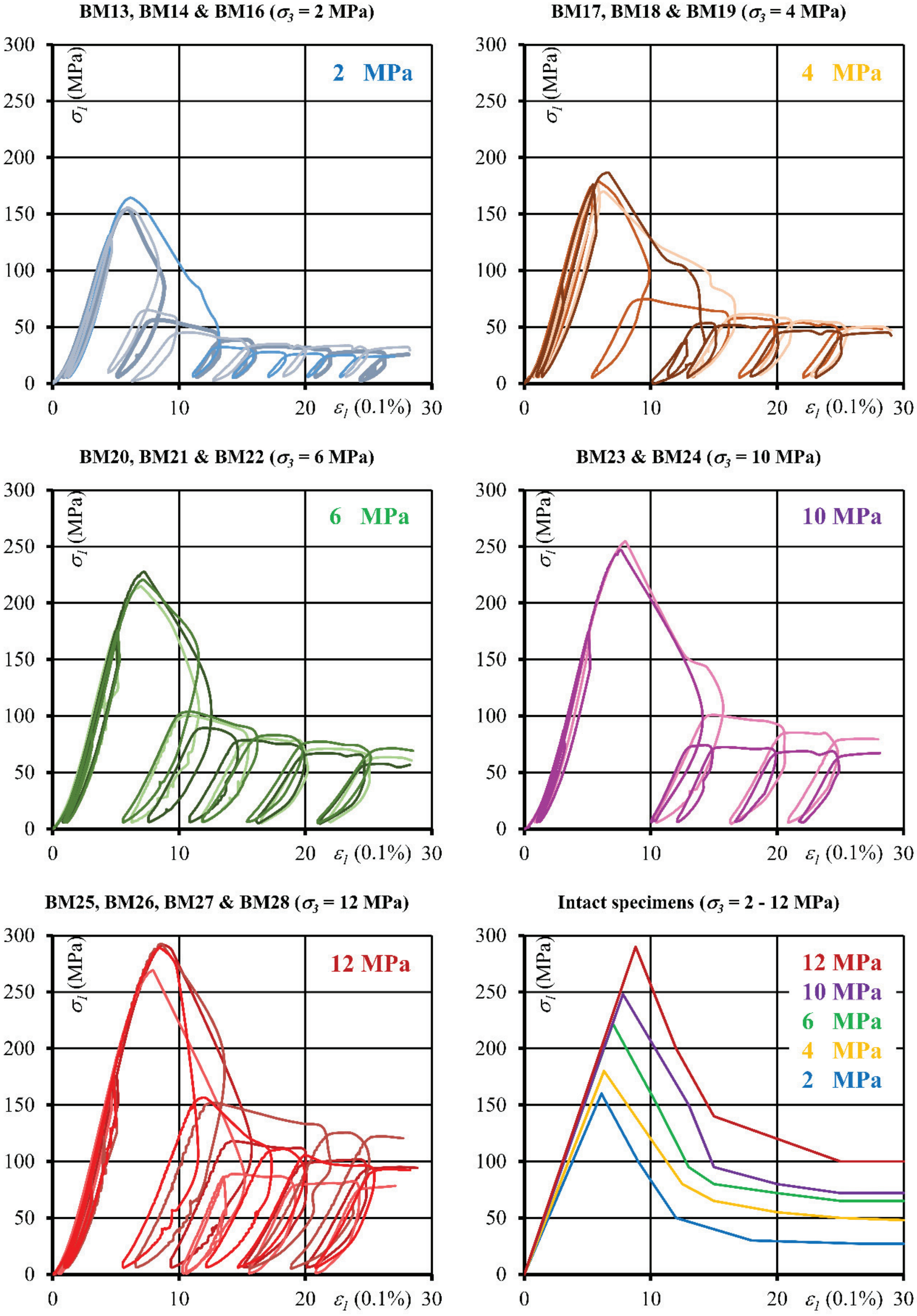

Fig. 6.6. Example of axial stress-axial strain curves with unloading-reloading cycles of triaxial tests in intact rock submitted to confinement stresses of 2, 4, 6, 10 and 12 MPa and averaged general trends representative of tests in intact rock.

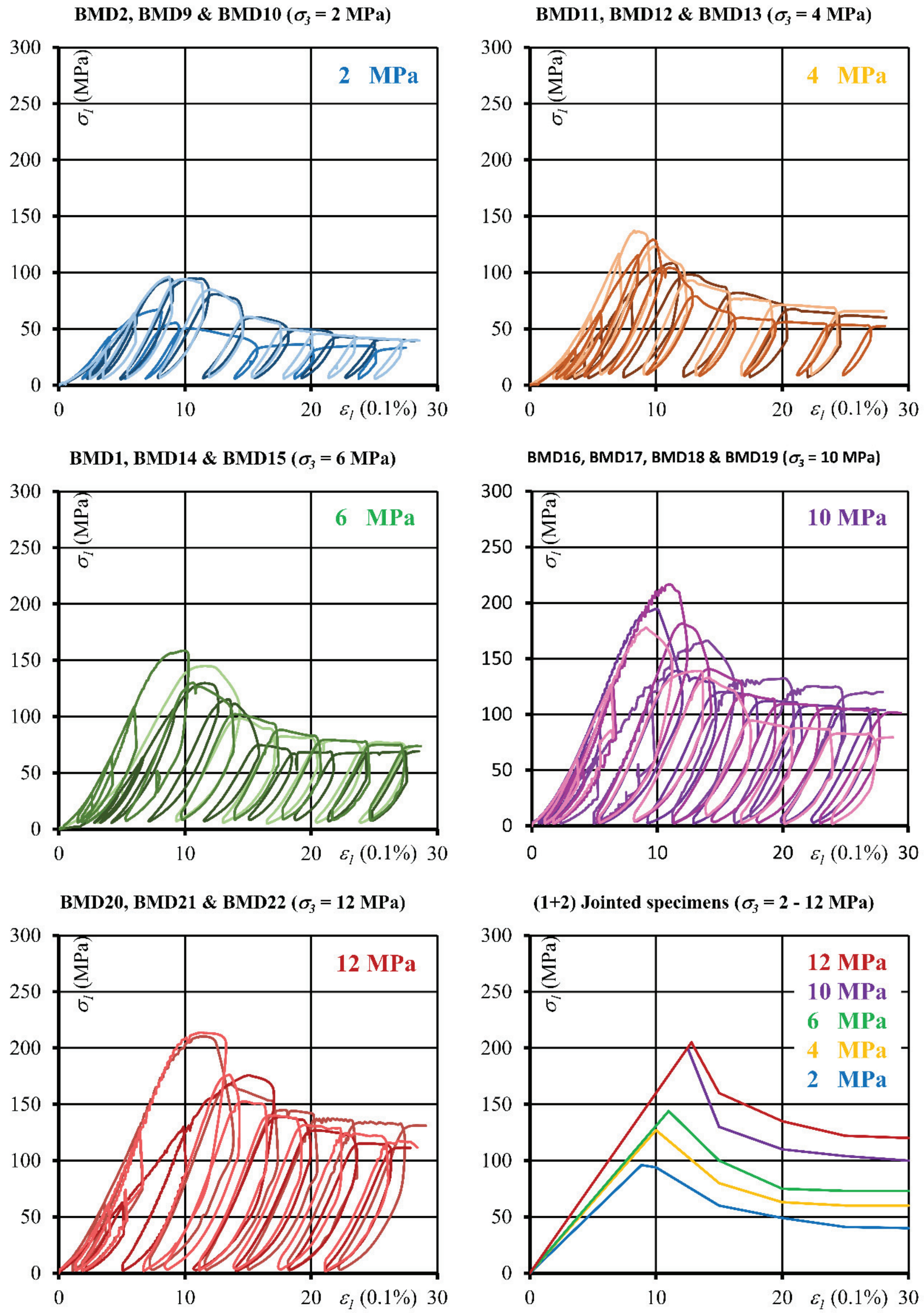

Fig. 6.7. Example of axial stress-axial strain curves with unloading-reloading cycles of triaxial tests in (1+2) artificially jointed rock specimens submitted to confinement stresses of 2, 4, 6, 10 and 12 MPa and averaged general trends representative of tests in (1+2) artificially jointed rock.

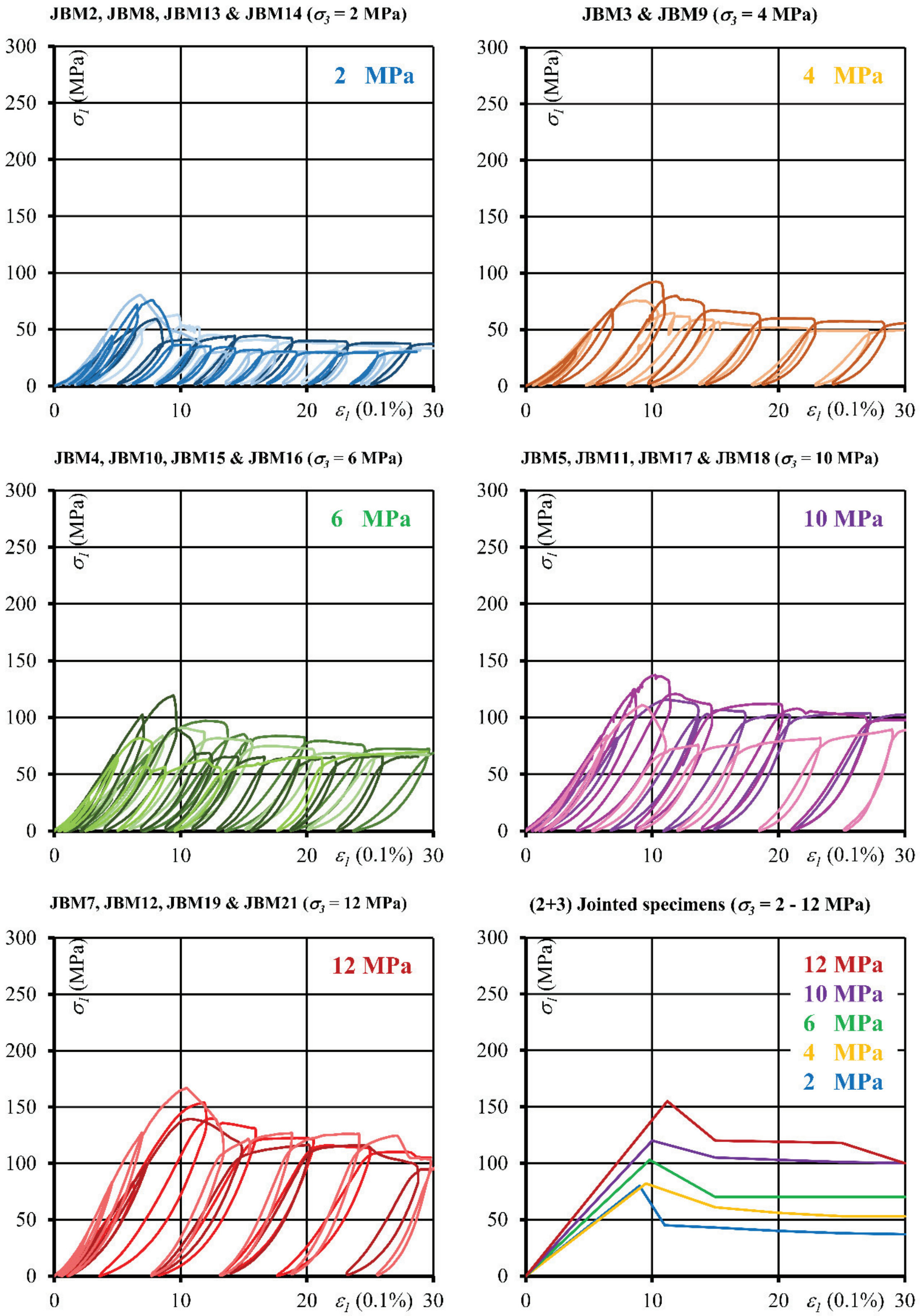
JBM2, JBM8, JBM13 & JBM14 (σ_3 = 2 MPa)

JBM3 & JBM9 (σ_3 = 4 MPa)

JBM4, JBM10, JBM15 & JBM16 (σ_3 = 6 MPa)

JBM5, JBM11, JBM17 & JBM18 (σ_3 = 10 MPa)

JBM7, JBM12, JBM19 & JBM21 (σ_3 = 12 MPa)

(2+3) Jointed specimens (σ_3 = 2 - 12 MPa)

Fig. 6.8. Example of axial stress-axial strain curves with unloading-reloading cycles of triaxial tests in (2+3) artificially jointed rock specimens submitted to confinement stresses of 2, 4, 6, 10 and 12 MPa and averaged general trends representative of tests in (2+3) artificially jointed rock.

Remark the repeatability of tests in terms of elastic modulus, peak and residual strength and dropping trends of the curves after peak, which seems rather regular for rock mechanics standards. See that however, occasionally tests response may vary significantly as it is the case of test at 2 MPa and 12 MPa in (1+2) jointed samples (Fig. 6.7) and tests at 6, 10 and 12 MPa in (2+3) jointed samples (Fig. 6.8). On the other hand, whereas for some tests, recorded parameters are quite regular (see residual strength in tests at 4 MPa in Fig. 6.6 or at 6 MPa in Fig. 6.7), in other cases certain scattering is recorded (see residual strength in tests at 10 MPa in Fig. 6.6 and in Fig. 6.7).

It is interesting to note how the classic initial concave curvature of the axial stress-axial strain curves is more significant in the fissured samples, particularly in the unloading-reloading cycles. It seems logical that this phenomenon, traditionally attributed to the closure of micro-cracks, was more relevant when more joints that are sub-horizontal exist in the tested sample.

The Blanco Mera granite is a brittle rock so in unconfined tests on intact rock it was difficult to control the failure of the samples and achieve a stable transition from peak to residual strength, as it happened with more confined cases and jointed samples. This suggests that the hydraulic press velocity could influence the rate of strength loss observed in unconfined tests. Although the stress-strain relationships during the strength loss portion of the tests may not be considered reliable for this rock type, the axial-radial-volumetric strains relationships should still be representative. After the period of strength loss, and once the press could control stable unloading-reloading cycles, the stress-strain relationships shown are, again, representative.

6.4. Interpretation of results

In this section, results of (2+3) jointed samples are analyzed together with those of the intact and (1+2) jointed specimens presented in previous chapters and published elsewhere (Arzúa & Alejano, 2013; Arzúa et al., 2014). As depicted in Fig. 6.5, such an interpretation can be of help to further insight rock and rock mass behavior. The analysis focuses on elastic parameters, peak and residual strength and dilatancy. Finally a brief comment is given on post-peak strain response.

6.4.1. Elastic parameters

Apparent tangent and secant elastic Young's moduli (Brady & Brown, 2006) and apparent Poisson's ratio have been computed for each test. Tangent elastic Young's modulus is estimated as the slope of the axial stress-axial strain curve between the 30% and 60% of the maximum strength as suggested by the ISRM (2007). Secant elastic Young's modulus is computed as the relation between peak axial stress and the corresponding axial strain. Apparent Poisson's ratio has been estimated starting from the slope of the axial stress-radial strain curve between the 20% and 40% of the maximum strength and the corresponding apparent tangent elastic Young's modulus (Fig. 6.3 and Fig. 6.9). It should be noted that jointed samples were not tested under unconfined conditions due to problems in initial stressing on the samples, so UCS results for intact samples are not computed in the presented results, even if available in Table B.8.

The apparent elastic Young's moduli have been plotted against the confining pressure (Fig. 6.9) and dependence on the confining stress as well as on the structure becomes evident. A logarithmic fit has been added to each group of results —intact, (1+2) jointed and (2+3) jointed specimens— although such a fit cannot be valid for null confinements. A straight line is added in order to estimate more reliably the Young's modulus for the unconfined tests. Estimates of tangent and secant elastic moduli derived from logarithmic and linear fits are presented in Table 6.1.

To remark is the relevant impact of confinement on elastic moduli. This confinement dependency of the elastic modulus has been put forward by different authors, in the lab (Heap & Faulkner, 2008) as well as when analyzing particular stability problems (Santarelli et al., 1986) or when trying to fit extensometer elastic data to modelling approaches in mines (Walton & Diederichs, 2015b). Moreover, this effect may lie behind some inaccuracies often observed in results of standard numerical models of excavations.

It is well known the dependence of the elastic modulus of jointed rock mass on its geotechnical quality (Serafim & Pereira, 1983), for instance, and to use the last relevant reference, the following formula by Hoek & Diederichs (2006):

$$E_{rm}\,(\mathrm{MPa}) = E_i \left(0.02 + \frac{1 - D/2}{1 + e^{\left(\frac{60+15D-GSI}{11}\right)}} \right) \tag{6.1}$$

where E_{rm} refers to the rock mass' elastic modulus, E_i that of the intact rock, D refers to the disturbance factor (considered 0 in our case) and GSI is the geological strength index.

a) Tangent Young's modulus

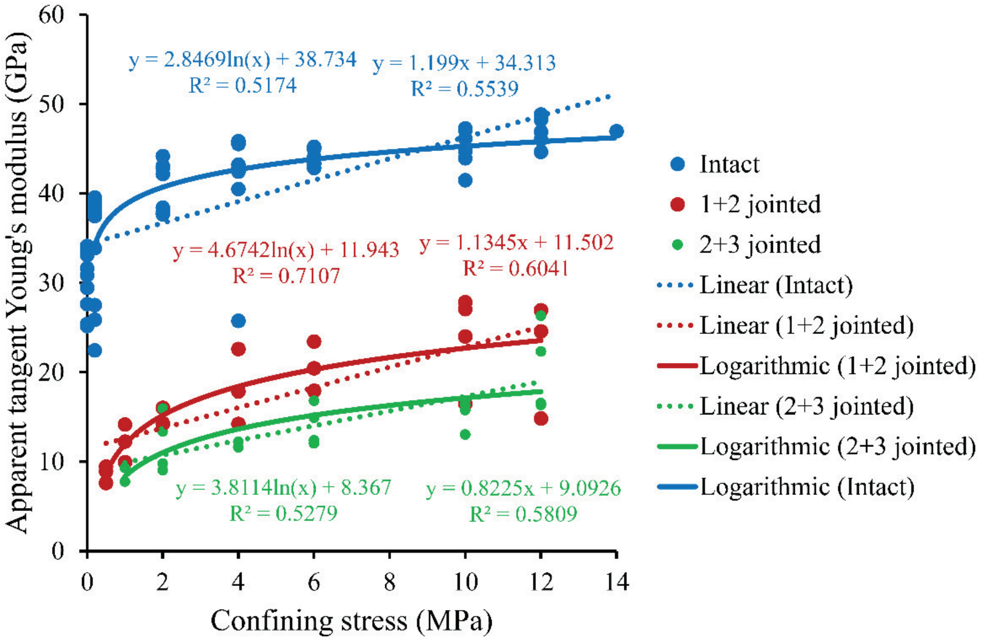

b) Secant Young's modulus

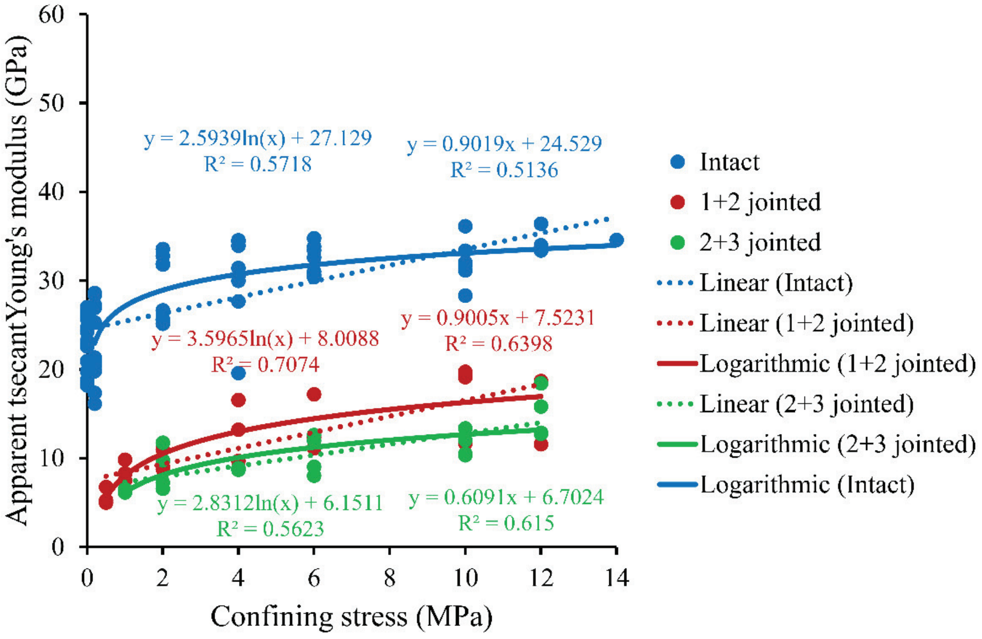

Fig. 6.9. Graphical representation of the apparent a) tangent (or average) and b) secant elastic Young's moduli.

Table 6.1. Tangent and secant elastic moduli for unconfined and various confinement levels as derived from fittings to test data.

		Elastic Young's moduli (GPa)					
		Tangent			Secant		
Approach	Test condition	Intact rock	(1+2) jointed	(2+3) jointed	Intact rock	(1+2) jointed	(2+3) jointed
Linear	Unconfined	34.31	11.50	9.09	24.52	7.52	6.70
Logarithmic	1 MPa	38.73	11.94	8.37	27.13	8.01	6.15
	2 MPa	40.71	15.18	11.01	28.93	10.50	8.11
	4 MPa	42.68	18.42	13.65	30.72	12.99	10.08
	6 MPa	43.83	20.32	15.20	31.78	14.45	11.22
	10 MPa	45.29	22.71	17.14	33.10	16.29	12.67
	12 MPa	45.81	23.56	17.84	33.57	16.95	13.19
	15 MPa	46.44	24.60	18.69	34.15	17.75	13.82

Introducing the Young's modulus of the jointed samples as E_{rm} and that of the intact samples as E_i (as in Table 6.1) in eq. (6.1) and for different confinements, one can obtain GSI values. The obtained GSI values are in the range of 50 to 60 (average 56) for the (1+2) jointed samples and 45 to 55 (average 50) for the (2+3) jointed samples, both and similarly for tangent and secant Young's moduli.

The apparent Poisson's ratio (Fig. 6.10), unlike elastic modulus, seems to be rather constant for variable confining stress in tests on intact specimens. However, when jointed samples are considered, the apparent Poisson's ratios present more variability in slightly confined tests and less variability for confined tests in the range 6-12 MPa. Average Poisson ratios are moreover higher for more jointed samples in slightly confined tests. However, they tend to converge towards a lower value (around 0.15) for every type of samples in the confined cases in the range of 10 to 12 MPa.

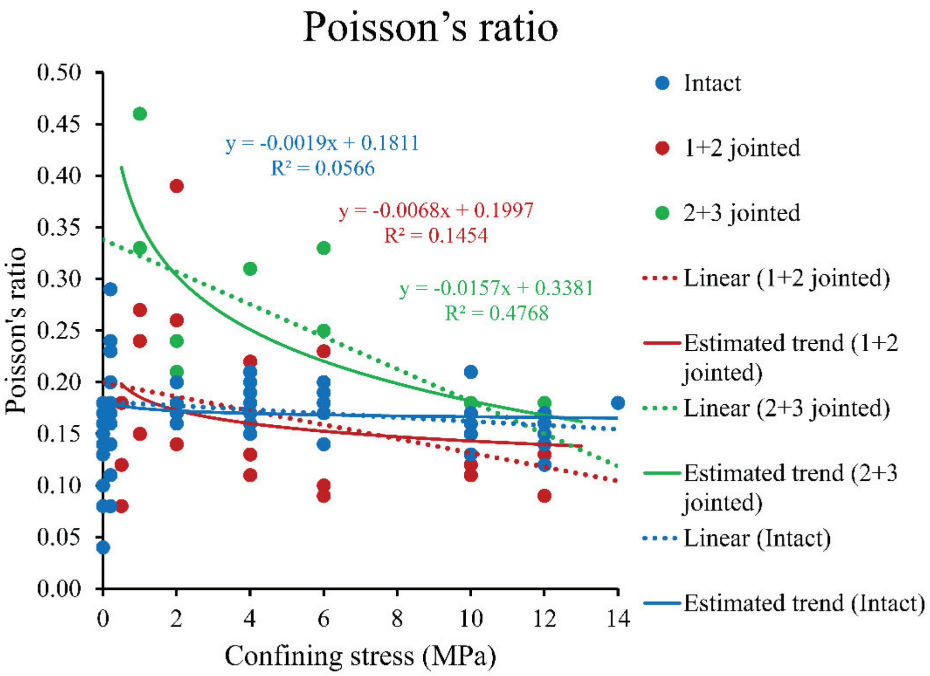

Fig. 6.10. Graphical representation of Poisson's ratios vs. confining pressure.

6.4.1. Peak strength parameters

Peak strength has been collected for each test (Table B.8), as the highest axial stress admitted by the sample. Since unconfined tests were not carried out in jointed samples, UCS tests in intact rock have not been considered in this analysis to make the original data on different jointing levels comparable.

In the case of the (2 + 3) jointed specimens, two different discontinuities' relative orientations were prepared (Fig. 6.2.c and Fig. 6.2.d) to check whether this feature has any influence on the results or not. A plot of the peak strength results in σ_1 - σ_3 axes (Fig. 6.11), reveals that even if a slightly higher value of strength of the angular patterned samples (Fig. 6.2.d) is reflected in the trends; for these relatively low confining pressures, peak strengths do not differ significantly. Since it is not possible to clearly discriminate results of the relative orientation of the joints, all the peak strength data coming from these more jointed samples are dealt uniformly. In the following sub-sections strength data are analyzed in terms of the two most used failure criteria: Mohr-Coulomb and Hoek-Brown.

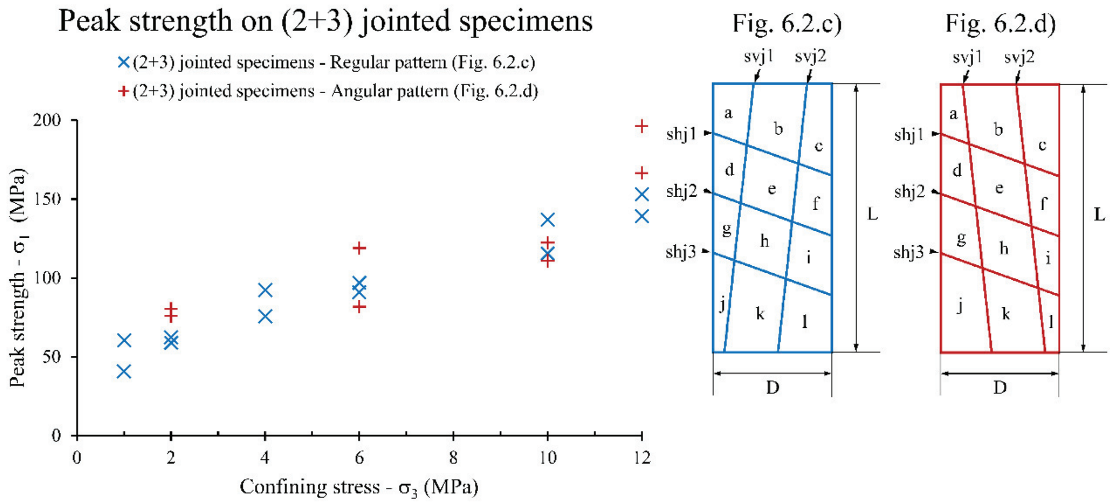

Fig. 6.11. Peak strength of the 2+3 jointed specimens depending on the relative orientation of the joints.

6.4.1.1. Interpretation of peak strength data in terms of Mohr-Coulomb failure criterion

The Mohr-Coulomb criterion can be fit in various ways and two approaches have been followed in this chapter. First, line has been fit in p-q space, where $p = (\sigma_1 + \sigma_3)/2$ and $q = (\sigma_1 - \sigma_3)/2$. As shown in Fig. 6.12, once one of these lines $q = p \cdot \tan\alpha + b$ has been fit to a number of tests, it can be easily demonstrated that the friction angle, ϕ, and cohesion, c, can be readily computed from:

$$\phi = \arcsin\alpha$$
$$c = \frac{b}{\cos\phi} \qquad (6.2)$$

This approach, traditionally used before the coming of the Hoek-Brown approaches, tends to offer more accurate fits than other approaches.

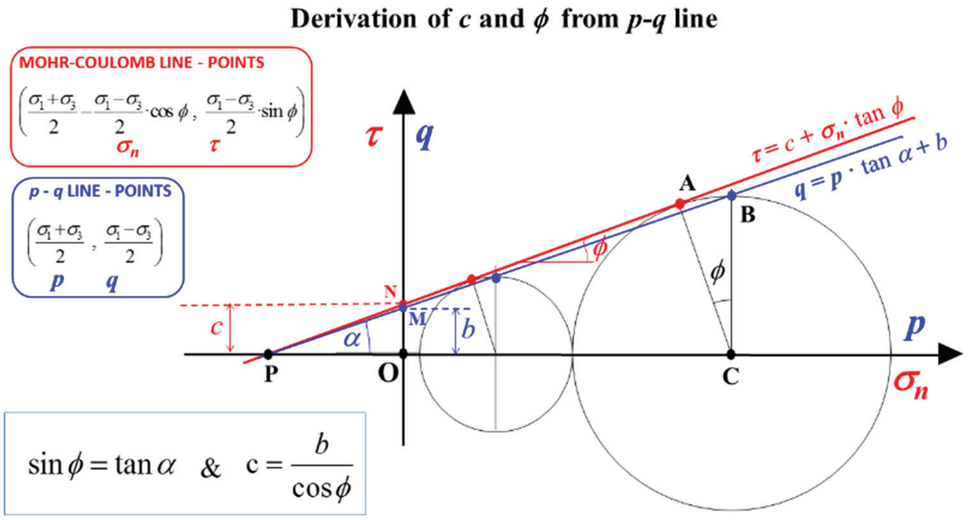
Derivation of c and φ from p-q line
MOHR-COULOMB LINE - POINTS
$\left(\frac{\sigma_1+\sigma_3}{2}-\frac{\sigma_1-\sigma_3}{2}\cdot\cos\phi,\ \frac{\sigma_1-\sigma_3}{2}\cdot\sin\phi\right)$
σ_n
τ
p - q LINE - POINTS
$\left(\frac{\sigma_1+\sigma_3}{2},\ \frac{\sigma_1-\sigma_3}{2}\right)$
p
q
τ
q
$\tau = c + \sigma_n \cdot \tan\phi$
$q = p \cdot \tan\alpha + b$
A
B
φ
φ
N
M
c
b
α
P
O
C
p
σ_n
$\sin\phi = \tan\alpha$ & $c = \frac{b}{\cos\phi}$

Fig. 6.12. Representation of maximum shear strength line (blue) in p-q axes, Mohr-Coulomb line (red) in τ-σ_n axes and their correlation.

It is also possible to fit a line to results in σ_1-σ_3 axes (Hoek-Brown axes) in such a way that:

$$\sigma_1 = \sigma_c + K_\phi \cdot \sigma_3$$

$$\text{Where } \sigma_c = 2 \cdot c \cdot \sqrt{K_\phi} \text{ and } K_\phi = \frac{1+\sin\phi}{1-\sin\phi} \qquad (6.3)$$

Both these approaches permit the use of linear regression analysis, which makes easier to handle and understand data.

Mohr-Coulomb failure peak criterion fitted relatively well to the results of all types of tests. Fig. 6.13.a shows the results of peak strength fits for intact, (1+2) jointed and (2+3) jointed samples in *p-q* axes for all analyzed tests. The derived parameters are presented in Table 6.2.

Good fits are observed with regression coefficients over R^2=0.99 in all cases. A noteworthy decrease in peak strength is observed when increasing jointing, although the slope of the fits remains similar. This suggests that the loss in strength mainly occurs in the cohesive component.

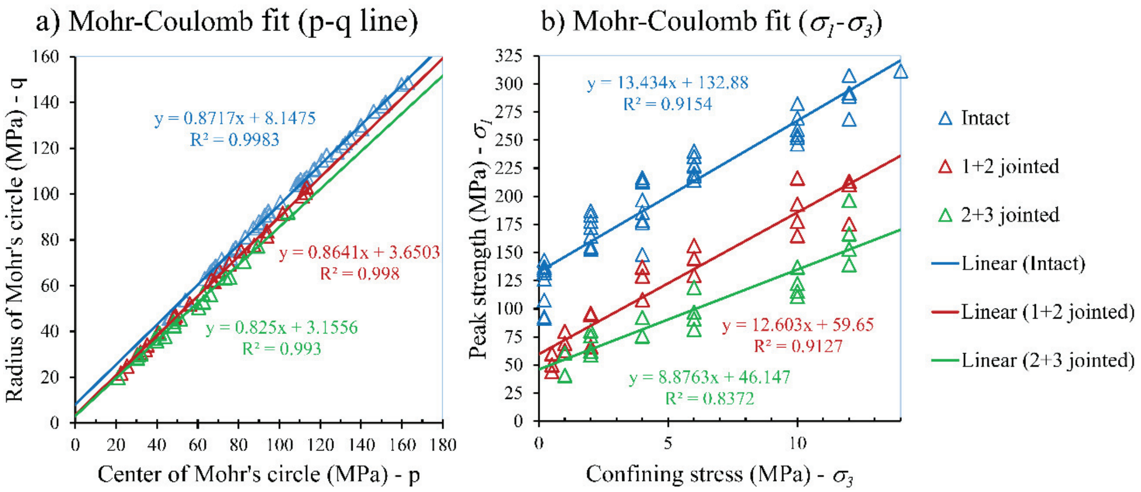

Fig. 6.13. Peak strength tests results and Mohr-Coulomb failure criterion fit for intact, (1+2) and (2+3) jointed specimens in terms of a) p-q line and b) results in σ_1-σ_3 axes.

Mohr-Coulomb failure peak criterion fits not so well in σ_1-σ_3 axes with regression coefficients in the range of R^2 from 0.83 to 0.92. In general, this approach presented in Fig. 6.13.b seems to be not as accurate as the classic one and it produces higher values of cohesion and lower friction angles than the previous fit approach.

It is also relevant to note that the statistical significance of the fitting of intact rock data (particularly high due to homogeneity of the samples) is not much higher than that of the jointed data samples. This suggests that it should be possible to develop a method able to predict strength in a reasonably accurate way, based on rock properties and the structure introduced in the sample.

Table 6.2. Mohr-Coulomb peak failure criterion parameters derived from two fit approaches.

			Intact specimens	(1+2) jointed specimens	(2+3) jointed specimens
Mohr-Coulomb failure criterion fit peak strength	Based on *p-q* representation	tan α*	0.8717	0.864	0.825
		b*	8.1475	3.6503	3.1566
		ϕ (º)	60.6	59.78	55.58
		c (MPa)	16.63	7.25	5.58
		σ_c^{pk} (MPa)	127.01	53.72	36.06
		R^2	0.9983	0.998	0.993
	Based on σ_1-σ_3 representation	σ_c^{pk} (MPa)*	132.88	59.65	46.17
		K_ϕ*	13.434	12.603	9.00
		ϕ (º)	59.48	58.54	52.89
		c (MPa)	18.13	8.40	7.74
		R^2	0.9154	0.9127	0.8372

* Fitted parameters, being the other ones derived values.

6.4.1.2. Interpretation of peak strength data in terms of Hoek-Brown failure criterion

Hoek-Brown failure criterion in its simpler form ($a = 0.5$, $s = 1$) is intended to be applied to intact specimens. It is possible to fit a line to results in $(\sigma_1$-$\sigma_3)^2$-σ_3 axes in such a way that:

$$\left(\sigma_1-\sigma_3\right)^2 = m\sigma_c\sigma_3+\sigma_c{}^2 \tag{6.4}$$

So the slope of the fitted line will be $m\cdot\sigma_c$, and the intercept will be $\sigma_c{}^2$.

Fig. 6.14.a shows the results of peak strength fits for intact, (1+2) jointed and (2+3) jointed samples in $(\sigma_1$-$\sigma_3)^2$-σ_3 axes for all analyzed tests. Numerical results are shown in Table 6.3.

Whereas fitting a simple H-B criterion to intact rock strength results, one obtains $\sigma_c = 126.2$ MPa and $m = 40.01$ with $R^2 = 0.934$; for the (1+2) jointed samples, one obtains $\sigma_c = 42.93$ MPa and $m = 67.98$ with $R^2 = 0.893$; and for the (2+3) jointed samples one gets $\sigma_c = 10.04$ MPa and $m = 162.9$ with $R^2 = 0.702$. Therefore, the fit of H-B for jointed specimens is not appropriate, since it does not only produce low values of the coefficient of regression but also values of m out of the standard range. That is, the H-B criterion for intact rock is not suitable for jointed specimens, as otherwise expectable.

So, in order to estimate jointed sample strength, it seems more reasonable to consider the jointed specimens as small-scale rock masses and assign them an equivalent Geological Strength Index (GSI) that will allow using the generalized Hoek-Brown failure criterion. The generalized Hoek-Brown criterion for rock masses is expressed as (Hoek et al., 2002):

$$\sigma_1 = \sigma_3 + \sigma_{ci}\left(m_b\frac{\sigma_3}{\sigma_{ci}}+s\right)^a \tag{6.5}$$

where:

$$\begin{aligned} m_b &= m \cdot \exp\left(\frac{GSI-100}{28-14D}\right) \\ s &= \exp\left(\frac{GSI-100}{9-3D}\right) \\ a &= \frac{1}{2}+\frac{1}{6}\left(e^{-GSI/15}-e^{-20/3}\right) \end{aligned} \tag{6.6}$$

and where D is the disturbance factor; m_b is a reduced value of the material constant, m (estimated in 40.01 in our case); and s and a are constants for the rock mass given by the presented relationships. σ_{ci} refers to the uniaxial compressive strength of the intact rock; σ_c, as tested in the lab, estimated in 126.2 MPa in our case.

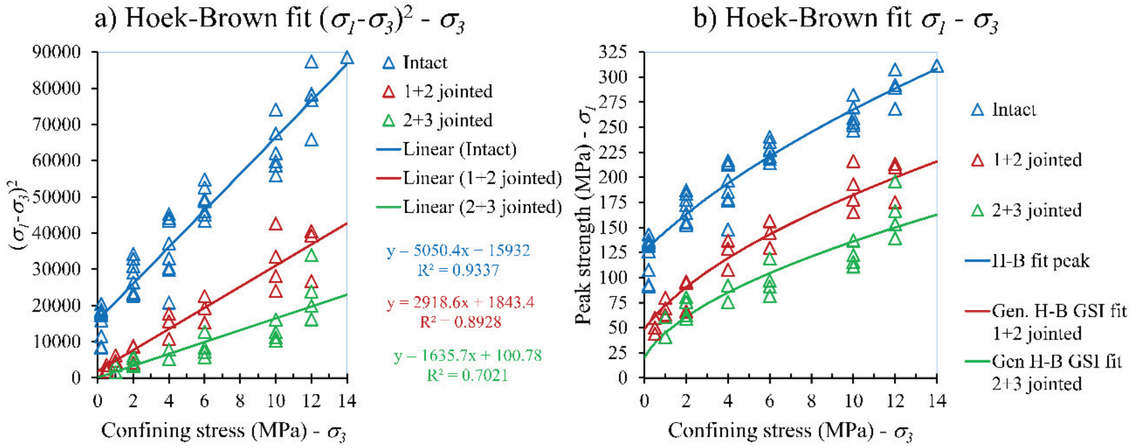

Fig. 6.14. Peak strength tests results and Hoek-Brown failure criterion fit for intact, (1+2) and (2+3) jointed specimens in terms of a) $(\sigma_1-\sigma_3)^2$ - σ_3 axes and b) results in σ_1-σ_3 axes.

This generalized Hoek-Brown failure criterion has been fit to the peak strength results of the jointed specimens by means of curve fitting toolbox^{TM} (Mathworks Inc., 2006). Within this software, the non-linear least squares approach with coefficient fitting carried out with the so-called trust-region algorithm was used. This approach does not only provide the coefficient of the regression, R^2, but also the root mean square error, *RMSE*, quite convenient to compare forecasting errors of different fittings. For a fixed disturbance factor ($D = 0$), values of GSI of 83 and 67 have been obtained for (1+2) and (2+3) jointed specimens respectively with regression coefficients as presented in Table 6.3 and illustrated in Fig. 6.14.b. However, if curves are fit with the same approach letting the algorithm to optimize the values of m_b, s and a independently it seems that the Hoek-Brown generalized failure criterion does not exactly fit these results, even if the increase of accurateness proportioned by this approach is not so relevant (see values of R^2 and *RMSE* in Table 6.3) in relation with the increase of complexity introduced.

Based on the comment by Martin et al. (2014) and in the classic figure by Hoek & Brown (1980a), let us now consider a reduction of strength in rock associated to scale up to a 70 %. In this way if the strength of all of the tests in fissured samples is reduced to a 70% of the recorded value (simulating large scale) and the second approach is repeated to derive the equivalent *GSI* of the jointed samples, the results presented in Table 6.4 are obtained. These values are more similar to those derived from elastic estimates of GSI.

Table 6.3. Hoek-Brown failure criterion parameters derived from various fit approaches for peak strength.

			Intact specimens	(1+2) jointed specimens	(2+3) jointed specimens
Hoek-Brown peak failure criterion	Intact rock (s=1, a=0.5)	m *	**40.01**	**67.98**	**162.94**
		σ_c *(MPa)**	**126.22**	**42.93**	**10.03**
		R^2	0.9337	0.8928	0.702
	Generalized Hoek-Brown strength with fixed σ_{ci} and m_i and fitting *GSI*	σ_{ci} *(MPa)*	126.22	126.22	126.22
		m_i	40.01	40.01	40.01
		D	0	0	0
		GSI *	**100**	**82.87**	**66.96**
		m_b from *GSI* (eq. 6.6)	40.01	21.70	12.29
		a from *GSI* (eq. 6.6)	0.5	0.5004	0.5017
		s from *GSI* (eq. 6.6)	1	0.149	0.0254
		R^2	0.9337	0.9319	0.8118
		RMSE	16.35	14.78	17.41
	Generalized Hoek-Brown strength with fixed σ_{ci} and m_i and fitting m_b, *a* and *s*	σ_{ci} *(MPa)*		126.22	126.22
		m_i		40.01	40.01
		D		0	0
		m_b (eq. 6.5)*		**23.41**	**10.12**
		a (eq. 6.5)*		**0.5**	**0.67**
		s (eq. 6.5)*		**0.0916**	**0.1847**
		GSI from m_b (eq. 6.6)		84,99	61.5
		GSI from *a* (eq. 6.6)		100	0
		GSI from *s* (eq. 6.6)		78.49	84.79
		R^2		0.9371	0.8279
		RMSE		14.55	17.1

* Fitted parameters. Underlined means fixed parameters. Bold means obtained during the fit. Being the other ones derived.

Table 6.4. Hoek-Brown failure criterion GSI and parameters derived from fitting the strength results obtained in jointed samples reduced to a 70 %.

		(1+2) jointed specimens	(2+3) jointed specimens
Generalized Hoek-Brown peak strength with fixed σ_{ci} and m_i and fitting *GSI*, with strength results scaled	σ_{ci} *(MPa)*	126.22	126.22
	m_i	40.01	40.01
	D	0	0
	*GSI**	**65.32**	**50.44**
	m_b from *GSI* (eq. 5)	11.59	6.81
	a from *GSI* (eq. 5)	0.5019	0.5055
	s from *GSI* (eq. 5)	0.0212	0.00405
	R^2	0.9307	0.8044
	RMSE	10.43	13.31

* Fitted parameters. Underlined means fixed parameters. Bold means obtained during the fit. Being the other ones derived.

6.4.2. Residual strength parameters

Some researchers consider that residual strength strongly depends on inhomogeneous deformation modes (bifurcation and localization modes) highly controlled by boundary conditions so it is not rigorous to compute it. However, other authors have checked that this residual strength can be relevant in practice and it seems to tend to a particular value (Cai et al., 2007). Based on the repeatability of the tests and on the fact that some relevant information can be derived, residual strength are estimated and analyzed. The authors recognize, however, that different interpretations of these results can be proposed.

Residual strength has been estimated for each test, although the selection is not as straight forward as it is in the case of peak strength. The residual strength has been estimated as the value of strength for an axial strain of 30 milistrain (typical end-point of the tests), when an increase in the last 5 mstr. of axial strain has not produced a significant decrease in strength (5 MPa). If this does happen, an estimation of the possible value is performed based on the main trend of the considered test. If still this latter method does not give a reasonable value, no valid residual strength is computed for the test. Obviously, these results cannot be considered as accurate as peak strength.

On the other hand, all residual strength results in the different types of jointed and unjointed samples tend to coincide. Moreover, both types of jointed specimens seem to slightly increase its residual strength with confining stress when compared to intact specimens, which could be attributed to the fact that macroscopic failure trace surfaces combining existing joints and new shear bands appear in the jointed samples (Fig. 6.4.b), while more simple shear bands occur in the case of intact samples.

6.4.2.1. Interpretation of residual strength data in terms of Mohr-Coulomb failure criterion

Mohr-Coulomb failure criterion fitted relatively well to the residual strength results of all types of tests. Fig. 6.15.a and Fig. 6.15.b show the results of residual fits for both types of fitting approaches previously presented for intact, (1+2) jointed and (2+3) jointed samples and for all the samples together in *p-q* axes and σ_1-σ_3 axes for all analyzed tests. The derived parameters are shown in Table 6.5.

Good fits are observed with regression coefficients over R^2 = 0.99 in all cases for the *p-q* approach and over 0.8 for the σ_1-σ_3 linear fit approach. Quite constant values of the friction angle are obtained in all cases. In general, the failure criteria are very similar for all types of tests, which suggest a similar residual strength behavior.

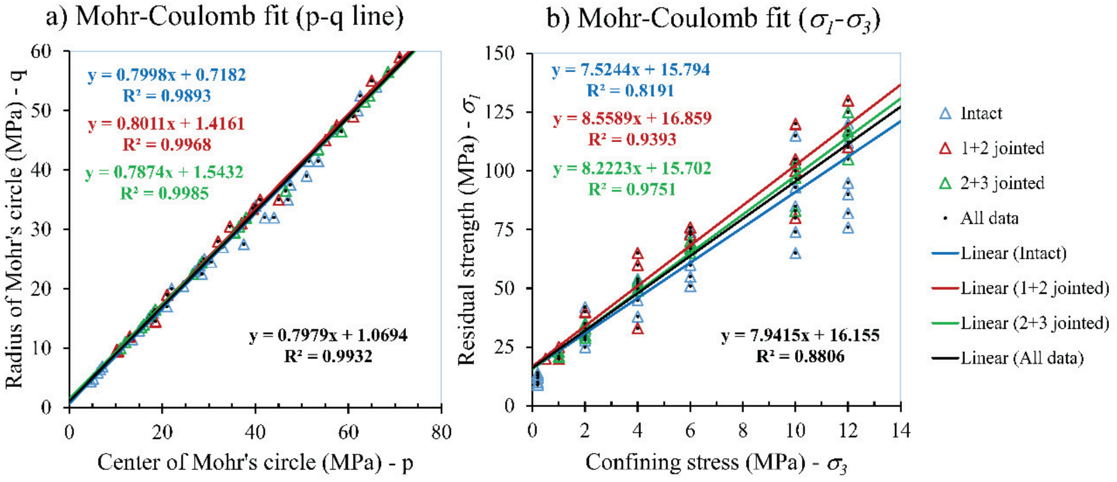

Fig. 6.15. Residual strength tests results and Mohr-Coulomb failure criterion fit for intact, (1+2) and (2+3) jointed specimens and all tests together in terms of a) p-q line and b) results in σ_1-σ_3 axes.

Table 6.5. Mohr-Coulomb residual failure criterion parameters derived from two fit approaches.

			Intact specimens	(1+2) jointed specimens	(2+3) jointed specimens	All specimens
Mohr-Coulomb failure criterion fit residual strength	Based on *p-q* representation	tan α*	0.7998	0.8011	0.7874	0.7979
		b *	0.718	1.416	1.543	1.069
		ϕ (°)	53.11	53.23	51.94	52.93
		c (MPa)	1.19	2.36	2.50	1.77
		σ_c^{pk} (MPa)	7.17	14.23	14.52	10.58
		R^2	0.9893	0.9968	0.9985	0.9932
	Based on σ_1-σ_3 representation	σ_c^{pk} (MPa)*	15.79	16.86	15.7	16.15
		K_ϕ*	7.52	8.56	8.22	7.94
		ϕ (°)	49.94	52.26	51.55	50.92
		c (MPa)	2.88	2.88	2.73	2.86
		R^2	0.8191	0.9393	0.9751	0.8806

* Fitted parameters, being the other ones derived values.

6.4.2.2. Interpretation of residual strength data in terms of Hoek-Brown failure criterion

For the case of the residual strength fitting of Hoek-Brown failure criterion, the same fitting approach based on fitting GSI by means of the MatLab tool (Mathworks Inc., 2006) was used, but thinking that due to the damaged nature of rock pieces, a not null disturbance factor could be obtained. Fitting in this way the generalized Hoek-brown criterion, a value of *D* practically null was obtained in all cases and it was possible to obtain a mean equivalent GSI for each case (intact and two types of jointed specimens and all together residual strength). The obtained parameters are presented in Table 6.6 and the graphical results are shown in Fig. 6.16.a.

Table 6.6. Hoek-Brown failure residual criterion parameters derived from fit approaches of GSI and D.

		Intact specimens	(1+2) jointed specimens	(2+3) jointed specimens	All specimens
Generalized Hoek-Brown residual strength with fixed σ_{ci} and m_i and fitting *GSI* and *D*	σ_{ci} *(MPa)*	126.22	126.22	126.22	126.22
	m_i	40.01	40.01	40.01	40.01
	*D**	**0**	**0**	**0**	**0**
	*GSI**	**41.62**	**48.13**	**45.66**	**44.32**
	m_b from *GSI* (eq. 6.6)	4.97	6.28	5.75	5.48
	a from *GSI* (eq. 6.6)	0.5102	0.5065	0.5077	0.5085
	s from *GSI* (eq. 6.6)	0.00152	0.00314	0.00239	0.00206
	R^2	0.7984	0.9192	0.9346	0.8566
	RMSE	15.88	10.77	8.86	13.48

* Fitted parameters. Underlined means fixed parameters. Bold means obtained during the fit. Being the other ones derived. The obtained value of *D* is not strictly zero but in the range of 1e-6.

The residual strength points for all the tests present, more or less, the same values in terms of compressive strength or equivalent GSI. This contributes to evidence that the residual strength of a rock does not show a relevant structure effect (probably also not scale effect). Similar observations have already been made by Exadaktylos & Tsoutrelis (1993) and Cai et al. (2007), who stated that the residual strength of intact rocks, as interpreted from triaxial tests, could be at the same level as the residual strength of the jointed rock mass.

A deeper analysis of the residual strength data shows that the obtained equivalent GSI for the jointed specimens increases with the confining pressure, meanwhile it remains more or less constant for the intact specimens (Fig. 6.16.b). This result is in line with the observations of Bahrani & Kaiser (2013), who indicated that in a jointed rock mass the generalized Hoek-Brown failure criterion tend to systematically underestimate the strength of the rock mass at high levels of confinement, when assuming a constant value of *GSI*.

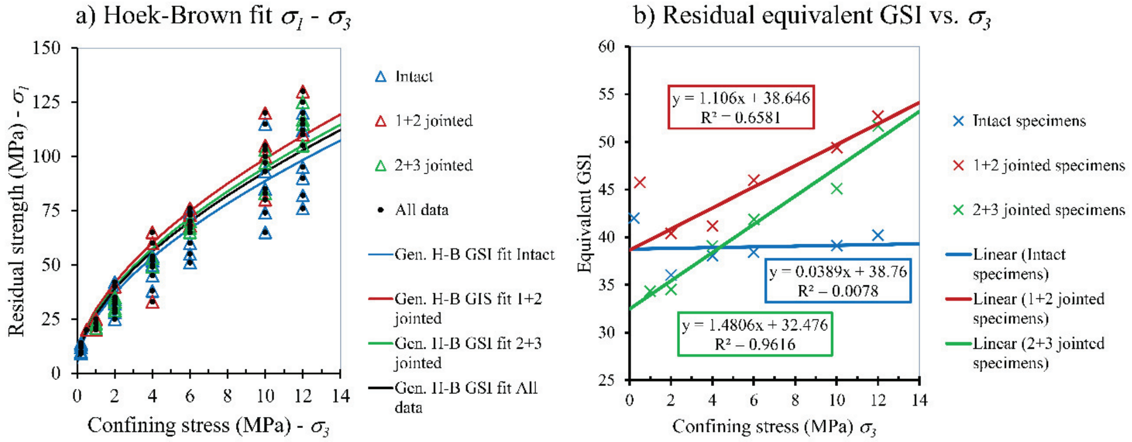

Fig. 6.16. a) Residual strength tests results and generalized Hoek-Brown failure criterion fit for intact, (1+2) and (2+3) jointed specimens. b) Residual strength GSI equivalent results for intact, (1+2) and (2+3) jointed specimens, suggesting a more relevant confinement effect in jointed samples.

6.4.3. Drop modulus

In previous chapters, the author have tried to compute the drop modulus of every test as the main trend of the slope of the axial stress-axial strain curve between peak and residual strength. This has revealed to be a difficult task and some data has been recorded which did not seem to follow clear trends. This is attributed to insufficient servo-control of the press system — particularly when testing brittle rocks under slightly confined conditions— to the limited range of confinement stresses and to variable response of rock samples (see, for instance, how in the tests with a confinement of 6 MPa in Fig. 6.7, whereas some tests present a pretty curved surface, other one shows a quite sudden drop).

However, drop modulus has been estimated in all confined tests in the following manner. First, the peak strength of each test was selected with its correspondent value of axial strain. Then, the residual strength is estimated. Later, the principal stress level corresponding to 50% of the drop is selected, that is the average value of peak and residual estimated strengths, and its corresponding axial strain value is computed as derived from the envelope of the curve. The average slope of the line joining the stress-strain peak and intermediate point is taken as the estimated drop modulus. This value appears in Table B.8 for all tests. This is a rough estimate and not a computed value. Because of this and because the inaccuracies produced by the above indicated reasons, results should be interpreted in a cautious manner.

Drop moduli estimates of intact samples showed to be rather erratic. However, those corresponding to jointed samples seem to follow clear trends. In particular the parameter called ω has been represented, which is the negative ratio of the drop modulus versus the secant elastic modulus (Alejano et al., 2010):

$$\omega = \frac{-M}{E_{secant}} \tag{6.7}$$

This is also a measure of the brittle response of the tests. Tests showing large ω values (over 2) are typically very brittle whereas when they show low ω values (less than 0.5) they are rather ductile.

Alejano et al. (2010), provide an estimate of this value derived from general observation in rock masses with the following form:

$$\omega = \left[0.0046 \cdot e^{0.0768 \cdot GSI} \right] \left(\frac{\sigma_3}{\sqrt{s^{peak}} \cdot \sigma_{ci}} \right)^{-1} \tag{6.8}$$

In Fig. 6.17.a the values of ω for the (1+2) and (2+3) jointed samples are presented in relation to confining stresses. It can be observed how more fissured samples tend to be less brittle, particularly for higher confinement (4-12 MPa), in line with general trends proposed by Hoek & Brown (1997). It can also be observed a more marked trend towards lower brittleness for more confined tests, as typically observed in lab tests (Von Kármán, 1911; Zhang et al., 2013).

The author has tried to identify trends in more detail, which have proved difficult. But representing the points (ω,σ_3) for the (2+3) jointed samples corresponding to the more perpendicular joint pattern (Fig. 6.2.c), these values match reasonably well the results derived from the application of eq. (6.8) considering a *GSI* = 40, as Fig. 6.17.b. illustrates. Remark that other obtained data do not seem to fit this tentative formulation.

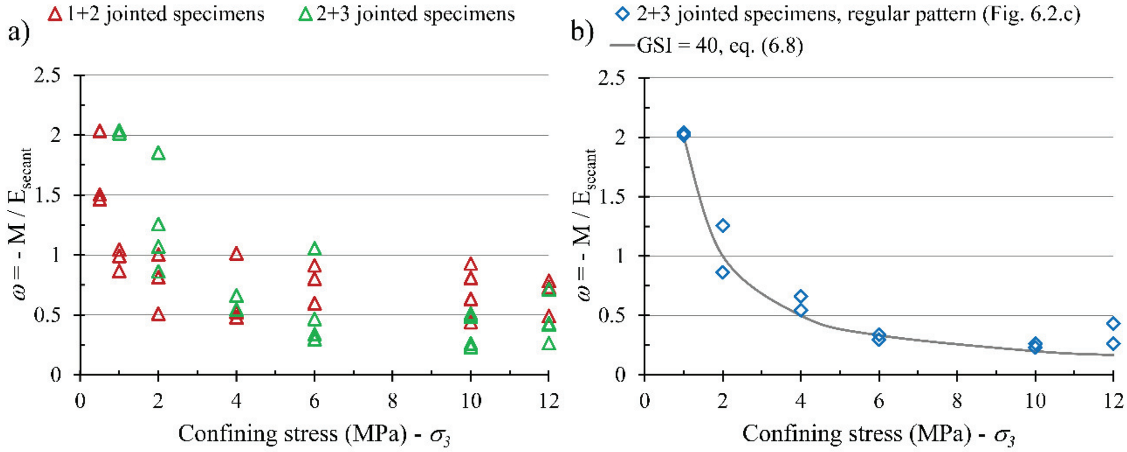

Fig. 6.17. Estimated drop modulus indicator results, ω, for the case of jointed samples b) ω values for (2+3) artificially jointed samples with normal pattern (Fig. 6.2.c) and representation of eq. 8 for the case of GSI 40.

6.4.4. Dilation angle

Due to the ability of the servo-controlled press set-up to monitor volumetric strain and perform unloading-reloading cycles, the irrecoverable strain locus can be obtained for every test as suggested by Medhurst & Brown (1998). From these irrecoverable strain loci, dilation angle was computed for a number of plastic strains and for each test, as presented in previous chapters. Results show the already known dependencies of the dilation angle (i.e. plastic strain and confinement, as pointed out by Alejano & Alonso, 2005) but also on the structure. As the level of jointing increases, the dilation angle decreases, but when increasing confining pressure, the differences in the dilation angle between intact and jointed specimens become smaller and even seem to present the same dilation angle for a low confining pressure of around 4 to 6 MPa (Fig. 6.19 and Fig. 6.21).

The dilation angle data was fitted to the available dilation angle models: Alejano & Alonso (2005), Zhao & Cai (2010a) and Walton & Diederichs (2015a).

Alejano & Alonso (2005) model was not able to capture the peak dilation angle, although the decay with plastic strain was quite well represented. Zhao & Cai (2010a) and Walton & Diederichs (2015a) models were able to capture the whole dilatational behavior of granite, although some concerns arose during the analysis.

6.4.4.1. Zhao & Cai (2010a) dilation angle model

Zhao & Cai (2010a) dilation model is based in nine coefficients (a_1, a_2, a_3, b_1, b_2, b_3, c_1, c_2 and c_3) and is able to capture the peak dilation angle (its value, its associated plastic strain and its dependence with confinement) as well as the decay of the dilation angle with the plastic strain. On the other hand, the coefficients used in the model have no physical significance since they are merely coefficients of an equation that fits quite well the observed behavior of the dilation angle, this makes the model difficult to examine or to modify its parameters in the context of other geomechanical parameters. Another problem is that the solution is not univocal because although each parameter (a, b and c, derived from the nine coefficients) mainly affects one aspect of the model, they also affect, in different degrees, the other aspects of the model, resulting in that two sets of coefficients can practically yield the same dilation angle curve.

As proposed in chapter 5 (Arzúa et al., 2014), the coefficients of the Zhao & Cai (2010a) dilation model that represent the decay of the dilation angle with plasticity (i.e. b_1, b_2, b_3, c_1, c_2 and c_3) have been set equal to those of the intact specimens due to the similarity in dilation decay trends. This consideration makes the fitting process easier and provides very good results as it can be observed in Fig. 6.19. Also considering coefficients a_2 and a_3 for (2+3) jointed specimens equal to those of the (1+2) jointed specimens, provided very good fits, so eight out of nine (i.e. a_2, a_3, b_1, b_2, b_3, c_1, c_2 and c_3) coefficients defining the Zhao & Cai (2010) dilation model of the (2+3) jointed specimens have been set equal to those of the (1+2) jointed specimens.

The coefficients that define the plastic shear strain and confining pressure dependent dilatational behavior of the three types of specimens as proposed by Zhao & Cai (2010a) are shown in Table 6.7. Derived from these coefficients one can obtain the confining stress dependent parameters (a, b and c) for each confinement as proposed by Zhao & Cai, and compare them with those obtained during the fit of the actual data to check if they really agree with the equations proposed by Zhao & Cai. This comparison is shown in Fig. 6.18, where it can be observed the good agreement between the obtained parameters during the fits and those obtained from the coefficients and equations proposed by Zhao & Cai (2010a).

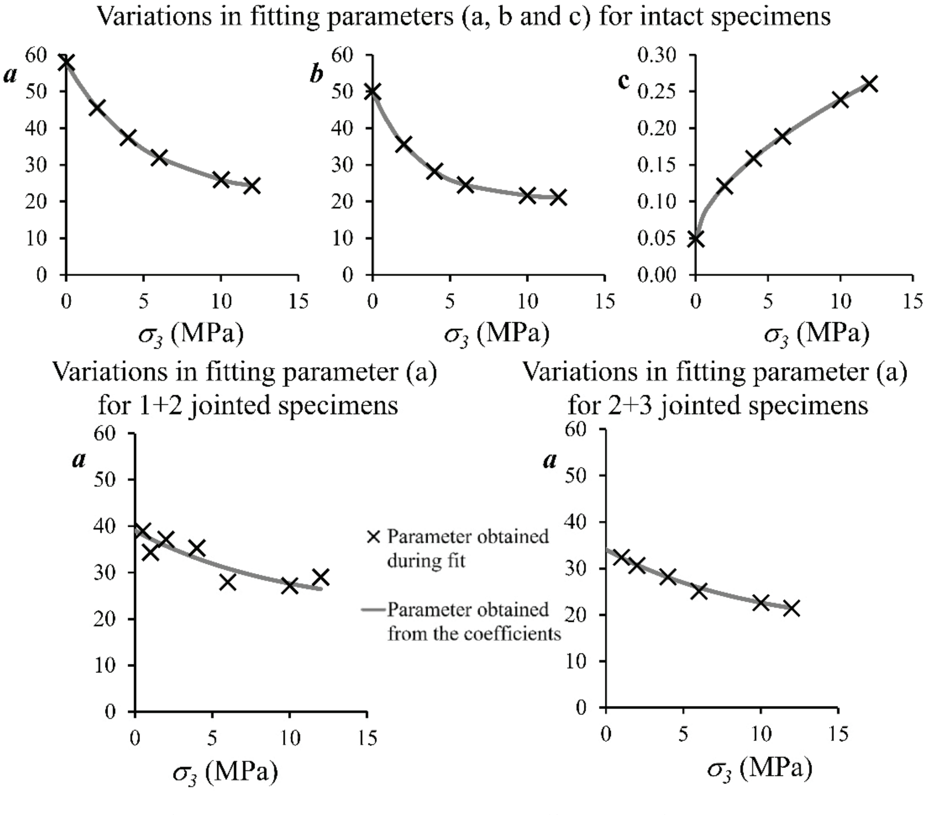

Fig. 6.18. Variations in fitting parameters (a, b and c) at different confining pressures and the best fit for each type of specimen. The parameters b and c of the jointed specimens (1+2 and 2+3) are the same than those of the intact specimens.

Table 6.7. Coefficients of the plastic shear strain and confining pressure dependent dilation angle model as proposed by Zhao & Cai (2010a) for the three types of specimens tested.

*	a_1	a_2	a_3	b_1	b_2	b_3	c_1	c_2	c_3
1	21.13	36.71	4.92	20.63	29.44	2.97	0.047	0.049	0.589
2	21.13	17.92	9.85						
3	16.13								

*1. Intact specimens, 2. 1+2 jointed specimens, 3. 2+3 jointed specimens

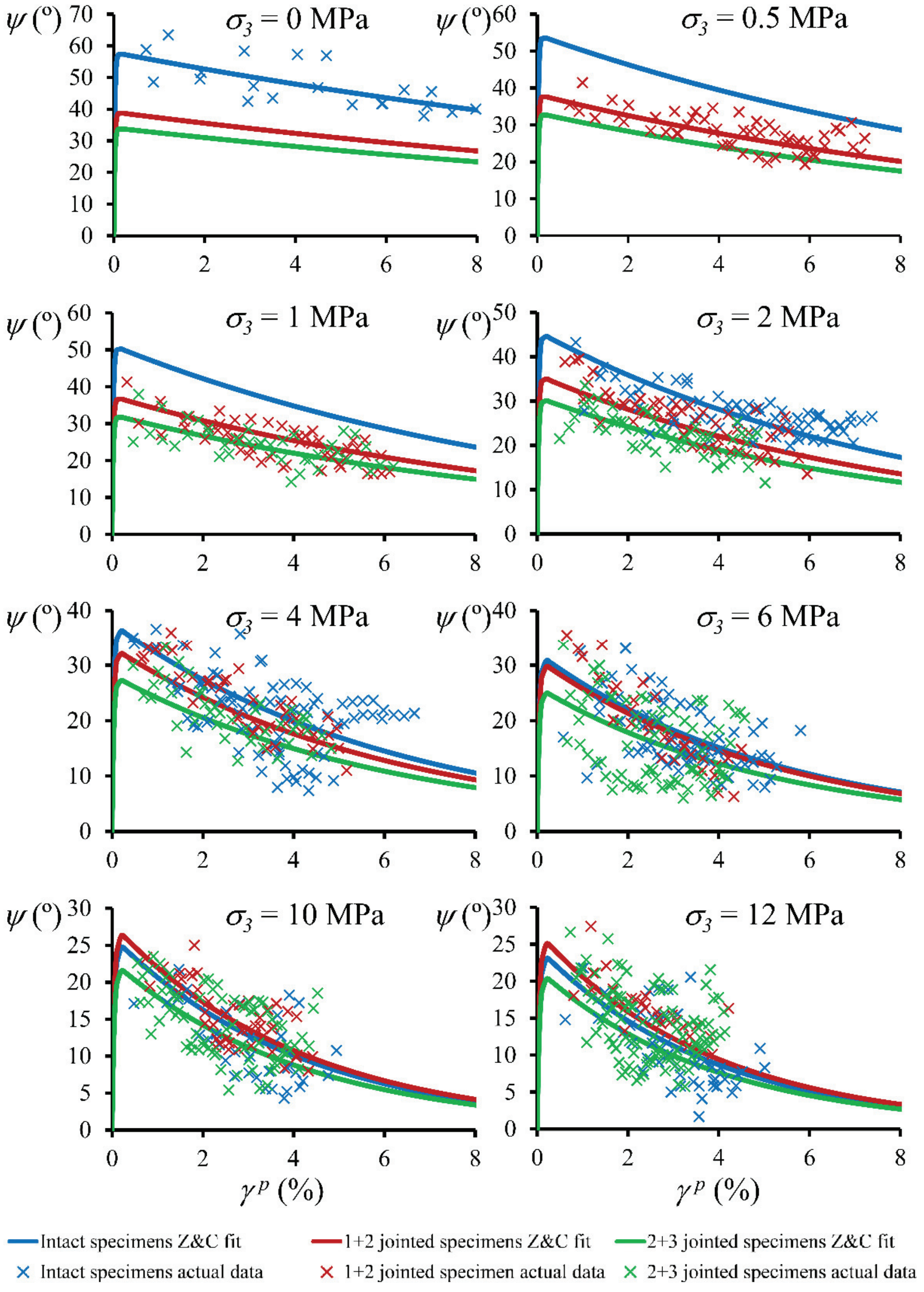

Fig. 6.19. Zhao & Cai (2010a) dilatancy model fits for different confining pressures and for the three types of specimens (intact, (1+2) joints and (2+3) joints). Please note the different vertical scale.

With the coefficients presented in Table 6.7, one can obtain the fit for the dilation data obtained in the lab as presented in Fig. 6.19. In this Fig. 6.19 it is represented the data as obtained from the lab for the intact (blue crosses), (1+2) (red crosses) and (2+3) (green crosses) jointed specimens as well as the Zhao & Cai (2010a) model for the intact (blue lines), (1+2) (red lines) and (2+3) (green lines) jointed specimens. At first sight, the dependencies of the dilation angle become evident: First, the dilation angle depends on the plastic shear strain: as the plastic shear strain increases, the dilation angle decreases; secondly, the dilation angle depends on confining stress: as the confinement increases, the dilation angle decreases; and finally, the dilation angle depends on the level of jointing: as the jointing increases, the dilation angle decreases, but this dependence is also dependent on the confining stress. The difference in the dilation angle between intact and jointed specimens is relatively high for low confinements, but this difference diminishes as the confining pressure increases, becoming almost imperceptible for confinements of around 6 MPa.

6.4.4.2. Walton & Diederichs (2015a) dilation angle model

Walton & Diederichs (2015a) have recently proposed a dilation model that requires between four and seven parameters (α_0, α', γ_m, β_0, β', γ_0 and γ') depending on the available data and the idiosyncrasy of the rock mass, to completely characterize the dilatational behavior. Mathematically it is based in a piecewise function that separates pre-mobilization of dilatancy, mobilization of peak dilatancy and post-mobilization of dilatancy. This division allows to consider each part separately, to perform a detailed study of the influence of each parameter on the model and to study correlations with other geomechanical parameters.

α_0 and α' parameters determine the curvature of the pre-mobilization portion of the model for unconfined and confined conditions respectively. In this study these parameters have been set to 0.1 and 0.01 respectively as these were the values recommended by the authors as a reasonable lower bound (Walton & Diederichs, 2015a).

γ_m parameter defines the plastic shear strain at which peak dilation is achieved. It has been set to 1 mstr. (0.1%) for this study as recommended by the authors (Walton & Diederichs, 2015a).

The peak dilation angle is forced to be equal to the peak friction angle for unconfined conditions. This worked fine for the intact specimens, but it did not for the (1+2) and (2+3) jointed specimens (which could not be tested under unconfined conditions), because the failure under unconfined conditions will not happen through the rock but following existing discontinuities. So it is not possible to correctly assign a peak dilation angle based solely on the friction angle of the rock for unconfined conditions and no laboratory data. For the fit of the model, a reasonable value for each type of specimen following the observed trends was selected.

β_0 and β' parameters define the dependence of the peak dilation angle with σ_3 for low and high confining pressures respectively. The authors (Walton & Diederichs, 2015a) define what are low and high confining pressures comparing the confinement with an exponential function depending on β_0 and β'. For intact specimens of the Blanco Mera granite low confinements were those below 2.4 MPa and for the (1+2) and (2+3) jointed specimens the low confining pressures are below 0.001 MPa. Walton & Diederichs suggest values of β_0 and β' of 0.97 and 0.054 respectively for the intact Blanco Mera Granite specimens, but a better fit was obtained using a value of β' equal to 0.24, this could better capture the peak dilation angle dependence with confinement, as it can be observed in Fig. 6.21.

Finally, γ_0 and γ' parameters define the decay rate of the dilation angle for unconfined and confined conditions respectively. The authors suggest a value of γ_0 of around 200 for a granite like the Blanco Mera one, but it became a quite high value and it had to be reduced to 132.74 to get a correct fit of the unconfined conditions. Moreover, a constant decay rate for the different confining pressures (i.e. a constant γ') became unrealistic and a quite good logarithmic fit depending on the confining pressure for this parameter was obtained (Fig. 6.20), a very low confining pressure (0.001 MPa) was considered as the unconfined condition to get rid of the problem of the natural logarithm of zero . Unfortunately, since unconfined tests could not be performed for jointed specimens, the logarithmic fit lacks of data near the unconfined conditions and therefore the curvature of the fit shown for these specimens in Fig. 6.20 should be considered only as an indicative of the trend of this parameter.

The required parameters for this dilation model are presented in Table 6.8., and the results of applying this model to the different specimens and the different confining pressures are shown in Fig. 6.21.

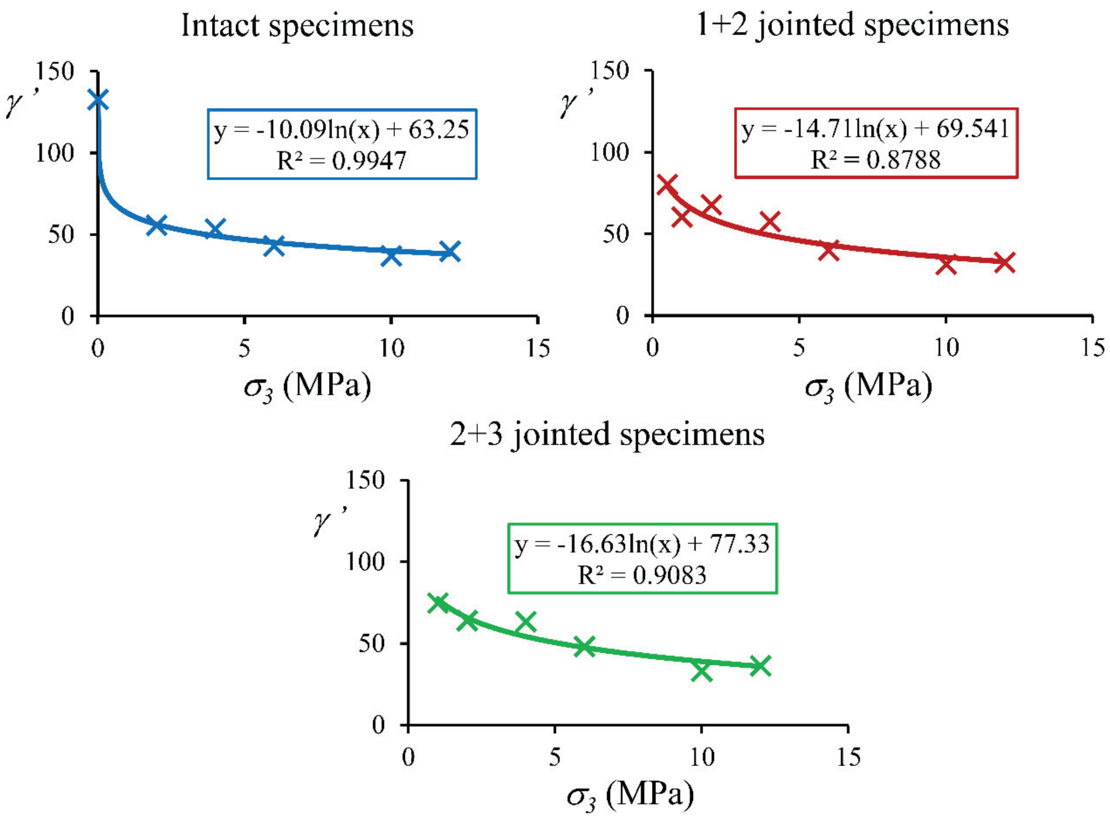

Fig. 6.20. Variation of the parameter γ' of the Walton & Diederichs (2015a) dilation model with confining pressure for the three types of specimens tested.

Table 6.8. Parameters of the dilation angle model proposed by Walton & Diederichs (2015a) for the three types of Blanco Mera granite specimens tested.

	Intact specimens	(1+2) jointed specimens	(2+3) jointed specimens
α_0	0.1	0.1	0.1
α'	0.01	0.01	0.01
γ^m (mstr)	1	1	1
β_0	0.97	0.7	0.59
β'	0.24	0.04	0.04
γ_0 (mstr)	132.736	132.736	132.736
γ' (mstr)	$10.09 \cdot \ln(\sigma_3) + 63.25$	$14.71 \cdot \ln(\sigma_3) + 69.541$*	$16.63 \cdot \ln(\sigma_3) + 77.33$*

* fits only given as indicative of the trend due to the lack of data for unconfined tests

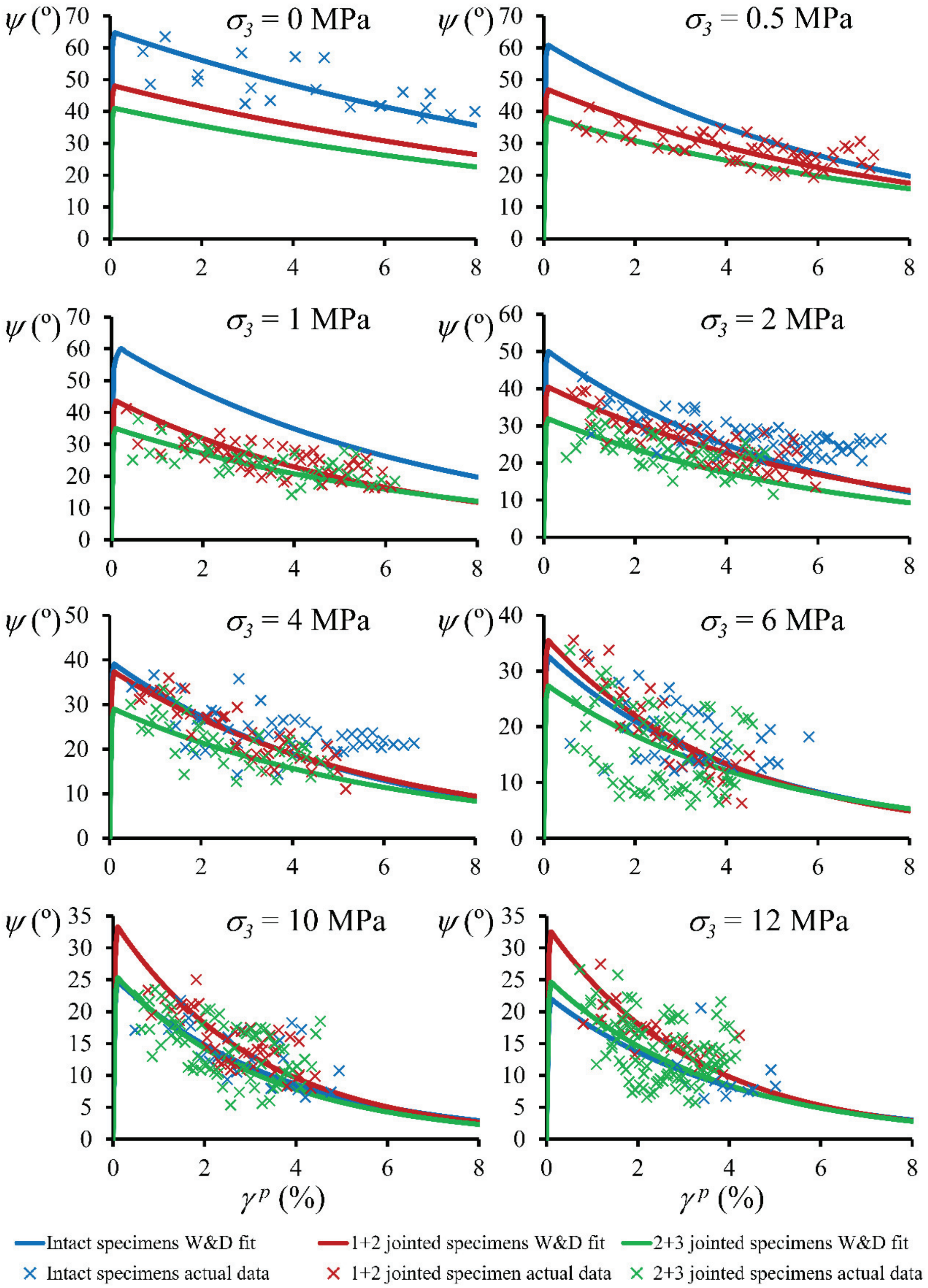

Fig. 6.21. Walton & Diederichs (2015a) dilatancy model fits for different confining pressures and for the three types of specimens (intact, (1+2) joints and (2+3) joints). Please note the different vertical scale.

6.4.5. A brief comment about the irrecoverable strain locus

As commented above, the irrecoverable strain locus was obtained for each test due to the ability of the press to perform unloading-reloading cycles and to measure the amount of hydraulic fluid displaced outwards or inwards the Hoek's cell in order to maintain the confining pressure.

The irrecoverable strain locus links the axial and volumetric plastic strains and allows to compute the dilation angle, as explained in previous chapters. Comparing the irrecoverable strain loci of two different specimens one can observe which specimen dilates more than the other without any kind of equation. This fact can be observed in Fig. 6.5 and in Fig. 6.22: (2+3) jointed specimens (green curve) do not present so much volumetric strain as intact specimens (blue curve), indicating that the jointed specimen dilate much less than intact one.

Additionally, it has been observed that moving the irrecoverable strain loci of fissured samples downwards and rightwards in a volumetric strain-axial strain diagram, this irrecoverable strain loci tend to superpose on the same curve for intact specimens and even for less fractured specimens, as illustrated in Fig. 6.22. This seems to suggest that in the process of rock fissuring in the lab or in the process of rock failure in nature to produce a jointed rock mass, an irrecoverable strain takes place in such a way that when the material is reloaded it retakes the volumetric strain process, stopped at a particular stage in the past.

This observation is consistent with the already commented (Chapter 5) behavior of axial and radial strains (this can also be observed in Fig. 6.5): in all cases, the stress-strain response of the jointed cores tends to approximate that for the intact cores for large strains, it is as if the jointed cores had already undergone the deformations corresponding to the earlier, steeper part of the softening portion of the curve.

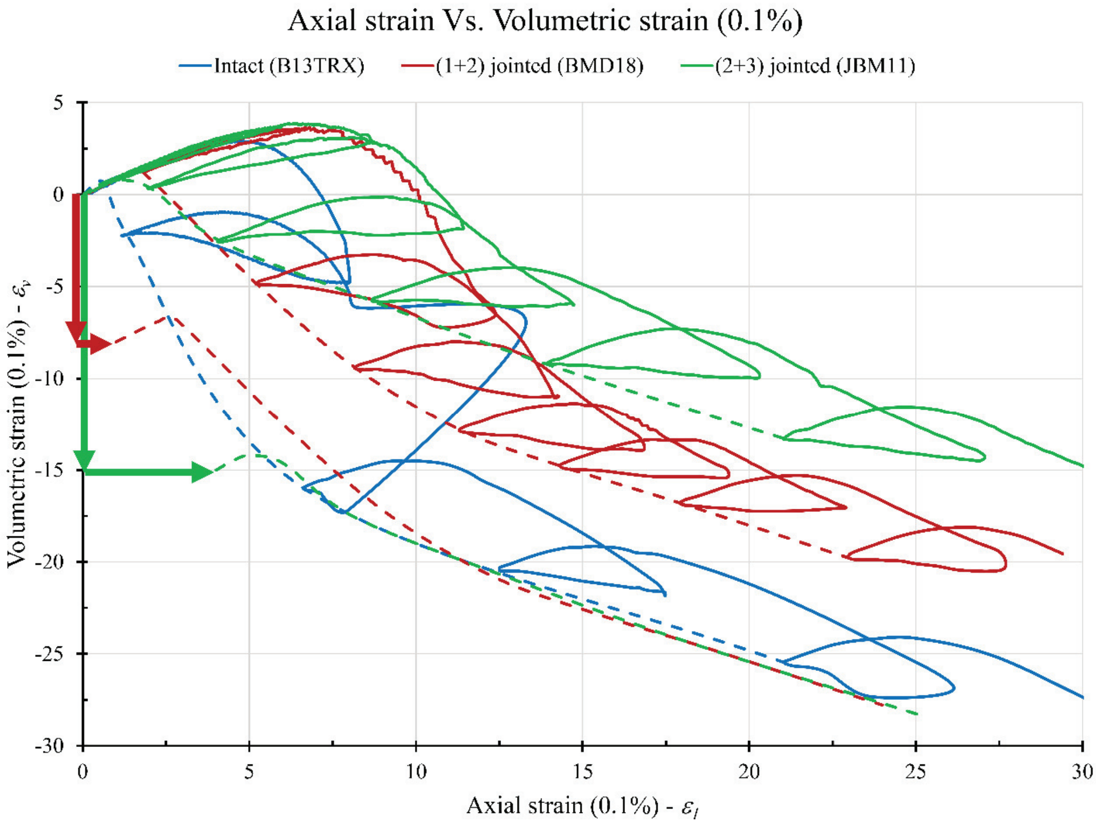

Fig. 6.22. Volumetric strain vs. axial strain response of three characteristic samples as in Fig. 6.5, where also the irrecoverable strain locus is delineated in dotted lines. Observe that moving the irrecoverable strain loci of fissured samples downwards and rightwards, these irrecoverable strain loci tend to superpose over the locus corresponding to intact rock sample.

6.5. Discussion

Results of tests on intact and jointed samples have been presented. Empirical based correlations (Hoek & Diederichs, 2006) of elastic moduli suggest that (1+2) and (2+3) jointed samples behave elastically similar to rock masses, presenting average values of GSI around 56 and 50 respectively. The application of the Hoek & Brown approach to peak strength results suggests that jointed and even more jointed samples' strength would correspond to rock masses presenting average values of GSI around 82 and 67, respectively. But if strength results are reduced to 70 % of the recorded values —in order to remove the scale-effect— the GSI value corresponding to (1+2) jointed samples becomes 65 and that for (2+3) jointed samples 50. Additionally, post-failure response indicates that the jointed samples behave as rock masses showing decreasing drop moduli and less dilation. In the case of (2+3) jointed samples a value of GSI of 40 can be roughly estimated from approaches regarding post-failure response of rock masses. In conclusion, the response of (2+3) jointed samples may represent a rock mass with average rock mass quality (*GSI*=50-40), whereas that of (1+2) jointed samples represent a somewhat better quality rock mass (55-65).

If we think now in a standard 4 m diameter tunnel excavated in a granitic rock mass showing a regular pattern of normal discontinuities with fair behavior and presenting an spacing of 0.9 m, an equivalent GSI of around 60 would be obtained. In the case of a spacing of 0.4 m, the estimated GSI would be around 50 (Fig. 6.23). If we could test a 1 m diameter and 2 m high sample in both cases, the presented structure would be homothetic to that presented in our jointed samples, as circles a, b and c in Fig. 6.1. The stress strain response of these samples would be representative of the rock mass at the scale of the tunnel. Since the rock structure in these samples would be homothetic to our samples, the response of our samples should be the same of the rock mass, once corrected the scale effect. We have corrected the scale effect (by considering 70% of peak strength) and we have shown that, in a rough way, the response of our samples is similar to that expectable for the equivalent rock mass.

This suggests that once reduced the scale effect, by considering a 70 % of the computed value of peak strength for every test in jointed samples, the stress-strain response could be similar to that expectable in equivalent rock masses at the scale of the engineering work. Therefore, tests in jointed samples as presented can be of interest to investigate rock mass behavior. Remark that, in the same way as in rock joints, peak strength seems to be affected by scale but residual strength does not seem to be (Barton & Bandis, 1982).

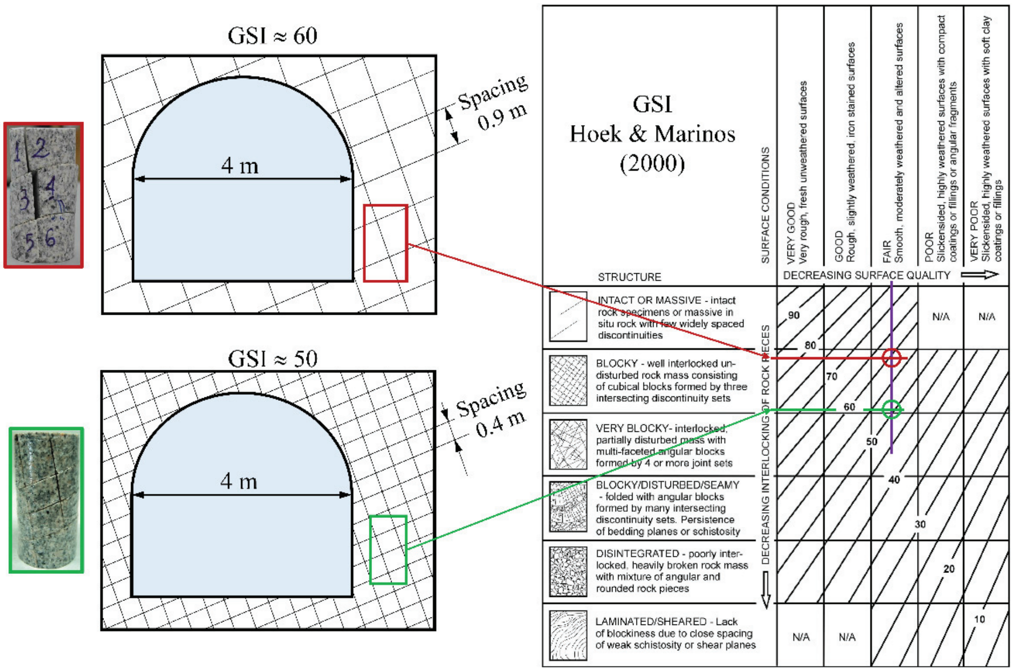
GSI ≈ 60
Spacing 0.9 m
4 m
1 2
3 4
5 6
GSI ≈ 50
Spacing 0.4 m
4 m
GSI
Hoek & Marinos
(2000)
SURFACE CONDITIONS
VERY GOOD Very rough, fresh unweathered surfaces
GOOD Rough, slightly weathered, iron stained surfaces
FAIR Smooth, moderately weathered and altered surfaces
POOR Slickensided, highly weathered surfaces with compact coatings or fillings or angular fragments
VERY POOR Slickensided, highly weathered surfaces with soft clay coatings or fillings
STRUCTURE
DECREASING SURFACE QUALITY
INTACT OR MASSIVE - intact rock specimens or massive in situ rock with few widely spaced discontinuities
BLOCKY - well interlocked un-disturbed rock mass consisting of cubical blocks formed by three intersecting discontinuity sets
VERY BLOCKY- interlocked, partially disturbed mass with multi-faceted angular blocks formed by 4 or more joint sets
BLOCKY/DISTURBED/SEAMY - folded with angular blocks formed by many intersecting discontinuity sets. Persistence of bedding planes or schistosity
DISINTEGRATED - poorly inter-locked, heavily broken rock mass with mixture of angular and rounded rock pieces
LAMINATED/SHEARED - Lack of blockiness due to close spacing of weak schistosity or shear planes
DECREASING INTERLOCKING OF ROCK PIECES
90
80
70
60
50
40
30
20
10
N/A
N/A
N/A
N/A

Fig. 6.23. An approach to estimate rock mass parameters based on tested jointed samples representative of rock mass structure and comparison with the traditional approach based on GSI.

Even if the jointed samples present very regular fracture patterns, and the showed results are limited, the above indicated approaches suggest that the behavior of rock masses is largely controlled by their structure, and this structure is associated to the geological stress history of the rock mass. Therefore, a continuous behavior in terms of the complete stress-strain curve can be derived as presented in Fig. 6.24. This is in line with Archambault et al. (1993) suggestion on the fact that patterns of shear and tension discontinuities and the resultant shear strength scale effects in rocks and rock masses are the end result of a progressive material and mass softening mechanism associated to progressive shear deformation and failure, and to rotational simple shear complexity, which takes place at all scales.

In Fig. 6.24, the evolution of axial stress-axial strain behavior for three different levels of confinement is represented (Fig. 6.24. a). The strength weakening is associated either to the occurrence of joint in a sample or to that of a joint structure in a rock mass. As far as the rock is more jointed or the rock mass more fractured, the peak strength diminishes even if residual strength seems to keep constant (Fig. 6.24.b), the material is more deformable (Fig. 6.24.d), and the capability of dilating is more limited (Fig. 6.24.c).

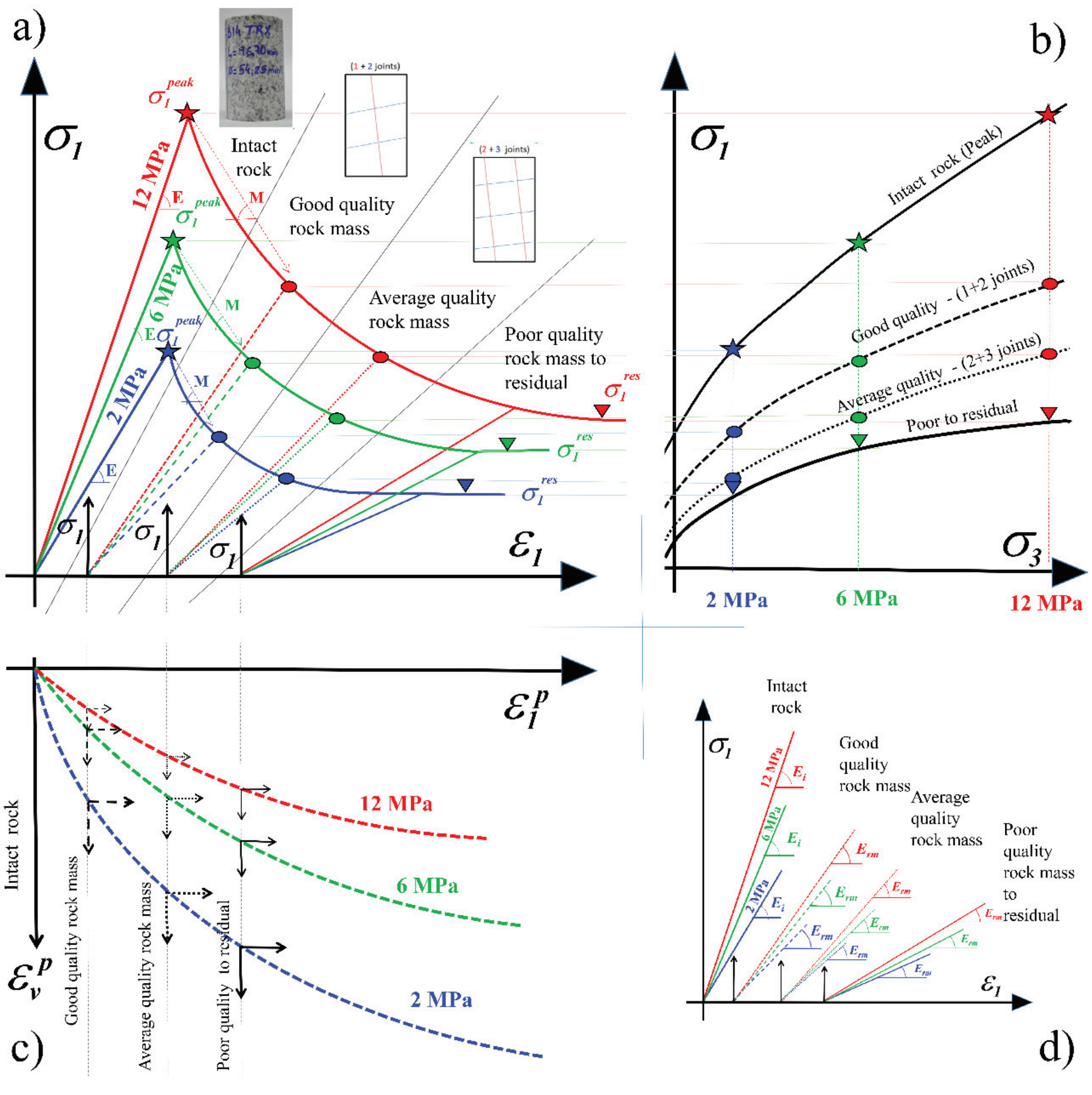

Fig. 6.24. Deduced behavior of intact and increasingly fissured rock samples in parallel with decreasing quality rock masses in terms of a) axial stress-axial strain, b) strength, c) volumetric strain response and d) elastic moduli.

6.6. Conclusions of this chapter

In previous chapters, the author performed lab studies on the effect of the structure in the strength, deformability and post-failure characteristics of granite at lab scale (Arzúa & Alejano, 2013; Arzúa et al., 2014). This experimental program included intact and artificially jointed samples (one sub-vertical and two sub-horizontal joints). In this chapter, the database has been enlarged with results of tests on even more jointed samples (two sub-vertical and three sub-horizontal joints). From the complete stress-strain curves, the elastic (tangent and secant Young's modulus and Poisson's ratio), peak (peak strength), and post-peak (residual strength, drop modulus and dilation trends) parameters have been computed or estimated for each performed test, the results of all the performed tests on the different granites and specimens are presented in the Appendix B.

Obtained results permit to observe the changes in deformability, peak and residual strength, and post-failure behavior of these 'small-scale rock masses' and the results for (2 + 3) jointed samples generally follow the trends derived from (1+2) jointed samples. Associating the role of the structure to the observed complete stress-strain response of the specimen can improve our understanding of the actual complete mechanical response of rock masses.

Peak strength and elastic Young's modulus clearly depend on jointing, even if the first parameter is also somewhat dependent in scale. The level of fracturing (joint intensity) or GSI at a larger scale can be used to control the evolution of these parameters under particular circumstances. However, results suggest that the structure seems to affect the elastic response more significantly than the peak strength response of the samples. These results evidence that strength and stiffness reduction in hard rock masses seems to be linked more relevantly to the structure than to scale.

As noted earlier by the author (Chapter 5), axial and radial strain curves (represented against stress) in jointed specimens, tend to mimic the equivalent curves for sound samples starting from a particular stress level in the descending branches of these curves, Accordingly, residual strength does not seem to be much affected by the degree of initial jointing. This suggests the possibility of estimating rock mass residual strength starting from lab testing, as otherwise suggested by other authors (Cai et al., 2007; Exadaktylos & Tsoutrelis, 1993).

Post-failure deformability is significantly depending on the level of confinement and it is clearly also sensible to the level of jointing. In this way, more fractured rock samples tend to dilate not so much as fresh rock or good quality rock masses at low confinement stress levels (i.e. those occurring in the vicinity of excavations). This can be associated to the presence of planar joints in the sample less rough than newly formed shear bands. This trend is also in line with Hoek & Brown (1997) guidelines for rock mass dilation estimate.

To conclude, the complete stress-strain curves of rock and small-scale rock mass samples, starting from laboratory strength tests were obtained. Some clear and interesting trends on the behavior of rocks compared to jointed rocks were captured. They could be of help to improve our insight on rock mass behavior, linking lab results on jointed tests to rock mass response.

7. Strain-softening characterization of granitic rocks and numerical simulation of servo-controlled strength tests.

7.1. Introduction

The relevance of a thorough knowledge of the complete stress-strain curve in rock has frequently been highlighted in the rock mechanics field, and most particularly, in its earlier breakthroughs (Hudson et al., 1971b). The aim of the present research is to study the actual behavior of rocks and to propose strain-softening and dilation models able to better represent the observed stress-strain response of rock samples.

It is widely acknowledged that rocks and also rock masses suffer a strain-softening or strength-weakening process after achieving peak stress. This is a complex behavior, so even simple strain-softening models need a good number of parameters to reproduce its most relevant features.

Simple strain-softening models for rocks require at least elastic parameters (E and ν), peak and residual strength envelopes (typically two parameters each, as for instance: c^{peak}, ϕ^{peak}, c^{res} and ϕ^{res}) and two post-failure parameters (for instance drop modulus, M, and dilatancy, ψ). These 8 parameters serve to recover the main features of this type of behavior (see upper graphs of Fig. 7.1). However, one must admit that this representation is still not very similar to the actual stress-strain response of rock tests, as it can be derived from the comparison of this representation to actual test results, as shown in the lower graphs of Fig. 7.1. In this chapter, a possible approach to provide a more accurate model to simulate strain-softening behavior of granitic rocks as observed in the lab is studied.

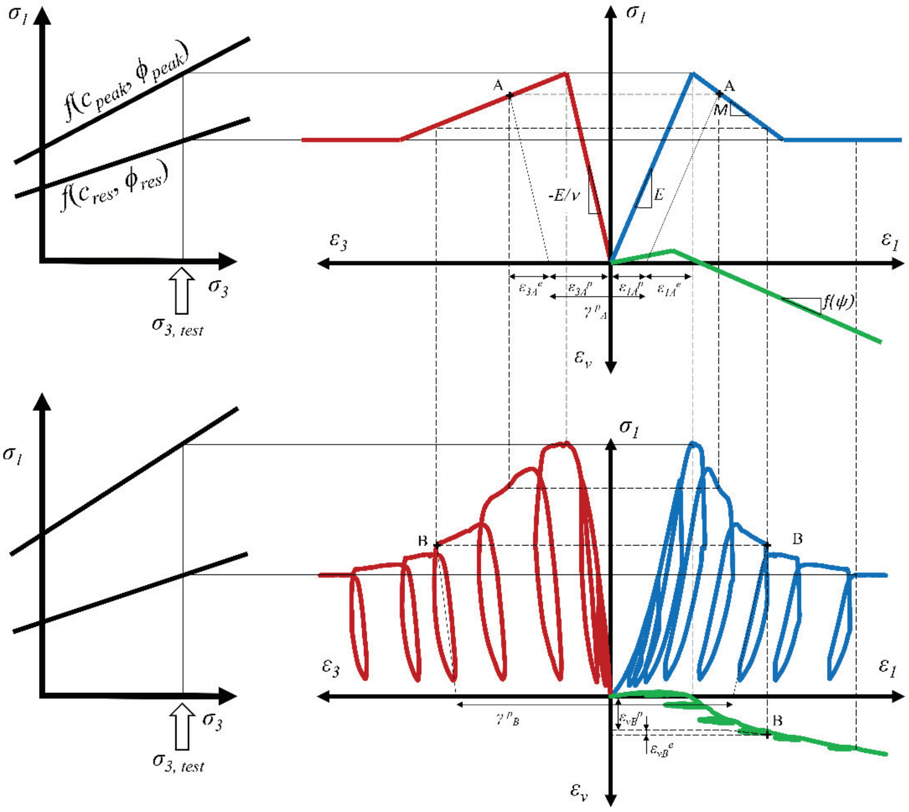

Fig. 7.1. Theoretical (simple strain-softening) and actual stress-strain response of a rock sample submitted to a triaxial test in the laboratory.

This chapter has been presented at the EUROCK 2013 Symposium with the following citation: Arzúa, J., Barbiero, J. & Alejano, L.R. 2013. Strain-softening characterization of granitic rocks and numerical simulation of servo-controlled strength tests. EUROCK2013. Rock Mechanics for Resources, Energy and Environment. Kwásniewski & Łydzba (eds). 23-26 September. Wrocław, Poland

To study this behavior the three series of around thirty unconfined and confined strength tests (σ_3 in the range 0-12 MPa) in three different granitic rocks named Amarelo País, Blanco Mera and Vilachán, respectively shown in Chapter 3 (Fig. 7.2) are considered. To do this, a servo-controlled press was modified to control the axial stress during tests and also to measure the volume of hydraulic fluid displaced from Hoek's cell in triaxial tests, so that the volumetric strain in the sample can be computed.

Fig. 7.2. Tested samples in the lab.

As a result complete stress-strain curves for different confinements in the three different granitic rocks have been obtained, one of these stress-strain curves is shown in Fig. 7.3.

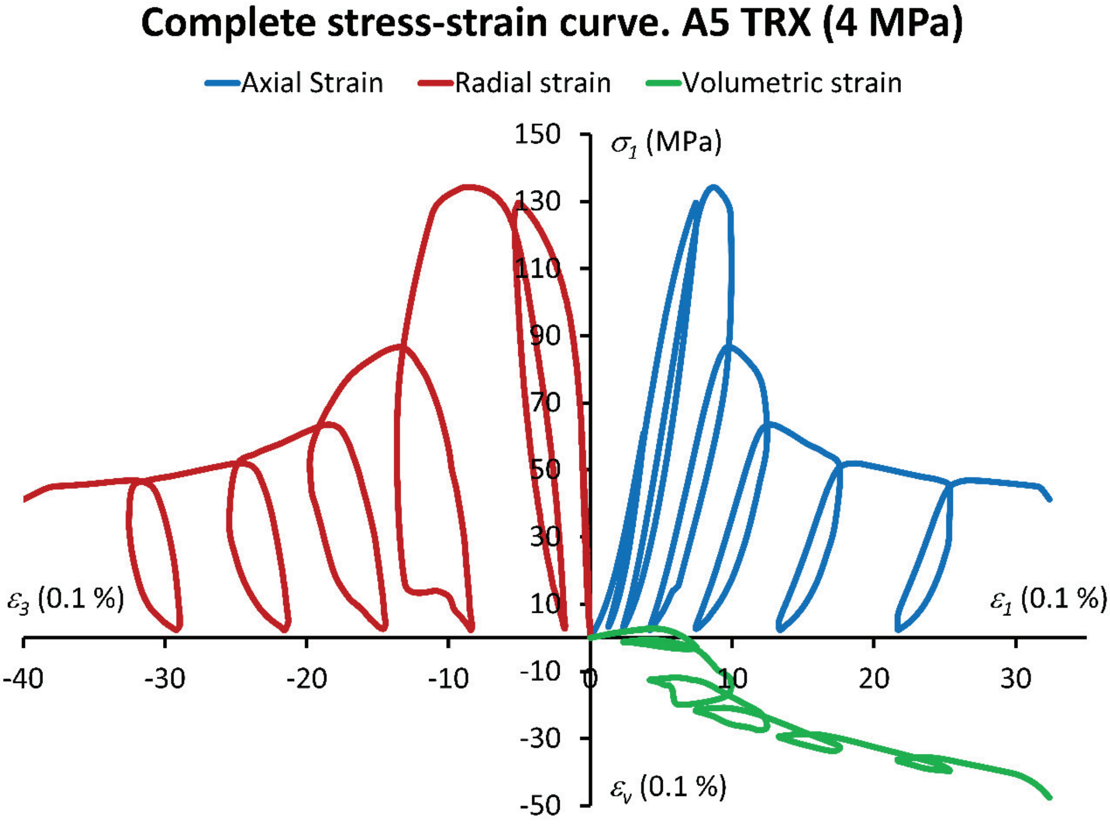

Fig. 7.3. Complete stress-strain curve from a triaxial test.

In what follows, a methodology to characterize this type of behavior is proposed in order to obtain numerical parameters able to reproduce the behavior observed in the lab.

In strain-softening behavior models, a softening parameter, η, controls strength capacity. Although η can be defined in a number of ways, the most widely used variable is shear plastic strain, obtained as the difference between the major and minor principal plastic strains, as follows:

$$\gamma^p = \varepsilon_1^p - \varepsilon_3^p \tag{7.1}$$

This variable can be computed as shown in Fig. 7.1 and Fig. 7.4.

7.2. Methodology

7.2.1. Correlation between strength and plastic strain

Based on results in confined tests (three or four tests for every granite and every confining stress of 2, 4, 6, 10 and 12 MPa) as shown in Fig. 7.4, the values of σ_1 corresponding to pre-peak (the point where the line σ_1 - ε_1 loses its linearity, related to the known as transition between stable and unstable crack propagation also called long term UCS) were marked. The values of peak and residual σ_1, and intermediate points between these values (25, 50 and 75%) were also computed.

Finally, the plastic shear strain values associated to all of these points have been estimated, as illustrated on Fig. 7.4. In this way, for each test, pairs of values σ_1 - γ^p representing yield envelopes for different levels of plasticity have been recovered. See for instance in Fig. 7.5 the graph of these results for σ_3 = 4 MPa for one of the tested granites.

Starting from these series of data points, a curve to adjust these results was searched in the literature, and a curve like the one presented in eq. (7.2) was found, which can accommodate the results reasonably well.

$$\sigma_1 = a\left[1-e^{-b\gamma^p}-\frac{c}{c+d}\left(1+\frac{be^{-(c+d)\gamma^p}-(c+d)e^{-b\gamma^p}}{c+d-b}\right)\right] \tag{7.2}$$

where a, b, c and d are constants that can be fitted for every rock and confinement level. These values have been fitted and the values of these constants against the confinement stress for every granite type were represented. In this way the values of these parameters as a function of σ_3 for every granite type as shown in Table 7.1 were obtained. In fact those are yield functions depending on σ_3 and the level of plasticity suffered in terms of γ^p.

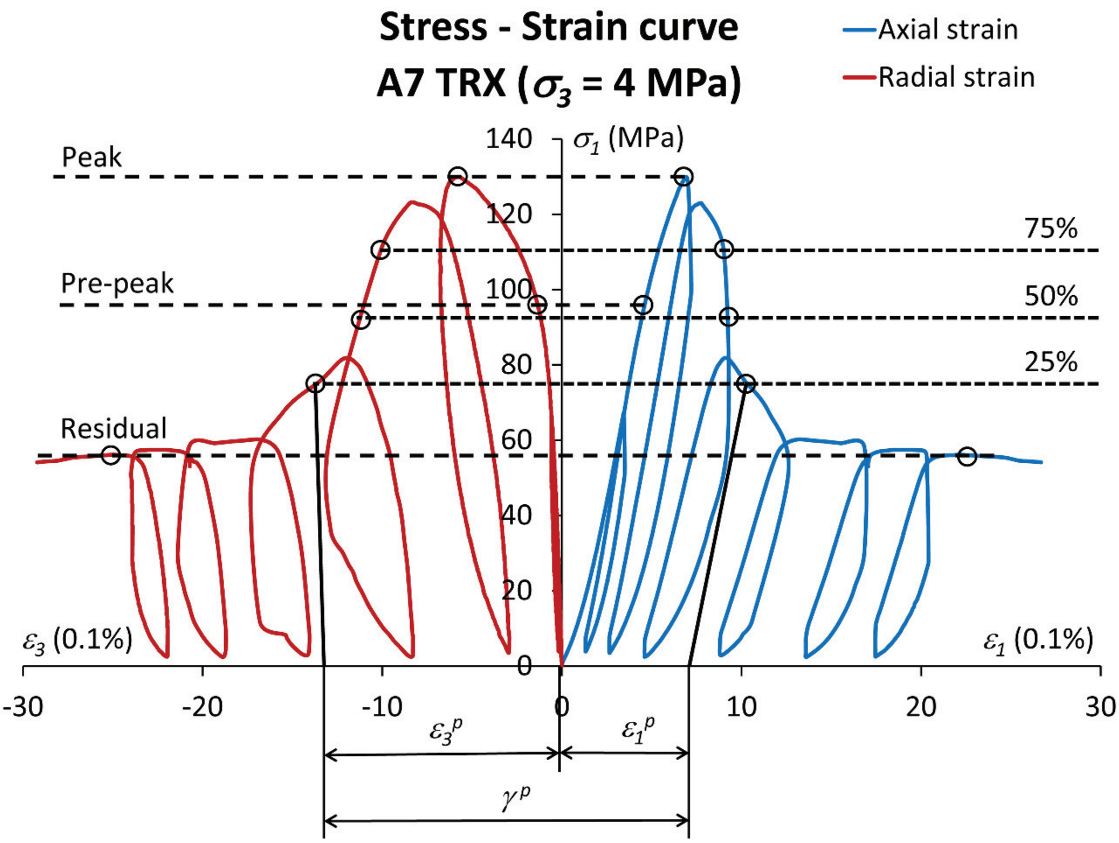

Fig. 7.4. Estimate of relevant σ_1-γ^p points from stress-strain complete curves as explained in the text.

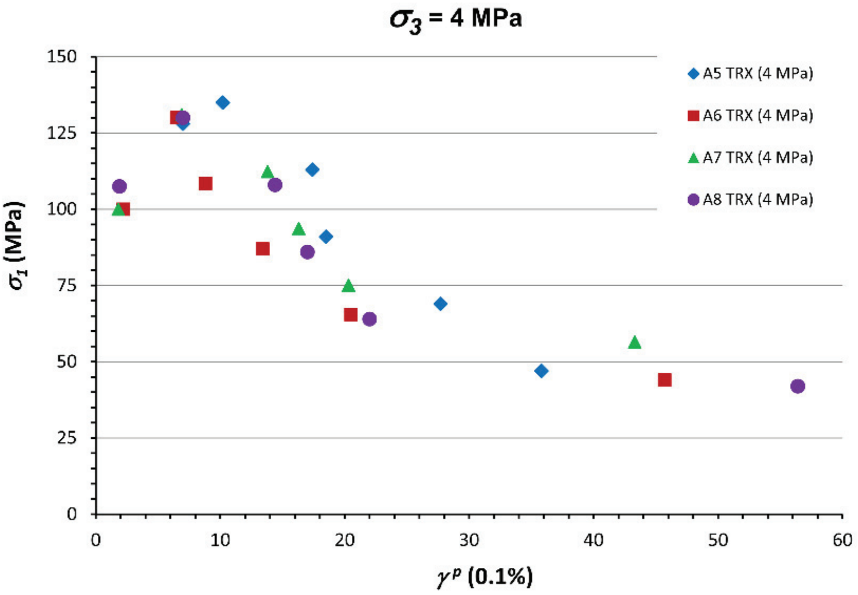

Fig. 7.5. Representation of σ_1-γ^p points for triaxial tests with σ_3 = 4 MPa for Amarelo País granite.

Table 7.1. Fit of parameters a, b, c and d dependent on σ_3 for the three different tested granites.

	Amarelo País	R^2
$a =$	$28.078 \cdot \sigma_3 + 212.74$	0.967
$b =$	$-0.0011 \cdot \sigma_3 + 0.1835$	0.385
$c =$	$0.0034 \cdot \sigma_3 + 0.1154$	0.437
$d =$	$0.0004 \cdot \sigma_3 + 0.0200$	0.139
	Blanco Mera	
$a =$	$13.918 \cdot \sigma_3 + 224.62$	0.933
$b =$	$0.0031 \cdot \sigma_3 + 0.6828$	0.156
$c =$	$-0.0004 \cdot \sigma_3 + 0.0610$	0.034
$d =$	$0.0007 \cdot \sigma_3 + 0.0091$	0.441
	Vilachán	
$a =$	$31.968 \cdot \sigma_3 + 282.93$	0.968
$b =$	$0.0005 \cdot \sigma_3 + 0.1611$	0.00003
$c =$	$0.0001 \cdot \sigma_3 + 0.1441$	0.0007
$d =$	$0.00002 \cdot \sigma_3 + 0.0167$	0.007

Results of these curves for the three different granites analyzed and for various confinements are presented in Fig. 7.6, Fig. 7.7 and Fig. 7.8, together with the original $\sigma_1 - \gamma^p$ points derived from actual tests.

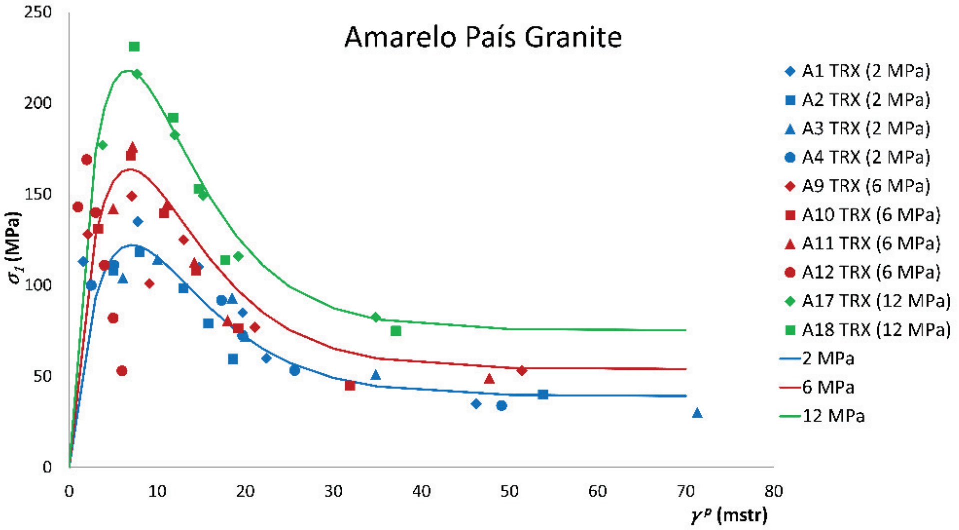

Fig. 7.6. Fitted curves relating σ_1 and γ^p for different confining stresses together with points derived from tests on Amarelo País granite samples.

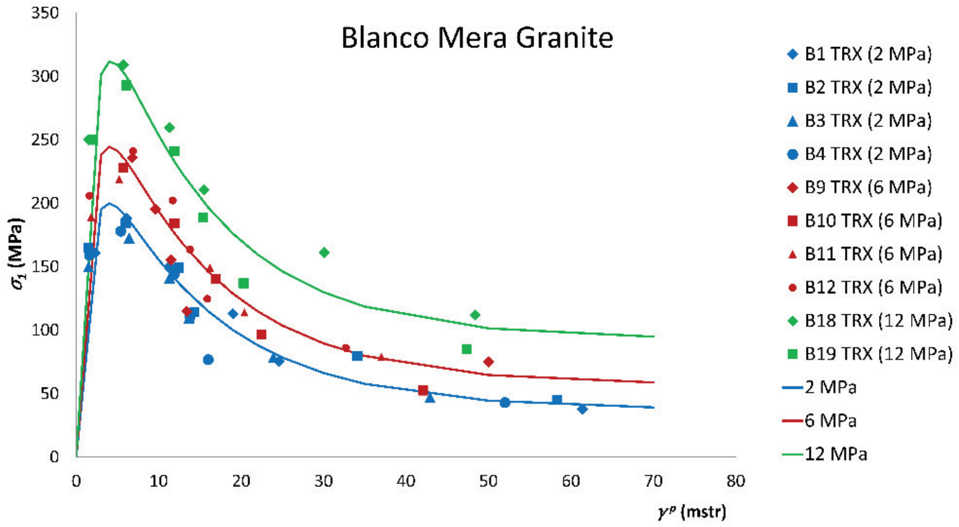

Fig. 7.7. Fitted curves relating σ_1 and γ^p for different confining stresses together with points derived from tests on Blanco Mera granite samples.

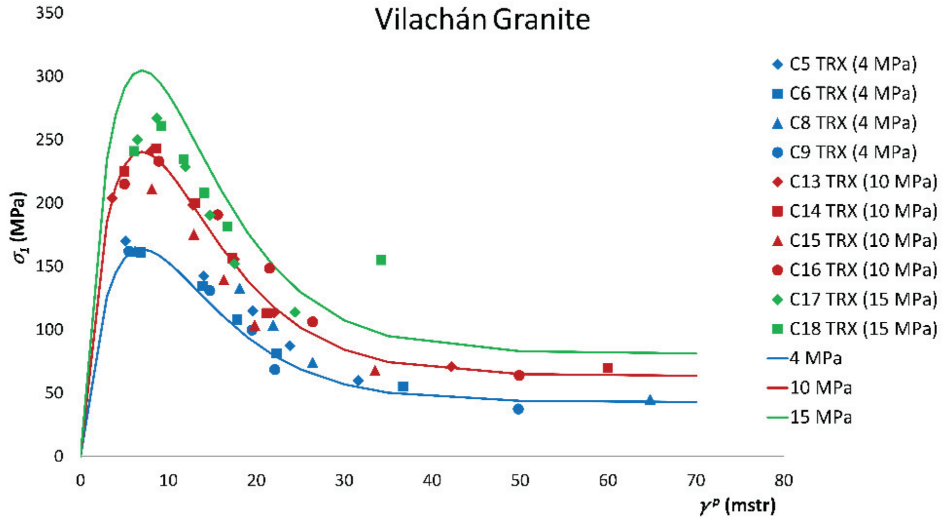

Fig. 7.8. Fitted curves relating σ_1 and γ^p for different confining stresses together with points derived from tests on Vilachán granite samples.

7.2.2. Correlation between dilatancy and plastic strain

For rocks the dilation angle is smaller than the friction angle (Vermeer & De Borst, 1984). These authors proposed as a suitable way to assess dilatancy:

$$\psi = \arcsin \frac{\dot{\varepsilon}_v^p}{-2\dot{\varepsilon}_1^p + \dot{\varepsilon}_v^p} \tag{7.3}$$

This formulation is valid for the interpretation of triaxial tests. The plastic axial strain can be obtained as shown in Fig. 7.1 and Fig. 7.4. Some unloading-reloading cycles are necessary to obtain more or less accurate values of the plastic volumetric strain (Fig. 7.1). Linking the points of minimum strain in every cycle, the called irrecoverable strain locus is obtained, and from it, values of ε_v^p and ε_l^p can be recovered. Based on this line, one can obtain a number of ψ-γ^p pairs, for every test.

This has been done in Chapter 3 and published elsewhere (Arzúa & Alejano, 2013) and dilatancy has been estimated according to the approach developed by Zhao & Cai (2010a), which relates dilation angle with plastic shear strain (expressed in percentage of deformation):

$$\psi = \frac{a'b'\left(e^{-b'\gamma^p} - e^{-c'\gamma^p}\right)}{c' - b'} \tag{7.4}$$

Where moreover *a'*, *b'* and *c'* fit the following expressions:

$$\begin{aligned} a' &= a'_1 + a'_2 \cdot e^{\frac{-\sigma_3}{a'_3}} \\ b' &= b'_1 + b'_2 \cdot e^{\frac{-\sigma_3}{b'_3}} \\ c' &= c'_1 + c'_2 \cdot \sigma_3^{c'_3} \end{aligned} \tag{7.5}$$

Using equations (7.5) another 3 coefficients are necessary to fit each confining dependent parameter in equation (7.4). These coefficients have been fitted following the ideas by Zhao & Cai (2010a) and they are presented in Table 7.2.

Table 7.2. Parameters of the plastic shear strain and confining stress dependent dilation angle model as proposed by Zhao & Cai (2010a) for the three studied granitic rocks.

	Amarelo País	Blanco Mera	Vilachán
a_1'	29.01	21.13	3.79
a_2'	28.05	36.71	53.65
a_3'	4.76	4.92	4.46
b_1'	8.26	20.63	10.38
b_2'	17.49	29.44	49.69
b_3'	1.5	2.97	2.19
c_1'	0.014	0.047	0.058
c_2'	0.0749	0.049	0.050
c_3'	0.711	0.589	0.295

There exist more simple models of dilatancy depending on confinement stress and plasticity such as that proposed by Alejano & Alonso (2005). However, the results on granite samples of this dissertation did not seemed to fit very well this model, which was initially developed back-analyzing test results on samples of sedimentary rocks, such as coal, mudstone, siltstone and sandstone.

7.3. Model results

With this information of evolving yield criteria, as in eq. (7.2) and Table 7.1, and dilation, as in eq. (7.4) and Table 7.2, and once also derived the elastic parameters (E and ν), it is possible to model or reproduce results of tests by means of calculation sheets, and compare them against actual results.

Let's start with the elastic phase, and then when arriving at pre-peak, the values of σ_1 according to eq. (7.2) and the values of ψ according to eq. (7.4) for every value of γ^p are recovered. Then and accounting for:

$$\gamma^p = \varepsilon_1^p - \varepsilon_3^p = \varepsilon_1^p - \frac{\mathrm{K}_\psi}{2}\varepsilon_1^p = \varepsilon_1^p\left(1-\frac{\mathrm{K}_\psi}{2}\right)$$
$$\mathrm{K}_\psi = \frac{1+\sin\psi}{1-\sin\psi} \tag{7.6}$$

It is possible to obtain the values of ε_1^p and ε_3^p associated to every σ_1:

$$\varepsilon_1^p = \frac{\gamma^p}{\left(1-\frac{\mathrm{K}_\psi}{2}\right)}$$
$$\varepsilon_3^p = \frac{\mathrm{K}_\psi}{2}\varepsilon_1^p \tag{7.7}$$

The corresponding elastic counterpart, ε_1^e and ε_3^e, are derived from the elastic constants:

$$\varepsilon_1^e = \frac{\sigma_1}{E}$$
$$\varepsilon_3^e = \frac{\sigma_1}{-E/\nu} \tag{7.8}$$

So one can obtain the corresponding ε_1 and ε_3, associated to every σ_1, as well as the corresponding value of ε_v:

$$\varepsilon_1 = \varepsilon_1^e + \varepsilon_1^p$$
$$\varepsilon_3 = \varepsilon_3^e + \varepsilon_3^p \tag{7.9}$$
$$\varepsilon_v = \varepsilon_1 + 2\varepsilon_3$$

In this way, the model of the complete stress-strain curve of any test can be obtained. Examples of the model and actual tests for samples of the three studied granites are shown in Fig. 7.9.

This representation of results is much more accurate and realistic than the typical simple strain-softening models usually used for standard modelling, as that presented in the upper graphs of Fig. 7.1.

Amarelo País - A12 TRX (6 MPa)

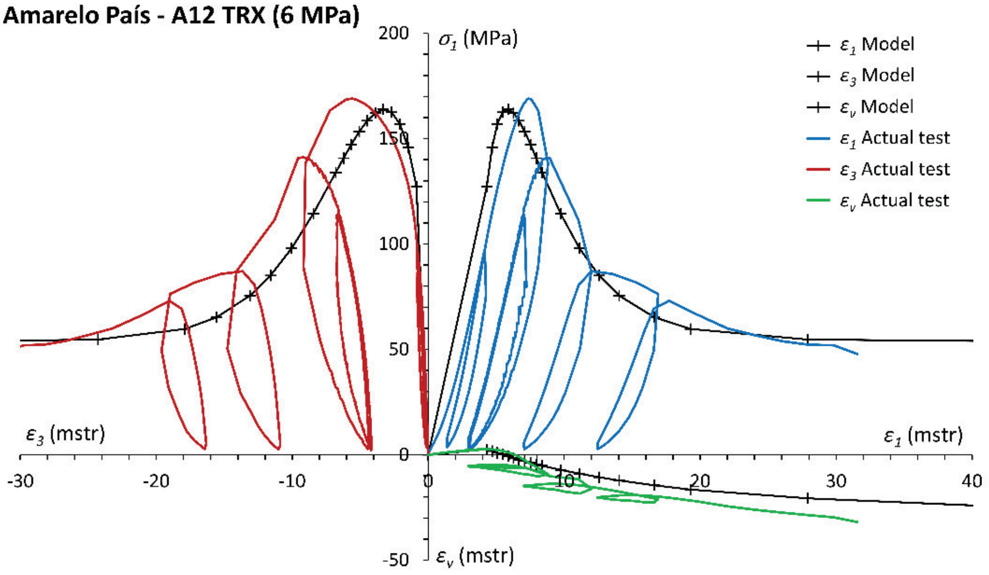

Blanco Mera - B12 TRX (6 MPa)

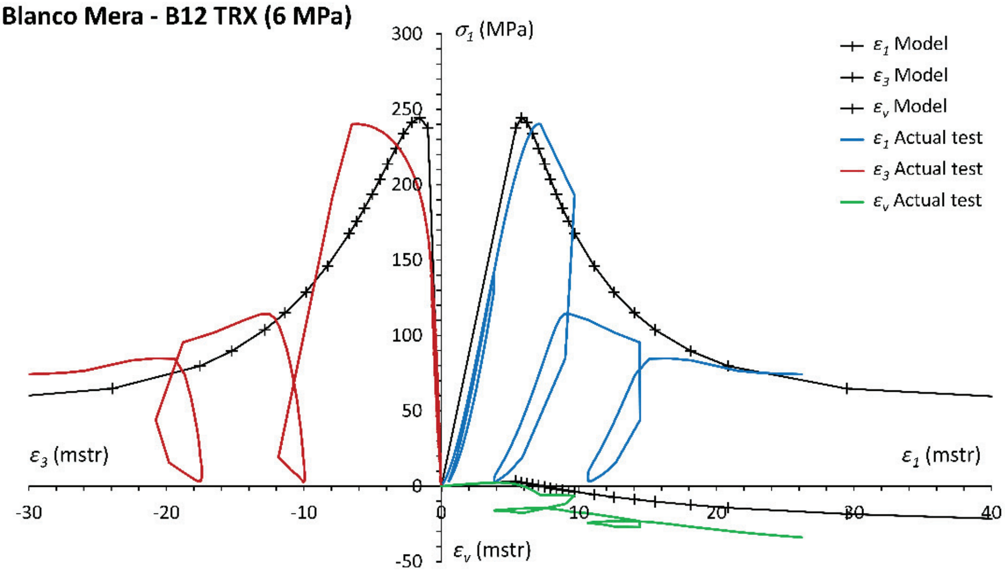

Vilachán - C12 TRX (6 MPa)

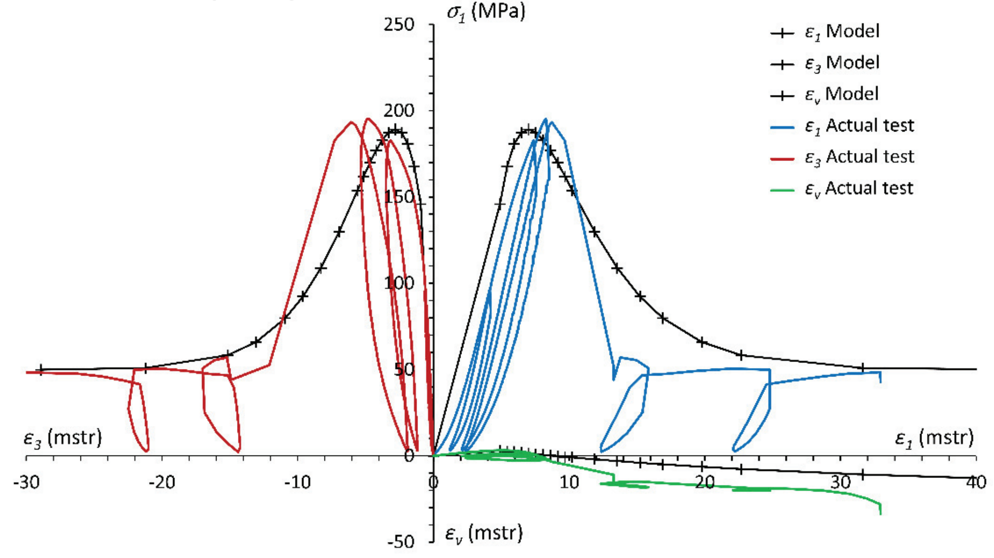

Fig. 7.9. Model and actual complete stress-strain curves of tests for samples of the three studied granites (Amarelo País, Blanco Mera and Vilachán), submitted to a confinement stress of 6 MPa.

7.4. Numerical approach

The code FLAC (Itasca, 2011) has been used to try to reproduce test results. In order to model numerically the laboratory triaxial strength tests, it is first necessary to implement the presented behavior model in the selected code.

7.4.1. Implementation of behavioral model

Code FLAC, implements an incremental plastic parameter e^{ps}, whose incremental form is:

$$\Delta e^{ps} = \left\{ \frac{1}{2}\left(\Delta\varepsilon_1^{ps} - \Delta\varepsilon_m^{ps}\right)^2 + \frac{1}{2}\left(\Delta\varepsilon_m^{ps}\right)^2 + \frac{1}{2}\left(\Delta\varepsilon_3^{ps} - \Delta\varepsilon_m^{ps}\right)^2 \right\}^{1/2} \tag{7.10}$$

where $\Delta\varepsilon_m^{ps} = \frac{1}{3}\left(\Delta\varepsilon_1^{ps} + \Delta\varepsilon_3^{ps}\right)$ and $\Delta\varepsilon_j^{ps}$ with j = 1, 2, 3 are the principal increments of the shear plastic strain.

This incremental plastic parameter can be related to the more standard γ^p or plastic shear strain. If a strain-softening material with constant dilation angle is considered, in addition characterized by a plastic potential, then, the following relationship between γ^p and η_{FLAC} can be deduced (Alonso et al., 2003):

$$\eta_{\mathrm{FLAC}} = \frac{\sqrt{3}}{3}\sqrt{1 + \mathrm{K}_\psi + \mathrm{K}_\psi^2}\,\frac{\gamma^p}{1 + \mathrm{K}_\psi} \tag{7.11}$$

The reader can check how for null dilation $\eta_{\mathrm{FLAC}} = \gamma^p/2$.

On the other hand and in order to obtain the evolving failure criteria starting from eq. (7.2) and parameters in Table 7.1, it is possible to obtain strength values for any confinement and for different values of γ^p. This has been done and linear strength envelopes have been fitted for a number of values of γ^p (from 3 to 13 mstr. 1 by 1, from 13 to 25 mstr. 3 by 3 and 25, 30, 35, 50 and 70 mstr.). For these linear envelopes, estimates of cohesion, *c*, and friction, ϕ, were obtained.

Also for every value of γ^p (and σ_3 and type of granite) one can compute dilatancy as per eqs. (7.4) and (7.5) with parameters in Table 7.2. And with dilatancy and γ^p it is possible to obtain η_{FLAC} as in eq. (7.11). An internal language subroutine has been created to update dilatancy values following Zhao & Cai (2010a) dilatancy angle model every certain number of steps.

To introduce the behavior model and parameters in FLAC, pairs of points (c, η_{FLAC}) and (ϕ, η_{FLAC}) for the failure criteria were used as those shown in Table 7.3, for the case of Vilachán granite.

7.4.2. FLAC models

Simple models of triaxial tests have been created resorting to the axi-symmetric geometrical possibilities of FLAC. Models present the half section of the cylindrical specimens with a rotation axis in its left part (Fig. 7.10). The servo-control has been modelled by means of a subroutine which induces a constant velocity (5e-8 m/step) in the upper and lower faces of the sample. Additionally, a confinement stress is induced on the right hand side (Fig. 7.10). Models corresponding to confinement stresses of 2, 6 and 10 MPa are run for the three different granites and for 5 different mesh sizes including 10×40, 15×60, 20×80, 25×100 and 40×160 (Fig. 7.10), in order to control and study the role of mesh in test result, which is known to control strain-softening numerical models. An example of a FLAC model (that one corresponding to the Amarelo Pais granite with a confining stress of 6 MPa and a mesh size of 40×80) is presented in Appendix C.

Table 7.3. Values of friction and cohesion for different values of the plastic parameters (first γ^p, and then, e^{ps}, obtained from γ^p, and dilatancy) for the case of Vilachán granite with a confining stress of 6 MPa (similar tables are obtained for different confinements and for the different granites).

Granite Vilachán				
γ^p	6 MPa		ϕ	c
(mstr.)	K_ψ	$e^{ps} = \eta_{FLAC}$	(°)	(MPa)
3	1.81	0.0015	57.87	11.17
4	1.81	0.0020	59.94	11.96
5	1.80	0.0025	61.03	12.40
6	1.79	0.0030	61.54	12.61
7	1.77	0.0035	61.69	12.65
8	1.76	0.0040	61.58	12.57
9	1.74	0.0046	61.28	12.40
10	1.73	0.0051	60.83	12.17
11	1.71	0.0056	60.26	11.51
12	1.70	0.0061	59.60	11.61
13	1.69	0.0066	58.86	11.29
16	1.65	0.0081	56.31	10.32
19	1.61	0.0096	53.48	9.41
22	1.58	0.0111	50.62	8.63
25	1.55	0.0126	47.94	7.99
30	1.50	0.0151	44.24	7.24
35	1.46	0.0176	41.68	6.79
50	1.35	0.0251	38.74	6.34
70	1.25	0.0351	38.27	6.28

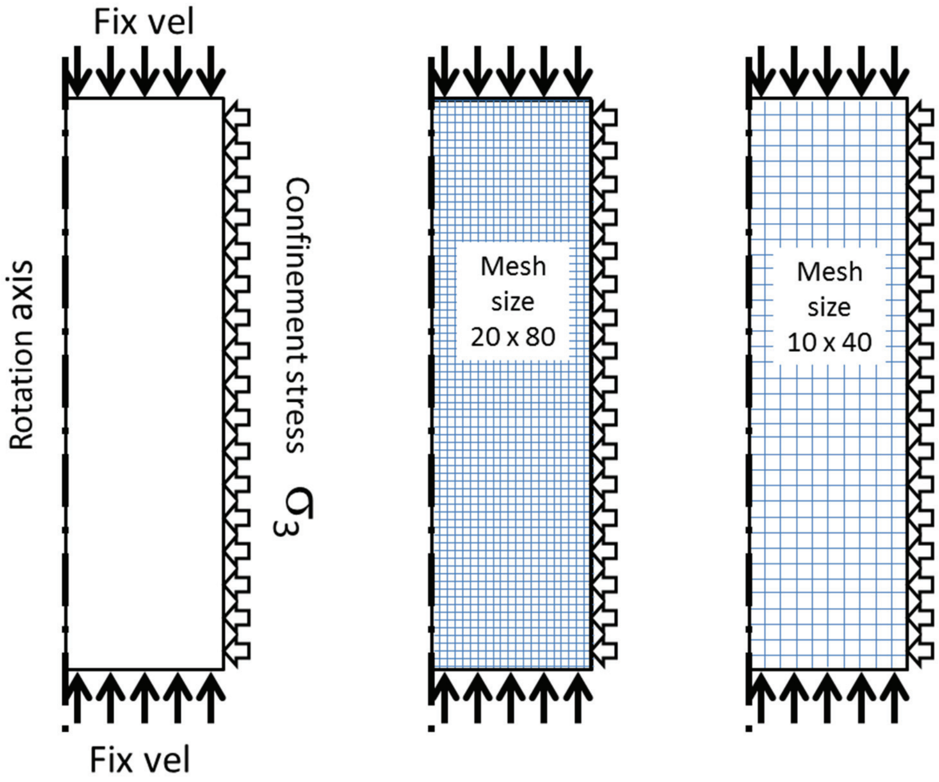

Fig. 7.10. Boundary conditions and example of two grids used to numerically model the triaxial tests.

7.4.3. FLAC results

As an example of the results obtained, the numerical results with mesh size 15 x 60 of two triaxial tests (2 and 6 MPa) on Amarelo Pais granite are presented together with actual test results in Fig. 7.11. Fig. 7.12 illustrates the numerical results of a triaxial test (6 MPa, Amarelo Pais) together with FLAC results in this case for three different mesh sizes.

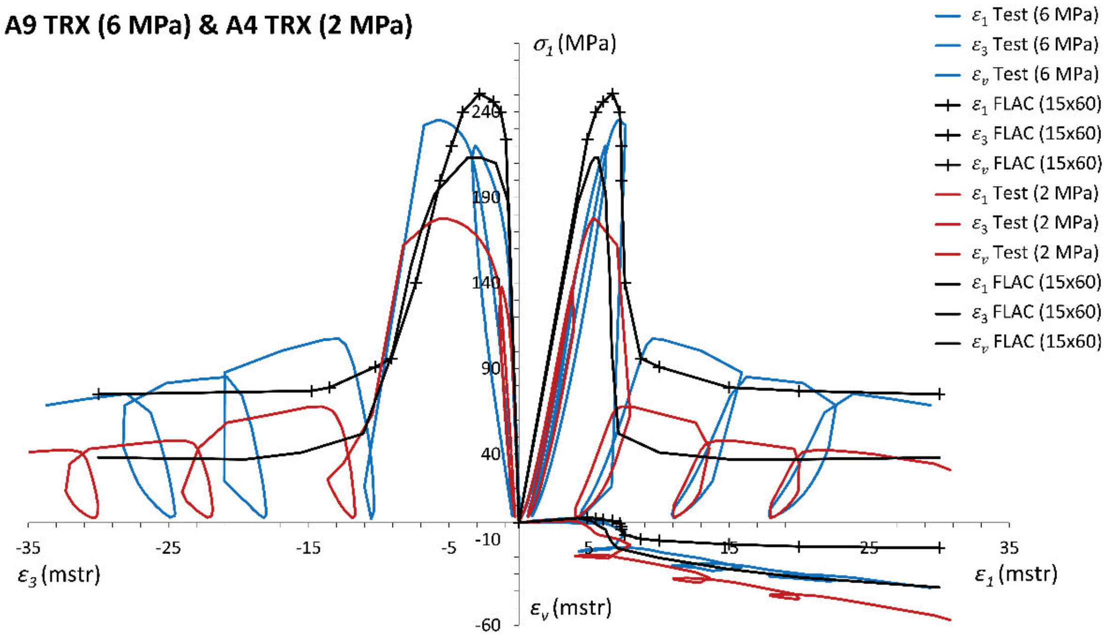

Fig. 7.11. Complete stress-strain curve (σ_1 - ε_1, σ_1 - ε_3 and ε_v - ε_1) for two triaxial tests (2 and 6 MPa) in Amarelo Pais granite. Actual tests and FLAC results with mesh size 15 x 60 corresponding to such confining pressures.

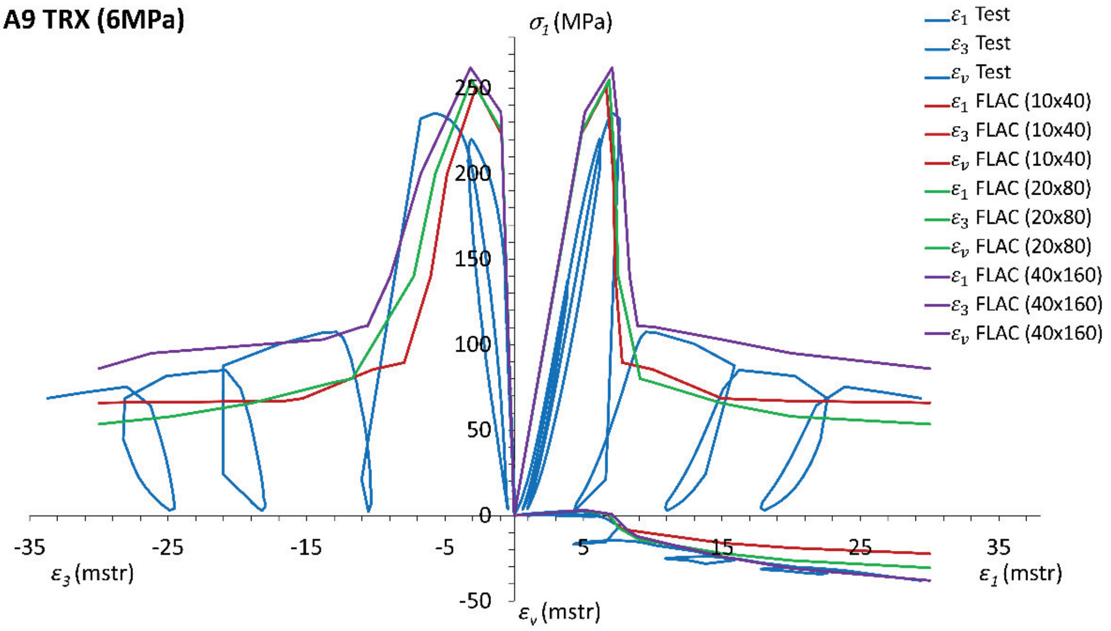

Fig. 7.12. Complete stress-strain curve (σ_1 - ε_1, σ_1 - ε_3 and ε_v - ε_1) for a triaxial test (6 MPa) in Amarelo Pais granite. Actual test and FLAC results with meshes 10x40, 20x80 and 40 x160.

The obtained numerical results can be considered a reasonably similar representation of tests even if, as usually happens in rock mechanics, there are slight discrepancies, so a number of points are to be remarked and some comments are in order.

Strength is well represented by models. Peak strength values observed in models tend to be slightly larger than those observed in tests. This trend is more marked for smaller meshes. Residual strength values are generally well captured by tests, particularly for average mesh sizes (15×60 and 20×40). Smaller meshes tend to overestimate the observed residual values. In the radial strain, ε_3, branch, the model does not capture well the large deformation in the phase between the elastic part and the peak. This is difficult to capture for every model and it is due to the 'negative dilatancy' of this phase.

The drop phase, between the peak and residual stage, is usually steeper in the models than in the tests in the axial branch, ε_1, especially for larger meshes. However, in the radial branch, actual tests and results are more alike. The behavior of this drop phase is partially controlled by the occurrence of shear bands, particularly for finer meshes. Some results concerning the orientation of shear bands are being derived, but for the sake of briefness they are not presented in this study.

Volumetric strain, ε_v, is in general well reflected in many tests, although in some cases, it is slightly underestimated. This fact can be associated to the steeper response of the axial strain in the drop phase.

Certainly, mesh size affect results, as it is well known for the case of strain-softening (Varas et al., 2005) and, there are a number of differences highlighted in the previous paragraphs. Most of these differences are however, within the limits of the natural variability of tests. All in all, the obtained results are more realistic than those derived by means of standard simple strain-softening approaches, as that shown in the upper part of Fig. 7.1.

7.5. Conclusions of this chapter

In this study, and starting from servo-controlled triaxial compressive strength tests with unloading-reloading cycles on granite samples, a strain-softening behavior model is proposed where evolving strength (from peak to residual values) is related to a plastic parameter and where dilation is a confinement stress and plastic shear strain dependent parameter.

Three different granite types are characterized according to the above indicated behavior models and simple computations are performed, able to represent the complete stress-strain curve as observed in the laboratory for granite samples with a good level of accuracy.

Moreover, this non-simple behavior model has been implemented in FLAC in our best possible way and accounting for the particularities of this code (different plastic parameter, evolving failure criteria in Mohr-Coulomb terms…). Axi-symmetric models of the tests in the different granites with different mesh sizes have been run to find out that numerical results of the complete stress-strain curve are a reasonably accurate representation of the actual observed behavior.

8. Impact of post-failure rock mass behavior on excavation response

8.1. Introduction

The extent of rock failure and the displacements induced by the process of excavation around an underground opening are closely related to the rock mass behavior. Whereas, at low depth, joints usually control instability mechanisms, in deep excavations the compression-induced failure processes of rocks and large deformations of the openings are the basic concern.

With the increasing use of numerical models in rock engineering in recent decades, excavation design has often come to rely on numerical studies. A visit to a number of publications on this topic reveals that in many cases simple behavior models, such as the elastic-perfectly-plastic one, are used to analyze rock mass behavior. More complex behavior models accounting for post-failure phase such as strain-softening are seldom utilized. Finally, the role of the dilation angle is rarely taken into account; and when it is considered, the approach tends to be extremely simplistic.

Hoek & Brown (1997) suggested that rock mass behavior may vary according to the quality of the rock mass. They proposed that the elastic-brittle (EB) behavior properly represents the behavior of good to very good quality rock masses (GSI > 75). Strain-softening (SS) behavior seems to adequately model the typical stress-strain response of average quality rock masses (25 < GSI < 75). Finally, elastic-perfectly-plastic (EPP) behavior seems to accommodate reasonably well the stress-strain response of low quality rock masses (GSI < 25) (Fig. 8.1). From a mathematical perspective, this last behavior, where peak and residual failure criteria are the same, is relatively easy to work with. Remark that EPP and EB behaviors can be considered as limiting cases of the more general SS behavior.

Alejano & Alonso (2005) described a new model to estimate the dilation angle in rocks and rock masses. It showed dependencies on confining stress, on the plasticity suffered by the material and indirectly on scale; the whole study was based on results of tests on sedimentary rocks. The model could be implemented in numerical codes such as FLAC (Itasca, 2011).

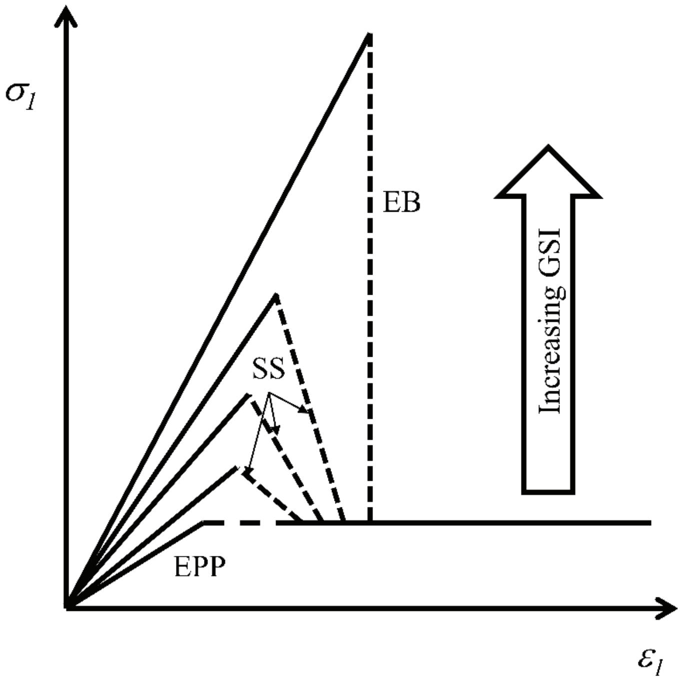

Fig. 8.1. Schematic behavior of rock masses according to rock mass quality, as suggested by Hoek & Brown (1997).

This chapter has been presented at the 46th US Rock Mechanics – Geomechanics Symposium with the following citation: Alejano, L.R., Arzúa, J., Alonso, E. 2012. *Impact of post-failure rock mass behavior on excavation response.* 46th US Rock Mechanics / Geomechanics Symposium. 24-27, June. Chicago. 3:2166-2176

Zhao & Cai (2010a) proposed an evolved mobilized dilation angle model. Based on the model response, and in combination with grain size description and uniaxial compressive strength of rocks, the approach was generalized for different rock types including hard rocks. In a subsequent study, Zhao & Cai (2010b) performed numerical simulations to study excavation-induced displacement around excavations located in different rock mass types using their model extended to rock masses. They showed that the displacement distributions obtained were more reasonable than standard models when compared to general trends observed underground.

Even if strain-softening (SS) behavior can reasonably represent average quality rock mass behavior, it was still not easy to obtain representative values for all the parameters needed to simulate this behavior. This includes peak and residual failure criteria (for instance, peak and residual cohesion, friction and tensile strength for the Mohr-Coulomb failure criterion). These parameters also include elastic properties, namely elastic Young's modulus, E, and Poisson's ratio, ν, and post-failure deformation parameters such as the drop modulus, M, and dilation, ψ.

Obtaining a reasonably accurate estimate of all these parameters for SS rock masses is not a simple matter, even with the helpful tools developed in recent years by Hoek & Brown (1997), Hoek et al. (2002), Crowder & Bawden (2006) and Cai et al. (2004, 2007). A general characterization approach has recently been proposed by Alejano et al. (2010) based on the indicated references and accumulated experience. It can be considered as a reasonable initial approach that should be fine-tuned on a case-by-case basis and it is used in this study to estimate some of the input parameters needed for the models and particularly shear plastic strain limit ($\gamma^{p}*$), or the value of the shear plastic strain ($\gamma^{p} = \varepsilon_{1}^{p} - \varepsilon_{3}^{p}$) at which the residual strength level is attained.

Within this framework, in this chapter the author first present a series of servo-controlled tests on a granite rock, from which the most relevant parameters have been derived. These tests also contribute as experimental data to complete the database needed to study dilation, so far non-existing in granitic rocks (Zhao & Cai, 2010a).

Then the author have considered three rock masses of different rock mass quality (GSI equal to 65, 50 and 35) formed by this granite and located at considerable depth. The author would like to highlight the fact that such rock masses had been once massive non-jointed granite masses formed deep in the earth crust. Once submitted to high stresses (over the strength of the rock) due to tectonic processes, the granitic rock failed, producing 2 or 3 joint sets and, as a consequence, the major principal stress is relaxed, so the stress energy has now become failure and deformation. Then it could be considered an average quality rock mass.

As previously stated, average quality rock masses behave in a strain-softening way. This behavior is also observed in triaxial tests in the laboratory for granites (Fig. 8.2). From the author's scope, as far as a rock is suffering more unloading-reloading cycles, it behaves in the same way as a worse quality rock mass and therefore in a more ductile (elastic-perfectly-plastic) way. Moreover and as stated by Archambault et al. (1993), this seems to be true at all scales. Remark that, however, lab scale parameters cannot be directly extended to underground excavation behavior.

Once the rock masses are characterized as mentioned above, the strain-softening and variable dilation behavior is implemented in the two-dimensional code FLAC (Itasca, 2011) and some examples of tunnel excavations are run. These numerical models show that the response of a tunnel excavation in its section boundaries and its face are different from the one that could be expected for ideally elastic-perfectly-plastic rock masses in terms of the extent of the plastic aureole and deformation.

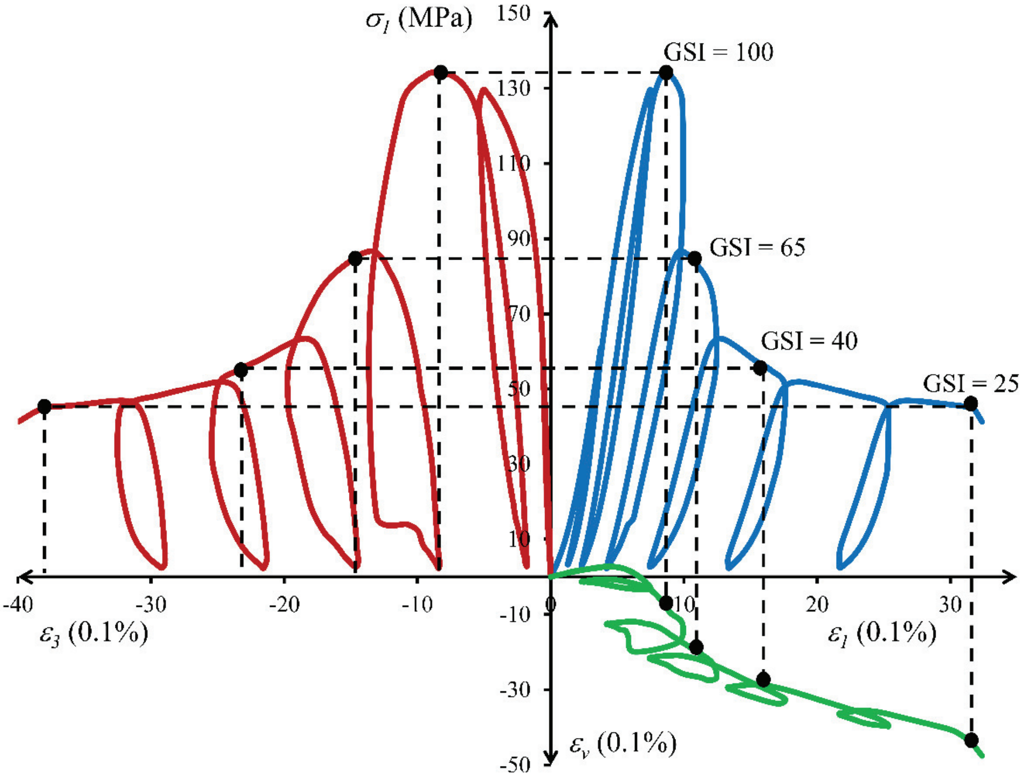

Fig. 8.2. Confined compressive test of a rock sample with unloading-reloading cycles and comparison to rock mass behavior, as explained in the text.

8.2. Laboratory characterization

In previous developments, the *John P. Harrison Rock Mechanics' Laboratory* of the University of Vigo set up a servo-control system in a standard 200 tons press, so that one can control the velocity of application of stress or strain, being able to perform different load path tests as desired and explained in Chapter 3. Reliable post-failure results in unconfined compressive tests in weathered granite were obtained (Alejano et al., 2009a).

A step forward has been to install a servo-control for the confinement stress in triaxial tests to control the confinement pressure while testing, but also to measure the volume of hydraulic fluid in the Hoek's cell, as proposed by Crouch (1970). Using water as hydraulic fluid it is possible to estimate the volumetric strain of the rock sample as far as the tests develop.

An experimental programme was planned to study a lightly weathered granitic rock, locally known as Amarelo Pais. It is a hard rock used in Galicia as a building material and it has been classified as adamellitic granite. It has a tan color and coarse texture. More than thirty 54 mm diameter specimens were cut from original 40 cm x 40 cm x 40 cm blocks provided by a quarry producer.

Typical results of unconfined tests are shown in Fig. 8.3.a, where it can be seen how to obtain the main parameters: peak and residual strength ($\sigma_{1,peak}$ and $\sigma_{1,res}$), elastic parameters (apparent Young's modulus, E; and apparent Poisson's ratio, ν) and also the drop modulus, M. Often, post failure parameters were not registered in unconfined tests because rock samples were too brittle for the press and the rock crushed in an explosive manner. However, these parameters have been computed whenever possible.

In triaxial tests (Fig. 8.3.b) it was impossible to directly measure radial deformation since strain gauges were previously discarded. On the other hand, one can measure volumetric strain and, starting from this value and from the axial strain, it was possible to estimate the radial strain. All the tests were performed meeting the basics of the standards (ISRM, 2007).

Table 8.1 shows the most relevant strength, elastic and post-failure parameters recovered from every test performed.

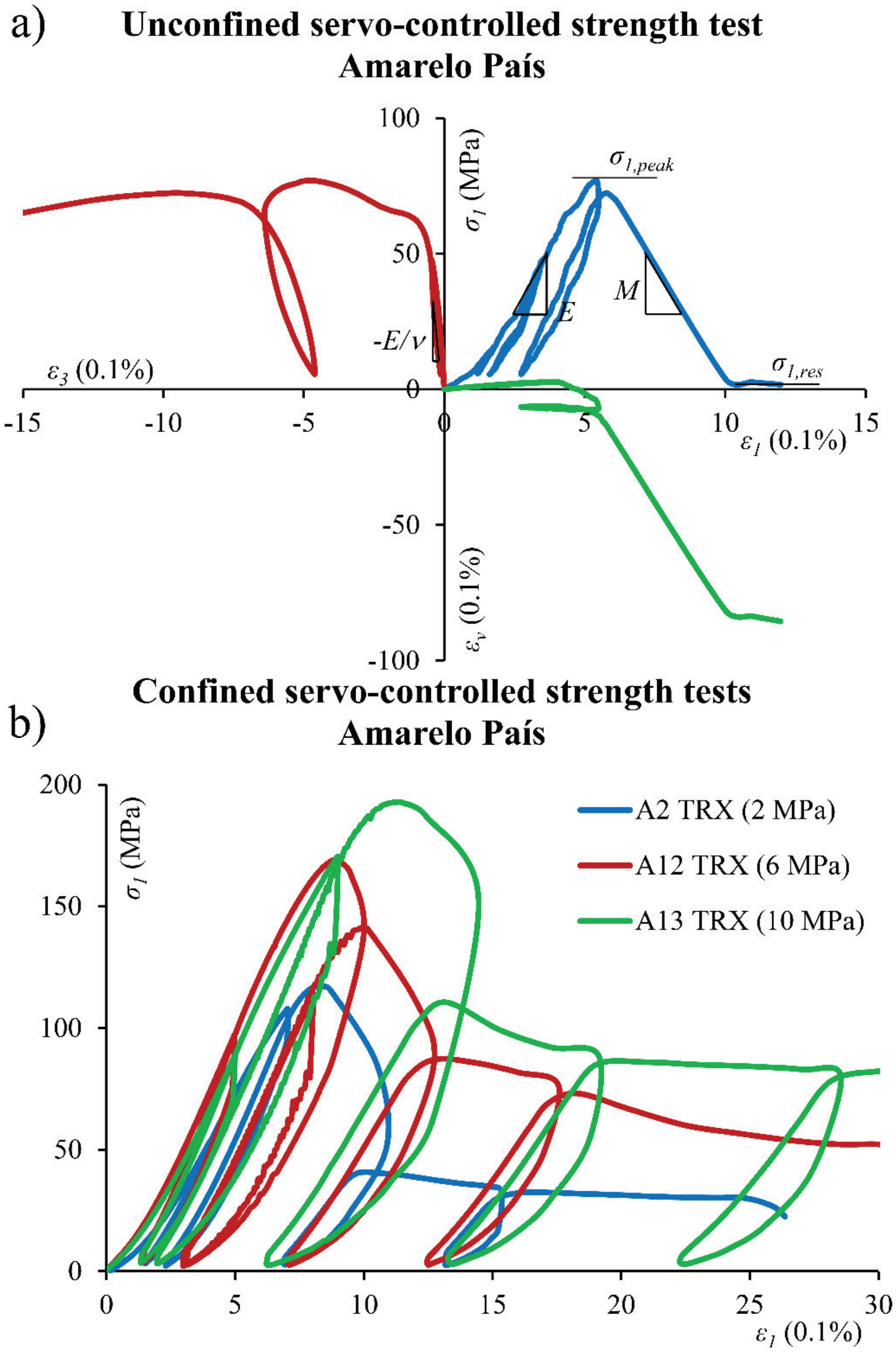

Fig. 8.3. Typical stress-strain graph for a) unconfined compression test on granite rock sample. It is shown how to obtain the values of peak and residual strength, apparent elastic Young's modulus, apparent Poisson's ratio and drop modulus b) confined triaxial tests for different values of confinement.

Table 8.1. Results of compressive tests on granite.

Sample	σ_3 (MPa)	$\sigma_{1,peak}$ (MPa)	$\sigma_{1,res}$ (MPa)	E (GPa)	ν	M (GPa)
A1 RCS	0	77.50	--	21.67	0.13	--
A2 RCS	0	84.64	--	22.36	0.19	--
A3 RCS	0	76.66	2	17.63	0.20	--
A4 RCS	0	75.60	5	22.92	0.18	--
A5 RCS	0	80.34	2	20.27	0.15	--
A6 RCS	0	76.91	2	18.59	0.18	--
A7 RCS	0	68.47	--	17.60	0.21	--
A8 RCS	0	77.19	2	19.30	0.17	--
A9 RCS	0	74.85	2	18.97	0.17	--
A10 RCS	0	76.17	--	16.35	0.19	--
A11 RCS	0	80.08	--	15.95	0.16	--
A12 RCS	0	74.74	1	16.00	0.15	-19.11
A1 TRX	2	130.42	32	30.54	0.19	-17.39
A2 TRX	2	117.33	30	23.40	0.19	-16.00
A3 TRX	2	112.29	27	22.32	0.22	-16.67
A4 TRX	2	110.31	31	23.95	0.20	-17.65
A5 TRX	4	134.20	44	25.06	0.19	-21.06
A6 TRX	4	130.02	43	24.36	0.22	-17.39
A7 TRX	4	129.89	54	25.25	0.20	-17.15
A8 TRX	4	129.50	46	23.84	0.22	-22.10
A9 TRX	6	153.90	51	27.48	0.21	-21.05
A10 TRX	6	170.72	45	30.02	0.21	-19.55
A11 TRX	6	175.43	48	30.01	0.20	-19.05
A12 TRX	6	169.00	51	30.40	0.18	-17.57
A13 TRX	10	192.75	80	28.06	0.22	-19.03
A14 TRX	10	213.99	75	35.49	0.19	-21.69
A15 TRX	10	200.71	87	33.69	0.15	-21.74
A16 TRX	10	193.09	68	29.45	0.21	-20.18
A17 TRX	12	214.99	81	31.20	0.20	-18.52
A18 TRX	12	230.14	80	36.08	0.20	-20.00

8.2.1. Interpretation of tests: elastic and strength parameters

Results obtained in Table 8.1 have been studied to obtain the main geomechanical features of the rock.

First, peak and residual Mohr-Coulomb (M-C) and Hoek-Brown (H-B) failure criteria have been fitted to the strength values obtained in tests. These curves, together with the original test data are presented in Fig. 8.4 and Table 8.2. Since triaxial tests were only performed up to 12 MPa of confining pressure, the curvature of the enveloping failure is not very marked for the contemplated range of confining stresses.

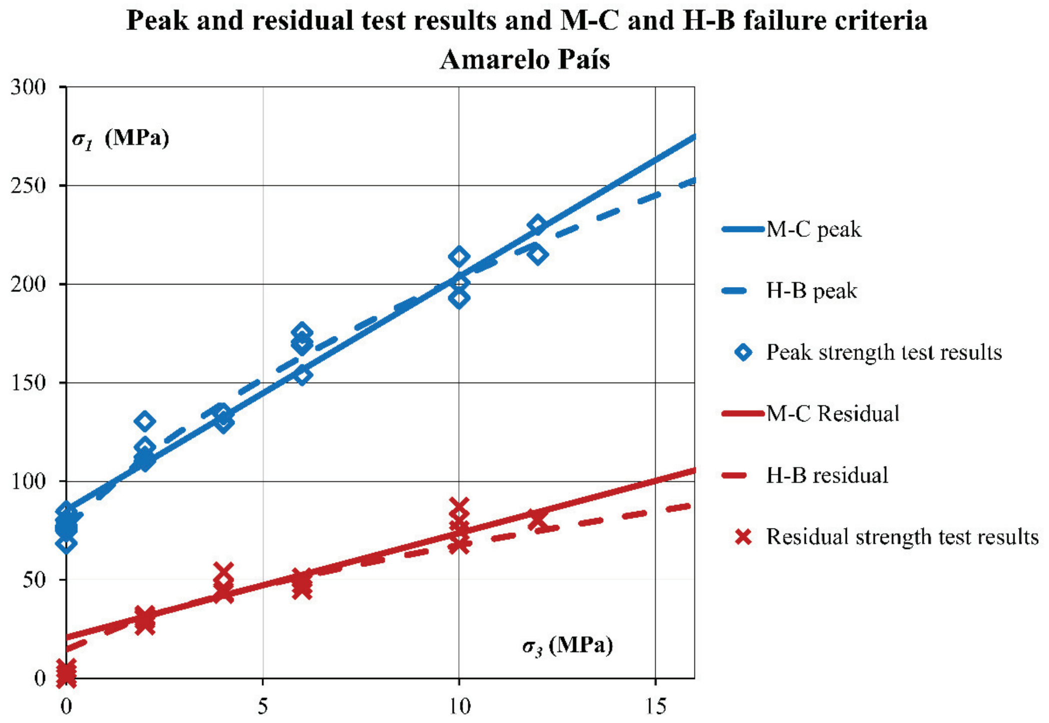

Fig. 8.4. Peak and residual strength test results and M-C and H-B failure criteria fit for the tested granite.

Table 8.2. Basic geomechanic results of Amarelo País granite.

	Hoek-Brown	Mohr-Coulomb
Peak Strength	$\sigma_{c,peak}$ = 76.59 MPa m = 40.96 R^2 =0.990	$\sigma_{c,peak}$ = 85.45 MPa ϕ_{peak} = 57.59 ° c_{peak} = 12.42 MPa R^2 =0.999
Residual strength	$\sigma_{c,res}$ = 14.68 MPa m = 21.14 R^2 =0.979	$\sigma_{c,res}$ = 20.71 MPa ϕ_{res} = 43.04 ° c_{res} = 4.5 MPa R^2 =0.994
E	$E = 19.91+1.256\cdot\sigma_3$ (GPa); E_{mean}= 19 MPa	
ν	ν = 0.19	
M	M = -19.73 GPa	

It should be highlighted that for the peak criteria, very good regression analyses were obtained for the M-C failure criterion, although H-B also fits well. The same happens for residual strength, M-C seems to fit results slightly better than H-B. One can highlight the very high values of Hoek-Brown parameter, m (in the upper range of typical values for rocks) and the friction angle, ϕ, and, in addition, the fact that this friction angle does not diminish in a significant manner from the peak to the residual case. It is also remarkable how the drop in strength occurs mainly in the cohesive component.

The apparent Young's modulus for the different samples have been obtained as the slope of the σ_1 - ε_1 curve between 30 and 60 % of the peak strength. A trend of growing E with increasing σ_3 is observed and presented in form of equation in Table 8.2.

8.2.2. Interpretation of tests: post-failure parameters

The values of drop modulus, M, or slope of the σ_1-ε_1 curve in post-failure stage, have also been estimated in an approximate way, since they do not show a clear straight trend. M has been estimated for each test, as Table 8.2 shows, an average value around –20 GPa is recovered.

For a standard triaxial test in which confining stress is applied to a sample peripherally and under homogeneous deformation conditions $\varepsilon_2 = \varepsilon_3$, and so $\varepsilon_v = \varepsilon_1 + 2\varepsilon_3$. Thus, dilation angle in these tests can be computed from:

$$\sin\psi = \frac{\dot{\varepsilon}_1^p + 2\dot{\varepsilon}_3^p}{-\dot{\varepsilon}_1^p + 2\dot{\varepsilon}_3^p} \tag{8.1}$$

Since it is possible to directly obtain the values of ε_v and ε_1 in the performed triaxial tests, the expression by Vermeer & De Borst (1984) can be used:

$$\sin\psi = \frac{\dot{\varepsilon}_v^p}{-2\dot{\varepsilon}_1^p + \dot{\varepsilon}_v^p} \tag{8.2}$$

The advantage of this approach (Alejano & Alonso, 2005) is that it is valid for triaxial tests, but that it can also be applied to plane strain conditions, and even to true triaxial situations. It should be pointed out that for plane strain conditions the fraction denominator represents in absolute terms, the plastic shear strain, γ^p, defined from internal variables:

$$\gamma^p = \varepsilon_1^p - \varepsilon_3^p \tag{8.3}$$

Consequently, to obtain dilatancy angle, it is necessary to obtain the incremental plastic strains, which means picking some arbitrary segments in complete stress-strain curve to get the incremental strain and make the decomposition of total strains into their elastic and plastic parts:

$$\varepsilon_i = \varepsilon_i^e + \varepsilon_i^p \tag{8.4}$$

Decomposition of total strains into their elastic and plastic parts can be done graphically as explained in Chapter 3 and depicted in Fig. 8.5.

Using this methodology a points' cloud is obtained for each confinement stress, as shown in Fig. 8.6. Then the approach developed by Zhao & Cai (2010a) has been applied in order to obtain the dilation angle parameters. The approach presented by Alejano & Alonso (2005) derived from sedimentary rocks did not fit the results obtained for granite.

The fitted parameters are shown in Table 8.3, in the first line of values. This table also shows the same parameters as obtained by Zhao & Cai (2010a) for a quartzite and a strong sandstone (second and third line of values respectively) in order to check that the recovered values are within a reasonable range. These parameters should be included in eq. (8.5) (Zhao & Cai, 2010a) to obtain an estimate of the dilation angle value corresponding to a confinement stress and to a level of plastic shear strain as follows:

$$\psi = \frac{ab\left(e^{-b\gamma^p} - e^{-c\gamma^p}\right)}{c-b}$$

where:

$$a = a_1 + a_2 \cdot \mathrm{e}^{\frac{-\sigma_3}{a_3}} \qquad (8.5)$$

$$b = b_1 + b_2 \cdot e^{\frac{-\sigma_3}{b_3}}$$

$$c = c_1 + c_2 \cdot \sigma_3^{c_3}$$

where, now, γ^p is expressed in percentage of deformation and σ_3 in MPa.

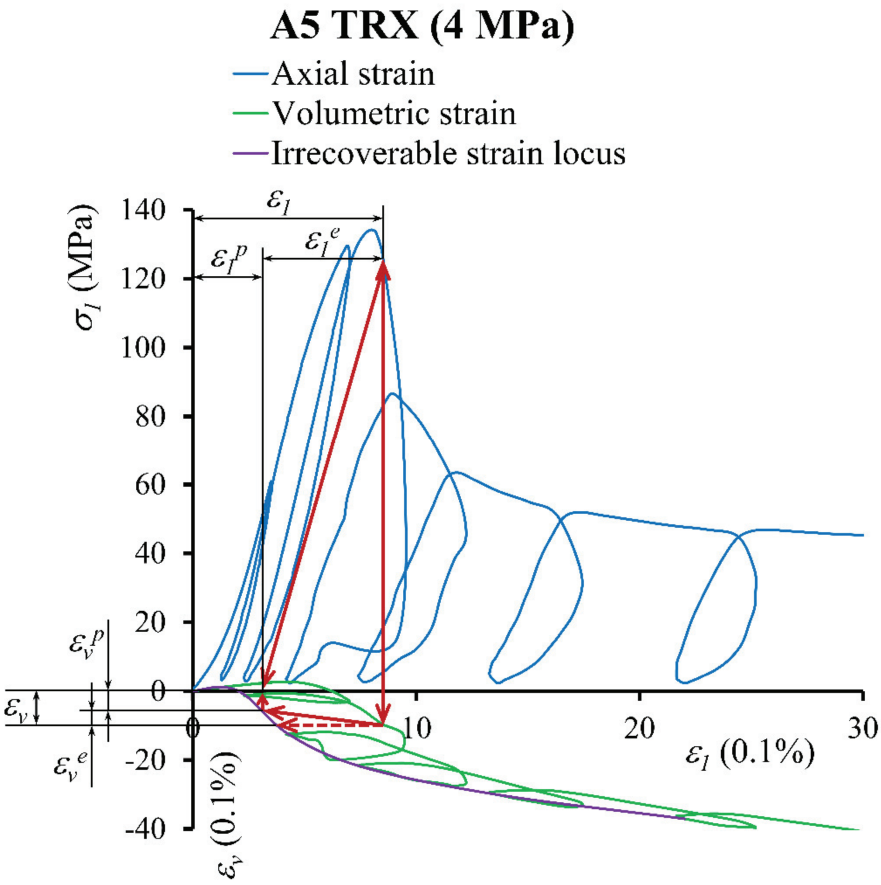

Fig. 8.5. Graphic estimate of axial and volumetric plastic strains.

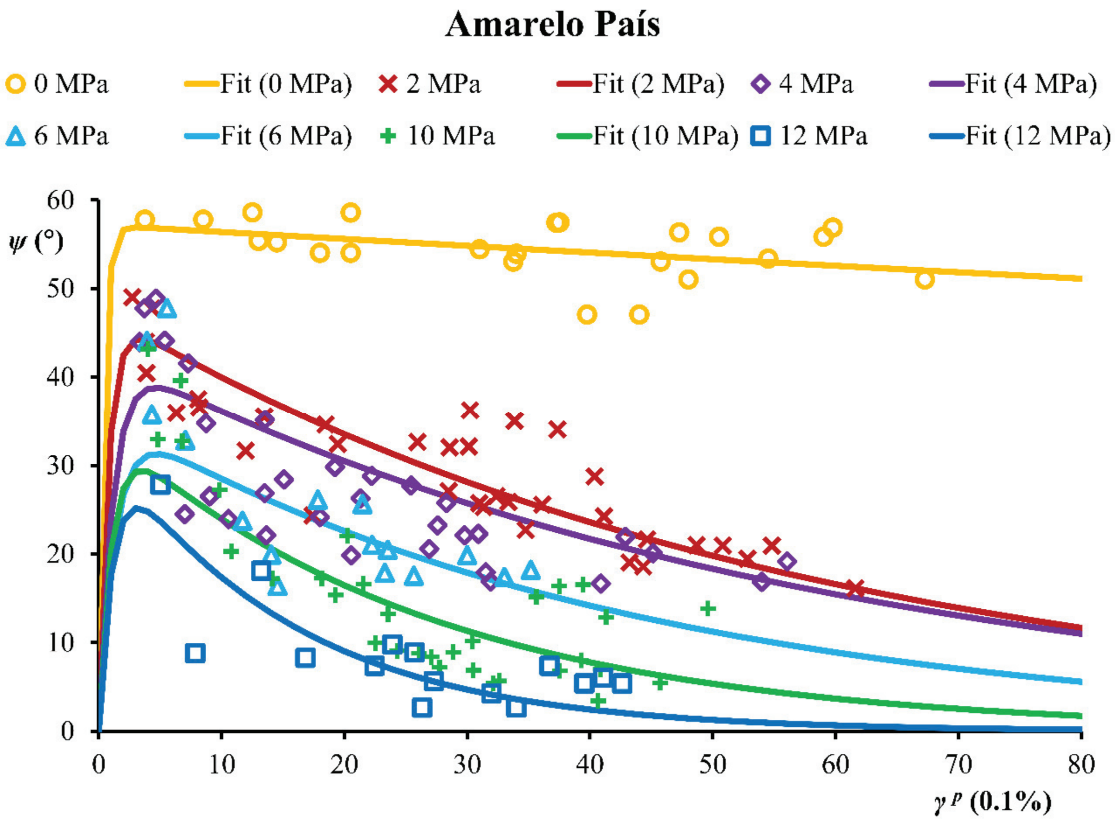

Fig. 8.6. Dilation angle vs. plastic shear strain for various confinement levels. Lab results and fits.

Table 8.3. Parameters of the plastic shear strain and confining stress dependent dilation angle model for the studied granite (this study) and two other rocks (Zhao & Cai, 2010a).

*	a_1	a_2	a_3	b_1	b_2	b_3	c_1	c_2	c_3
1	29.01	28.1	4.8	8.26	17.5	1.5	0.014	0.075	0.71
2	63.17	11.9	2.8	5.8	36.2	6.8	0.14	1.14	1.23
3	14.63	34.9	3.4	4.06	15.6	5.5	0.08	0.4	0.58

* [1] granite this text, [2] quartzite (Zhao & Cai, 2010a) and [3] sandstone (Zhao & Cai, 2010a)

8.3. Rock mass characterization and models

Under this heading rock mass characterization techniques and the models to be performed are presented.

8.3.1. Rock mass characterization techniques

The simulated rock masses to be studied have been characterized as strain-softening and variable dilation materials presenting Mohr-Coulomb strength criteria.

In what concerns peak strength and elastic parameters, the rock mass characterization approach used in this study is based on the one proposed by Hoek et al. (2002) implemented in the code RocLab (Rocscience, 2009). In order to obtain residual strength values and based on the approach by Cai et al. (2007), a reasonable guess has been made, concerning the value of the residual GSI, based on the following equation:

$$\mathrm{GSI}^{\mathrm{res}} = 17.25 \cdot e^{0.0107 \cdot \mathrm{GSI}} \tag{8.6}$$

With this value of $\mathrm{GSI}^{\mathrm{res}}$ and using again RocLab, residual strength parameters can be computed.

Tensile strengths are obtained by means of the expression (Hoek et al., 2002):

$$\sigma_t = \frac{s \cdot \sigma_{ci}}{m} \tag{8.7}$$

For both peak and residual values.

The value of the drop modulus, and consequently, that of γ^{p*} is estimated following the approach by Alejano et al. (2010), which is briefly exposed in what follows. The value of the drop modulus is a value depending on the Young's modulus of the rock mass, *E*, obtained as suggested by Hoek et al. (2002), according to (Alejano et al., 2010):

$$M = -\omega \cdot E \tag{8.8}$$

The value of the ratio ω depends on the GSI^{peak} and confinement-stress level and can be estimated according to:

$$\begin{aligned}
\omega &= \left(0.0046 \cdot e^{0.0768 \cdot \mathrm{GSI}^{\mathrm{peak}}}\right) \cdot \left(\frac{\sqrt{s^{\mathrm{peak}}} \cdot \sigma_{ci}}{\sigma_3}\right)^{-1} \quad \text{for } \sigma_3 \geq 0.1 \\
\omega &= \left(0.0046 \cdot e^{0.0768 \cdot \mathrm{GSI}^{\mathrm{peak}}}\right) \cdot \left(\frac{\sqrt{s^{\mathrm{peak}}} \cdot \sigma_{ci}}{2 \cdot \sigma_3} + 0.05\right)^{-1} \quad \text{for } \sigma_3 \leq 0.1
\end{aligned} \tag{8.9}$$

where s^{peak} refers to the Hoek-Brown parameter *s* of the rock mass, and σ_3 is the average confinement stress, which for the case of tunnels can be estimated as half the value of the so-called critical pressure, that is:

$$P_i^{cr} = \sigma_0 - \left[\frac{\mathrm{K}_\phi - 1}{\mathrm{K}_\phi + 1} \left(\sigma_o + \frac{\sigma_c}{\mathrm{K}_\phi - 1} \right) \right] \tag{8.10}$$

where:

$$\begin{gathered} \mathrm{K}_\phi = \frac{1 + \sin\phi}{1 - \sin\phi} \\ \sigma_c = 2c\sqrt{\frac{1 + \sin\phi}{1 - \sin\phi}} \end{gathered} \tag{8.11}$$

and where c and ϕ refer to peak values and σ_0 denotes the average field stress.

Introducing this value of $\sigma_3 = P_i^{cr}/2$, in the following equations, it is possible to obtain the values of the principal strains corresponding to the achievement of residual state (Fig. 8.7):

$$\varepsilon_1^p = \left[\sigma_{1,peak}(\sigma_3) - \sigma_{1,res}(\sigma_3) \right] \cdot \left(\frac{1}{E} - \frac{1}{M} \right) \tag{8.12}$$

And

$$\varepsilon_3^p = -\frac{1}{2} \cdot \frac{1 + \sin\psi}{1 - \sin\psi} \cdot \varepsilon_1^p \tag{8.13}$$

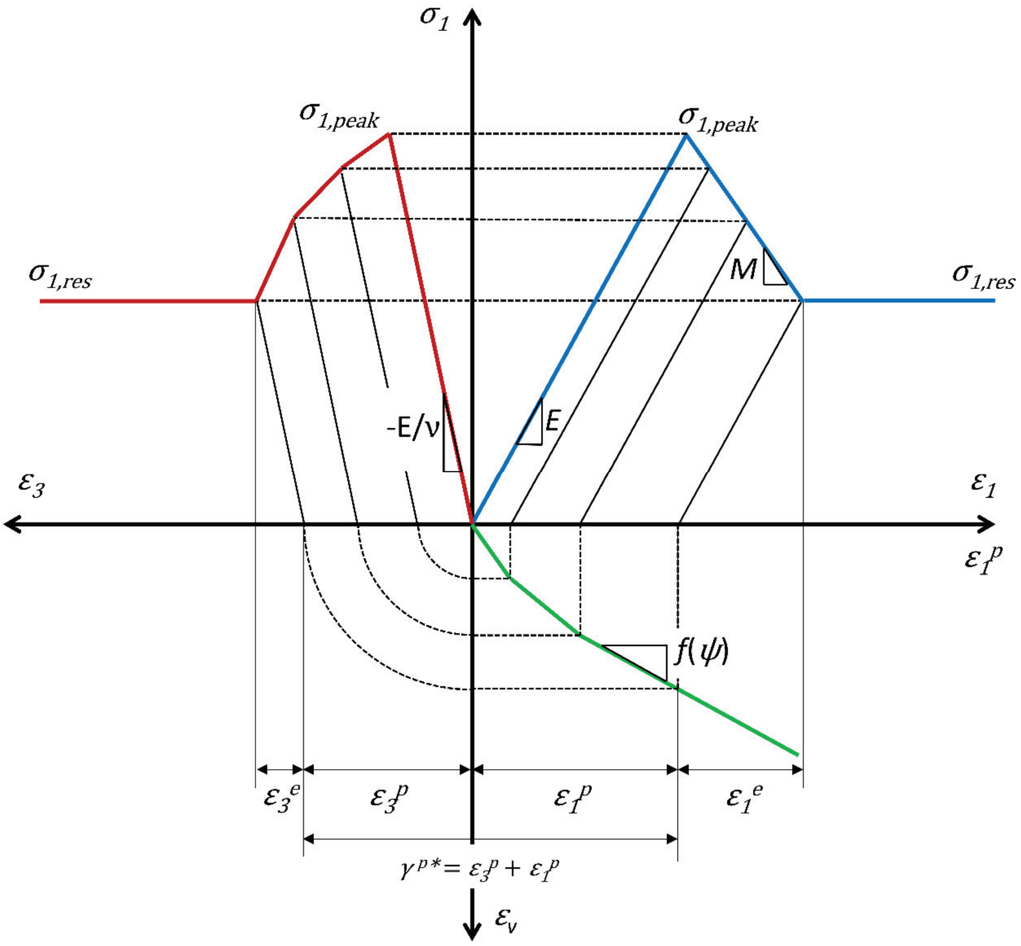
σ_1
$\sigma_{1,peak}$
$\sigma_{1,peak}$
$\sigma_{1,res}$
M
$\sigma_{1,res}$
-E/ν
E
ε_3
ε_1
ε_1^p
$f(\psi)$
ε_3^e
ε_3^p
ε_1^p
ε_1^e
$\gamma^{p*} = \varepsilon_3^p + \varepsilon_1^p$
ε_v

Fig. 8.7. Stress-strain relationships for a modelled SS rock mass to estimate the value of γ^{p*}.

For the sake of simplicity, a constant value of dilatancy is considered in this formula as shown in eq. (8.17). Finally, the critical plastic parameter corresponding to a particular value of σ_3 is obtained from the results of Eqs. (8.12) and (8.13) as:

$$\gamma^{p*} = \varepsilon_1^p - \varepsilon_3^p \tag{8.14}$$

in which γ^{p*} is confinement-stress-dependent. Remark that γ^{p*} can be translated to the plastic parameter used by FLAC (Itasca, 2011), as proposed by Alonso et al. (2003) and explained in Zhao & Cai (2010a) according to:

$$e^{ps}_{\mathrm{FLAC}} = \eta^*_{\mathrm{FLAC}} = \frac{\sqrt{3}}{3}\sqrt{1+\mathrm{K}_\psi+\mathrm{K}_\psi^2}\cdot\frac{\gamma^{p*}}{1+\mathrm{K}_\psi} \tag{8.15}$$

where:

$$\mathrm{K}_\psi = \frac{1+\sin\psi}{1-\sin\psi} \tag{8.16}$$

Again, for the sake of simplicity, a value of constant dilatancy as shows eq. (8.17) is used in the previous expressions.

This model is implemented in FLAC (Itasca, 2011) by means of the strain softening/hardening model, in such a way that peak strength parameters (c, ϕ, σ_t) are associated to no plastic strain and these values diminish linearly to achieve the residual ones for the calculated value of η^*_{FLAC}.

Remark that, in this approach, the rock mass post-failure behavior only depends on rock mass quality and stress level, but not on post-failure behavior of samples.

Finally the plastic shear strain and confinement stress dependent dilation angle is estimated following the guidelines given by Zhao & Cai (2010b) to obtain these values starting from lab data. This involves re-estimating the values of a_1 and a_2, so that for the unconfined case the peak dilation angle equals that of peak friction of the rock mass. The rest of the parameters (a_3 and the b_i and c_i) are kept as for the rock at lab scale (Table 8.3).

For modelling purposes and also for the estimate of γ^{p*}, average constant dilation angles have been estimated by means of the following expression, proposed by Alejano et al. (2010) in the light of the guidelines given by Hoek & Brown (1997):

$$\psi = \frac{5\cdot\mathrm{GSI}-125}{1000}\cdot\phi \quad \text{for} \quad 25 < \mathrm{GSI} < 75 \tag{8.17}$$

8.3.2. Model basics

A 5 m radius tunnel located at a depth of 1500 m excavated in different quality rock masses (GSI 35, 50 and 65) have been selected to analyze the response of excavations to different rock mass behavior models. This analysis focuses on plastic zones and displacements. An isotropic stress field has been chosen for comparative purposes, since in this case, the convergence-confinement technique can be applied to obtain the displacement in the tunnel spring-line and the extent of the plastic zone when using some simple models.

FLAC (Itasca, 2011) has been used to study the response of excavations. Since the author are particularly interested in the response of the tunnel face, an axi-symmetric model was set up. The discretized area was 50 m x 85 m. Mesh size was gradually reduced towards the tunnel face. A symmetry axis was set for $x = 0$. The tunnel was presented as a rectangle of length 45 m, in such a way that the excavation of the tunnel can be performed sequentially. The normal displacements were fixed in the symmetry axis and on the bottom part of the model. Normal pressure of 40.5 MPa was applied to the remaining (upper and right) boundaries of the model (Fig. 8.8).

A simple subroutine has been created in the FLAC (Itasca, 2011) internal language to implement the dilation angle model as presented in eq. (8.5) accounting for the utilized units and FLAC variables.

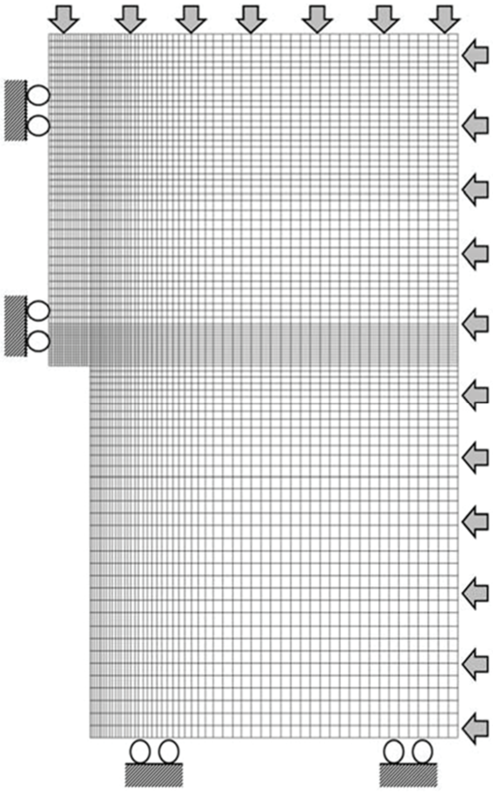

Fig. 8.8. FLAC mesh used to perform the tunnel simulations to investigate face behavior.

8.3.3. Rock masses parameters

The needed parameters obtained for the three granitic rock masses to analyze, derived from the above rock mass characterization approach are presented in Table 8.4.

Table 8.4. Relevant parameters of the modelled rock masses.

Parameter	unit	GSI 35	GSI 50	GSI 65
GSI_{res}		25.08	29.44	34.57
c_{peak}	MPa	4.57	5.69	6.95
ϕ_{peak}	°	38.7	43.0	47.2
$\sigma_{t,peak}$	kPa	13.9	43	134
c_{res}	MPa	3.85	4.23	4.66
ϕ_{res}	°	35.66	36.85	38.25
$\sigma_{t,res}$	kPa	6.59	9.15	13.5
E	GPa	3.69	8.75	20.75
ν	-	0.28	0.25	0.22
M	GPa	-0.089	-2.046	-50.87
ψ (constant)	°	1.93	5.37	9.49
γ^{p*}	str.	0.1372	0.0154	0.0027
e^{ps}_{FLAC}	str.	0.0686	0.0077	0.00137
a_1 (Z&C)	-	21.1	26.5	31.2
a_2 (Z&C)	-	17.8	16.7	16

8.3.4. Numerical models

A number of simulations for the 3 different quality rock masses (GSI 35, 50 and 65) are run. The most realistic models from the authors' point of view are those considering strain-softening behavior and a mobilized dilation angle model as the behavior shown in Fig. 8.9. This dilation angle model adjusted for the rock mass of GSI = 50 as indicated above is presented in Fig. 8.10.

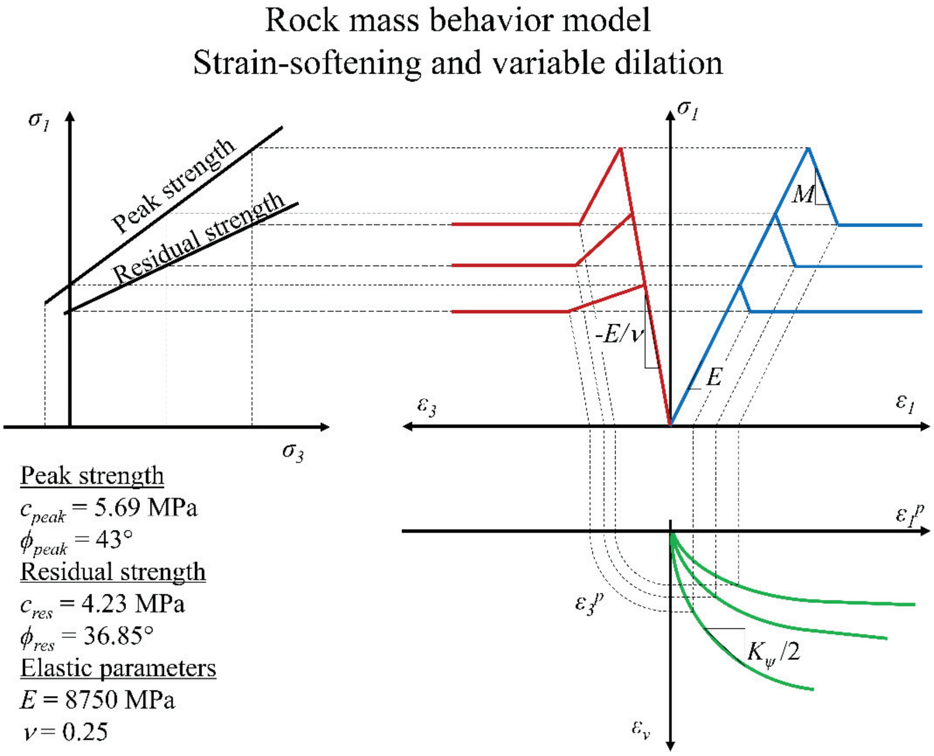
Rock mass behavior model
Strain-softening and variable dilation
σ_1
Peak strength
Residual strength
σ_3
σ_1
M
-E/ν
E
ε_3
ε_1
ε_1^p
ε_3^p
$K_\psi/2$
ε_v
Peak strength
c_{peak} = 5.69 MPa
ϕ_{peak} = 43°
Residual strength
c_{res} = 4.23 MPa
ϕ_{res} = 36.85°
Elastic parameters
E = 8750 MPa
ν = 0.25

Fig. 8.9. Stress-strain behavior response of a strain-softening and mobilized dilation angle model material, as that representing a rock mass.

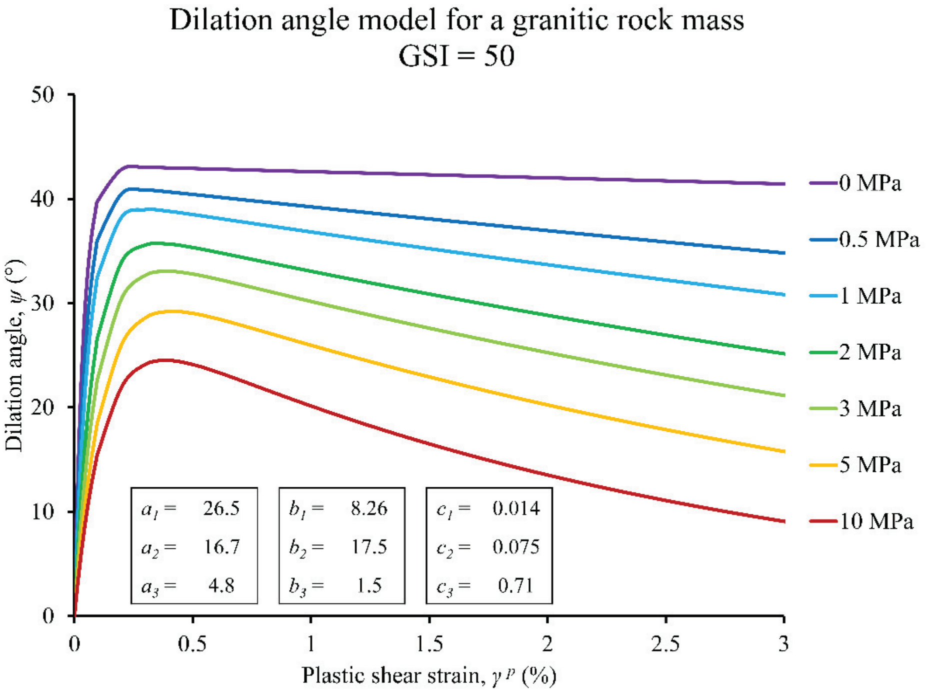

Fig. 8.10. Dilation angle model for the granitic rock mass (GSI = 50) obtained based on lab data and following the approach suggested by Zhao & Cai (2010b).

For each rock mass six different models have been run, considering EPP (elastic-perfectly-plastic), SS (strain-softening) and EB (elastic-brittle) (Fig. 8.1) rock masses and in each case for constant dilation as derived from eq. (8.8) and with the mobilized dilation angle model. This has been done in this way in order to compare and better understand results of excavation response. An example of a model is presented in Appendix C (the model corresponding to a strain-softening rock mass, GSI = 50 and variable dilation).

8.4. Numerical results

For the most realistic cases (strain-softening and variable dilation) the dilation distributions obtained in the three cases are shown in Fig. 8.11. It can be observed how the plastic zone shrinks for increasing rock mass quality, whereas dilation tends to be higher in the plastic zones of the better quality rock mass. It is also to be remarked that the values attained by dilation in the plastic zones are larger than those average values derived from simple approaches and that they produce larger displacements in excavations.

Although extensometric measurements in deep excavation are not very common, some authors have reported values larger than expected (Zhao & Cai, 2010b). Remark that in any case, the application of reinforcement and support can mitigate this effect, and this can be one of the reasons of the good results obtained when applying them.

As indicated for illustrative purposes in Fig. 8.11, in every model the author have computed the plastic radius (R_{pl}), the extent of the plastic zone in front of the face (R_{pl}^{f}), the maximum displacement in the spring-line (u_r) and the displacement in the tunnel face center (u_f). These data have been recovered because they may be indicative of tunnel behavior.

Results of these values are presented in Table 8.5 for all the run models, together with basic results obtained by means of code RocSupport (Rocscience, 2011) for particular simple models. RocSupport data refer to constant dilation EPP (M-C and H-B) and EB (H-B) models. These results are presented for comparative purposes. Observe that the values of R_{pl} and u_r obtained for FLAC EPP models with constant dilation basically coincide (are approximately 10% larger due to boundary conditions) with those obtained for equivalent materials with RocSupport.

A comparison of results shows that dilation plays a relevant role in the deformations of tunnel walls and faces. This role is captured by the dilation approach used, even if further research is needed to calibrate it more accurately. The behavior of face has been claimed to control tunnel behavior (Lunardi, 2008), and it is largely affected by dilation. However, dilation does not significantly affect the extent of the plastic zones around the excavations. This can be seen by comparing the plastic radii of the different models with constant and variable dilation.

It is also to remark, in line with the ideas by Hoek & Brown (1997), that whereas for the low quality rock mass (GSI = 35) EPP and SS models yield similar results (and EB differs); for the higher quality rock mass (GSI = 65) SS and EB yield comparable figures, and EPP is somewhat different (See Table 8.5 and Fig. 8.1).

When an EB behavior is mentioned, it is referred to a rock mass following standard failure criteria (H-B or M-C) and it does not refer to those producing spalling associated to the propagation of cracks. These spalling mechanisms have been modelled by means of the so called CWFS (Cohesion-Weakening-Friction-Strengthening) approach. According to Diederichs & Martin (2010), the upper limit up to where the EB model can well represent rock masses is established in GSI 80 for soft rocks and in GSI 65 for hard rocks.

On the other hand, the selected behavior model does not seem to relevantly affect the levels of deformation observed in the tunnel face and in the tunnel spring-line. For instance for the GSI = 50 and constant dilatancy model, results show displacements in the tunnel face (and on the tunnel spring-line) of 28 (32), 32 (59) and 41 (60) mm respectively for the EPP, SS and EB model. However, for the above indicated behavior models the extent of the plastic zone in front of the face grows from 1.7, to 2.3 and 2.7 meters, respectively.

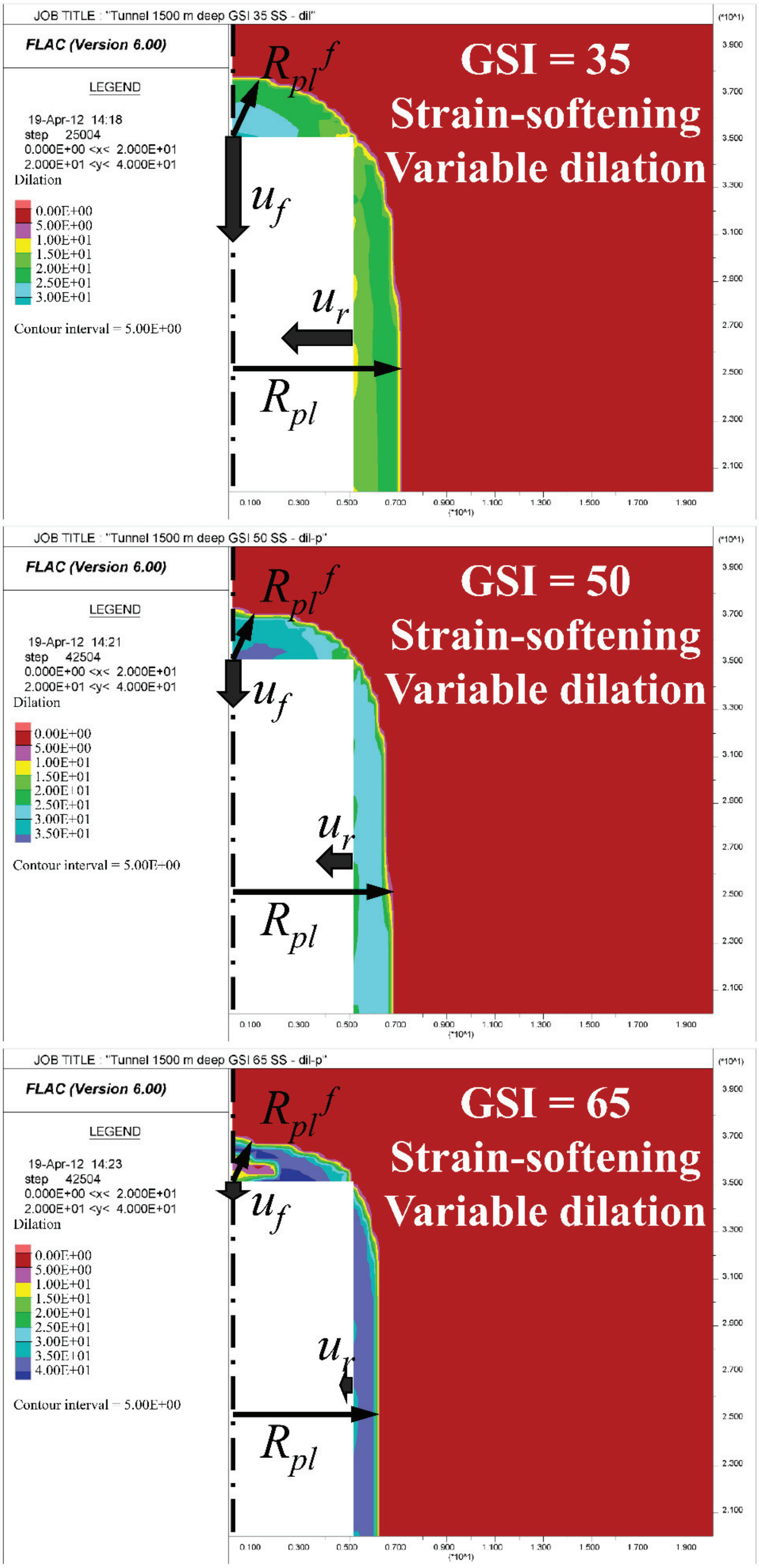

Fig. 8.11. Dilation angle distribution around tunnels. The dark sections indicate the plastic zones and the values attained by the dilation angle. The illustrated values of R_{pl}, R_{pl}^f, u_r and u_f are shown in Table 8.5 for all the models performed.

Table 8.5. Results of the extent of the plastic zone and displacement observed in tunnel models, as obtained with FLAC, except those obtained with RocSupport.

GSI	MOD-DIL	R_{pl} (m)	R_{pl}^{f} (m)	u_r (mm)	u_f (mm)
35	EPP-ct.dil.	7.1*	2.7*	124.9	80.5
35	EPP-var.dil.	7.1*	2.7*	158.1	107.5
35	SS-ct.dil.	7.1*	2.7*	131	83.06
35	**SS-var.dil.**	**7.1***	**2.7***	**178.1**	**118.8**
35	EB-ct.dil.	7.7*	3.3*	158.6	98.4
35	EB-var.dil.	7.7*	3*	216.6	146.7
35	RocS EPP MC	6.97		109.42	
35	RocS EPP HB	7.34		128.78	
35	RocS EB HB	8.14		167.02	
50	EPP-ct.dil.	6.15*	1.7*	42.03	28.48
50	EPP-var.dil.	6.15*	1.7*	52.15	31.54
50	SS-ct.dil.	6.75*	2.3*	53.61	32.3
50	**SS-var.dil.**	**6.75***	**2.3***	**84.84**	**59.32**
50	EB-ct.dil.	6.75*	2.7*	58.9	40.59
50	EB-var.dil.	6.75*	2.3*	86.83	59.73
50	RocS EPP MC	6.15		37.04	
50	RocS EPP HB	6.31		42.47	
50	RocS EB HB	7.22		62.63	
65	EPP-ct.dil.	5.55*	1*	15.41	11.27
65	EPP-var.dil.	5.55*	0.7*	17.43	11.25
65	SS-ct.dil.	6.15*	1.7*	21.86	13.5
65	**SS-var.dil.**	**6.15***	**2***	**32.47**	**21.61**
65	EB-ct.dil.	6.15*	2*	22.3	15.7
65	EB-var.dil.	6.15*	2*	33.64	21.98
65	RocS EPP MC	5.64		13.43	
65	RocS EPP HB	5.71		14.83	
65	RocS EB HB	6.52		23.00	

Fig. 8.12 shows different results of deformation of a tunnel face for the case of the rock mass with GSI = 50. In this case, for an elastic-perfectly-plastic model a tunnel extrusion of 28 mm is observed (Fig. 8.12.a). In the case of a strain-softening model with constant dilation this value would increment to 32 mm (Fig. 8.12.b). Finally a strain-softening model with variable dilation would take that value to 59 mm (Fig. 8.12.c), nearly the double of the expected values derived from conventional models.

It is relevant to finally consider the fact that in some models, particularly in those with GSI = 65, tensile failure is observed on the tunnel face. If a null residual tensile strength is considered, this will involve spalling in the face. Further studies on this topic could be of interest.

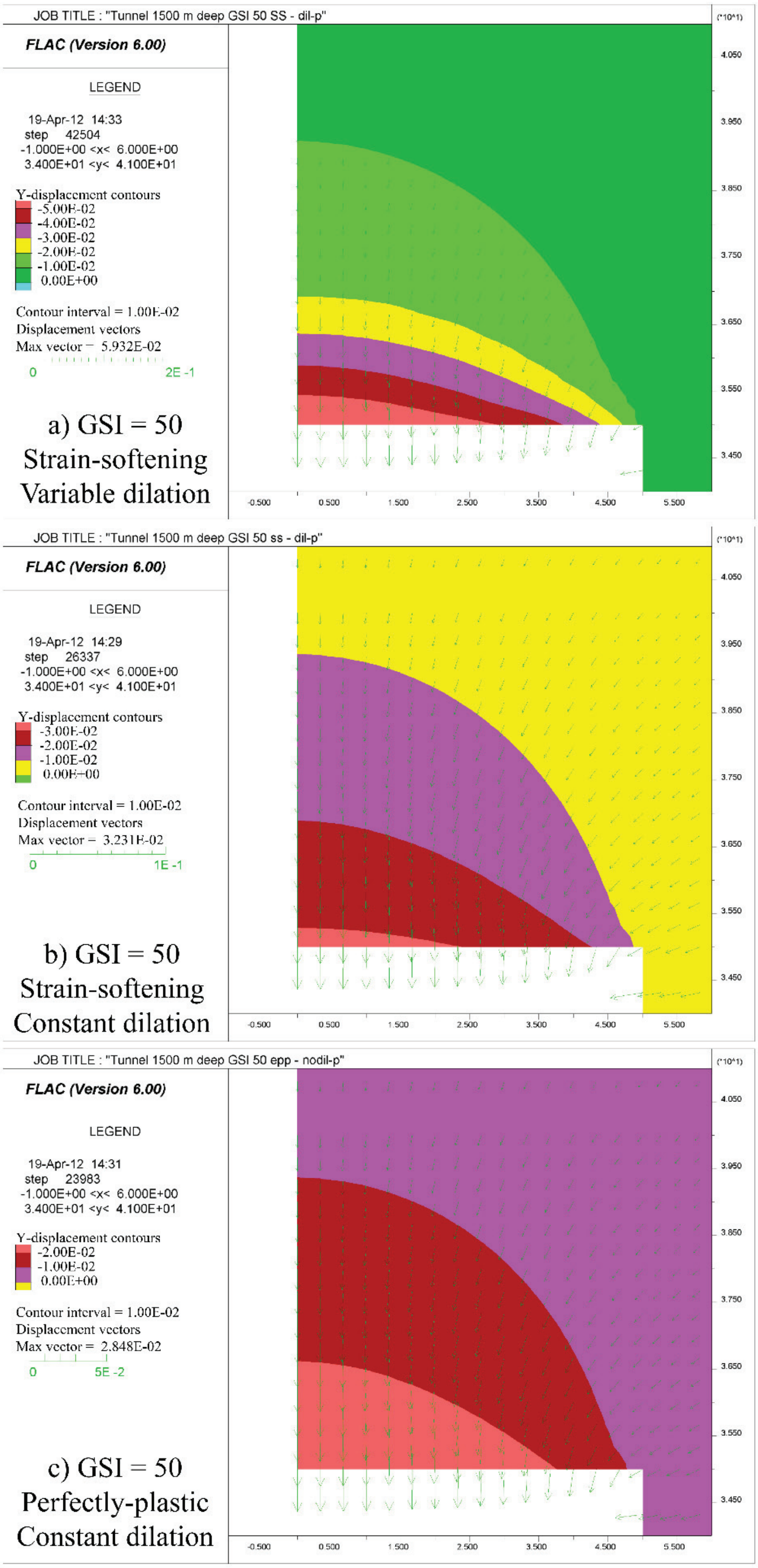

a) GSI = 50
Strain-softening
Variable dilation

b) GSI = 50
Strain-softening
Constant dilation

c) GSI = 50
Perfectly-plastic
Constant dilation

Fig. 8.12. Displacement distributions around the tunnel face for different behaviors of the average quality rock mass.

8.5. Conclusions of this chapter

The role of dilation in rocks and rock masses behavior has been largely overlooked in the past probably due to its complex nature. However, based on recent developments of different authors it is possible now to include this behavior in numerical models, considering the shear plastic strain and confining stress dependent nature of the dilation angle.

The parameters needed to apply this model to rocks can be reasonably estimated from servo-controlled unconfined and confined compressive tests with unloading-reloading cycles in laboratory. The extrapolation of these parameters to the rock mass scale can be done assuming that the peak value of the dilation angle tends to be equal to the friction angle of the rock mass. Even if this seems reasonably true for good quality rock masses, for low quality ones the role of discontinuities should be also taken into account. This is why the above indicated assumption deserves further research.

Oversimplified behavior models —for instance elastic-perfectly-plastic (EPP) approaches, commonly used in daily practical engineering modelling— may produce high levels of errors in the analysis and design of excavations. These errors can be particularly more relevant for tunnels and drifts excavated in average to good quality rock masses in the range of GSI 40 to 60, where a strain-softening modelling approach could be more rigorous.

In this chapter the author, using 30 performed compression strength tests in a granitic rock, obtained the parameters needed to estimate dilation in a reasonably accurate way. Different quality rock masses made of this rock have been characterized according to present trends in order to obtain all the parameters needed to simulate these rock masses as strain-softening and variable dilation materials.

In order to study the role of post-failure rock mass stress-strain behavior on the response of underground excavations and for illustrative purposes, models of a tunnel excavated in these rock masses at great depth have been performed, and displacements and extensions of the plastic zones have been analyzed.

As a result, it has been observed that the dilation model affects in a significant manner the level of displacements observed in the tunnel face and walls; however, this dilation does not relevantly control the extent of the plastic zones. On the other hand, the selected behavior model, namely EPP, SS or EB, seems to be relevant in what concerns the extent of the plastic zone around the tunnel and in front of its face, but its influence on the displacement level in the analyzed cases is scarce.

Moreover, this type of models can be interesting to study the expected stress-strain response of excavations, including the estimate of face extrusion as suggested by Lunardi (2008). This could be useful to account for the behavior of the tunnel core, which could be of help to be able to provide a more sensible design. However, more research is convenient to fine-tune the presented techniques and specially to contrast results with the response of actual excavations.

Finally, the author would like to emphasize that these applications should be used on a site specific basis, with certain caution and within the framework of wider methodological approach, such as that suggested by Starfield & Cundall (1988).

9. Conclusions

The main aim of this doctoral work was to provide laboratory data to further investigating the dilatant behavior of rocks and rock masses. To do that, the existing press in the *John P. Harrison Rock Mechanics' Laboratory* of the University of Vigo was modified in order to not only servo-control the axial loading but also the confining pressure in triaxial strength testing. Moreover, this fully servo-controlled press allowed to measure axial and radial displacements in unconfined strength tests, and, for the case of confined tests —carried out with the help of a Hoek's cell— the displaced volume of hydraulic fluid in order to maintain the confining stress could be also measured at all times. This displaced volume could be correlated to the volumetric strain of the tested specimen, allowing to recover the complete stress-strain curve of each test. That is, the axial and confinement stresses together with the axial and volumetric strains can be controlled at all times all along a confined test.

The strength tests were performed, when possible, reaching the residual state. This discarded the strain gauges for strain measures due to both its limited measure range and its uselessness if a shear band appears. Instead the axial and radial displacements in unconfined tests and axial displacement in confined tests were measured using LVDTs, which showed adequate precision and a relatively large range of measurement.

The controlling software of the press allowed to perform the strength tests with unloading-reloading cycles, which are very convenient to get the locus known as *irrecoverable strain locus*, which, in turn, allows to distinguish the plastic and elastic components of the volumetric and axial (and, indirectly, radial) strains.

Once the equipment allowed to collect the applied stress and the plastic components of the strains during a strength test and reaching the residual state, it is possible to obtain the evolution of the dilation angle for each tested specimen. The dilation angle is a suitable parameter to describe the dilatant behavior of rock. Dilatancy is the change in volume of a material, in this case rock, resulting from the shear distortion of its components.

As part of this Ph.D. work, 230 rock specimens of 8 different rocks (3 granites, a marble, two limestones, an amphibolite and a gneiss) were prepared and tested in unconfined and confined conditions. The interpretation of these tests provided the evolution of the dilation angle for each test depending on the plastic strain and confining stress, as well as all other relevant geomechanic parameters (Young's modulus, Poisson's ratio, peak strength, residual strength…). The contribution to the world database on complete stress-strain curves for different kinds of rocks able to provide data in the post-failure behavior range of rocks is a relevant achievement of this Ph.D. study.

The dilation angle is known to show dependency on rock and rock mass scale and/or structure, so the idea was developed to test jointed rock samples as if they were small-scaled rock mass analogues. In this way, a new type of strength test was performed using artificially jointed specimens (22 specimens featuring 3 joints and 20 specimens featuring 5 joints) aimed to study this scale/structure dependence. Probably this development is one of the most relevant contribution of this dissertation to rock mechanics knowledge.

Young's modulus demonstrated its dependency with confining stress and structure, increasing as the confining stress increased and diminishing when level of jointing increased. However, the relationship with confining stress was not linear as commonly accepted so far, turning to be logarithmic dependent. Young's moduli showed a great increase in the first tenths of MPa of confining stresses, slowing down the increase ratio when confining stress grows.

Poisson's ratio does not show any clear trend when varying confining stress or structure. This parameter showed a relatively high spread for low confining stresses, tending to a more stable value for higher confinements.

Most commonly used failure criteria (Mohr-Coulomb and Hoek-Brown) were fitted to peak strength results. Due to the relatively low range of confining stresses (up to 12 MPa), both criteria fitted the tests results quite well, although the use of generalized Hoek-Brown criterion for jointed specimens greatly improved the quality of the fit for this small-scaled rock mass analogues. The obtained failure functions showed typical dependencies: as confining stress increases, peak strength increases and as structure increases (number of joints), peak strength decreases.

Both failure criteria also were fitted to residual strength tests results, it has to be pointed out that it was needed to use the generalized Hoek-Brown failure criterion to fit the residual strength results of all the tests. The residual strength increased as confining stress increased, but it did not show any clear dependence with structure. Residual strength remained the same when increasing jointing, only a slight trend towards higher values of the residual strength of jointed specimens compared to intact ones was observed when increasing confinement.

It is also remarkable that the stress-strain curves of the jointed specimens tended to mimic those of the intact specimens starting from certain points of the softening part of the axial stress-axial (and radial) strain.

Drop modulus, or slope of the softening part of the axial stress-axial strain curve was recovered when possible and some challenges arose. First, this parameter does not seem to remain constant during the softening process, so a more precise definition of this parameter could be convenient. Second, although the unloading-reloading cycles were intended also to better control this softening phase, the fact is that they introduce some uncertainties in the stress-strain path that make even more difficult the acquisition of this parameter.

Obtaining dilation angle during strength tests was meant to be one of the main goals of this dissertation, and it has been achieved in a significant manner. This parameter showed its already acknowledged dependencies (it diminishes when confining stress, plasticity or scale/structure increases).

Three variable dilation angle models were fitted to the results and the strengths and weaknesses of each model were identified. Alejano & Alonso (2005) model was not able to correctly predict the peak dilation angle although it correctly captured the decay with plasticity and confinement. Zhao & Cai (2010a) model correctly captured dilation angle variation as also did Walton & Diederichs (2015a) model, but that of Zhao & Cai presents some inherent difficulties associated with the physical meaningless of the parameters and the non-univocal solution.

But dilation angle itself is not enough to simulate post-failure behavior of a strain-softening material like rock or rock mass. In addition, to fully characterize this behavior, a model that also links stresses with strains in post-failure phase is required.

With the aim of creating a model capable to simulate the stress-strain response, a mathematical equation was fitted to the tests data. It was then implemented in numerical code (FLAC) to simulate the strength tests, in order to validate its utility. Although the simulation does not exactly replicate the tests results, we obtained much better results than the commonly used approaches. Problems associated to numerical bifurcation and localization were identified, but their study falls well beyond the scope of this study.

Finally in this Ph.D. thesis and with the aim of highlighting the relevance of post-failure behavior of rocks for practical applications, a deep tunnel was modelled using different rock mass' post-failure behavior approaches (different rock mass' geotechnical qualities and with or without considering variable dilatancy). The results of this part of the thesis show that the use of variable dilatancy modifies the amount of deformation in the tunnel, but, on the other hand, it does not significantly affect the extent of the yielded zone.

Detailed conclusions relating the individual developments of this doctoral work can be found at the end of every chapter of this dissertation.

As a final statement, the real significance of this thesis as contribution to rock engineering discipline can be abstracted as a couple of steps towards a better understanding and insight on the post-failure (particularly volumetric) behavior of rock and rock masses in terms of experimental results and small-scaled rock mass testing. This was materialized in a few papers on the most relevant rock mechanic scientific journals (IJRM&MS, RM&RE) and technical symposia (EUROCK, ARMA, ISRM).

10. Future research lines

Some ideas concerning future developments are stated in the following lines:

- To perform more strength tests on intact and jointed specimens and at different scales of other type of rocks, in order to confirm all the results derived from this thesis.
- To deeper study the drop modulus, defining it in a more precise way, indicating a correct way to measure it and trying to obtain a model that correctly describes this parameter and its dependencies, since it is one of the key aspects to define post-failure behavior (like Young's modulus is one of the key aspects to define elastic behavior).
- To study the stress-strain curves of the jointed and intact specimens in terms of energy, since it could explain the decrease in strength and in Young's modulus of the jointed specimens with respect to the intact ones.
- To extend existing models or provide new ones to implement dilatancy and post-peak behavior of rocks and rock masses.
- To extend the experimentation to larger scales, in order to check in detail the scale problem (not only the structure problem). For instance and to say it in a few words, it could be possible to install extensometers in a pillar of an underground mine and measure the deformations as the excavation develops.
- To implement these behavior models in numerical modelling software, first trying to simulate the laboratory strength tests in a more precise way than showed in this dissertation and later extending the simulation to larger scales (pillar and rock mass scales).

Publications totally or partially derived from this Ph.D. thesis:

Conference papers:

Alejano, L.R., Arzúa, J., Alonso, E. 2012. *Impact of post-failure rock mass behavior on excavation response*. 46th US Rock Mechanics / Geomechanics Symposium. 24-27, June. Chicago. 3:2166-2176. Available on Scopus. Publication totally derived from this Ph.D. thesis.

Arzúa, J., Barbiero, J. & Alejano, L.R. 2013. *Strain-softening characterization of granitic rocks and numerical simulation of servo-controlled strength tests*. EUROCK2013. Rock Mechanics for Resources, Energy and Environment. Kwásniewski & Łydzba (eds). 23-26 September. Wrocław, Poland. Available on Web of Science. Publication totally derived from this Ph.D. thesis.

Pérez-Rey, I., Arzúa, J., Barbiero, J., Alejano, L.R. & Walton G. *A lab-testing based geomechanical characterization of metamorphic rocks focusing on post-failure behavior*. EUROCK2014 - Rock Engineering and Rock Mechanics: Structures in and on Rock Masses – Alejano, Perucho, Olalla & Jiménez (Eds). 27-29, May. Vigo, Spain. CRC Press, Taylor and Francis Group, London. Available on Scopus. Publication totally derived from this Ph.D. thesis.

Walton, G., Diederichs, M.S. & Arzúa J. 2014. *A detailed look at pre-peak dilatancy in a granite – determining "plastic" strains from laboratory test data*. EUROCK2014 - Rock Engineering and Rock Mechanics: Structures in and on Rock Masses – Alejano, Perucho, Olalla & Jiménez (Eds). 27-29, May. Vigo, Spain. CRC Press, Taylor and Francis Group, London. Available on Scopus. Publication partially derived from this Ph.D. thesis.

Arzúa, J., Alejano, L.R., Clérigo, I., Pons, B., Méndez, F. & Prada, F. 2014. *Stability analysis of a room & pillar hematite mine and techniques to manage local instability problems*. EUROCK2014 - Rock Engineering and Rock Mechanics: Structures in and on Rock Masses – Alejano, Perucho, Olalla & Jiménez (Eds). 27-29, May. Vigo, Spain. CRC Press, Taylor and Francis Group, London. Available on Scopus. Publication partially derived from this Ph.D. thesis.

Arzúa, J., Alejano, L.R. & Pérez-Rey, I. 2015. *Effect of scale and structure on the strength and deformability of rocks*. 13th ISRM Congress 2015. International Symposium on Rock Mechanics. 10-13, May. Montreal, Canada. Publication totally derived from this Ph.D. thesis.

Arzúa, J., Alejano, L.R. & Pérez-Rey, I. 2015. *Compressive strength tests of cabled rock specimens as pillar analogues*. EUROCK2015 & 64th Geomechanics Colloquium. Future Development of Rock Mechanics. Schubert (ed.). 7-10, October. Salzburg, Austria. Publication partially derived from this Ph.D. thesis.

Scientific journal papers:

Arzúa, J., & Alejano, L. R. 2013. *Dilation in granite according to servo-controlled strength tests*. International Journal of Rock Mechanics and Mining Sciences, 61, 43-56. Publication totally derived from this Ph.D. thesis.

Arzúa, J., Alejano, L.R., Walton, G. 2014. *Strength and dilation of jointed granite specimens in servo-controlled triaxial tests*. International Journal of Rock Mechanics and Mining Sciences. 69:93-104. Publication totally derived from this Ph.D. thesis.

Walton, G., Arzúa, J., Alejano, L.R., Diederichs, M.S. 2015. *A Laboratory testing-based study on the strength, deformability and dilatancy of carbonate rocks at low confinement*. Rock Mechanics and Rock Engineering. 48:941-958. Publication developed in parallel to this Ph.D. thesis.

Two other journal papers associated to some of the contents of this Ph.D. work are under preparation.

References

Alejano, L.R., Alonso, E. 2005. *Considerations of the dilatancy angle in rocks and rock masses*. Int J Rock Mech Min. 42(4): 481-507

Alejano, L.R., Posada, D., Rodriguez-Dono, A. 2009a. *Servo-controlled strength tests on moderately weathered granite*. In: Proc. of the EUROCK 2009 symposium. Rock engineering in difficult ground conditions. London: CRC. Taylord & Francis Gr.; Soft Rock & Karst. 181-6.

Alejano, L.R., Rodríguez-Dono, A., Alonso, E., Fdez-Manin, G. 2009b. *Ground reaction curves for tunnels excavated in different quality rock masses showing several types of post-failure behavior*. Tunn Undergr Sp Tech. 24(6): 689-705

Alejano, L.R., Alonso, E., Rodriguez-Dono, A., Fernández-Manín, G. 2010. *Application of the convergence–confinement method to tunnels in rock masses exhibiting Hoek–Brown strain-softening behavior*. Int J Rock Mech Min Sci. 47(1): 150–60.

Alejano, L., Rodríguez-Dono, A., Veiga, M. 2012a. *Plastic radii and longitudinal deformation profiles of tunnels excavated in strain-softening rock masses*. Tunn and Undergr Sp Tech. 30:169-82

Alejano, L.R., Arzúa, J., Alonso, E. 2012b. *Impact of post-failure rock mass behavior on excavation response*. 46th US Rock Mechanics / Geomechanics Symposium. 3, pp. 2166-2176.

Alejano, L.R., González, J., Muralha, J. 2012c. *Comparison of different techniques of tilt testing and basic friction angle variability assessment*. Rock Mech Rock Eng. 45: 1023-1035.

Alonso, E. 2001. *Curvas convergencia-confinamiento: resolución numérica y aplicación a macizos rocosos con comportamiento elastoplástico con reblandecimiento*. Ph.D. Thesis. University of Vigo. Spain

Alonso, E., Alejano, L. R., Varas, F., Fdez-Manin, G., Carranza-Torres, C. 2003. *Ground reaction curves for tunnels in strain-softening rock masses*. International Journal for Numerical and Analytical Methods in Geomechanics, 27: 1153-1185.

Alonso, E., Alejano, L.R., Fdez-Manin, G., Garcia-Bastante, F. 2008. *Inluence of post-peak properties in the application of the convergence-confinement method for designing underground excavations*. In: Proceedings of the 5th international conference and exhibition on massive mining technology. Lulea, Sweden: 793-802

Archambault, G., Roleau, A., Daigneault, R., Flamand, R. 1993. *Progressive failure of rock masses by a self-similar anastomosing process of rupture at all scales and its scale effect on their shear resistance*. Scale effects in rock masses 93, Pinto da Cunha (ed.). Balkema, Rotterdam: 133-41

Arzúa, J., & Alejano, L. R. 2013. *Dilation in granite according to servo-controlled strength tests*. Int J Rock Mech Min Sci, 61: 43-56.

Arzúa, J., Barbiero, J. & Alejano, L.R. 2013. *Strain-softening characterization of granitic rocks and numerical simulation of servo-controlled strength tests*. Rock Mechanics for Resources, Energy and Environment Eurock2013 Symposium. Kwásniewski & Łydzba (eds). 23-26 September. Wrocław, Poland.

Arzúa, J., Alejano, L.R., Walton, G. 2014. *Strength and dilation of jointed granite specimens in servo-controlled triaxial tests*. Int J Rock Mech Min Sci. 69:93-104.

Bahrani, N., Kaiser, P.K. 2013. *Strength degradation of non-persistently jointed rock mass*. Int J Rock Mech Min Sci. 62:28-33

Barton, N. 1976. *The shear strength of rock and rock joints*. Int J Rock Mech Min Sci 1976;13:1–24.

Barton, N.R., Lien, R., Lunde, J. 1974. *Engineering classification of rock masses for the design of tunnel support*. Rock Mech. 6(4):189-239.

Barton, N., Bandis, S.C. 1982. *Effects of block size on the shear behavior of jointed rocks*. 23rd US Symposium on Rock Mechanics. Rotterdam, Balkema. 10:739-760.

Barton, N., Grimstad, E. 1994. *The Q-system following 20 years of application in NATM support selection*. Felsbau. 6/94:428-36

Besuelles, P., Desrues, J., Raynaud, P. 2000. *Experimental characterization of the localization phenomenon inside a Vosgues sandstone in a triaxial cell*. Int J Rock Mech Min Sci. 37:1123–237.

Bieniawski, Z.T. 1968. *The effect of specimen size on compressive strength of coal*. Int J Rock Mech Min Sci Geomech Abstr. 5(4):325-335.

Bieniawski, Z.T. 1976. *Rock mass classification in rock engineering*. In: Proceedings of the symposium on exploration for rock engineering, Johannesburg. Vol. 1:97-106

Bieniawski, Z.T. 1989. *Engineering rock mass classifications*. New York: Wiley.

Brady, B.G.H., Brown, E.T. 2006. *Rock mechanics for underground mining*. 3rd ed. Dordrecht: Springer.

Brown, E.T., Trollope, D.H. 1970. *Strength of a model of jointed rock*. ASCE J Soil Mech Found Div. 96:685-704.

Brown, E.T., Bray, J.W., Santarelli, F.J. 1987. *Influence of stress-dependent elastic moduli on stresses and strain around axisymmetric boreholes*. Rock Mech Rock Eng. 22:189–203.

Bukowska, M. 2005. *Mechanical properties of carboniferous rocks in the upper Silesian coal basin under uniaxial and triaxial compression tests*. J Min Sci. 41(2):129–33.

Cai, M., Kaiser, P.K., Uno, H., Tasaka, Y., Minamic, M. 2004. *Estimation of rock mass deformation modulus and strength of jointed rock masses using the GSI system*. Int J Rock Mech Min Sci. 41(1): 3-19

Cai, M., Kaiser, P.K., Tasaka, Y., Minamic, M. 2007. *Determination of residual strength parameters of jointed rock masses using the GSI system*. Int J Rock Mech Min Sci. 44(2): 247-65

Cargill, J. S., Shakoor, A. 1990. *Evaluation of empirical methods for measuring the uniaxial compressive strength of rock*. Int J Rock Mech Min Sci and Geomech Abstr, 27(6): 495-503.

Carranza-Torres, C. 1998. *Self-similarity analysis of the elastoplastic response of underground openings in rock and effects of practical variables*. Ph.D. Thesis. University of Minnesota. United States

Carranza-Torres, C. 2000. *Personal communication*.

Carranza-Torres, C., Alonso, E., Alejano, L.R., Varas, F., Fdez-Manin, G. 2002. *Elastoplastic analysis of deep tunnels in brittle rock using a scaled form of the Mohr-Coulomb failure criterion*. In: Hamma et al. (ed.). Proceedings of the 5th North American Rock Mechanics Symposium – Tunn. Assoc. Can., Toronto: 283-93.

Carter, J., Diederichs, M.S., Carvalho, J.L. 2008. *Application of modified Hoek-Brown transition relationships for assessing strength and post-yield behavior at both ends of the rock competence scale*. 6th International Symposium on Ground Support in Mining and Civil Engineering Construction, Cape Town, South Africa.

Cipullo, A., White, W., Lee, I.K. 1985. *Computer controlled volumetric strain measurements in metadolerite*. Bull Eng Geol Environ. 32(1):55–65.

Cook, N.G.W. 1970. *An experiment proving that dilatancy is a pervasive volumetric property of brittle rock loaded to failure*. Rock Mech. 2(4):181–8.

Coulomb, C.A. 1773. *Essai sur une application des régles de maximis & minimis à quelques problèmes de statique, relatifs à l'architecture*. Acad. Roy. Sci. Mem. Math. Phys. 7:343-382

Crouch, S.L. 1970. *Experimental determination of volumetric strains in failed rock*. Int J Rock Mech Min. 7(6): 589-603

Crowder, J.J., Bawden, W.F. 2004. *Review of post-peak parameters and behavior of rock masses: current trends and research*. Available online for discussion. http://www.rocscience.com

Crowder, J.J., Bawden, W.F. 2006. *The estimation of post-peak rock mass properties: numerical back- analysis calibrated using in situ instrumentation data*. Rocnews, available online from: http://www.rocscience.com/library/rocnews.

Detournay, E. 1986. *Elasto-plastic model of a deep tunnel for a rock with variable dilatancy*. Rock Mech Rock Eng. 19: 99-108

Dershowitz, W.S., Herda, H. 1992. *Interpretation of fracture spacing and intensity*. In proceedings of the 33rd US Symposium on Rock Mechanics. Santa Fe, NM. 8-10 June, 1992. pp: 757-766.

Diederichs, M. S. 1999. *Instability of hard rock masses: The role of tensile damage and relaxation*. (Unpublished PhD). University of Waterloo, Waterloo, Ontario, Canada.

Diederichs, M. S. 2003. *Rock fracture and collapse under low confinement conditions*. Rock Mech Rock Eng. 36: 339-381.

Diederichs, M. S., Martin, C. D. 2010. *Measurement of spalling parameters from laboratory testing*. In Zhao, Labiouse, Dudt & Mathier (Eds.), Rock mechanics in civil and environmental engineering. London: Taylor & Francis Group.

Doruk, P. 1991. *Analysis of the laboratory strength data using the original and modified Hoek-Brown criteria*. MSc thesis. University of Toronto. Canada

Duncan-Fama, M.E., Trueman, R., Craig, M.S. 1995. *Two and three dimensional elastoplastic analysis for coal pillar design and its application to highwall-mining*. Int J Rock Mech Min Sci & Geomech Abstr. 32(3): 215-25

Dunham, R. J. 1962. *Classification of carbonate rocks according to depositional texture*. American Association of Petroleum Geologists Memoirs, 1, 108-121.

Edmond, J. M., Paterson, M. S. 1972. *Volume changes during the deformation of rocks at high pressures*. Int J Rock Mech Min Sci. 9: 161-182.

Elliot, G.M., Brown, E.T. 1985. *Yield of a soft, high porosity rock*. Geotechnique. 35(4):413–23.

Exadaktylos, G.E., Tsoutrelis, C.E. 1993. *Scale effect on rock mass strength and stability*. In proceedings of Symposium on scale effect in rock masses. Lisbon, Portugal. 25 June, 1993. Pp 101-110.

Farmer, I.W. 1983. *Engineering behavior of rocks*. 2nd ed. London: Chapman & Hall.

Fredrich, J. T., Evans, B., Wong, T. 1989. *Micromechanics of the brittle to plastic transition in Carrara marble*. J Geophys Res. 94: 4129-4145.

Fredrich, J. T., Evans, B., Wong, T. 1990. *Effect of grain size on brittle and semi-brittle strength: Implications for micromechanical modelling of failure in compression*. J Geophys Res. 95: 10,907-10,920.

Gercek, H. 2007. *Poisson's ratio values for rocks*. Int J Rock Mech Min Sci. 44(1):1–13.

Griggs, D. T., Turner, F. J., Heard, H. C. 1960. *Deformation of rocks at 500 to 800 degrees C*. Geol Soc Amer Mem. 79: 39-104.

Hadizadeh, J., Rutter E. H. 1983. *The low temperature brittle-ductile transition in quartzite and occurrence of cataclastic flow in nature*. Geol Rundsch. 72(2): 493-503

Hart, D. J., Wang, H. F. 1995. *Laboratory measurements of a complete set of poroelastic moduli for berea sandstone and indiana limestone*. J Geophys Res. 100: 17,741-17,751.

Hassani, F.P., White, M.J., Branch, D. 1984. *The behavior of yielded rock in tunnel design. Stability in underground mining II*. Lexington, Kentucky.

Heap, M.J., Faulkner, D.R. 2008. *Quantifying the evolution of static elastic properties as crystalline rock approaches failure*. Int J Rock Mech Min Sci. 45:564-573

Hill, J. R. 2013. *Indiana Limestone*. Retrieved 08/01, 2013, from: http://igs.indiana.edu/MineralResources/Limestone.cfm

Hoagland, R. G., Hahn, G. T., Rosenfield, A. R. 1973. *Influence of microstructure on fracture propagation in rock*. Rock Mech. 5: 77-106.

Hoek, E., Brown, E.T. 1980a. *Empirical strength criterion for rock masses*. J Geotech Eng Div ASCE. 1013-1025.

Hoek, E., Brown, E.T. 1980b. *Underground excavations in rock. The Institution of Mining and Metallurgy*. London, Chapman & Hall.

Hoek, E. 1983. *Strength of jointed rock masses*. 1983 Rankine lecture. Géotechnique. 23(3):187-223

Hoek, E. Brown, E.T. 1988. *The Hoek-Brown failure criterion – a 1988 update*. In Curran J.C. (ed.). Proc. of the 15th Canadian Rock Mechanics symposium. Toronto, Canada. 31-38

Hoek, E., Wood, D, Shah, S. 1992. *A modified Hoek-Brown criterion for jointed rock masses*. In: Hudson JA, editor. Proceedings of the rock characterization, EUROCK 1992. London: British Geotechnical Society: 209-214.

Hoek, E. 1994. *Strength of rock and rock masses*. ISRM News Journal. 2(2): 4-16

Hoek, E., Kaiser, P. K., Bawden W. F. 1995. *Support of Underground Excavations in Hard Rock*. Balkema, Rotterdam

Hoek, E., Brown, E.T. 1997. *Practical estimates of rock mass strength*. Int J Rock Mech Min. 34(8): 1165-87

Hoek, E., Marinos, P., Benissi, M. 1998. *Applicability of the Geological Strength Index (GSI) classification for very weak and sheared rock masses. The case of the Athens Schist Formation*. Bull Eng Geol Env. 57: 151-160

Hoek, E., Carranza-Torres, C., Corkum, B. 2002. *Hoek-Brown failure criterion – 2002 edition*. In: Proceedings of the NARMS-TAC 2002, Mining innovation and technology. Toronto, Canada. Vol. 1: 267-73

Hoek, E., Diederichs, M.S. 2006. *Empirical estimation of rock mass modulus*. Int J Rock Mech Min Sci. 43(2): 203-215

Holcomb, D.J. 1978. *Quantitative model of dilatancy in dry rock and its application to Westerly granite*. J Geophys Res. 83(B10):4941–50.

Howarth, D. F., Rowlands, J. C. 1987. *Quantitative assessment of rock texture and correlation with drillability and strength properties*. Rock Mech Rock Eng. 20: 57-85.

Hudson, J.A., Brown, E.T., Fairhurst, C. 1971a. *Optimizing the control of rock failure in servo-controlled laboratory tests*. Rock Mech. 3(4):217–24.

Hudson, J.A., Brown, E.T., Fairhurst, C. 1971b. *Shape of the complete stress–strain curve for rock*. In: Proceedings of the 13th symposium on rock mechanics. University of Illinois.

Hudson, J.A., Crouch, S.L., Fairhurst, C. 1972. *Soft, stiff and servo-controlled testing machines: a review with reference to rock failure*. Eng Geol. 6:155–89.

ISRM. 2007. *The complete ISRM suggested methods for rock characterization, testing and monitoring: 1974–2006*. Prepared by the commission on testing methods, ISRM. Ankara, Turkey: Ulusay R, Hudson JA.

Itasca Consulting Group. 2011. *FLAC version 7.0 - theory and background* (Fifth ed.). Minneapolis, Minnesota:

Jaeger, J., Cook, N.G.W., Zimmerman, R.W. 2007. *Fundamentals of rock mechanics*. 4th ed. Oxford: Wiley-Blackwell.

Ji, Y., Baud, P., Wong, T. 2012. *Characterization of pore geometry of Indiana limestone in relation to mechanical compaction*. Oil Gas Sci Technol. 67(5): 753-775.

Kudoh, K., Koyama, T., Nambo, S. 1999. *Support design of a large underground cavern considering strain-softening of the rock*. Ninth ISRM congress, Paris. Balkema, Rotterdam. 1, 407-411.

Kulatilake, P.H.S.W., He, W., Um, J., Wang, H. 1997. *A physical model study of jointed rock mass strength under uniaxial compressive loading*. Int J Rock Mech Min Sci Geomech Abstr. 34 (3-4): 692-693.

Kulatilake, P.H.S.W., Liang, J., Gao, H. 2001. *Experimental and numerical simulations of jointed rock block strength under uniaxial loading*. J Eng Mech. 127 (12): 1240-1247.

Kwásniewski, M., Rodríguez-Oitabén, P. 2012. *Study on the dilatancy angle of rocks in the pre-failure domain*. Harmonising Rock Engineering and the Environment – Qian & Zhou (eds). I: 681-686. Taylor & Francis Group, London.

Levkovitch, V., Reusch, F., Beck, D. 2010. *Application of a non-linear confinement sensitive constitutive model to mine-scale simulations subject to varying levels of confining stress*. In "Rock Mechanics in Civil and Environmental Engineering”. Zhao J, Labiouse V, Dudt JP, Mathier JF (Editors), CRC Press, 161-164.

Loew, S., Ziegler, H., Keller, F. 2000. *ALPTRANSIT: Engineering geology of the world's longest tunnel system*. GeoEng2000, an International Conference on Geotechnical and Geological Engineering, Melbourne. 1: 927-937.

Lunardi, P. 2008. *Design and construction of tunnels Analysis of controlled deformation in rocks and soils*. Wien, Austria: Springer.

Marinos, P., Hoek, E. 2000. *GSI – A geologically friendly tool for rock mass strength estimation*. Proc. GeoEng 2000 Conference. Melbourne, Australia. pp .1422-1442.

Martin, C.D., Read, R.S. 1996. *AECL’s mine by experiment: a test tunnel in brittle rock. Rock mechanics: tools & techniques*. In: Proc. of the NARMS’96 symposium. In Aubertin, Hassani and Mitri, Montreal, 19–21 June. Balkema: Rotterdam.

Martin, C. D. 1997. *Seventeenth Canadian geotechnical colloquium: The effect of cohesion loss and stress path on brittle rock strength*. Can Geotech J. 34: 698-725.

Martin, C.D., Lu, Y., Lan, H., Christiansson, R. 2014. *Numerical approaches for estimating the effect of scale on rock mass strength*. In proceedings 7th Nordic Grouting Symposium and 2nd Nordic Rock Mechanics Symposium. Ghotemburg, 13-14 November, 2014. pp: 93-106

Mas Ivars, D., Pierce, M.E., Darcel, C., Reyes-Montes, J., Potyondy, D.O., Paul Young, R., Cundall, P.A. 2011. *The Synthetic Rock Mass approach for jointed rock mass modelling*. Int J Rock Mech Min Sci. 48: 219-244.

Mathworks Inc. 2006. *Curve fitting toolbox 1: User’s guide*. Mathworks Inc.

Medhurst, T.P. 1996. *Estimation of the in situ strength and deformability of coal for engineering design*. Ph.D. thesis. University of Queensland.

Medhurst, T.P., Brown, E.T. 1998. *A study of the mechanical behavior of coal for pillar design*. Int J Rock Mech Min. 35(8): 1087-105

Mogi, K. 1966. *Pressure dependence of rock strength and transition from brittle fracture to ductile flow*. Bulletin of the Earthquake Research Institute, 44, 215-232.

Mohr, O. 1900. Welche umstände bedingen die elastizitätsgrenze und den bruch eines materials?. Zeitschrift des Vereins Deutscher Ingenieure. 44:1524-1530, 1572-1577

Nuclear Waste Management Organization (NWMO). 2015. *About the DGR*. Retrieved 08/07, 2015, from: http://www.nwmo.ca/dgr

Olsson, W. A. 1974. *Grain size dependence of yield stress in marble*. J Geophys Res. 79(32): 4859-4862.

Ord, A. 1991. *Deformation of rock: A pressure-sensitive, dilatant material*. Pure and Applied Geophysics, 137, 337-366.

Panet, M., 1995. *Le calcul des tunnels par la méthode des curves convergence-confinement*. Presses de l’École Nationale des Ponts et Chaussés. Paris, France.

Peck, L., Barton, C. C., Gordon, R. B. 1985. *Microstructure and the resistance of rock to tensile fracture*. Journal of Geophysical Research, 90, 1533-1546.

Pérez-Rey, I., Arzúa, J., Barbiero, J., Alejano, L.R. Walton G. *A lab-testing based geomechanical characterization of metamorphic rocks focusing on post-failure behavior*. EUROCK2014 - Rock Engineering and Rock Mechanics: Structures in and on Rock Masses – Alejano, Perucho, Olalla & Jiménez (Eds). 27-29, May. Vigo. CRC Press, Taylor and Francis Group, London

Price, A.M., Farmer, I.W. 1979. *Application of yield models to rock*. Int J Rock Mech Min Sci. 16(2):157–60.

Ramamurthy, T. 1986. *Stability of rock masses*. Indian Geomechanics Journal. 16(1): 1-74.

Ramamurthy, T., Arora, V.K. 1994. *Strength predictions for jointed rocks in confined and unconfined states.* Int J Rock Mech Min Sci Geomech Abstr. 31:9-22

Ramamurthy, T. 2001. *Shear strength response of some geological materials in triaxial compression*. International Journal of Rock Mechanics and Mining Sciences, 38, 683-697.

Ramírez-Oyanguren, P., Alejano, L.R. 2008. *Mecánica de Rocas: Fundamentos e ingeniería de taludes*. *Máster Internacional "Aprovechamiento sostenible de los recursos minerales"* Castroviejo-Bolibar, R., Espí-Rodriguez, J.A. (Ed.).728 pp. Madrid.

Robinson, R. H. 1959. *The effect of pore and confining pressure on the failure process in sedimentary rocks*. Colo School Mines Q. 54: 177-199.

Rocscience. 2009. *RocLab – freeware*. Rocscience Inc. Toronto, Canada. http://www.rocscience.com

Rocscience. 2011. *RocSupport –Rock support interaction and deformation analysis for tunnels in weak rock. Tutorial Manual*. Rocscience Inc. Toronto, Canada. http://www.rocscience.com

Rocscience. 2013. *Unwedge*. Rocscience Inc. Toronto, Canada. http://www.rocscience.com

Rodriguez-Dono, A., Alejano, L.R. 2012. *Comportamiento post-rotura de los macizos rocosos y su aplicación al diseño de excavaciones subterráneas*. EAE, Germany.

Rummel, F., Fairhurst, C. 1970. *Determination of the post-failure behavior of brittle rock using a servo-controlled testing machine*. Rock Mech. 2(4): 189–204.

Santarelli, F.J., Brown, E.T., Maury, V. 1986. *Analysis of borehole stresses using pressure-dependent linear elasticity*. Int J Rock Mech Min Sci Geomech Abstr. 23:445-449

Schmidt, R. A., Huddle, C. W. 1977. *Effect of confining pressure on fracture toughness of Indiana limestone*. Int J Rock Mech Min Sci Geomech Abstr. 14: 289-293.

Scholz, C.H. 1968. *Micro-fracturing and the inelastic deformation of rock in compression*. J Geophys Res. 73:1417–32.

Serafim, J. L., Pereira, J. P. 1983. *Consideration of the geomechanical classification of Bieniawski*. Proc. Int. Symp. On Engineering Geology and Underground Construction. Lisbon 1(II): 33-44.

Singh, A.B. 1997. *Study of rock fracture by permeability method*. J Geotech Geoenviron. 123(7):601–8.

Starfield, A.M., Cundall, P.A. 1988. *Towards a methodology for rock mechanics modelling*. Int J Rock Mech Min Sci Geom Abstr. 25(3): 99-106.

Turner, F.J., Griggs, D.T., Heard, H.C. 1954. *Experimental deformation of calcite crystals*. Geol Soc Amer Bull. 65: 883-934.

USGS. 2013. *Mineral Commodity Summaries 2013*. Retrieved 01/11/2013 http://pubs.er.usgs.gov/publication/mineral2013

Vajdova, V., Baud, P., Wong, T. 2004. *Compaction, dilatancy, and failure in porous carbonate rocks*. J Geophys Res. 109(5): B05204 1-16.

Varas, F., Alonso, E., Alejano, L.R., Fdez.-Manin, G. 2005. *Study of bifurcation in the problem of unloading a circular excavation in a strain softening material*. Tunn undergr Sp Tech. 20: 311-322.

Vardoulakis, I.G., Sulem, J. 1993. *Application of bifurcation theory of rock mechanics problems*. In: Hudson. J, editor. Comprehensive rock engineering, vol. 1. Oxford: Pergamon Press. p. 576–610.

Vardoulakis, I.G., Sulem, J. 1995. *Bifurcation analysis in geomechanics*. Blackie academic and professional. London

Vermeer, P.A., de Borst, R. 1984. *Non-associated plasticity for soils, concrete and rock*. Heron. 29(3): 3-64

Von Kármán, Th. 1911. *Festigkeitsversuche unter allseitigem druck*. Verh Dtsch Ing. 55:1749–57.

Walton, G., Diederichs, M.S. 2012. *Comparison of approaches for modelling dilation of brittle rock masses around circular excavations and associated issues*. 46th US Rock Mechanics / Geomechanics Symposium. 4: pp. 2757-2766.

Walton, G. 2014. *Improving continuum models for excations in rockmasses under high stress through and enhanced understanding of post-yield dilatancy*. Ph.D. Thesis. Queen's University.

Walton, G., Arzúa, J., Alejano, L.R., Diederichs, M.S. 2015. *A Laboratory testing-based study on the strength, deformability and dilatancy of carbonate rocks at low confinement*. Rock Mech Rock Eng. 48:941-958.

Walton, G., Diederichs, M.S. 2015a. *A new model for the dilation of brittle rocks based on laboratory compression test data with separate treatment of dilatancy mobilization and decay*. Geotech Geol Eng. 33:661-679.

Walton, G., Diederichs, M.S. 2015b. *A mine shaft case study on the accurate prediction of yield and displacements in stressed ground using lab-derived material properties*. Tun Undergr Sp Tech. 49:98-113.

Wawersik, W. R., Fairhurst, C. 1970. *A study of brittle rock fracture in laboratory compression experiments*. Int J Rock Mech Min Sci. 7(5): 561-564.

Wawersik, W.R., Brace, W.F. 1971. *Post-failure behavior of a granite and diabase*. Rock Mech. 3(2):61–85.

Wawersik, W.R. 1975. *Technique and apparatus for strain measurements on rock in constant confining pressure experiments*. Rock Mech. 7(4):231–41.

World Bank Group. 2015. Retrieved 08/06/2015. http://www.worldbank.org/

Yuan, S-C., Harrison, J.P. 2004. *An empirical dilatancy index for the dilatant deformation of rock*. Int J Rock Mech Min Sci. 41(4): 679-86

Zhang, K., Zhou, H., Shao, J. 2013. *An experimental investigation and an elastoplastic constitutive model for a porous rock*. Rock Mech Rock Eng. 46:1499-1511.

Zhao, X.G., Cai, M. 2010a. *A mobilized dilation angle model for rocks*. Int J Rock Mech Min Sci. 47(3): 368-84

Zhao, X.G., Cai, M. 2010b. *Influence of plastic shear strain and confinement-dependent rock dilation on rock failure and displacement near an excavation boundary*. Int J Rock Mech Min Sci. 47(5): 723-38

Zhao, X., Cai, M., Cai, M. 2010. *Influence of dilation on rock mass displacement around underground excavations-a case study of Donkin-Morien tunnel in Canada*. Chin J Rock Mech Eng. 2(4): 338-49

Zheng, Z., Cook, N. G. W., Myer, L. R. 1989. *Stress induced microcrack geometry at failure in unconfined and confined axial compressive tests*. U.S. Rock Mechanics Symposium. 30: 749-756.

Zhou, Y., Wu, S.C., Gao, Y.T., Misra, A. 2014. *Macro and meso analysis of jointed rock mass triaxial compression test by using Equivalent Rock Mass (ERM) technique*. J Central South Univ. 21:1125-1135.

Appendices

Appendix A. Complete development of the strains relationship

Traditional approaches to estimating the radial strain starting from the axial and volumetric strain are reflected in:

$$\varepsilon_v = \varepsilon_1 + 2 \cdot \varepsilon_3 \rightarrow \varepsilon_3 = \frac{\varepsilon_v - \varepsilon_1}{2} \tag{A.1}$$

Consider the model of deformation of a cylindrical sample as seen in Fig. A.1.

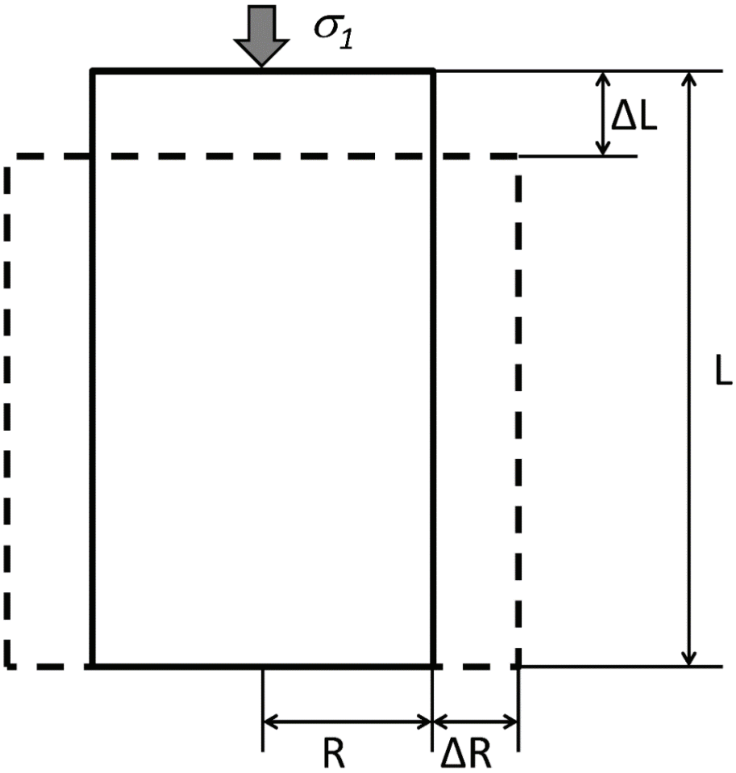

Fig. A.1. Unconfined test diagram, idealized deformational behavior and notation used.

The volumetric strain can be accurately calculated as sample volume change in relation to the original volume of the sample:

$$\varepsilon_v = \frac{\Delta V}{V} = \frac{L\pi R^2 - \left[\left(L - \Delta L \right) \pi \left(R + \Delta R \right)^2 \right]}{L\pi R^2} \tag{A.2}$$

By developing the terms in this equation we obtain:

$$\varepsilon_v = \frac{\Delta V}{V} = -\frac{2\Delta R}{R} - \frac{\Delta R^2}{R^2} + \frac{\Delta L}{L} + \left(\frac{2\Delta L}{L} \cdot \frac{\Delta R}{R} \right) + \left(\frac{\Delta L}{L} \cdot \frac{\Delta R^2}{R^2} \right) \tag{A.3}$$

And, considering the definition of strain terms in a cylindrical sample test:

$$\varepsilon_1 = \frac{\Delta L}{L}$$

$$\varepsilon_2 = \varepsilon_3 = -\frac{\Delta R}{R} \tag{A.4}$$

$$\varepsilon_v = \frac{\Delta V}{V}$$

The following expression is obtained:

$$\varepsilon_v = 2\varepsilon_3 - \varepsilon_3^2 + \varepsilon_1 + 2\varepsilon_1\varepsilon_3 + \varepsilon_1\varepsilon_3^2 \tag{A.5}$$

Which can be represented as a quadratic equation:

$$0 = (\varepsilon_1 - \varepsilon_v) + 2(1-\varepsilon_1)\varepsilon_3 - (1-\varepsilon_1)\varepsilon_3^2 \tag{A.6}$$

It can easily be solved as follows:

$$\varepsilon_3 = \frac{-2(1-\varepsilon_1) \pm \sqrt{4(1-\varepsilon_1)^2 + 4(1-\varepsilon_1)(\varepsilon_1 - \varepsilon_v)}}{-2(1-\varepsilon_1)} = 1 \mp \sqrt{\frac{1-\varepsilon_v}{1-\varepsilon_1}} \tag{A.7}$$

Since the positive root has no physical meaning, the final valid equation remains:

$$\varepsilon_3 = 1 - \sqrt{\frac{1-\varepsilon_v}{1-\varepsilon_1}} \tag{A.8}$$

It is important to note that Eq. (A.1) will be produced if second and third order infinitesimal terms are rejected during development of the equation.

If the two formulations are compared, a slight difference can be observed at very high strain levels, as depicted in Figure A.2. This difference is not relevant in this study, so the simplified formulation was used to obtain radial strain.

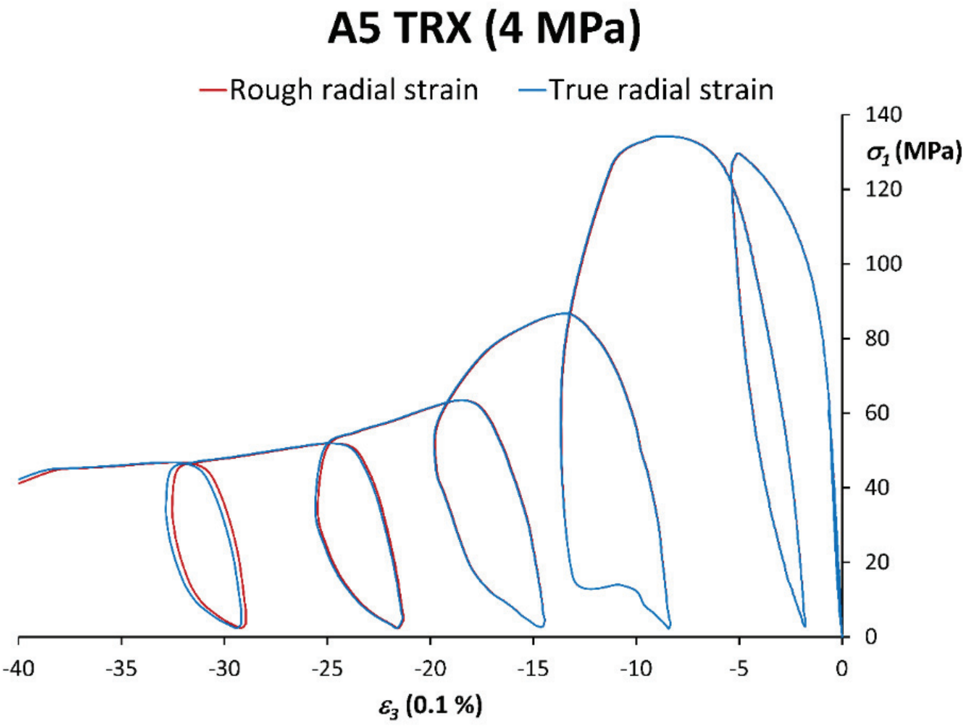

Fig. A.2. Comparison between approximate and true formulations for deformation model.

Appendix B. Tables of tests results

Table B.1. Summary of results of elastic, strength and post-failure parameters obtained for each tested specimen of the Amarelo País granite.

Type	Specimen name	Diameter (mm)	Length (mm)	Confinement (MPa)	Peak strength (MPa)	Residual strength* (MPa)	Tangent Young's mod. (GPa)	Poisson's ratio	Secant Young's mod. (GPa)	Drop modulus* (GPa)
Unconfined	A1 RCS	54.40	107.05	0	77.50	--	21.67	0.13	14.51	--
	A2 RCS	54.05	109.40	0	84.64	--	22.36	0.19	15.47	--
	A3 RCS	54.40	111.70	0	76.66	2	17.63	0.20	13.86	--
	A4 RCS	54.40	111.10	0	75.60	5	22.92	0.18	--	--
	A5 RCS	54.40	109.15	0	80.34	2	20.27	0.15	14.16	--
	A6 RCS	54.05	109.70	0	76.91	2	18.59	0.18	13.60	--
	A7 RCS	54.40	110.40	0	68.47	--	17.60	0.21	13.27	--
	A8 RCS	54.40	110.70	0	77.19	2	19.30	0.17	13.67	--
	A9 RCS	54.40	108.00	0	74.85	2	18.97	0.17	13.46	--
	A10 RCS	54.40	107.30	0	76.17	--	16.35	0.19	11.16	--
	A11 RCS	54.55	106.00	0	80.08	--	15.95	0.16	11.53	--
	A12 RCS	53.30	105.40	0	74.74	1	16.00	0.15	11.17	-19.11
Confined	A1 TRX	54.00	99.70	2	130.42	32	30.54	0.19	17.33	-17.39
	A2 TRX	54.40	99.65	2	117.33	30	23.40	0.19	14.26	-16.00
	A3 TRX	54.40	99.55	2	112.29	27	22.32	0.22	13.37	-16.67
	A4 TRX	54.40	98.65	2	110.31	31	23.95	0.20	15.58	-17.65
	A5 TRX	54.45	99.00	4	134.20	44	25.06	0.19	14.33	-21.06
	A6 TRX	54.40	100.05	4	130.02	43	24.36	0.22	16.23	-17.39
	A7 TRX	54.40	99.55	4	129.89	54	25.25	0.20	16.20	-17.15
	A8 TRX	54.40	98.00	4	129.50	46	23.84	0.22	14.31	-22.10
	A9 TRX	54.40	98.20	6	153.90	51	27.48	0.21	17.49	-21.05
	A10 TRX	54.40	99.50	6	170.72	45	30.02	0.21	16.55	-19.55
	A11 TRX	54.15	99.95	6	175.43	48	30.01	0.20	18.05	-19.05
	A12 TRX	54.40	100.50	6	169.00	51	30.40	0.18	19.15	-17.57
	A13 TRX	54.40	100.30	10	192.75	80	28.06	0.22	17.20	-19.03
	A14 TRX	54.05	100.05	10	213.99	75	35.49	0.19	21.34	-21.69
	A15 TRX	54.40	99.80	10	200.71	87	33.69	0.15	20.09	-21.74
	A16 TRX	54.40	101.00	10	193.09	68	29.45	0.21	17.67	-20.18
	A17 TRX	54.40	99.60	12	214.99	81	31.20	0.20	19.12	-18.52
	A18 TRX	54.40	100.10	12	230.14	80	36.08	0.20	21.33	-20.00

Table B.2. Summary of results of elastic, strength and post-failure parameters obtained for each tested specimen of the Vilachán granite.

Type	Specimen name	Diameter (mm)	Length (mm)	Confinement (MPa)	Peak strength (MPa)	Residual strength* (MPa)	Tangent Young's mod. (GPa)	Poisson's ratio	Secant Young's mod. (GPa)	Drop modulus* (GPa)
Unconfined	C1 RCS	54.15	109.40	0	127.45	--	27.27	0.11	19.50	--
	C2 RCS	54.10	108.85	0	116.92	--	25.84	0.17	18.11	--
	C3 RCS	54.15	110.60	0	114.17	--	22.92	--	14.64	--
	C4 RCS	54.10	109.50	0	121.22	--	23.09	0.19	16.75	--
	C5 RCS	54.15	111.10	0	119.09	--	25.53	0.15	18.82	--
	C6 RCS	54.10	108.75	0	104.30	--	21.13	0.17	14.45	--
	C7 RCS	54.15	109.60	0	129.18	--	23.51	0.12	17.67	--
	C8 RCS	54.10	109.70	0	117.96	--	23.07	0.28	18.42	--
	C9 RCS	54.10	110.00	0	113.53	--	21.88	0.19	15.65	--
	C10 RCS	54.10	109.55	0	106.61	--	21.03	0.14	14.78	--
	C11 RCS	54.10	109.90	0	113.60	--	24.09	0.20	17.76	--
	C12 RCS	54.10	111.55	0	108.77	--	22.39	0.11	15.09	--
Confined	C1 TRX	54.10	99.10	2	146.25	--	24.00	0.11	15.83	-13.37
	C2 TRX	54.15	98.65	2	141.99	40	23.16	0.17	14.05	-15.32
	C3 TRX	54.10	99.10	2	140.91	34	24.45	0.20	15.61	-17.97
	C4 TRX	54.10	99.00	2	146.13	36	24.14	0.22	16.06	-18.18
	C5 TRX	54.10	100.10	4	169.53	52	29.41	0.17	19.00	-15.68
	C6 TRX	54.10	99.95	4	160.13	53	27.82	0.18	17.96	-19.05
	C7 TRX	54.15	99.80	6	185.76	50	29.27	--	18.70	-15.29
	C8 TRX	54.15	99.15	4	161.01	43	27.21	0.22	17.90	-15.49
	C9 TRX	54.15	99.50	4	160.88	35	27.04	0.20	18.08	-20.07
	C11 TRX	54.10	99.30	6	187.84	49	27.79	0.19	18.71	-19.17
	C12 TRX	54.10	100.85	6	195.46	47	31.70	0.18	19.68	-19.05
	C13 TRX	54.10	99.90	10	239.61	71	33.10	0.20	20.35	-22.03
	C14 TRX	54.10	99.85	10	241.22	70	34.85	0.18	20.71	-21.51
	C15 TRX	54.15	101.50	10	209.77	64	27.82	0.21	17.63	-22.72
	C16 TRX	54.15	100.15	10	231.61	63	30.23	0.17	19.23	-19.84
	C17 TRX*	54.15	101.90	15	266.22	--	32.12	0.14	19.52	--
	C18 TRX*	54.10	99.60	15	259.45	--	31.29	0.19	18.91	--

* These tests overpassed the confining stress limit of the press, blocking the confining stress system after specimen failure, so there are no values for post-peak parameters.

Table B.3. Summary of results of elastic, strength and post-failure parameters obtained for each tested specimen of the Carrara marble.

Type	Specimen name	Diameter (mm)	Length (mm)	Confinement (MPa)	Peak strength (MPa)	Residual strength* (MPa)	Tangent Young's mod. (GPa)	Poisson's ratio	Secant Young's mod. (GPa)	Drop modulus* (GPa)
Unconfined	CM1	54.00	97.10	0	95.06	--	45.88	0.11	35.26	-21.71
	CM2	54.00	99.15	0	91.65	--	50.34	0.18	34.51	-22.68
	CM3	53.90	96.10	0	89.93	--	40.51	0.26	34.50	-19.91
	CM4	53.90	99.15	0	93.17	--	42.03	0.17	37.94	-23.00
	CM5	53.90	98.30	0	95.54	--	46.52	0.16	33.92	-20.68
	CM6	53.90	96.45	0	98.04	--	42.30	0.15	35.27	-16.20
Confined	CM7	53.90	96.00	1	95.28	19	46.91	0.20	36.11	--12.18
	CM8	53.90	97.90	1	96.15	9	45.94	0.15	33.86	-14.64
	CM9	53.90	97.45	1	93.13	12	46.05	0.14	34.63	-10.70
	CM10	53.90	97.60	2	100.14	18	45.97	0.11	36.12	-8.37
	CM11	54.00	99.15	2	99.73	18	46.49	0.15	38.34	-9.00
	CM12	53.90	95.45	2	101.55	25	46.17	0.16	30.79	-12.04
	CM13	53.90	94.95	4	103.47	33	43.85	0.15	28.76	-7.50
	CM14	53.90	95.35	4	102.90	32	44.34	0.10	31.77	-10.24
	CM15	53.90	98.15	4	107.72	35	45.67	0.17	37.29	-6.55
	CM16	53.90	98.30	6	112.02	35	46.63	0.14	28.99	-14.22
	CM17	53.90	97.45	6	112.15	37	48.50	0.15	24.51	-8.74
	CM18	53.90	95.50	6	109.70	42	45.68	0.15	29.66	-5.98
	CM19	53.90	97.20	8	113.20	45	47.81	0.15	28.42	--
	CM20	53.90	95.95	8	117.23	46	48.40	0.14	29.03	-11.27
	CM21	53.90	98.00	10	120.70	57	55.03	0.18	26.30	-5.62
	CM22	53.90	98.65	10	119.73	64	52.5	0.17	35.09	-4.49
	CM23	53.90	95.05	12	125.78	68	52.08	0.17	27.75	-12.68
	CM24	53.90	97.75	12	123.41	67	51.74	0.12	32.46	-6.54
	CM30	53.90	97.15	12	128.89	68	52.32	0.17	20.54	-9.40

Table B.4. Summary of results of elastic, strength and post-failure parameters obtained for each tested specimen of the Indiana limestone.

Type	Specimen name	Diameter (mm)	Length (mm)	Confinement (MPa)	Peak strength (MPa)	Residual strength* (MPa)	Tangent Young’s mod. (GPa)	Poisson’s ratio	Secant Young’s mod. (GPa)	Drop modulus* (GPa)
Unconfined	IBL-1	54.17	99.84	0	60.18	--	24.80	0.10	21.83	--
	IBL-2	54.14	99.85	0	61.64	0	26.18	0.10	22.43	--
	IBL-3	54.16	99.91	0	62.29	2	24.19	0.11	20.58	--
	IBL-4	54.14	99.81	0	59.86	3	25.88	0.17	21.35	--
	IBL-5	54.13	99.82	0	61.88	--	26.78	0.14	20.33	--
	IBL-6	54.14	99.83	0	60.94	3	22.48	0.14	20.28	--
	IBL-7	54.14	99.88	0	59.77	--	26.51	0.09	21.74	--
	IBL-8	54.13	99.89	0	59.14	1	24.45	0.12	19.92	--
	IBL-9	54.16	99.89	0	60.68	--	20.86	0.17	21.81	-65.92
	IBL-10	54.16	99.90	0	61.98	3	24.72	0.15	20.88	--
Confined	IBL-11	54.16	99.88	1	72.84	18	26.26	0.11	21.07	-27.45
	IBL-12	54.15	99.84	1	65.93	18	24.76	0.19	19.18	-47.77
	IBL-13	54.06	99.89	1	64.83	17	24.37	0.16	19.76	-30.18
	IBL-14	54.08	99.85	2	73.40	18	25.25	0.18	19.36	-27.76
	IBL-15	53.98	99.90	2	69.17	21	24.54	0.14	19.60	-25.69
	IBL-16	54.02	99.82	2	71.12	23	25.04	0.17	18.85	-44.04
	IBL-17	54.11	99.84	4	76.58	27	24.95	0.20	19.69	-22.93
	IBL-18	54.14	99.81	4	76.28	32	25.00	0.19	18.83	-21.07
	IBL-19	54.13	99.84	4	76.09	33	25.19	0.13	19.19	-38.26
	IBL-20	54.14	99.80	6	87.44	47	28.69	0.17	18.91	-10.31
	IBL-21	54.16	99.90	6	87.46	60	27.88	0.20	18.72	-16.45
	IBL-22	54.09	99.88	6	85.30	47	27.58	0.16	19.41	-21.63
	IBL-23	54.18	99.92	8	91.52	60	25.59	0.17	18.57	-7.46
	IBL-24	53.97	99.86	8	89.92	60	26.89	0.19	19.04	-24.89
	IBL-25	54.17	99.89	8	92.29	63	26.51	0.18	18.70	-15.38
	IBL-26	53.96	99.81	10	93.19	68	25.15	0.14	17.54	-16.44
	IBL-27	54.02	99.86	10	94.16	66	25.25	0.13	18.10	-6.67
	IBL-28	54.18	99.85	10	97.85	70	26.04	0.17	18.31	-9.71
	IBL-29	54.18	99.83	12	98.42	67	25.64	0.16	17.39	-21.13
	IBL-30	54.01	99.86	12	93.97	70	24.68	0.14	18.49	-5.91
	IBL-31	53.96	99.80	12	93.23	73	24.46	0.17	17.60	-9.22

Table B.5. Summary of results of elastic, strength and post-failure parameters obtained for each tested specimen of the Toral de los Vados limestone.

Type	Specimen name	Diameter (mm)	Length (mm)	Confinement (MPa)	Peak strength (MPa)	Residual strength* (MPa)	Tangent Young's mod. (GPa)	Poisson's ratio	Secant Young's mod. (GPa)	Drop modulus* (GPa)
Unconf.	CTV1	54.45	99.60	0	148.89	--	46.13	0.04	39.55	--
	CTV2	54.40	97.20	0	112.55	--	39.96	0.11	36.97	-24.10
	CTV3	54.40	100.10	0	102.35	13	35.89	0.11	28.42	--
	CTV4	54.35	100.00	0	108.71	9	43.67	0.08	35.64	--
	CTV21	54.40	99.45	0	125.37	12	40.64	0.15	34.10	--
Confined	CTV5	54.40	99.75	2	108.38	42	56.96	0.17	34.94	-87.41
	CTV6	54.40	99.15	2	150.76	31	59.30	0.06	49.31	--
	CTV7	54.40	98.10	2	143.57	27	61.72	0.15	49.73	-49.61
	CTV8	54.35	101.60	4	174.31	38	61.34	0.18	50.46	-31.08
	CTV10	54.30	100.80	4	120.13	32	48.10	0.19	43.26	-18.33
	CTV11	54.40	100.40	4	144.39	42	47.85	0.18	38.35	--
	CTV12	54.40	99.15	6	162.67	55	54.10	0.15	38.43	--
	CTV13	54.40	99.80	6	149.47	47	58.15	0.17	46.63	--
	CTV14	54.40	101.60	6	195.16	41	60.79	0.21	48.55	--
	CTV15	54.40	99.60	8	196.28	57	54.59	0.2	41.92	-36.64
	CTV16	54.40	99.70	8	203.12	69	60.22	0.18	46.55	--
	CTV17	54.40	100.45	10	168.27	89	57.68	0.17	39.62	-57.39
	CTV18	54.40	100.80	10	219.08	69	59.75	0.15	46.44	-41.42
	CTV19	54.40	100.40	12	215.08	72	60.62	0.14	47.20	-24.64
	CTV20	54.40	101.05	12	233.15	79	51.87	0.15	41.04	--

Table B.6. Summary of results of elastic, strength and post-failure parameters obtained for each tested specimen of the Noia gneiss. Observe that this rock should be classified as Class II (Hudson et al., 1972) due to its brittleness (results of drop modulus > 0, marked in bold in the table).

Type	Specimen name	Diameter (mm)	Length (mm)	Confinement (MPa)	Peak strength (MPa)	Residual strength* (MPa)	Tangent Young's mod. (GPa)	Poisson's ratio	Secant Young's mod. (GPa)	Drop modulus* (GPa)
Confined	GN2	54.90	100.00	2	285.99	26	51.62	0.14	47.08	-162.52
	GN3	53.80	100.90	2	259.23	39	52.00	0.07	43.48	**580.14**
	GN4	53.70	100.20	2	308.19	36	53.68	0.09	43.56	**241.36**
	GN5	54.90	101.50	4	317.29	48	55.21	0.06	45.98	-89.87
	GN6	53.90	99.20	4	286.23	45	53.66	0.12	46.45	-32.18
	GN7	55.00	99.40	4	332.09	68	53.44	0.12	47.08	**129.36**
	GN8	54.90	100.10	6	340.78	68	54.96	0.09	46.81	**57.90**
	GN9	53.90	98.60	6	299.33	61	53.53	0.07	47.00	**61.61**
	GN10	55.00	99.00	6	336.14	73	56.58	0.09	47.80	**57.71**
	GN22*	55.00	100.20	12	405.96	--	33.26	0.13	44.08	--
	GN23*	53.90	101.50	10	367.83	--	48.70	0.15	46.53	--
	GN24*	53.60	100.80	8	351.04	--	47.96	0.15	44.85	--
	GN25	55.00	98.50	6	313.15	73	56.82	0.09	43.74	-267.09
	GN26	55.00	100.70	4	344.74	--	57.87	0.10	51.09	-38.80
	GN27	54.70	100.90	2	289.75	27	52.31	0.09	46.38	-121.98
	GN28	55.00	99.40	4	271.61	62	60.63	0.10	43.95	-64.73

* These tests overpassed the confining stress limit of the press, blocking the confining stress system after specimen failure, so there are no values for post-peak parameters.

Table B.7. Summary of results of elastic, strength and post-failure parameters obtained for each tested specimen of the Touro amphibolite.

Type	Specimen name	Diameter (mm)	Length (mm)	Confinement (MPa)	Peak strength (MPa)	Residual strength* (MPa)	Tangent Young's mod. (GPa)	Poisson's ratio	Secant Young's mod. (GPa)	Drop modulus* (GPa)
Unconf.	ANF18	54.20	107.9	0	84.47	--	14.50	0.08	11.13	-12.74
	ANF19	54.20	107.2	0	102.07	--	17.16	0.09	14.04	-14.59
	ANF20	54.30	107.65	0	99.67	--	21.38	0.05	16.28	-9.40
	ANF21	54.00	101.30	0	118.72	--	29.52	0.12	20.64	-5.39
	ANF22	54.05	100.20	0	115.32	--	24.82	0.11	19.22	--
Confined	ANF1	54.30	100.00	2	99.58	18	28.53	0.16	22.07	-9.31
	ANF2	54.50	99.80	2	134.69	23	30.11	0.14	21.78	-11.96
	ANF3	53.00	99.50	2	151.12	18	26.96	0.13	22.33	-16.71
	ANF4	54.15	99.85	4	159.27	45	29.63	0.15	21.36	-20.93
	ANF5	54.50	97.20	4	146.95	30	27.93	0.18	22.45	-12.60
	ANF6	54.50	100.2	4	151.96	30	31.02	0.18	22.97	-22.30
	ANF7	54.50	99.45	6	176.44	40	33.40	0.14	26.28	-20.54
	ANF8	54.50	100.45	6	130.53	44	31.42	0.17	12.85	-17.08
	ANF9	54.15	100.55	6	136.53	44	23.83	0.16	18.23	-14.34
	ANF10	54.50	100.70	10	145.10	50	31.27	0.18	24.29	-14.92
	ANF11	54.55	99.45	10	169.35	60	31.39	0.18	20.13	-12.89
	ANF12	54.20	101.10	10	149.23	60	22.75	0.18	16.00	-13.86
	ANF13	54.50	99.65	12	160.75	57	32.35	0.15	27.24	-39.10
	ANF14	54.50	99.65	12	196.71	58	33.17	0.13	23.18	-18.27
	ANF15	54.05	101.10	12	185.45	66	31.96	0.19	25.82	-21.21

Table B.8. Summary of results of elastic, strength and post-failure parameters obtained for each tested specimen of the Blanco Mera granite.

Type	Specimen name	Diameter (mm)	Length (mm)	Confinement (MPa)	Peak strength (MPa)	Residual strength* (MPa)	Tangent Young's mod. (GPa)	Poisson's ratio	Secant Young's mod. (GPa)	Drop modulus* (GPa)
Intact specimens. Unconfined	B1 RCS	54.30	109.45	0	125.77	--	33.11	0.15	27.01	--
	B2 RCS	54.40	109.70	0	116.5	--	33.83	0.18	24.70	--
	B3 RCS	54.40	109.60	0	110.18	--	29.48	0.15	23.21	--
	B4 RCS	54.40	109.20	0	100.48	--	27.63	0.10	20.93	--
	B5 RCS	54.40	110.10	0	121.32	--	34.14	0.17	26.42	--
	B6 RCS	54.40	110.70	0	79.26	--	29.44	--	18.20	--
	B7 RCS	54.40	111.60	0	84.57	2	25.40	0.16	19.81	--
	B8 RCS	54.40	109.15	0	110.77	--	33.66	0.14	24.30	--
	B9 RCS	54.40	110.00	0	106.66	--	25.17	0.08	18.79	--
	B10 RCS	54.15	107.60	0	118.26	--	33.26	0.13	22.58	--
	B11 RCS	54.40	111.20	0	111.43	--	31.64	0.16	24.24	--
	B12 RCS	54.40	106.60	0	125.34	--	30.88	0.10	25.71	--
Intact specimens. Confined	B1 TRX	54.40	100.70	2	187.03	30	42.86	0.16	31.81	-25.00
	B2 TRX	54.40	98.95	2	183.41	42	44.19	0.17	33.56	-21.05
	B3 TRX	54.25	100.25	2	172.44	40	42.18	0.16	31.92	-23.52
	B4 TRX	54.40	100.50	2	177.82	34	43.07	0.18	32.80	-18.47
	B5 TRX	54.40	99.00	4	216.71	38	45.86	0.15	34.45	-18.38
	B6 TRX	54.40	99.40	4	212.58	50	42.82	0.16	33.93	-17.24
	B7 TRX	54.40	100.60	4	196.84	52	42.65	0.18	31.42	-21.52
	B8 TRX	54.40	98.10	4	214.13	54	45.55	0.17	34.55	-22.72
	B9 TRX	54.40	99.20	6	235.39	65	42.86	0.18	32.61	-24.46
	B10 TRX	54.20	100.20	6	228.20	51	43.41	0.18	33.42	-20.83
	B11 TRX	54.40	98.70	6	218.35	70	44.10	0.17	34.77	-17.24
	B12 TRX	54.40	99.25	6	240.16	74	45.17	0.20	33.83	-18.97
	B13 TRX	54.30	98.10	10	282.30	93	47.28	0.15	36.13	-22.05
	B14 TRX	54.25	96.70	10	252.18	74	41.49	0.21	28.32	-22.56
	B15 TRX	54.40	99.10	10	259.22	115	46.17	0.16	33.37	-21.74
	B16 TRX	54.40	100.50	10	269.80	85	47.12	0.17	31.15	-22.25
	B17 TRX	54.40	100.10	14	311.62	180	46.96	0.18	34.58	-21.82
	B18 TRX	54.40	98.50	12	307.62	112	48.26	0.15	36.41	-19.76
	B19 TRX	54.25	100.05	12	291.80	82	44.66	0.17	33.50	-24.88
	BM1	54.15	101.30	0.2	132.44	--	38.80	0.14	27.27	-9.02
	BM2	54.15	99.05	0.2	107.69	--	25.88	0.29	19.80	-15.24
	BM3	54.10	99.65	0.2	134.51	--	39.18	0.20	28.40	-20.18
	BM4	54.30	100.00	0.2	136.37	--	38.74	0.24	20.75	-13.71
	BM5	54.10	100.20	0.2	132.07	14	37.74	0.14	25.27	-21.83
	BM6	54.15	99.20	0.2	137.56	--	39.55	0.16	28.59	-10.20
	BM7	54.15	99.90	0.2	131.83	13	38.18	0.08	26.94	-8.36
	BM8	54.15	99.60	0.2	126.45	9	33.89	0.11	21.33	-21.56
	BM9	54.15	94.20	0.2	143.21	--	37.48	0.17	20.45	--
	BM10	54.15	100.40	0.2	91.53	12	22.46	0.23	16.13	-14.28
	BM11	54.15	100.40	4	148.2	60	25.75	0.20	19.58	-12.17
	BM12	54.15	100.10	0.2	93.05	10	27.52	0.18	17.35	-17.30

Table B.8 (cont.). Summary of results of elastic, strength and post-failure parameters obtained for each tested specimen of the Blanco Mera granite.

Type	Specimen name	Diameter (mm)	Length (mm)	Confinement (MPa)	Peak strength (MPa)	Residual strength* (MPa)	Tangent Young's mod. (GPa)	Poisson's ratio	Secant Young's mod. (GPa)	Drop modulus* (GPa)
Intact specimens. Confined	BM13	53.9	100.8	2	154.62	28	37.76	0.18	25.68	-23.94
	BM14	53.90	99.60	2	164.39	25	38.42	0.20	26.66	-17.93
	BM15	53.90	100.10	2	152.73	--	37.96	0.20	25.15	-19.59
	BM16	53.60	101.90	2	155.38	32	37.69	0.17	25.58	-31.04
	BM17	54.00	100.60	4	178.45	50	42.45	0.19	29.99	-24.86
	BM18	53.55	99.60	4	176.58	53	40.50	0.21	30.49	-11.39
	BM19	53.60	99.00	4	185.87	45	43.24	0.17	27.67	-17.26
	BM20	53.75	99.45	6	214.27	60	45.23	0.19	30.40	-31.24
	BM21	53.80	100.95	6	227.03	55	44.98	0.18	31.02	-19.17
	BM22	53.70	99.30	6	220.59	67	43.32	0.14	30.67	-16.92
	BM23	53.80	100.20	10	254.57	80	43.95	0.13	31.77	-21.74
	BM24	53.80	99.60	10	246.52	65	44.76	0.13	32.06	-22.15
	BM25	53.55	99.80	12	291.85	95	46.92	0.12	33.40	-26.65
	BM26	53.85	100.50	12	268.67	76	46.06	0.16	33.64	-24.67
	BM27	53.55	99.65	12	292.11	120	48.84	0.16	33.61	-19.57
	BM28	53.70	99.85	12	289.11	90	48.54	0.14	33.98	--
(1+2) jointed specimens. Confined	BMD1	54.05	103.20	6	144.87	76	20.45	0.23	12.36	-19.67
	BMD2	53.80	103.95	2	66.34	35	14.30	0.39	8.78	-8.64
	BMD3	54.10	101.75	0.5	44.24	20	9.46	0.18	5.24	-2.13
	BMD4	54.00	103.20	0.5	60.17	20	7.62	0.12	6.75	-18.27
	BMD5	54.10	94.05	0.5	50.20	20	8.93	0.08	4.98	-5.92
	BMD6	54.10	101.00	1	69.34	25	9.95	0.15	7.51	--
	BMD7	54.10	98.90	1	62.90	20	12.25	0.27	8.28	-7.64
	BMD8	54.15	101.00	1	79.94	20	14.16	0.24	9.83	-14.05
	BMD9	54.10	103.60	2	94.66	33	16.03	0.14	9.06	-8.17
	BMD10	54.15	101.90	2	96.09	40	14.21	0.26	10.97	-6.33
	BMD11	54.15	101.50	4	108.12	60	14.23	0.13	9.68	-6.22
	BMD12	54.15	101.85	4	137.08	65	22.61	0.22	16.55	-10.92
	BMD13	53.40	101.60	4	129.13	33	17.85	0.11	13.21	-14.60
	BMD14	54.30	101.25	6	129.63	68	17.93	0.10	11.12	-9.32
	BMD15	53.90	101.95	6	156.33	73	23.45	0.09	17.19	-57.37
	BMD16	53.25	103.10	10	193.13	105	27.07	0.12	19.12	-40.55
	BMD17	54.15	104.55	10	165.14	120	16.49	0.11	11.69	-19.16
	BMD18	54.10	102.10	10	216.38	100	27.84	0.18	19.74	-25.05
	BMD19	54.00	102.70	10	177.76	80	24.01	0.11	19.49	-8.99
	BMD20	53.35	98.90	12	210.30	130	24.59	0.15	18.69	-26.69
	BMD21	53.30	104.20	12	175.51	110	14.84	0.13	11.57	--
	BMD22	53.85	102.35	12	213.35	115	26.94	0.09	18.61	--

Table B.8 (cont.). Summary of results of elastic, strength and post-failure parameters obtained for each tested specimen of the Blanco Mera granite.

Type	Specimen name	Diameter (mm)	Length (mm)	Confinement (MPa)	Peak strength (MPa)	Residual strength* (MPa)	Tangent Young's mod. (GPa)	Poisson's ratio	Secant Young's mod. (GPa)	Drop modulus* (GPa)
(2+3) jointed specimens. Confined	JBM1	54.00	100.15	1	40.83	23	7.77	0.33	6.48	-13,21
	JBM2	54.00	100.50	2	62.31	33	9.04	0.24	6.56	-8,25
	JBM3	54.05	100.45	4	75.79	49	11.6	0.19	8.69	-4,74
	JBM4	53.70	97.90	6	96.96	70	12.39	0.25	8.03	-2,72
	JBM5	53.95	97.10	10	115.62	103	13.04	0.18	10.34	-2,41
	JBM6	53.80	98.60	1	60.53	21	9.3	0.46	6.13	-12,35
	JBM7	53.45	101.70	12	153.18	105	16.55	0.18	12.86	-3,41
	JBM8	53.80	102.10	2	58.86	35	9.79	0.21	7.26	-6,27
	JBM9	53.65	101.70	4	92.32	53	12.23	0.31	8.88	-5,88
	JBM10	54.00	101.05	6	90.95	67	12.05	0.33	9.03	-2,69
	JBM11	53.65	100.00	10	137.04	97	16.85	0.13	13.36	-3,52
	JBM12	54.00	100.90	12	139.24	115	16.34	0.15	12.75	-5,50
	JBM13	53.55	98.35	2	80.37	30	15.94	0.18	11.74	-12,58
	JBM14	53.10	100.60	2	75.86	29	13.38	0.28	9.76	-18,1
	JBM15	53.45	100.50	6	119.04	65	16.82	0.16	12.61	-13,3
	JBM16	53.60	99.75	6	81.72	65	14.91	0.09	11.98	-5,60
	JBM17	53.80	98.60	10	122.42	83	15.77	0.11	10.48	-5,35
	JBM18	53.40	98.35	10	110.96	--	16.36	0.1	12.04	-5,85
	JBM19	53.65	97.30	12	196.27	117	26.32	0.2	18.43	-13,15
	JBM21	53.65	99.75	12	166.59	125	22.33	0.13	15.82	-6.63

Appendix C. Examples of FLAC models.

C.1. Example of a FLAC model like those presented in chapter 7, that corresponding to an Amarelo Pais granite specimen, a confining stress of 6 MPa and a mesh size of 40x80.

```
Triaxial tests of strain-softening material (Granite Amarelo Pais 54
; mm tests results) small grid considered 0.054m * 0.1m cylindrical sample
; with controlled velocity. The dilatancy model is included
title
  Triaxial test of strain-softening granite rock (conf. 6 MPa)
g 40 80
gen 0,0 0,0.1 0.054,0.1 0.054,0 i=1,41 j=1,81
mo ss
call servo.fis
call DIL_Amarelo_Pais.fis
fix y j 1
ini yvel -2e-7 j 81

pro den 2610 bul 1.26398e10 sh 9.87815e9 co 10e6 fri 46 ten 6.65e6 dil 40
pro ftab 1 ctab 2
table 1 0.0,46.0 0.001561,51.003427 0.002087,53.067107 0.002610,53.998869
table 1 insert 0.003129,54.272879 0.003646,54.120568 0.004161,53.671774
table 1 insert 0.004674,53.007067 0.005186,52.182194 0.005696,51.237935
table 1 insert 0.006205,50.207356 0.006713,49.117719 0.008231,45.722388
table 1 insert 0.009741,42.518628 0.011245,39.837874 0.012744,37.812937
table 1 insert 0.015234,35.769639 0.017718,34.862937 0.025157,34.444940
table 1 insert 0.035088,34.507759
table 2 0.0,10.0e6 0.001561,13.873932e6 0.002087,15.148380e6 0.002610,16.017942e6
table 2 insert 0.003129,16.597884e6 0.003646,16.961622e6 0.004161,17.159073e6
table 2 insert 0.004674,17.223110e6 0.005186,17.180602e6 0.005696,17.054642e6
table 2 insert 0.006205,16.859609e6 0.006713,16.609078e6 0.008231,15.628013e6
table 2 insert 0.009741,14.466445e6 0.011245,13.284131e6 0.012744,12.193184e6
table 2 insert 0.015234,10.736367e6 0.017718,9.763050e6 0.025157,8.646159e6
table 2 insert 0.035088,8.450027e6
app pres 6e6 i 1
app pres 6e6 i 41
ini sxx -6e6 syy -6e6 szz -6e6

app yvel -2e-7 j 81

def sigmav
   sum=0.0
   loop i (1,igp)
      sum=sum+yforce(i,jgp)
   end_loop
   sigmav=sum/(x(igp,jgp)-x(1,jgp))
end
def evaxi
   evaxi=(ydisp(21,1)-ydisp(21,81))/(y(21,81)-y(21,1))
end

def evtrans
    evtra01=-(xdisp(1,21)-xdisp(41,21))/(x(1,21)-x(41,21))
    evtra02=-(xdisp(1,41)-xdisp(41,41))/(x(1,41)-x(41,41))
    evtra03=-(xdisp(1,41)-xdisp(41,41))/(x(1,41)-x(41,41))
    evtra04=-(xdisp(1,41)-xdisp(41,41))/(x(1,41)-x(41,41))
    evtra05=-(xdisp(1,61)-xdisp(41,61))/(x(1,61)-x(41,61))
    evtrans=(evtra01+evtra02+evtra03+evtra04+evtra05)/5
end

def evvol
   evvol=evaxi+(2*evtrans)
end

hist sigmav
hist evaxi
hist evtrans
hist evvol
hist dilation i 1  j 40
hist dilation i 12  j 40
hist dilation i 21  j 40
hist dilation i 40 j 40
hist dilation i 40 j 1
hist dilation i 40 j 12
hist dilation i 40 j 21
hist dilation i 40 j 36
hist dilation i 40 j 48
hist dilation i 40 j 60
hist dilation i 40 j 72
hist dilation i 40 j 80
hist yv i 1 j 1
hist unbal
hist sh
set high_unbal=2e4
set low_unbal=2e3
set high_vel=2e-7

set ns=10
set nsup=1500
supsolve
```

DIL Amarelo Pais.fis

```
; FISH funtion to define variable dilation angle
def cfi
  loop i (1,izones)
    loop j (1,jzones)
       effsxx = sxx(i,j)  + pp(i,j)
       effsyy = syy(i,j)  + pp(i,j)
       effszz = szz(i,j)  + pp(i,j)
       temp1=-0.5*(effsxx+effsyy)
       temp2=sqrt(sxy(i,j)^2+0.25*(effsxx-effsyy)^2)
       s3=min(temp1-temp2,-effszz)
                    if s3<0.0 then
              s3=0.0
                    end_if
                                       a_dil=adil1+adil2*2.7182^(-(s3/1e6)/adil3)
                                       b_dil=bdil1+bdil2*2.7182^(-(s3/1e6)/bdil3)
                                       c_dil=cdil1+cdil2((s3/1e6)^cdil3)
                                       dexp_1=2.7182^(-b_dil*2000*(e_plastic(i,j)))
                                       dexp_2=2.7182^(-c_dil*2000*(e_plastic(i,j)))
                    dilation(i,j)=a_dil*b_dil*((dexp_1-dexp_2)/(c_dil-b_dil))
     end_loop
  end_loop
end

def supstep
   cfi
   if ns=0 then
     ns=5
   end_if
   command
      step ns
      print k
   end_command
end

def supsolve
loop k (1,nsup)
   supstep
end_loop
end


set  adil1=29.01
set  adil2=28.05
set  adil3=4.76
set  bdil1=8.26
set  bdil2=17.49
set  bdil3=1.5
set  cdil1=0.014
set  cdil2=0.0749
set  cdil3=0.711

set ns=15

set nsup=300
```

C.2. Example of a FLAC model like those presented in chapter 8, that corresponding to a strain-softening rock mass with GSI = 50 and variable dilation.

```
*chi-cast-SS-con-dil.DAT

Title
"Tunnel 1500 m deep GSI 50 SS - dil-p"
config axisymmetry
grid 70,90
model elastic

gen   0,-10  0,20    5,20    5,-10    rat 1,1         i=1,16    j=1,21
gen   0,20   0,35    5,35    5,20     rat 1,0.95      i=1,16    j=21,36
gen   0,35   0,40    5,40    5,35     rat 1,1         i=1,16    j=36,51
gen   0,40   0,55    5,55    5,40     rat 1,1.03      i=1,16    j=51,66
gen   0,55   0,75    5,75    5,55     rat 1,1         i=1,16    j=66,91

gen   5,-10  5,20    10,20   10,-10   rat 1.03,1      i=16,31   j=1,21
gen   5,20   5,35    10,35   10,20    rat 1.03,0.95   i=16,31   j=21,36
gen   5,35   5,40    10,40   10,35    rat 1.03,1      i=16,31   j=36,51
gen   5,40   5,55    10,55   10,40    rat 1.03,1.03   i=16,31   j=51,66
gen   5,55   5,75    10,75   10,55    rat 1.03,1      i=16,31   j=66,91

gen   10,-10  10,20  20,20   20,-10   rat 1.05,1      i=31,46   j=1,21
gen   10,20   10,35  20,35   20,20    rat 1.05,0.95   i=31,46   j=21,36
gen   10,35   10,40  20,40   20,35    rat 1.05,1      i=31,46   j=36,51
gen   10,40   10,55  20,55   20,40    rat 1.05,1.03   i=31,46   j=51,66
gen   10,55   10,75  20,75   20,55    rat 1.05,1      i=31,46   j=66,91

gen   20,-10  20,20  50,20   50,-10   rat 1,1         i=46,71   j=1,21
gen   20,20   20,35  50,35   50,20    rat 1,0.95      i=46,71   j=21,36
gen   20,35   20,40  50,40   50,35    rat 1,1         i=46,71   j=36,51
gen   20,40   20,55  50,55   50,40    rat 1,1.03      i=46,71   j=51,66
gen   20,55   20,75  50,75   50,55    rat 1,1         i=46,71   j=66,91

his unbalanced

;MARCAR HISTORIA DEL CENTRO DEL TÚNEL
his ydis i=1 j=26
his yvel i=1 j=26

; MARCA ESQUINA
his xdis i=11 j=26
his ydis i=11 j=26

; MARCA CONVERG
his xdis i=11 j=21
his xdis i=11 j=16
his xdis i=11 j=11
his xdis i=11 j=6
his xdis i=11 j=1

initial sxx -40.5e6 syy -40.5e6 szz -40.5e6

;CONDICIÓN DE CONTORNO STRESS EN I 71  J 91
fix  y j 1
fix  x i 1

apply nstress -4.05E7 from 71,91 to 71,1
apply nstress -4.05E7 from 1,91 to 71,91

model elastic notnull
prop density=2700.0 bulk=5.83E9 shear=3.5E9 notnull
history 999 unbalanced

solve elastic
step 1000

ini xdis 0 ydis 0 xvel 0 yvel 0

model mohr ss notnull

prop density=2700.0 bulk=5.83E9 shear=3.5E9 c=5.692e6 ctable=1 f=43 ftable=3 dil=5.37
ten=0.043e6 ttable=4 notnull
table 1 0,5.692e6 0.0077,4.23e6
table 3 0,43      0.0077,36.85
table 4 0,0.043e6 0.0077,0.0091e6

*********************************************************
def cfi
 loop i (1,izones)
  loop j (1,jzones)

    effsxx = sxx(i,j)  + pp(i,j)
    effsyy = syy(i,j)  + pp(i,j)
    effszz = szz(i,j)  + pp(i,j)

    temp1=-0.5*(effsxx+effsyy)
    temp2=sqrt(sxy(i,j)^2+0.25*(effsxx-effsyy)^2)
    s3=min(temp1-temp2,-effszz)

          if s3<0.0 then
       s3=0.0
          end_if

                   a_dil=adil1+adil2*2.7182^(-(s3/1e6)/adil3)
                   b_dil=bdil1+bdil2*2.7182^(-(s3/1e6)/bdil3)
                   c_dil=cdil1+cdil2((s3/1e6)^cdil3)

                   dexp_1=2.7182^(-b_dil*200*(e_plastic(i,j)))
                   dexp_2=2.7182^(-c_dil*200*(e_plastic(i,j)))

             dilation(i,j)=a_dil*b_dil*(dexp_1-dexp_2)/(c_dil-b_dil)
   end_loop
 end_loop
end

def supstep
  cfi
  if ns=0 then
   ns=5
  end_if
  command
    step ns
    print k
  end_command
end

def supsolve
loop k (1,nsup)
  supstep
end_loop
end

set  adil1=26.5
set  adil2=16.7
set  adil3=8.7
set  bdil1=10
set  bdil2=16.1
set  bdil3=3
set  cdil1=0.014
set  cdil2=0.08
set  cdil3=0.14

set ns=15
set nsup=300
**********************************************************
model null i=1,15 j=1,10
supsolve

model null i=1,15 j=10,15
supsolve

model null i=1,15 j=16,20
supsolve
step 1000

save ar-55-ss-dil-01.sav

model null i=1,15 j=21,25
supsolve

model null i=1,15 j=26,28
supsolve

model null i=1,15 j=29,31
supsolve

save ar-55-ss-dil-02.sav

model null i=1,15 j=32,34
supsolve

model null i=1,15 j=35
supsolve
supsolve

save ar-55-ss-dil-03.sav
```